EVALUATING THE ROLE OF CROSS-FRAMES IN STRESS DISTRIBUTION OF STEEL I-GIRDER BRIDGES BY "HOLISTIC" ASSESSMENT OF FINITE ELEMENT ANALYSIS DATA

by

Matija Radovic

A dissertation submitted to the Faculty of the University of Delaware in partial fulfillment of the requirements for the degree of Doctor of Philosophy in Civil Engineering

Summer 2017

EVALUATING THE ROLE OF CROSS-FRAMES IN STRESS DISTRIBUTION OF STEEL I-GIRDER BRIDGES BY "HOLISTIC" ASSESSMENT OF FINITE ELEMENT ANALYSIS DATA

by

Matija Radovic

Approved: ____

Harry Shenton, Ph.D.
Chair of the Department of Civil and Environmental Engineering

Approved: ____

Babatunde Ogunnaike, Ph.D.
Dean of the College of Engineering

Approved: ____

Ann L. Ardis, Ph.D.
Senior Vice Provost for Graduate and Professional Education

I certify that I have read this dissertation and that in my opinion it meets the academic and professional standard required by the University as a dissertation for the degree of Doctor of Philosophy.

Signed: ____
Jennifer McConnell, Ph.D.
Professor in charge of dissertation

I certify that I have read this dissertation and that in my opinion it meets the academic and professional standard required by the University as a dissertation for the degree of Doctor of Philosophy.

Signed: ____
Michael Chajes, Ph.D.
Member of dissertation committee

I certify that I have read this dissertation and that in my opinion it meets the academic and professional standard required by the University as a dissertation for the degree of Doctor of Philosophy.

Signed: ____
Nii O. Attoh-Okine, Ph.D.
Member of dissertation committee

I certify that I have read this dissertation and that in my opinion it meets the academic and professional standard required by the University as a dissertation for the degree of Doctor of Philosophy.

Signed: ____
Tobin Driscoll, Ph.D.
Member of dissertation committee

ACKNOWLEDGMENTS

First, I would like to thank to my advisor Dr. Jennifer McConnell, for all the support and endless hours she spent on this project. I would also like to thank my parents for being patient and understanding for all these years they spent without me. I would also like to thank to my girlfriend Amira, for being there for me in the most difficult times. I would also like to extend my gratitude to my American family, Sharon and Dan Halm from Omaha, for opening their home and their hearts for me. Furthermore, I would also like to thank to my friend, Sasa Potkonjak from Chicago, for his financial and moral support for the better part of this decade. And finally, I would like to acknowledge former and current grad students from the UD Bridge Engineering Lab (Philipp, Shafique, Hadi, Arsha, Ali and Matt) for keeping me grounded and sharpening my research and analytics skills through, sometimes heated, but insightful debates and arguments that we had over the years.

TABLE OF CONTENTS

LIST OF TABLES

LIST OF FIGURES

ABSTRACT

Cross-frames are bridge structural members that provide lateral-load resistance and stability during construction, reduce buckling length of the compression flanges of steel girders, and to contribute to distribution of traffic loads among girders at in-service bridges. It is hypothesized that cross-frames, play positive role in load distribution among the girders, and by extension contribute in increasing bridge system capacity. Furthermore, understanding the mechanisms behind the load sharing among bridge components at design and inelastic load levels could help with better understanding system-level behavior of bridges, In the light of the nationwide high inventory of structurally deficient bridges, the application of system-level analysis would allow for better identification and prioritization of the most critical structures and allow for a more efficient use of the limited financial resources available for infrastructure investments. Therefore, to goal of this study was to investigate the role that cross-frame play in bridge stress distribution at in-service bridge. Prior research showed that for highway steel I-girder bridges, bridge skew, cross-frame type, and cross-frame placement can significantly affect bridge response in terms of stress distribution. Cross-fame designs (K-frame vs. X-frame), cross-frame layouts (inline vs. staggered) and bridge five skews (0°, 25°, 46°, 55° and 63°) were selected as parameters of interest. Additionally, FE models without the cross-frames (No-frame models) were added to each bridge skew. Combining all parameters of interest total of 25 bridge FE modes were built and analyzed.

Stress distributions of main bridge components (girders, deck and cross-frames were extracted) from the models and evaluated using “holistic” level approach. The “holistic” level approach refers to comprehensive assessment of all FEA stress distribution data, not only peak values. The results showed that by using “holistic” evaluation of stress distribution data, we were able to identify and quantify best performing cross-frame configuration. However, results also indicate that removing cross-frames from bridges did not substantially affected stress distributions throughout the bridge. This finding was further strengthen by Tensor decomposition analysis of stress distribution data. This method found that removing cross-frames from the bridge models did not affect substantially stress distributions at design load levels. Although, removing cross-frames from the bridge models did affect stress distribution at first yield and system yield load level, it did not affect overall system capacity of the bridge.

Chapter 1

INTRODUCTION

1.1 Current State of Practice

Cross-frames are bridge structural members that are intended to provide lateral-load resistance and stability during construction, reduce the buckling length of the compression flanges of steel girders, and contribute to distribution of traffic loads among girders for in-service bridges in current practice. Because cross-frames have significant detailing demands, they are very expensive to fabricate and install, especially at highly skewed bridges. All this motivates bridge engineers to search for the optimal cross-frame design in terms of size, spacing, and connectivity that will make cross-frames efficient, inexpensive, and reliable.

Furthermore, based on the experimental testing conducted by Jorgenson at el. (1972) Burdette and Goodpasture (1973), Miller et al. (1992), Bakht and Jaeger (1992) Aktan et al. (1994) and McConnell et al. (2014a), it is known that bridges have system capacity much greater than predicted by the current design code. Simplistically stated, this occurs in part because the load redistribution between the members comprising the bridge is not explicitly considered in design codes; rather design codes are based on designing each member individually. Cross-frames provide transverse load paths enabling this redistribution, and thus may be able to be optimized to lead to increasing system capacity of bridges. Bridge system capacity is a measure of the capacity of the bridge when load redistribution between members is considered, in contrast to the present design philosophy where the capacity is limited by the most heavily stressed member.

With the development of computing powers in the late 20th and early 21st century, engineers and researchers started numerically analyzing detailed three dimensional models of the bridge structures. Three dimensional models are advantageous compared to one dimensional models ("line" models), because they can capture the response of bridge structure as a system, therefore enabling predictions of bridges' system capacity. Detailed 3D numerical models allowed for in depth investigation of how the load is distributed among the bridge components. Using advanced mathematical modeling in terms of finite element analysis (FEA), researchers were able to investigate the role that load transferring components (such as cross-frames) might play in the bridge system capacity (e.g., Chen et all. 1986). However, typically, engineers and researchers, when analyzing FEA data, implement a "discrete" approach for data assessment, which means that they tend to evaluate only peak values in the data. While "discrete" analysis is deemed sufficient when analyzing certain bridge behaviors, it might not be sufficient to capture the mechanisms leading to the observed stress distribution in steel I-girder bridges. This study suggests that to better understand the stress distribution in steel I-girder bridges, a comprehensive "holistic" data assessment of all FEA stress distribution data is needed.

1.2 Goal of the Study

The main goal of the study is to evaluate the role that cross-frames play in stress distributions for steel I-girder bridges in general, and at skewed bridges in particular, using a "holistic" assessment of FEA data. The holistic approach to stress data assessment refers to comprehensive and thorough analysis of the stress distribution as opposed to selective evaluation of peak values at specific locations. This approach includes identifying and designing a proper set of measurements capable of comprehensive and thorough exploration of the role that cross-frames play in stress distribution. An additional goal of the study is to identify optimal cross-frame configurations (in terms of cross-frame type and cross-frame layout) that could efficiently distribute stresses in bridges at different skews and under different load levels.

1.3 Significance of the Study

The results of this research could lead to fundamental changes in the manner in which cross frames are analyzed, designed and, most importantly, deployed, especially for skewed steel I-girder bridges. A possible unique and distinguishing result of this study is to see if the quantity of cross-frames may be eliminated for certain bridge configurations. Furthermore, this study introduces completely new approach (holistic analysis) in evaluating FEA data, which be used in other engineering disciplines that employ FEA.

Finally, quantifying how much cross-frames assist in distributing stresses in steel I-girder bridges could help with:

a) Suggesting the best performing cross-frame configurations that could maximize live load distribution in steel I girder bridges.

b) Identifying the optimal number of cross-frames in the bridge to efficiently distribute live load. This could lead to decreasing the number of cross-frames needed in the bridge, and consequently a reduction in construction costs due to eliminating labor intensive and expensive cross-frame installations.

c) Identifying the optimal size of the cross-frames needed to efficiently distribute live load. Optimizing the size of the cross-frame could reduce potential issues related with distortion induced fatigue associated with oversized and improperly detailed cross-frames.

1.4 Research Plan

To achieve the objectives of this study following research plan was developed:

- Validate and calibrate a FE model of a representative highway steel I-girder bridge.
- Create and conduct a FEA parametric study.
- Design and implement "holistic" evaluation of FEA stress distribution data.
- Authenticate "holistic" evaluation of FEA data results using multiway analysis.

Each of these aspects of the research plan are detailed on in the following subsections.

1.4.1 Validation and Calibration of Finite Element Model

McConnell at al. (2015) instrumented and destructively tested a full scale steel I-girder bridge, labeled “7R”. McConnell at al. (2015) also built finite element model of the bridge. Radovic and McConnell (2014) modified and improved this FE model making it more suitable for the “holistic” type analysis. The field data was used to validate and calibrate this improved finite element model. This improved finite element model was then used as a template for building other bridge models with varying bridge design parameters.

1.4.2 Parametric Finite Element Analysis

To investigate the influence of cross-frames on stress distribution, 25 finite element parametric models were built and analyzed. The structural elements of these models have the same geometry and cross-sectional properties, but the bridges have varying skews, cross-frame types and cross-frame layouts. A total of five bridge skews (0°, 25°, 46°, 55°, and 63°), two cross-frame types (K-frame and X-frame) and two cross-frame layouts (inline and staggered) were incorporated in the parametric study. Additionally, at each skew, bridge models without cross-frames were also analyzed. Different cross-frame types and different cross-frame layouts serve to identify the best performing cross-frame combination in distributing stresses at different skews.

1.4.3 Design Numerical Instruments for “Holistic” Evaluation of Stress Distribution Data

Four specially designed numerical instruments (metrics) were developed to comprehensively evaluate stress distribution data. These “holistic” metrics were designed with the intent of revealing the trends in the data that would otherwise remain undetected if traditional approach to data evaluation was conducted.

1.4.4 Authenticate "holistic" evaluation of FEA data

A special case of tensor decomposition method called Tucker decomposition was used to validate the "holistic" evaluation results. The differences in stress distributions among bridge structural elements when employing or eliminating cross-frames were analyzed at different load levels for different cross-frame layouts and configurations.

1.5 Dissertation Organization

Chapter 1: Introduction

This is the introductory chapter which identifies the problem that needs to be addressed, outlines study objectives, and the research plan.

Chapter 2: Background and Literature Review

The second chapter provides background on bridge system capacity and the different bridge design philosophies. The reader is introduced with bridge engineering terminology, different cross-frame designs and layouts. Furthermore, the current state of evaluating the output from finite element analysis in bridge engineering is also discussed. The background section is followed by a literature review that gives a historical overview of cross-frames in current and prior bridge design manuals and examines the role of cross-frames in bridge system capacity. Furthermore, the literature review also covers the role of cross-frames play in distortion induced fatigue at straight and skewed bridges and the effects that removing cross-frame from the bridge could have on stresses associated with this phenomenon. The main goal of this chapter is to familiarize readers with the previous work in this field and to introduce readers with the dissertation's main topics and terminology.

Chapter 3: Finite Element Analysis Validation and Calibration

The third chapter details the validation and calibration procedure of finite element (FE) modeling of the "7R" bridge. Additionally, this chapter covers in detail all steps that are necessary to build accurate and well performing finite element models, including accurately and efficiently reproducing cross-frame stresses. The first section in the Chapter 3 provides readers with information on how the element mesh was built and boundary conditions and composite action were modeled. It also covers material properties modeling and load modeling. This section is followed with discussing the validation of the modeling techniques by comparing to theoretical solutions and calibration of specific input parameters to field results. Additionally, this chapter makes recommendations for what type of FE modeling should be used for parametric FEA models such as those that are built and analyzed in Chapter 4.

Chapter 4: "Holistic" Evaluation of Stress Distribution Data

This chapters introduces reader the parametric study's design as well as the associated motivation and research hypothesis relative to the background presented in Chapter 2. This chapter also introduces "holistic" metrics for assessment of stress distribution data. It compares and contrast the difference between "discrete" and "holistic" data assessment approaches. This is followed by the results of the parametric models using these approaches and discussion of the main findings. The chapter ends with the summary of the findings and its implications on the current bridge engineering practice.

Chapter 5: Tensor decomposition of Finite Element Analysis Data

This chapter introduces readers to the basic operations and mathematical background of the tensor decomposition algorithms. This is followed by the review of the applications of the tensor decomposition in engineering and other fields. It also explains the benefit of multiway data analysis of the finite element data. This chapter ends with presenting the results of multiway analysis of the FEA data obtained from Chapter 4 FE parametric models.

Chapter 6: Conclusion & Recommendations

This is the concluding chapter of the dissertation. It summarizes the problem that this dissertation addressed and the associated findings. It also suggests possible applications and limitations of the findings. Additionally, it lists recommendations for future research in this area.

REFERENCES

American Association of State Highway and Transportation Officials -AASHTO (2015). "LRFD Bridge Design Specifications". *6th Edition.* AASHTO, Washington, DC.

Aktan, A.E., Naghavi, R., Farney, D.N., Lee, K.L., Aksel, T., Hebbar, K. (1994). "Nondestructive/Destructive Tests and Associated Studies on Two Decommissioned Steel Truss Bridges". *Final Report FHWA/OH-95/013.* Cincinnati Infrastructure Institute, University of Cincinnati, Cincinnati, Ohio Report No. UC-CII 94/03.

Bakht, B., Jaeger, L.G. (1992). "Ultimate Load Test of Slab-on-Girder Bridge". *Journal of Structural Engineering* 118(6), 1608-1624.

Burdette, G., Goodpasture, W. (1973). "Test of Four Highway Bridges to Failure". *Journal of the Structural Division* 99(3), 335-348, ASCE.

Chen, S. S., Daniels, J. H., Wilson, J. L. (1986). "Computer study of redundancy of a single span welded two-girder bridge". *Interim Report. June 85-Feb. 86.* Lehigh University, Bethlehem, Pa., Fritz Engineering Lab.

Fu, C., Shuqing, W. (2014). "Computational Analysis and Design of Bridge Structures". *CRC Press*. 106-107.

Helba, A., Kennedy, J. (1995)."Skew composite bridges-analyses for ultimate load". *Canadian Journal of Civil Engineering.* (22.6), 1092-1103.

Jorgenson, J., Larson, W. (1972). "Field Testing of a Reinforced Concrete Highway Bridge to Collapse". *Transportation Research Record*. (607), 66-7.

Miller, R. A., Aktan, A.E., Shahrooz, B. M. (1992). "Nondestructive and Destructive Testing of a Three Span Skewed R.C. Slab Bridge". *Nondestructive Testing of Concrete Elements and Structures,* ASCE NY. 150-161.

McConnell, J., Chajes, M., Michaud, K. (2015). "Field Testing of a Decommissioned Skewed Steel I–Girder Bridge: Analysis of System Effects". *J. Struct. Eng*., 10.1061/(ASCE)ST.1943-541X.0001112, D4014010.

Radovic, M. & McConnell, J. (2014). "Evaluation of Cross-frame Designs for Highly Skewed Steel I-Girder Bridges". *Proceedings of 48th International Bridge Conference,* Pittsburg. IBC-14-47

Chapter 2

BACKGROUND & LITERATURE REVIEW

The main purpose of the background section is to familiarize reader with three main concepts:

a) how different design philosophies quantify bridge capacity;

b) the current state of practice in evaluating finite element analysis data in the bridge engineering; and

c) the roles that cross-frames play in stress distribution of steel I-girder bridges in general and at highly skewed steel I-girder bridges in particular.

2.1 Bridge Design Philosophies – Line Girder Design vs. System Level Design

In current bridge engineering practice, structural elements such as girders, decks, cross-frames and diaphragms are designed to resist externally applied loads. While they are analyzed and designed as individual components, in reality they act as a system of interconnected and dependent elements. The contention stated in this dissertation is that bridges should not be perceived as a simple sum of individual components, but as complex collection of interactions of individual components.

Furthermore, beside the fact that in current code all bridge elements are analyzed independently, line girder analysis is commonly used to determine the force effects within the girder. Line girder analysis simplifies the three dimensional bridge structure to one dimension (line) configurations and essentially treats system capacity as the lowest component capacity. This simplification, severely underestimates the system redundancy and ductility that exists in the real three-dimension structure. The reason why line girder design philosophy underestimates the 3D structure's redundancy is because it does not account for the abundance of redundant load paths, provided by bridge decks and cross-frames, and the ductility of the members that allows for loads exceeding the capacity of a single member to be redistributed to lower stressed members through these load paths. These factors can significantly increase capacity of the bridge, well above values predicted by a single member. Furthermore, out-of-plane deformations present at more complex geometries such as found at skewed bridges (bridges where girders are not perpendicular to the bridge supports) are also not accounted for in line girder analysis, further undermining the accuracy of the line girder analysis assessment.

However, in the current AASHTO LRFD Bridge Design Specifications (2015) the bridge capacity is measured by evaluating capacity of individual members. According to this document the factored resistance of a structural member (ϕR_n)has to be larger than a factored load ($\gamma_i Q_i$) applied on the structure (Equation 2.1). In order to address resistance and load uncertainties, resistance of the structural member (R_n) is reduced by resistance factor ϕ ($\leq$1.00), while load effects (Q_i) are magnified by load factors γ_i (generally ≥1.00). The product of nominal resistance of a structural member, R_n, and resistance factor, ϕ, is the girder capacity and by extension bridge capacity (2.2).

$$\phi R_n \geq \sum \gamma_i Q_i \tag{2.1}$$

The design philosophy behind this approach can be called single element capacity (SEC), and this design philosophy assumes that an entire system has reached its load capacity once one of its members has reached its capacity. This approach may produce inefficient bridge designs and could also underestimate the load ratings of existing bridges.

Alternatively, a system level capacity (SLC) approach assumes that a system has reached its capacity only after all members of the system have reached theirs or all load redistribution paths have been exhausted. The SLC measures how much loading the whole system can bear before it structurally fails. This design philosophy relies on the assumption that the bridge is a system with sufficiently ductile elements, that is, system of elements that are able to maintain load-carrying capacity even after yielding (Nowak A., Collins K. (2012)). Therefore, it is not a coincidence that field testing has shown that bridges' system capacity is much greater than predicted by the design code (Jorgenson et al. (1972), Burdette and Goodpasture, (1973), Miller et al. (1992), Bakht and Jaeger. (1992) and Aktan et al. (1994), McConnell et al. (2015)).

If an SLC approach is assumed and a bridge is considered to be a system of inter-depended load carrying elements, then the load carrying capacity of the bridge can be described as a function of the capacities of all load carrying components in the bridge. However, it would not be correct to assume that the load carrying capacity of the bridge system is a simple sum of the load carrying capacity of its load carrying members. In order for that to be true, the bridge would have to have a very efficient load transferring mechanism. This mechanism should be able to transfer the load among primary load carrying members in the bridge. In highway bridges the load transferring members are bridge decks and cross-frames. However, it was found that load transferring members can fail before all bridge main load carrying members reached their capacity, reducing the theoretical bridge system capacity (McConnell et al., 2015).

There were attempts in the past to utilize a system capacity approach in bridge rating procedures. The importance of quantifying bridge rating in the bridge engineering field is enormous. Bridges are rated to ensure they are safe for use by the general public and to help determine federal funding for bridge replacement or rehabilitation. Bridge load rating is a method that quantifies the safe live-load carrying capacity of any bridge structure, expressed as a rating factor (RF), which is a multiple of the number of the design vehicles the bridge can safely carry. The RF can be conceptually expressed as

$$\mathrm{RF} = \frac{C - f_D \cdot D}{f_L \cdot L \cdot (1+I)} \tag{2.2}$$

where, f_D = factor for dead loads, f_L = factor for live load, D = dead load effect, I = impact factor, L = live load effect and C = capacity of the bridge.

In 1993, Galambos, et al. proposed inelastic rating procedures for the highway bridges based on system level considerations. The idea behind the study was to define the strength limit state in terms of deflection stability or a specified maximum permanent deflection. This inelastic rating procedure takes advantage of the system strength inherent in multi-girder structures of multi-span bridges by using system level considerations to lower the live load effect. However, this novel idea was soon abandoned due to perceptions of being time prohibitive and overly complex, and was never implemented in AASHTO bridge rating manuals.

2.2 Calculating Bridge System Level Capacity

Although the AASHTO LRFD Bridge Design Specifications (AASHTO LRFD for brevity, 2015) currently provides no direct method by which bridge system level capacity can be directly calculated, ways to determine it have been suggested. McConnell et al., (2015) suggests calculating bridge system level capacity as the sum of the moment capacities of all girders in the bridge cross-section. If this method is used to calculate bridge system capacity, two assumptions had to be met:

1) that structural elements are sufficiently ductile; and
2) that load-transfer mechanisms can redistribute loads from the most heavily stressed girders to the remainder of the girders.

The first step in this procedure is to calculate the moment capacities of all girders in the bridge. If calculations show that the yield moment is the governing capacity then the next step in determining this quantity is calculating the live load moment (MAD) that causes yielding in the girder's cross-section. MAD can be obtained by Equation 2.3,

$$\mathrm{M_{AD}} = \mathrm{S_n}\left[\mathrm{F_y} - \frac{\mathrm{M_{D1}}}{\mathrm{S_s}} - \frac{\mathrm{M_{D2}}}{\mathrm{S_{3n}}}\right] \tag{2.3}$$

where M_{D1} is moment due factored permanent loads on the steel cross-section, M_{D2} is moment due factored permanent loads (such as wearing surface and barriers) on the long term composite section; F_y is yielding strength of the steel and S_n, S_s and S_{3n} are section moduli of composite section, steel section, and long term composite section.

Once calculated, M_{AD} can be compared to an applied moment resulting from positioning an HS-20 design vehicle on a bridge structure in a way to produce the maximum possible bending moment in the girders. If, for example, M_{AD} of one girder is calculated to be 10 kip·ft, then a total live-load capacity of a 4-girder bridge will be 40 kip·ft (if we assume all girders have the same geometry). If the maximum applied bending moment for this four-girder bridge is 8 kip·ft, then system capacity of the bridge can be expressed as the ratio of these two moments (40/8=5). Theoretically, this ratio $\frac{\Sigma M_{AD}}{M_a}$ (where M_a is maximum applied moment) **is the number of HS-20** vehicles the bridge can hold before reaching its system capacity, given that yielding moment (M_y) governs girder design.

However, destructive testing of bridges (McConnell et al., 2015) has shown that elastic-system capacity can be greater than the sum of girder capacities in skewed bridges due to longitudinal and transverse spreading of plasticity. Furthermore, Betchel et al. (2011) tested the ultimate bridge capacity of a 1/5th scaled bridge model. Using the sum of girder capacities, the authors calculated that bridge ultimate capacity was equivalent to twenty HS-20 design trucks. According to the authors' calculations, plastification of all girders should have happened/occurred at that load level. However, results showed that when the scaled bridge specimen were destructively tested in the lab, it failed at the load equivalent to 22 HS-20 design trucks. However, failure mode of the structures was due to concrete cracking, not due to steel girders yielding. The authors noted that only two out of four girders yielded and none of the girders were plastified at this load level.

In conjunction with Bechtel's findings, McConnell et al. (2015) conducted destructive testing of a full scale four-girder steel highway bridge. Using AASHTO LRFD equations to determine moment capacity, the authors calculated that full bottom flange cross-sectional yielding of one girder should have happened at a load magnitude that corresponds to fifteen HS-20 design trucks. However, during destructive testing of the bridge, yielding was not observed at any location even after load equivalent to 17 HS-20 trucks was applied.

Bridge system capacity can also be numerically evaluated, using the Modified Riks Method (Riks method in further text). This is an arc-length method used for assessing nonlinear post-buckling behavior of structures, developed by Edward Riks (1979), and used in the finite element analysis applications. The Riks method applies progressively larger magnitudes of load, while simultaneously searching for a combination of forces and displacements (and thus other associated structural response metrics such as stress) that satisfy equilibrium at each magnitude of loading. The Riks method is ideally suited to analyzing behavior after a peak loading is reached. This method can obtain solutions for cases involving complex unstable responses such as buckling and collapse (Abaqus Documentation, 2013). Algorithms for this method exist in commercial FEA software, such as Abaqus 6.11, which was used in this dissertation. A number of studies have successfully used modified Riks method in assessment of the bridge system level capacity (Ross (2007), Betchel et al. (2011), and McConnell et al. (2015).

2.3 State of Practice in Interpreting Finite Element Analysis (FEA) Data in Bridge Engineering

Finite element analysis (FEA) is commonly used to predict behavior of various structures and their assembled members. For example, FEA can be used to determine maximum strength or displacements of a structural member under a variety of loading conditions or to investigate distribution of stress among various members. As a research tool, FEA is routinely used to investigate complex structures such as bridges or buildings.

FEA discretizes structural parts into geometric shapes (elements) bounded at their corners with nodes, while assigning material properties to each element. The grid lines seen in the left of Figure 2.1 denote element boundaries for an I-shaped member. The response of these elements to input loading is calculated via a system of partial differential equations, each element containing multiple unknown quantities calculated by the FEA method (Bathe, 1982).

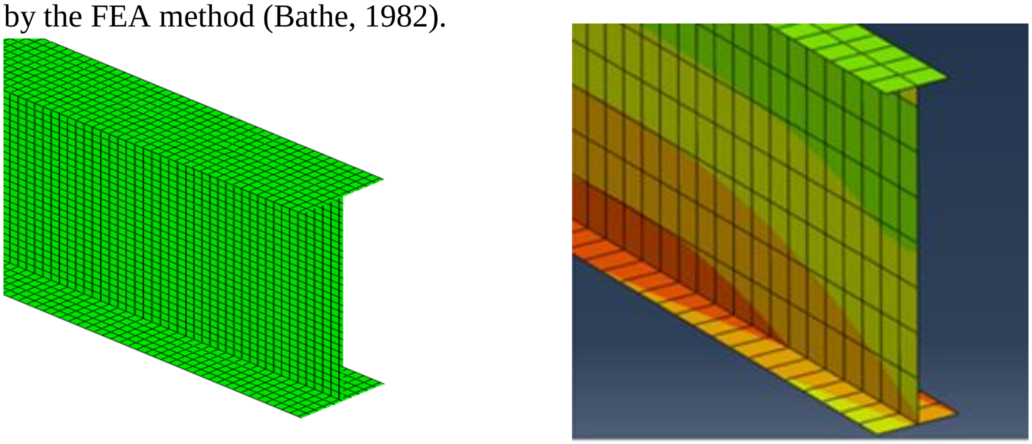

Figure 2.1 Element mesh of the finite element model (FEM) of a steel bridge I-girder (on the left) where rectangles represent discretized geometrical shapes (elements) that can be numerically modeled with a system of partial differential equations. Stress contours (on the right) show the spatial variation of stress magnitudes due to imposed loads.

Because the solution for the set of differential equations is based on numerical approximations, a more detailed set (i.e., a finer FEA mesh with a larger number of elements) will theoretically yield more accurate solutions, up to a point where the influence of mesh size converges to a common solution.

The number of elements in a typical model could vary anywhere from hundreds to millions. As a result of a typical FEA, displacements, stresses, and strains in multiple directions are computed for each element. Furthermore, one FEA may realistically contain anywhere from one to hundreds of loading conditions, producing a unique data set for each loading. Thus, the potential output from these analyses is immense. For perspective, Figure 2.2 shows a subset of potential FEA data, showing one type of output (von Mises stresses) for the elements in one structural part (bottom flange) of one highway bridge component (one girder) that was subjected to 60 load increments.

In current practice, only a small fraction of this available data is quantitatively analyzed. For example, it is often the case that only the extreme values in the data set (such as minimum/maximum stresses or maximum displacements) at a particular region of interest are analyzed. A possible exception to this statement are contour plots allowing visualization of the spatial distribution of the magnitudes of a specific output variable that can be produced by some FEA post-processing software (as seen in Figure 2.1 on the right).

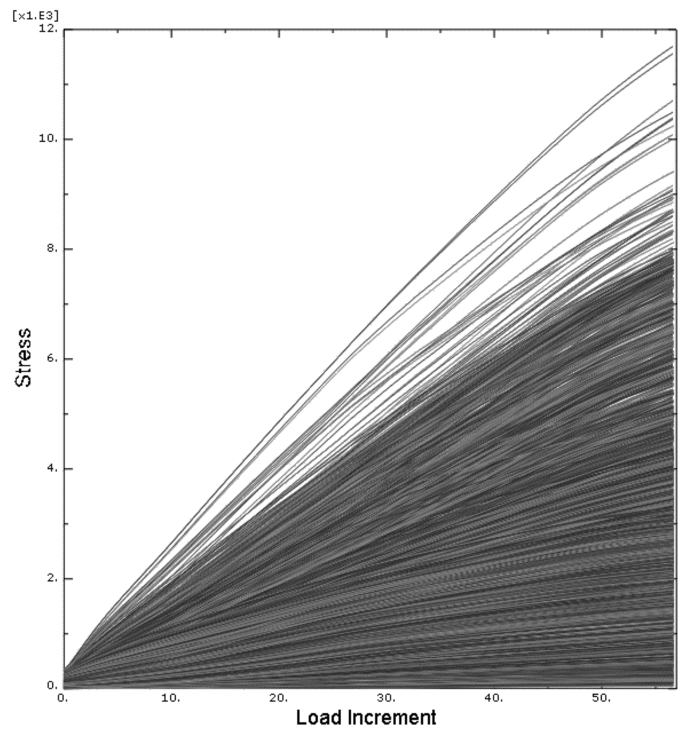

Figure 2.2 FEA output of bottom flange element stresses from bridge girder, subjected to 60 load increments. Each line represents a single bottom flange element and each point on the line represents the stress value measured at increasing load increments

While this type approach might be sufficient in some research applications, it is a premise of this dissertation that this approach limits the ability for fully understanding stress distributions in bridges. This is because when thoroughly assessing the cumulative contribution of the bridge components to the bridge stress distribution, one has to quantify stresses in all elements that represent these components. The problem arises in the fact that each bridge component, such as girders or cross-frames, might consist of thousands of elements (depending of the mesh density), and consequently thousands of stress data points. This raises a question of how to analyze the cumulative effect of that many outputs. The traditional approach would assume that the bridge component (girder, cross-frame) reached its capacity if one of the elements on the bridge component finite element mesh exceeded some pre-defined value. It is not hard to conclude that this type of approach results in a very limited view of the results.

2.4 Cross-frames in Steel I-girder Bridges

This section reviews prior findings on different roles that cross-frames play in steel bridges frames in general and role that cross-frames play in stress distribution in highly skewed bridges in particular. It also reviews studies that investigated the effect of skew on bridge behavior. The section is divided into five subsections: overview of cross-frames in steel bridges; cross-frame design in current practice; the role of cross-frames at skewed bridges; cross-frames effect on distortion induced fatigue; and role of cross-frames in bridge system capacity.

2.4.1 Overview

Cross-frames are bridge structural members that are intended to provide lateral-load resistance and stability during construction, reduce the buckling length of the compression flanges of steel girders, and contribute to distribution of traffic loads among girders. This latter role is perhaps the most uncertain. The magnitude of this role in load distribution depends on the stiffness of the cross-frames relative to the stiffness of the girders. Research showed that cross-frames actively distribute the load only when a load is directly placed above cross-frame location (Degenkolb, 1977). “Remote” cross-frames (cross-frames not in the proximity of the load) do not participate in load distribution actions. Furthermore, for more uniform transverse distribution of the live load, several closely spaced cross-frames have to be present.

“The diaphragms spacing should be as close as girder spacing…” in order to achieve significant lateral load transfer (Degenkolb, 1977).

In most cases, cross-frames are made of single or double angle steel profiles. Typical cross-frame configurations consist of diagonals, top chords, and /or bottom chords as well as gussets plates used for member connections (Figure 2.3).

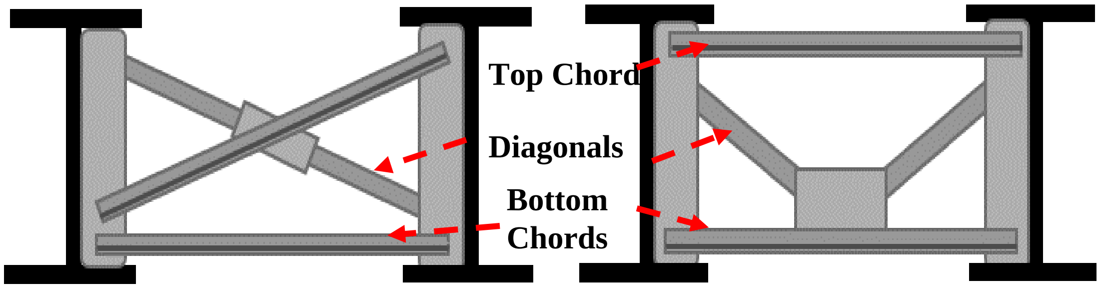

Figure 2.3The figure on the left shows a typical X-frame type consisting of diagonals and bottom chord. The figure on the right shows a typical K-frame type with diagonals, bottom chord and top chord. Girders in both figures are denoted with black color, while connection plates and cross-frame members are represented with gray color.

The most commonly used cross-frame types are X-frame and K-frame (Figure 2.3). Depending upon placement of cross-frames with respect to girder lines, a cross-frame layout can be inline or staggered, the former referring to cross-frames placed in the same transverse plane and the latter to cross-fames being longitudinally offset from each other, usually at constant distances (Figure 2.4).

Figure 2.4Inline cross-frame layout (left) and staggered cross-frame layout (right). Note that cross-frames on the left side have top chords incorporated in their design configuration, while cross-frames on the right are without the top chord members.

2.4.2 Cross-frames in Steel I-girder Bridges – Past and Current Design Guidelines

In one of the first comprehensive bridge engineering books (Bridge Engineering, 1917), J.A.L. Waddell called for bracing of top and bottom flange of girders using lateral braces. Starting in 1949, the AASHTO Standard Specifications, specified maximum limits of 25ft for cross-frame spacing. Later, this maximum spacing was investigated by experimental research (DeCatro and Kostem (1975), Zellin et al. (1975), Degenkolb (1977), and Kostem (1984)), but resulted in no conclusive explanation of why this limit was set. Eventually, the 25ft maximum spacing requirement was removed from the AASHTO Specifications (2012) and replaced with a requirement that maximum cross-frame spacing should be based on rational analysis. This new requirement also resulted in the reduction of fatigue prone attachment details associated with cross-frame to girder connection by potentially allowing fewer cross-frames.

Article 6.7.4 of AASHTO LRFD Bridge Design Specifications (2015) specifies that the general **role** for diaphragms or cross-frames in steel girder superstructures is to:

1. Transfer of lateral wind load from the bottom of the girders to the deck and from the deck to the bearings.
2. Stability of the top flange in compression prior to curing of the deck
3. Stability of the bottom flange for all loads when it is in compression.
4. Consideration of any flange lateral bending effects.
5. Distribution of vertical dead and live loads applied to the structure.

Article 6.7.4 AASHTO LRFD Bridge Design Specifications (2015) also specifies some general cross-frame **design requirements** pertaining to steel I-girder highway bridges:

1. Intermediate diaphragms or cross-frames should be provided at nearly uniform spacing in most cases for efficiency of structural design, constructability and to allow simplified methods of analysis for calculating flange lateral bending stresses. Closer spacing may be necessary adjacent to interior piers, in the vicinity of skewed supports and for some cases near mid-span.

2. Cross-frames should be as deep as practical, but the minimum should be at least one-half of beam depth for rolled beams and three-fourths the depth for plate girders.

3. Where supports are not skewed, intermediate diaphragms and cross-frames should be placed in contiguous lines normal to girders.

4. Where supports are skewed more than 20º, diaphragms or cross-frames should be placed in contiguous lines normal to girders or in staggered patterns.

2.4.3 Cross-frames in Steel I-girder Bridges –Effects of Bridge Skew and Cross-Frame Configuration

Skewed bridges are often built due to geometric restrictions, such as obstacles, complex intersections, rough terrain or space limitations (Menassa et al., 2007). In 1916, design recommendation was made to avoid building skewed bridges because of lack of understanding of their complex behavior and load distribution (Fu & Wang, 2014). However, an infrastructure boom in the early 1960's led to significant changes in construction practices. The old infrastructure was being replaced with the new, right-of-way became more difficult and expensive to acquire, and bridges were being constrained by less available space, resulting in a large number of skewed bridges being built.

A number of studies investigated the relationship between cross-frames and bridge skew. For example, (Ozgur (2011) and Radovic & McConnell (2013)) showed that as the bridge skew increases, the lateral-bending stresses in girders, is increasing. McConnell et al. (2016) tested two steel I-girder bridges with moderate (32°) and high (62°) skew. The study found that the cross-frame forces at the bridge with high skew was three times larger than cross-frame forces in the moderately skewed bridge. Similarly, Bishara & Elmir (1990) found that the higher the skew angle, the higher the maximum forces are induced in cross-frame members.

Krupicka &Poellot (1993) reported that unwanted transverse stiffness in bridge girders, if often located near skewed supports. They attributed this unwanted "nuisance" stiffness to the presence of cross-frames in the proximity of skewed supports. In order to facilitate larger load transfer between girders, designers can increase the size of the cross-frames, in some cases causing the cross-frame stiffness to approach that of the girders. However, increasing the size of the cross-frames increases the nuisance stiffness at girders' bottom flanges. The problem is that this stiffness is not typically accounted for during design. To mitigate this problem, White et al. (2012) recommended that the first intermediate cross-frames from the end support of a skewed bridge should be placed far from the support. Moving cross-frames away from the supports, especially in skewed bridges, should minimize the effects of excessive transverse stiffness that cross-frames cause.

Cross-frame layout on peak stresses in bridge girders was also investigated by McConnell et al. (2014). This study showed that cross-frame layout influences bottom flange stresses, especially if a staggered cross-frame layout is used. The staggered cross-frame layout was shown to reduce cross-frame forces at the expense of increased lateral bending stresses in the bottom flange. Furthermore, Wang at al. (2011) and Schafer (2012) also found that staggered cross-frame layouts reduces cross-frame forces at skewed bridges.

Wang and Helwig (2008) evaluated the strength and stiffness requirements for the two cross-frame layouts of perpendicular to the girders versus parallel to the skew, in moderately skewed bridges (45°). They found that the stiffness and strength requirements of the cross-frames placed parallel to the skew were more affected by the skew than the stiffness and strength requirements of the cross-frames placed perpendicular to the skew.

2.4.4 Cross-frames in Steel I-girder Bridges – Effects on Distortion Induced Fatigue

Distortion induced fatigue in steel bridges is caused by out-of-plane girder deflections, possibly resulting in cracking of girder connections due to improper detailing. This type of fatigue crack often occurs in the web near flanges at a location of welded transverse stiffener that also serves as a connection plate for the cross-frame. This type of fatigue cracking is commonly known as a “web-gap cracking”, which refers specifically to fatigue cracks induced by out-of-plane distortion in regions of girders’ web gaps. The cause of this problem originated from construction practices recommending not to weld transverse web stiffeners to a tension flange. Distortion induced fatigue is amplified by the presence of the cross-frames, because cross-frames provide additional out-of-plane load paths. The majority of steel girder highway bridges that were built in late 1960’s initially did not demonstrate any problems, but by late 1990’s, a survey of state transportation officials showed that “distortion-induced fatigue cracking is the most frequently encountered type of fatigue distress observed by various state transportation agencies” (Bowman et al. (2012)).

Furthermore, a number of studies investigated distortion induced fatigue cracking and found that cracking occurs at the web in the vicinity of the connection plate of cross-frames and girders (Keating et al. (1997), Stallings et al. (1997), Barth & Bowman (2001), Connor & Fisher (2006), McDonald & Frank

(2009)).Furthermore, researchers investigated the role of cross-frame layout, cross-frame types, and cross-frame member on the development of fatigue cracks.

Two different cross-frame layouts (staggered versus inline) were investigated by Wang et al. (2011) and Hartman et al. (2010). Wang et al. (2011) showed that staggering cross-frames will lower cross-frame forces, thus reducing the risk of fatigue problems. Hartman et al. (2010) found that staggering cross-frames can change the location of the maximum web gap stress, however the difference in the magnitude of the maximum web gap stress was very small (1%). Similarly, Hassel et al. (2013) investigated the effect that bridges with different skews, cross-frame layout and cross-frames of different sizes have on web gap stresses. The study found that the staggered cross-frame layout was least prone to distortion induced fatigue. Additionally, if the size of cross-frame members and the size of the connection stiffeners is increased, greater web gap stresses are induced.

2.4.5 Cross-frames in Steel I-girder Bridges – Effects on Bridge Capacity

A recent study (McConnell et al., 2014) found the bridge skew, cross-frame layout, and cross-frame design affect vertical and lateral peak bending stresses in steel I-girder bridges. Another study (McConnell et al, 2015) suggested that bridge system capacity of bridges with large skews can be limited because the load transferring paths (provided by cross-frames and deck) are not sufficient to allow all bridge girders' cross-sections to yield. In other words, cross-frames may yield before girders, inhibiting load transferring paths in the system.

Furthermore, it has been shown that bridge skew also affects bridge system ultimate capacity and bridge overall behavior. Helba (1995) found that as skew of the bridge increases, the system level capacity of the bridge increases. Similarly, Bechtel et al. (2011) investigated ultimate capacity of skewed, simple-span bridges by evaluating six bridge FE models having skews ranging from zero to seventy-five degrees (0°, 10°, 25°, 45°, 60°, 75°) while girder length, width and cross-frame spacing (25ft) remaining constant. The study showed that the magnitude of load needed to cause yielding in each girder increases with increasing skew angle. At 60° bridge skew, system capacity of the bridge was 19% larger than that of the model 0°. The authors concluded that large bridge skews have a beneficial effect on the system capacity of the bridges, because skewed arrangement caused major differences in the magnitude of the moments in adjacent girder cross-sections in the same transverse plane.

A few studies investigated what effect of removing cross-frames from the bridge will have on the peak stresses in the bridge. Azizinamini et al. (1995) showed that the maximum bottom flanges strain in the straight steel I- girder bridge was not affected significantly (less than 16%) by removing cross-frames. Similarly, Tedesco et al. (1995) investigated bridge behavior under live load, with and without the cross-frames. The study used validated FE models for the comparison. The results showed that removing the cross-frames from the bridge, had a "modest" effect on the overall bridge response. Specifically, if cross-frames were removed, the flexural stress and vertical deflection for "the most highly stressed girders" increased by only 8% and 9%, respectively. Stalling et al. (1997) found moderate increase (15%) in peak bottom flange stresses once the diaphragms were removed from the multi girder steel bridge. Keating & Crozier (1992) found that peak bottom flange stresses were 25% higher when cross-frames were removed from the bridge. Furthermore, Keating et al., (1997) found that up to 50 percent of the diaphragms can be removed from the bridge "without altering the load distribution characteristics of the bridge." The study was motivated by fatigue damage observed from out-of-plane web bending (distortion) at cross-frame attachments where a web gap existed.

2.5 Literature Review Summary

The foregoing literature review has showed that while the effect of skew, different cross-frame designs and placements have been investigated in straight and skewed bridges, no comprehensive research has investigated the role that cross-frames play in stress distribution under service loads or system level capacity loads. Furthermore, current bridge design specifications (AASHTO, 2015) assume that cross-frames contribute to the stress distribution in steel I-girder bridges, although some studies indicated that contribution is minimal, especially at skewed bridges (Keating, et al. (1992), Stallings, et al. (1999) and Moore, et al. (1990))

The literature reviews also showed that a link exists between bridge skew, cross-frame forces and system capacity, yet the mechanism behind mutual inter-correlation between such parameters is not clearly understood or quantified. There are two main issues when analyzing the effectiveness of the cross-frames designs when considering bridge system capacity. First issue is quantifying the degree of cross-frames yielding. The question is what would be the proper metric to evaluate cross-frame yielding. The second issue is quantifying the effect of cross-frame designs on the bridge system capacity, and the effect of cross-frame designs on the stress distribution on other bridge components (girders, deck and etc). Finally, the literature review also shows that there are no prior studies that approached investigating the role of cross-frames in the bridge stress distribution from a holistic perspective. In general, studies used discrete approach in analyzing data, i.e., analyzing only a limited number of data points.

We hypothesize that in order to accurately understand overall system behavior, comprehensive stress evaluation of bridge components is needed under both service level loads and under system level capacity loads. Such an approach should incorporate comparing and evaluating overall stress distributions throughout the bridge. For that reason, a new investigative method, termed a “holistic” approach to data analysis, such as comprehensively analyzing stress distribution of bridge components obtained from the bridge finite element analysis (FEA) data, is proposed in Chapter 4 Section 4.3.2 of this dissertation.

REFERENCES

Abaqus Version 11.3 Documentation (2012). Simulia.

American Association of State Highway and Transportation Officials –AASHTO. (2015). "LRFD Bridge Design Specifications". *6th Edition.* AASHTO, Washington, DC.

Azizinamini, A., Kathol, S., and Beacham, M. (1995). "Influence of cross-frames on load resisting capacity of steel girder bridges". *Eng. J. AISC*, 32(3), 107–116.

Barth, A. S., and Bowman, M. D. (2001). "Fatigue behavior of welded diaphragm-to-beam connections". *J. Struct. Eng*.,10.1061/(ASCE)0733-9445(2001)127:10(1145), 1145–1152.

Bathe, K.J. (1982). "Finite element procedures in engineering analysis". Englewood Cliffs, N.J: Prentice-Hall.

Bechtel, A., McConnell, J., Chajes, M. (2011)." Ultimate Capacity Destructive Testing and Finite-Element Analysis of Steel I-Girder Bridges". *J. Bridge Eng., 16(2), 197–206.*

Bishara, A. G., Elmir, W. E. (1990). "Interaction between cross-frames and girders". *J. Struct. Eng.,* 10.1061/(ASCE)0733-9445(1990)116: 5(1319), 1319–1333.

Bowman, M. D., Fu, G., Zhou, Y. E., Connor, R., Godbole, A. (2012). "Fatigue evaluation of steel bridges". *Rep. No. 721*, National Cooperative Highway Research Program, Transportation Research Board, Washington, D.C.

Connor, R. J., and Fisher, J. W. (2006). "Identifying effective and ineffective retrofits for distortion fatigue cracking in steel bridges using field instrumentation". *J. Bridge Eng*.,10.1061/(ASCE)1084-0702(2006)11: 6(745),745–752.

FHWA (Federal Highway Administration). (2012a). "Steel bridge design handbook: Bracing system design". *Publication No. FHWA-IF-12-052*, Vol.13, U.S. Dept. of Transportation, Washington, DC.

Galambos, T. V. (1998). "Guide to Stability Design for Metal Structures". 5th Edition. Wiley.

Keating, P. B., Saindon, K. C., Wilson, S. D. (1997). “Cross frame diaphragm fatigue and load distribution behavior in steel highway bridges”. *Rep. No. FHWA/TX-98/1360-2F*, National Technical Information Service, Alexandria, VA.

Keating, P. B., and A. R. Crozier. (1992). “Evaluation and Repair of Fatigue Damage of Midland County Bridges”. *Final Report. No. Tx-92/1313-1f*, Texas Transportation Institute, the Texas A & M University System.

Krupicka, G., Poellot, B. (1993). “Nuisance stiffness”. *Bridgeline*, 4(1), 3-7.

Hartman, A., Hassel, H., Adams, C., Bennett, C., Matamoros, A., Rolfe, S. (2010). “Effects of cross-frame placement and skew on distortion-induced fatigue in steel bridges”. *Transportation Research Record*, 2200, 62–68.

Hassel, H. L., Bennett, C. R., Matamoros, A. B., Rolfe, S. T. (2013). “Parametric analysis of cross-frame layout on distortion-induced fatigue in skewed steel bridges”. *J Bridge Eng.,*10.1061 /(ASCE)BE.1943-5592 .0000388,601–611.

McDonald, G., Frank, K. (2009). “The fatigue performance of angle cross-frame members in bridges”. *Rep. No. FSEL 09-1*, Univ. of Texas at Austin, Ferguson Structural Engineering Laboratory, Austin, TX.

Menassa, C., Mabsout, M., Tarhini, K., Frederick, G. (2007). "Influence of skew angle on reinforced concrete slab bridges". *Journal of Bridge Engineering,* 12, no. 2, 205-214.

Mconnell, J., Chajes, M., Michaud, K. (2015). "Field Testing of a Decommissioned Skewed Steel I–Girder bridge: Analysis of System Effects". *Journal of Structural Engineering*, 141.1 D4014010.

McConnell, J. R., Radovic, M., & Ambrose, K. (2016). Field Evaluation of Cross-Frame and Girder Live-Load Response in Skewed Steel I-Girder Bridges. *Journal of Bridge Engineering*, *21*(3), 04015062.

McConnell, J., Radovic, M., Ambrose, K. (2014) “Cross-Frame Forces in Skewed Steel I-Girder Bridges: Field Measurements and Finite Element Analysis”. *Final Report to Delaware Department of Transportation*, University of Delaware Center for Bridge Engineering.

Nowak, A., Collins, K. (2012). “Reliability of structures”. *CRC Press.* 120-126.

Ozgur, C. (2011). "Influence of cross-frame detailing on curved and skewed steel I-girder bridges". *Doctoral Dissertation*, Georgia Institute of Technology.

Radovic, M., McConnell, J (2014). “Evaluation of Cross-frame Designs for Highly Skewed Steel I-Girder Bridges”. *Proceedings of 48th International Bridge Conference, Pittsburg,* IBC-14-47.

Riks, E. (1979). "An incremental approach to the solution of snapping and buckling problems". *International Journal of Solids and Structures*, 15.7, 529-551.

Ross, J. H. (2007). “Evaluating Ultimate Bridge Capacity Through Destructive Testing of Decommissioned Bridges.” *Master Thesis*. University of Delaware.

Stallings, J., T. Cousins, and J. Tedesco. (1997): "Fatigue of diaphragm-girder connections". *Transportation Research Record: Journal of the Transportation Research Board*, 1594, 34-41.

Schaefer, A (2012). Crossframe analysis of highly-skewed and curved steel I-girder bridges. *Mater Thesis,* University of Colorado at Denver.

Tedesco, J. W., Stallings, J. M., and Tow, D. R. (1995). “Finite element method analysis of bridge girder-diaphragm interaction”. *Comput Struct*., 56(2–3), 461–473

Wang,W., Battistini, A., Helwig, T., Engelhardt,M., Frank, K.(2011). “Staggered bracing in skewed steel bridge”. *Proc., Annual Stability Conf. Structural Stability Research Council*, Structural Stability Research Council, Rolla, MO, 70–81.

White, D., et al. (2012). “Guidelines for analysis methods and construction engineering of curved and skewed steel girder bridges”. *Rep. No. 725*, National Cooperative Highway Research Program, Transportation Research Board, Washington, DC.

Chapter 3

FINITE ELEMENT MODELING, VALIDATION, AND CALIBRATION

Finite element analysis (FEA) is based on a discretization of structural parts into geometric shapes (elements) that are bounded by vertices (nodes). The response of these elements to an input loading is calculated via a system of partial differential equations, with each element containing multiple unknown quantities that are calculated by the FEA method (Bathe, 1982). These quantities, representing the response of the system, need to be validated to make sure that the model follows governing theoretical assumptions.

Sometimes approximating complex physical objects, such as bridge structures, can be challenging due to uncertainty of the physical parameters that constitute the object, such as material strength, degree of composite action between concrete deck and steel girders, boundary conditions, etc. All these uncertainties can lead to approximation errors in the results. To reduce these errors, the model can be tuned by varying some of the parameters in question. This procedure is called model calibration. The purpose of the calibration procedure is to better approximate the input for unknown parameters in the FEA model.

A three-dimensional finite element model of “Bridge 7R”, described in this chapter, was built and analyzed. The location of a neutral axis and system level capacity of the bridge were two metrics that were used to validate the FE model. A calibration of FE model was conducted by determining two unknown parameters: a) the compressive strength of concrete; and b) the level of composite action between steel girders and concrete deck. This chapter is divided into four sections: FE modeling methodology, FE model validation, FE model calibration, and FE parameter selection.

3.1 FE Modeling Methodology

This section details the procedure used for building a three-dimensional finite element model of "Bridge 7R". This section is divided into thirteen sub-sections: bridge geometry, element mesh, checking mesh quality, element selection, material modeling, cross-frame modeling, end diaphragm modeling, deck modeling, composite action modeling, boundary conditions, load modeling, Riks analysis, and processing and output.

3.1.1 Bridge 7R

3.1.1.1 Bridge Description

All finite element models presented in the following sections of this dissertation are based on a representative highway bridge, labeled "7R". This bridge is selected on the basis of extensive prior evaluation of this structure's behavior, including in-service and destructive testing and a corresponding FEA (McConnell, 2015). Bridge "7R" consists of three independent simply spans and is a 63° skewed steel I-girder structure, with the span of interest being 105.3ft long (Figure 3.1). The bridge has 4 plate girders spaced 8ft on center. All four plate girders were fabricated from A7 steel (with nominal yielding strength of 33ksi) and had a web depth of 60in.

and a web thickness of 3/8in. Other geometry varied between girders and along the length of the girders as described below.

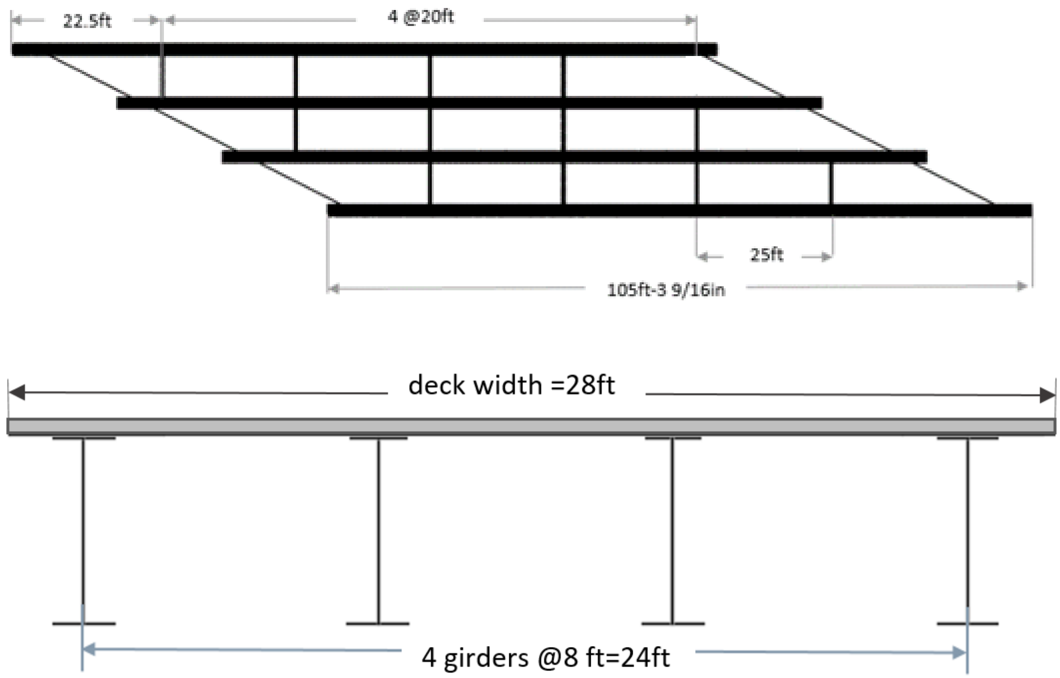

Figure 3.1 Front view and dimension of the Bridge 7R (top), cross-section view of Bridge 7R (bottom).

Top flange dimensions are 20 x 1in. for the exterior girders and 18 x $^7/_8$in. for the interior girders. Bottom flange dimension for the exterior girders are 20 x 1 ¼ in, while bottom flange dimensions for the interior girders are 20 x 1in. To add to the girder flexural strength, full-width cover plates are welded to the bottom flanges of the girders. The exterior girders have cover plates welded at 32.25ft on each side of the girder centerline. The interior girders have cover plates welded at 32.75ft on each side of the girder centerline. The effective dimensions of the bottom flanges at mid-span (including cover plates that exist in this location) are 20 x $3^{1/8}$ in. for the exterior girders /and 20 x $2^{1/2}$in for the interior girders. The webs of the interior girders were stiffened with double-sided transverse stiffeners spaced every 4ft. The webs on the exterior girders were stiffened with the single-sided transverse stiffeners on the interior face and single-sided longitudinal stiffeners on the exterior face of the exterior girders. A composite 8 in.-thick concrete deck with a 2in. haunch is connected to the girder by shear connectors. A photograph of Bridge 7R while it was in service can be seen at the Figure. 3.2.

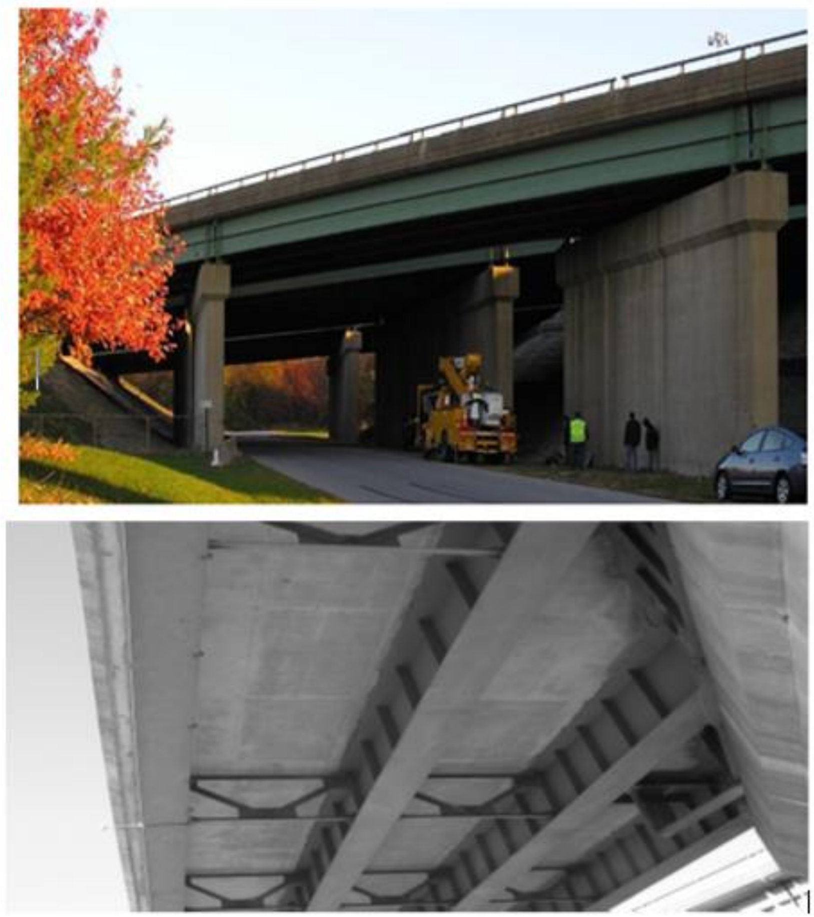

Figure 3.2 Bridge 7R photographs taken during in-service field-testing. Photograph on the top the shows the view of the bridge from the side, while photograph on the bottom shows the bridge cross-frames and girders as viewed from below.

The transverse stiffeners also serve as connection plates for the cross-frames. The transverses stiffeners are 5in wide and 0.375in thick. The longitudinal stiffeners are located at the mid-height of the web along the full length of the exterior girders. All girders have bearing stiffeners at the bridge supports, which are 0.75in thick and 8in wide.

Additionally, end diaphragms, steel I-sections of equal depth to the girders, connects the girders at each end of the member. The steel diaphragm consists of a 1in thick and 7.5in wide bottom flange, 60in high and 0.375in thick web, and 7.5in wide and 0.375in thick top flange. Lateral bracing consisted of K-frames that were spaced at 20ft along the length of the girders, with variable spacings between the cross-frames and the diaphragms, as shown in Figure 3.1. All cross-frames are composed of 4x3½ x3⁄8in angles and connected to gusset plates by four bolts at the end of each member; the gusset plates are connected to transverse stiffeners welded to the girders' web.

3.1.1.2 Instrumentation and Data Collection

Multiple locations on the bridge were strategically selected and instrumented with strain gauges to capture the bridge system response to increasing load (McConnell, et al. 2015). The strain data were collected during 17 load increments, with each load increment being equivalent of the magnitude of load of one HS-20 vehicle. Figure 3.3 shows the locations where data was collected from 16 gauges located near mid-spans of Girder 2 (G2-A) and Girder 3 (G3-A) and bottom and top chord of cross-frame CF3.

The gauges that instrumented the girder cross-sections were placed in the following positions:

a. Two gauges were placed on the top face of the bottom flange, two inches from each edge (BF1 and BF2).

b. Two gauges were placed on opposing sides of the web at a distance of 25in from the top face of the bottom flange (W1 and W2).

c. Two gauges were placed on the bottom face of the top flange, two inches from each edge (TF1 and TF2).

The two gauges that instrumented the cross-frame’s bottom chord were placed at the quarter point along the length of the cross-frame (CF3 BA1-A and CF3 BA2-A) and one of these was placed in the center of the cross-section of the concentric leg and the other was placed in the center of the cross-section of the eccentric leg of the angle member. The two gauges that instrumented cross-frame’s top chord (CF3 TA1-A and CF3 TA2-A) were placed in the same positions on the cross-section but were placed at the mid-point along the length of the cross-frame.

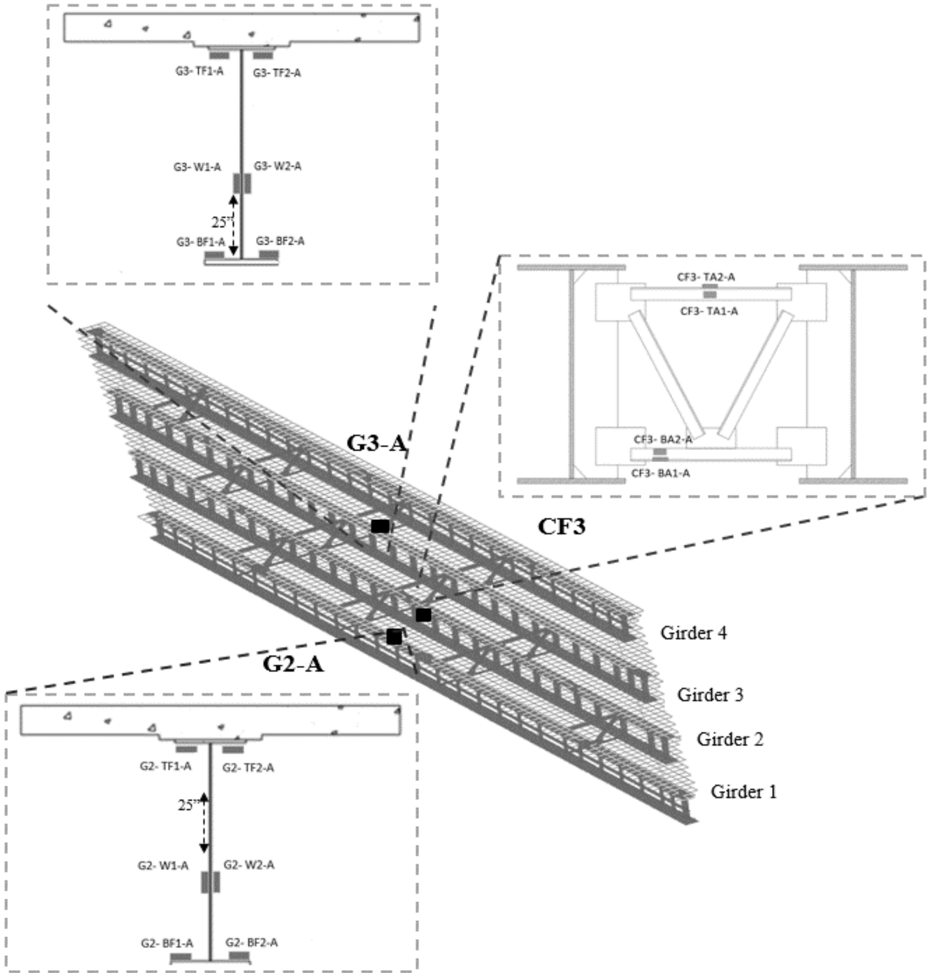

Figure 3.3 Location and labeling of the girders and cross-frame strain gauges used for the experimental data collection.

Placing gauges on the bottom flange, web, and top flange made calculation of the neutral axis theoretically possible, assuming longitudinal bending without warping is taking place. Under this same assumption, placing gauges on the opposite sides of each girder element provided data redundancy in case of any gauge malfunction and allowed for lateral bending to be assessed.

3.1.2 Building Finite Element Mesh

Building the finite element mesh started with importing a previously created 3D Auto-Cad drawing into the Femap interface. Femap is commercial finite element software that was used for building the finite element mesh. Once imported into the Femap interface, the model consisted of lines with geometric coordinates that represent the geometry of Bridge 7R. Based on the line geometry, surfaces are created for each bridge structural component such as webs; top and bottom flanges; haunches; deck; connection plates; cross-frames; longitudinal and transverse stiffeners; bearing stiffeners and end diaphragms. Surfaces are special modeling features that can be used to manipulate the size of the element meshes, element properties, and element orientations.

Additionally, in order to achieve a uniform element mesh distribution throughout the bridge model, surfaces were carefully designed to capture any intersection between different bridge components. Modeling bridge geometry with surfaces ensures that whole bridge model has conforming finite element mesh (Figure 3.4). In a conforming finite element mesh each element shares its boundary nodes with is neighboring element (Figure 3.4 left). On the other hand, non-conforming meshes have boundary nodes that are not aligned with neighboring elements (Figure 3.4 right). A general rule of thumb for good FE modeling is that, if possible, the model should have conforming element meshes. This is especially true if the elements are expected to experience large deformations. Once the whole bridge is modeled by surfaces (Figure 3.5), all surfaces are assigned the same element size to ensure conforming element meshes throughout the bridge model. Additionally, discretizing the surfaces allowed creation and testing of different mesh sizes fairly easily for the entire bridge model.

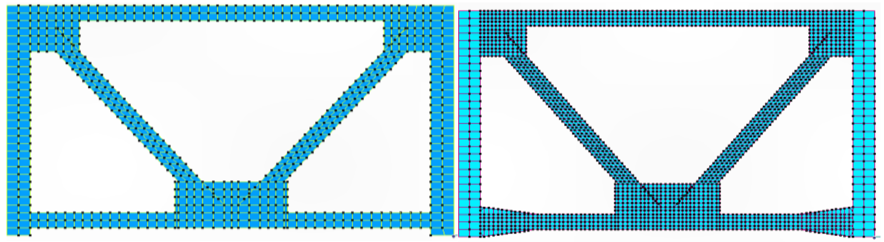

Figure 3.4 Conforming (left) and non-conforming (right) element mesh between cross-frames and connection plates.

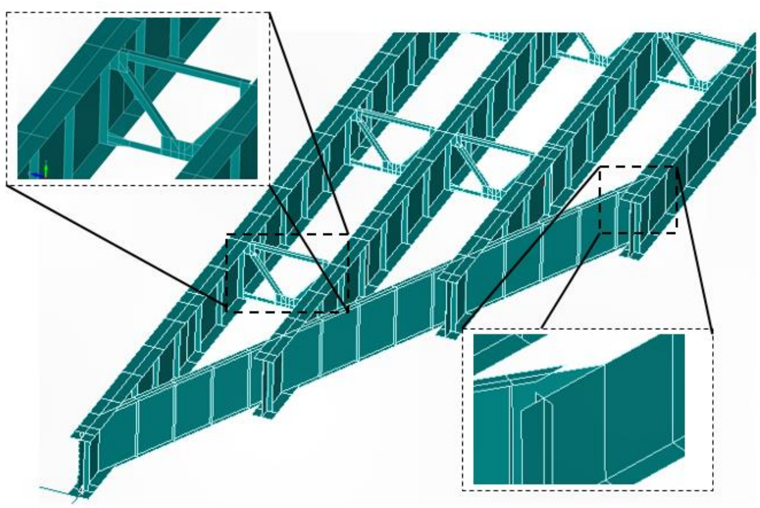

Figure 3.5 Modeling using surfaces. Top left figure shows detailed surface modeling of the connection between the cross-frame and the vertical stiffener. Bottom right figure shows detailed surface modeling of the bracing point between end diaphragm and the girder's web.

A six different element meshes were evaluated. Large meshes with element sizes of 4, 6 and 8in did not produce conforming meshes throughout the bridge and they were not further considered in the analysis. Small meshes with element sizes of 2, 1, 0.5in produced conforming meshes throughout the model and they were further evaluated. Due to computational intensive analysis that was planned for this study, it was important to find the best combination between model's accuracy and the model's size. A mesh with a 2in element size produced a model with over 150,000 elements, a mesh with a 1in element size produced a model with 600,000 elements and a mesh with a 0.5in element size produced a model with 2,400,000 elements. The difference in peak bottom flange stresses between the model with 150,000 elements and the model with 600,000 elements was only 1%. With such small difference in bottom flange stresses, it was concluded that the mesh with the element size of 2in was acceptable. The model with the size of 2,400,000 elements was not further considered because it was deemed that this model would produce an output file of such size that file post-processing would be unmanageable with the computing power available at the time.

Additional consideration was given to the size of the deck elements. It seemed that the size of the deck mesh was too dense relative to the objective of this study. After much of consideration, it was decided that the size of the deck elements could be increased, without compromising the mesh conformity between other elements. Therefore, the elements of the deck mesh were increased to 12in. This significantly reduced the size of the FE model from over 150,000 elements to 114,000 elements, while not affecting the peak stresses at the bottom flange at the mid-point of the bridge, where stresses were being compared in this mesh sensitivity study.

3.1.3 Checking Mesh Quality and Connectivity

Once all surfaces are meshed to create elements, element quality was tested using a built-in function in FEMAP. The element quality check consists of comparing element geometry in the model to the geometry of "ideally shaped" elements. The "ideally shaped" element refers to a set of parameters that when met, give the most accurate results. Specifically, the element's aspect ratio, taper, skew, warping and Jacobian were checked against default values provided by Femap "element quality check" function. If the elements did not pass this test, a group with distorted elements was created. The distorted elements were re-checked and re-evaluated to make sure that their geometry will not interfere with further analysis. Some of the distorted elements were deleted because it was determined that their geometry would negatively contribute to model results (more detailed explanation about this procedure was given in the Section 3.1.6 Cross-frame Modeling).

Following element quality check, the coinciding node check was conducted for the whole model. The coincident node check is a function available in the Femap which evaluates if elements that form bordering surfaces share the same nodes. For example, web elements and bottom and top flange elements should share the nodes where these two surfaces meet in order for the physical connectivity of the elements to be mathematically represented. Applying a small search radius to this function (this value can be defined by the user and in this case a 0.3in search radius was used), the program searches for the nodes within this radius of all other nodes. Nodes within the prescribed radius of one another can then be merged at the user's discretion. Using this function ensured that model does not have any unconnected regions or "floating" elements, as this would cause a numerical singularity problem during the analysis.

3.1.4 Elements Selection

Two types of elements were used: shell and beam. The girder flanges and webs, stiffeners, deck, haunch, and connection plates were modeled using 4-node, reduced integration shell elements, labeled as type S4R in Abaqus (Figure 3.6). End diaphragms were modeled using beam elements (B31). The reason for the end diaphragm being modeled as beam elements is further explained in detail the Section 3.1.7). B31 is computationally efficient, one-dimensional line element that can be used for modeling of three-dimensional structures. B31 elements have 3 translational and 3 rotational degrees of freedom at each node. The shell elements also have 3 translational and 3 rotational degrees of freedom at each node.

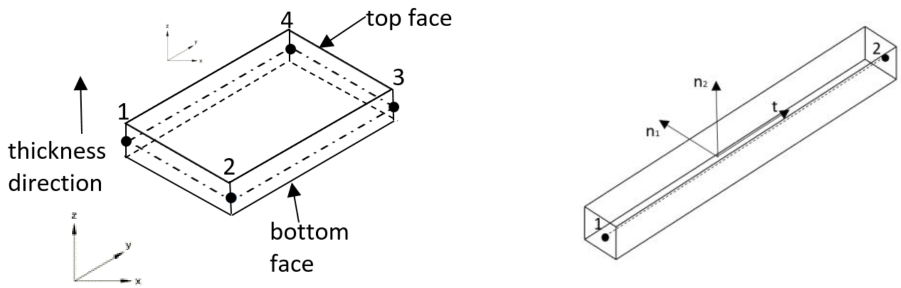

Figure 3.6 S4 Shell element orientation (left) and B31 beam element orientation (right) in Abaqus

3.1.5 Material Modeling

Once the elements passed the element quality check, concrete and steel material properties were created. Material properties and cross-sectional properties of the elements are then assigned to the element properties. For example, the web element property was assigned a steel material with a thickness of 0.375in, the concrete deck property was assigned a concrete material with a thickness of 8in, etc.

Concrete and steel are the materials that are modeled for the purpose of this study. The concrete was modeled as isotropic linear elastic material. Figure 3.7 shows the input for this material in the units of pounds and inches.

```
** Femap with NX Nastran Material 2: concrete
*Material, name=MCONCRETE
*Density
 0.000225,
*Elastic
 3.834e+06, 0.2
```

Figure 3.7 Example of the Abaqus command for modeling of concrete with compressive strength of f'c=4,500psi. Concrete was modeled as isotropic elastic material. Concrete cracking or plasticity features were not included in this model.

The steel was modeled as elastic-plastic isotropic material. Abaqus requires plastic material input to be expressed in terms of true stress and logarithmic plastic strain. True stress (σ_T) is defined as the ratio of the external load to the instantaneous cross-sectional area of the loaded element and can be related to engineering stresses by (3.1),

$$\sigma_T = \sigma_E(1 + \epsilon_E) \tag{3.1}$$

where σ_E is engineering stress and ϵ_E is engineering strain. Engineering strain (ϵ_E) is related to logarithmic plastic strain (ϵ_{ln}) by (3.2),

$$\epsilon_{ln} = \ln(1 + \epsilon_E) - \frac{\sigma_T}{E_s} \tag{3.2}$$

where E_s is modulus of elasticity of steel. For small deformation, the difference between engineering and true stress is negligible. However, as strains exceed the elastic limit, the change in cross-sectional area increases, resulting in true stresses that can be significantly higher that engineering stresses.

The plastic properties of steel were adopted from McConnell et al. (2015), with a steel yield strength of 36,045psi and strain hardening. The yield strength represents a 36ksi yield stress in terms of engineering stress, which equals a 10% increase over the minimum specified yield strength of the material to account for typical material over-strength. The plastic region of the analysis was assumed to have a strain hardening behavior, represented by a variable slope of the stress-strain curve as reflected by the stress-strain data points used to define the constitutive relationship shown in Figure 3.8 and Table 3.1. The first number in the Figure 3.8 is the value of the true stress, while the second number represents the corresponding logarithmic plastic strain.

Table 3.1 Plastic Material Properties used for Girders, Connection Plates and Stiffeners

True Stress (psi)	**Logarithmic Plastic Strain**
36045	0
36611	0.0111
69020	0.1716
85463	0.3335

```
*PLASTIC, HARDENING=ISOTROPIC
 36045,0.0000
 36611,0.0111
 69020,0.1716
 85463,0.3335
```

Figure 3.8 Abaqus command that models steel material as isotropic elastic-plastic material

3.1.6 Cross-frame Modeling

Because the role of cross-frames in stress distribution throughout skewed steel I-girder bridges is one of the main objectives of this study, detailed consideration was given to cross-frame modeling. An initial obstacle was that the structural drawings and documents for Bridge 7R were not detailed with respect to finer details of the cross-frame geometry. Therefore, photos from Ross (2007) were used to quantify these details (Figure 3.10a). The cross-frame length from the image was compared to the known length from the plans in order to obtain an approximate dimensions of cross-frame members. Furthermore, width to length ratios of commonly used gusset plates in bridge design were analyzed to approximate dimension of the connection plates.

Figure 3.9 shows the evolution of refining the cross-frame meshes of Bridge 7R. Figure 3.9 (a) shows the image that was used to approximate the cross-frame connection plate dimensions and lengths of the top, bottom, and diagonal chords with greater precision than available in the structural drawings. Figure 3.9 (b) shows the scaled drawing that was used for cross-frame modeling. Figure 3.9 (c) shows a rendered view of a cross-frame mesh using beam elements, which was determined to be of insufficient accuracy in preliminary work by the author. Note that the dashed black lines show the location of the beam elements. Figure 3.9 (d) shows the cross-frame modeled with shell elements in a prior parametric study by the author (Radovic & McConnell (2014)).

Figure 3.9 (e) represents a very detailed shell element mesh before the element quality check was performed. This more detailed cross-frame model that appropriately represented the physical geometry of the cross-frame had distorted elements within the tapered connection plate that connected the transverse stiffener and bottom chord of the cross-frame. Because of the shape of the tapered end of the connection plate and because the element mesh size was kept constant for all bridge components (2in), elements of the tapered connection plate were severely distorted and could not pass the element quality check. In general, elements with distorted shapes tend to develop “phantom” stresses or unrealistic distortions. Furthermore, distorted elements in the models could cause convergence issues during the analysis.

Therefore, it was decided to remove the elements from the tapered connection plate from the model. Figure 3.9 (e) contains arrows pointing to the location of these distorted elements. It was recognized that removing these elements would reduce the stiffness of the cross-frame. However, considering the total size of the cross-frame compared to the total size of the removed elements, the difference in the cross-frame stiffness was considered to be negligible. The final cross-frame mesh used for FE model validation and calibration is shown in Figure 3.9(f).

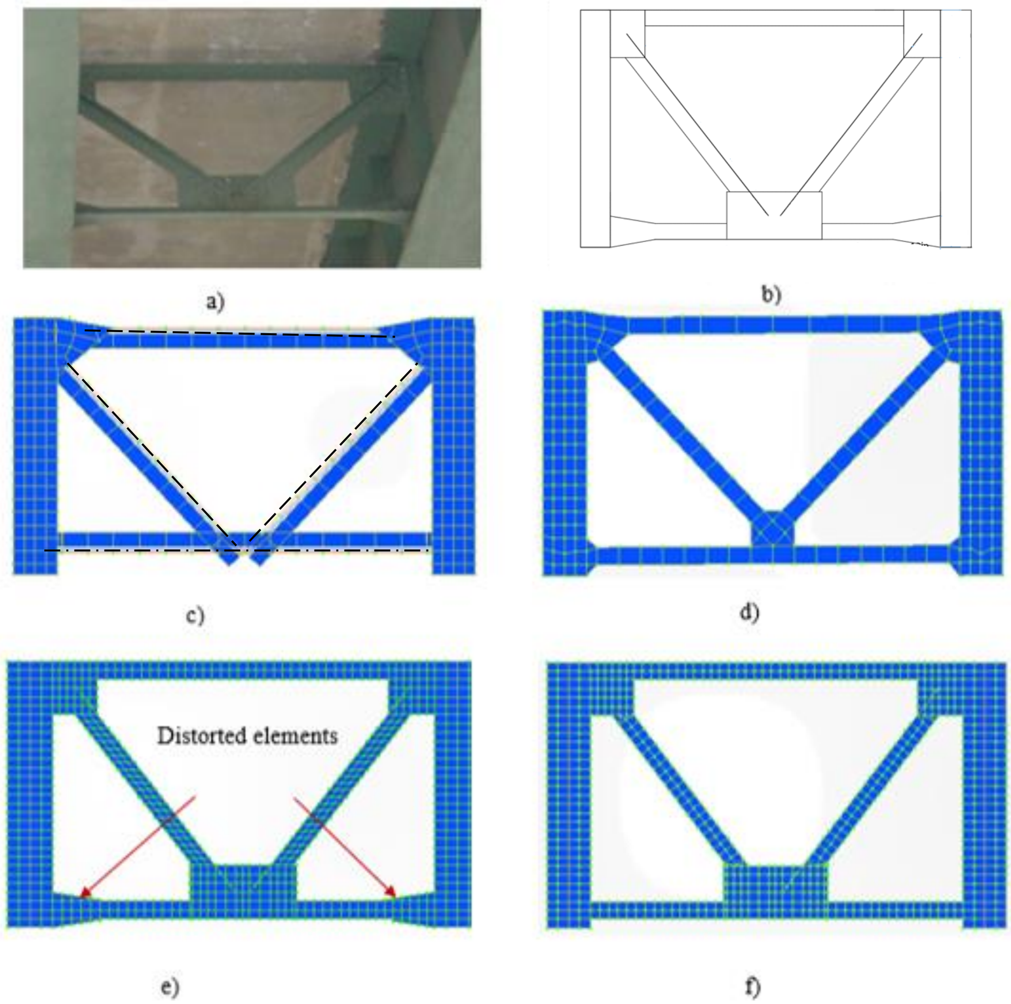

Figure 3.9 “Evolution” of cross-frame element mesh modeling

3.1.7 End Diaphragm Modeling

The girders of Bridge 7R are laterally supported at the supports by a steel diaphragm (Figure 3.10). Initially, the end diaphragm was modeled using shell elements. However, due to the skew of the bridge and mesh size being 2in, the element mesh of the top and bottom flange diaphragm became severely distorted (Figure 3.10). As explained in Section 3.1.6 it was very important that the model had an element mesh with a minimum number of distorted elements. To remedy this issue, it was decided to model end diaphragms with beam elements, while preserving diaphragm stiffness properties.

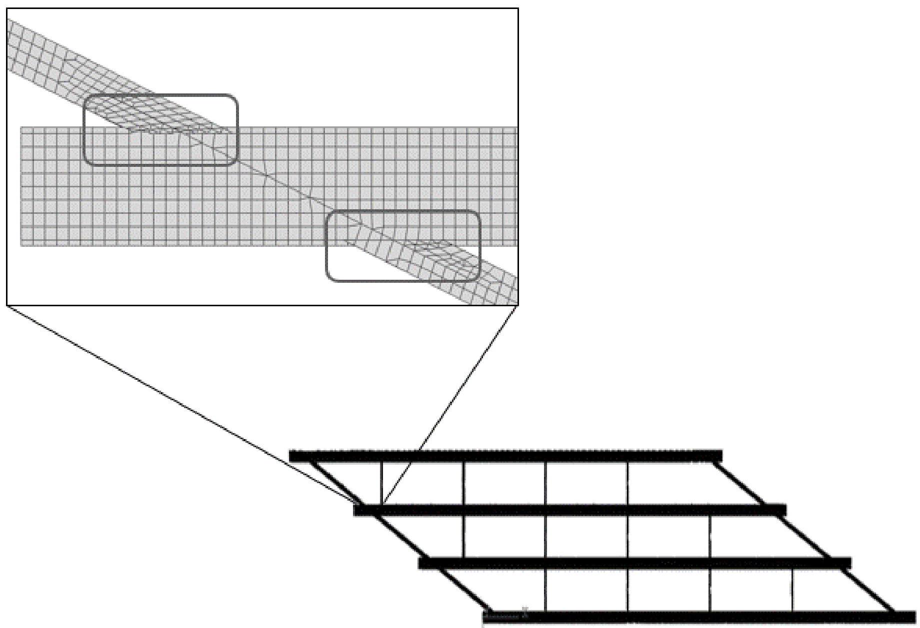

Figure 3.10 Prior shell modeling of the end diaphragms. Top figure highlights the non-conforming and distorted mesh at the location where top and bottom flange of diaphragm connect to the top and bottom flange of the girder.

The beam elements were defined by an orientation vector perpendicular to the length of the element to define the orientation of the cross-section. The result of the end diaphragm modeling can be seen in Figure 3.11, where the figure on the left shows the model of the end diaphragm (where beam elements are shown as a line in non-rendered view) and the figure on the right shows the realistic rendering of the same end diaphragm.

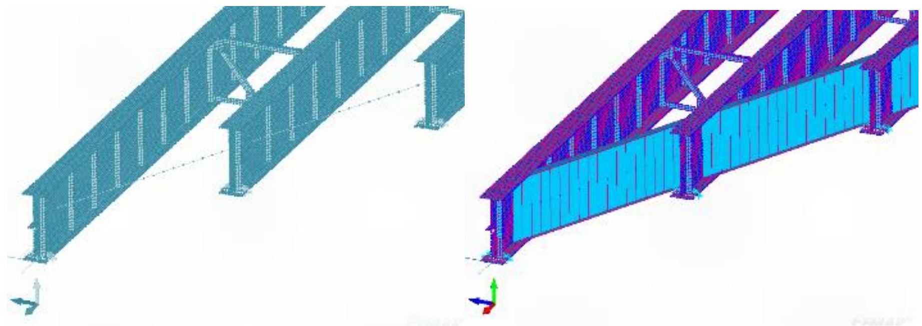

Figure 3.11 Using beam elements to model end diaphragm.

In order to confirm that modeling the end diaphragm as shell or beam elements did not significantly affect stresses throughout the bridge, bottom flange stresses at the girder's mid-point were compared. Results showed that there was a minimal difference between stresses obtained from the two alternative models. The graph on the left of Figure 3.12 shows the difference in bottom flange stresses at ten elements evaluated along the width of the bottom flange. The graph on the right of Figure 3.12 shows the percent difference between the beam and shell models, with an average percent difference of only 0.3%.

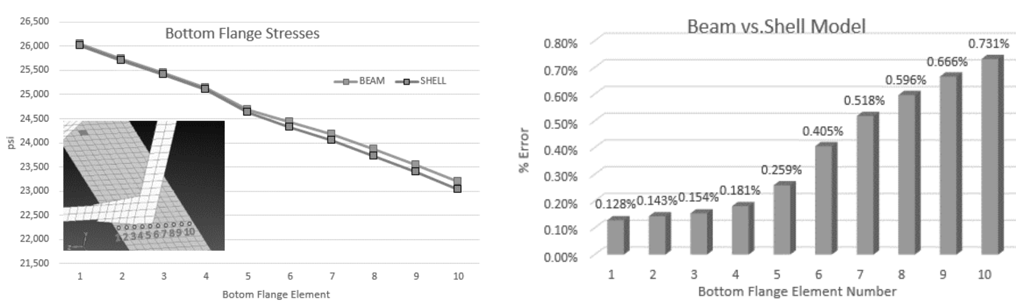

Figure 3.12 Difference in bottom flange stresses in models with end diaphragm modeled with beam elements and end diaphragm modeled with shell elements is shown to be negligible.

3.1.8 Deck Modeling

The bridge deck was modeled as shell elements with a thickness of 8 in and concrete material properties described in Section 3.1.5. Additionally, the reinforcement in the deck was modeled with the rebar layer command which is used to define layers of bi-axial reinforcement in shell elements in Abaqus. The rebar layer command defines the rebar cross-sectional area, rebar spacing, cover from the top or bottom of a shell element, rebar material, and rebar orientation (Figure 3.13). The concrete deck of Bridge 7R had four reinforcing layers, two in the longitudinal direction and two in the transverse direction.

```
*Rebar Layer
REBAR_TOP_LONG, 0.19635, 9.5, 2.09503, MAISI_4340_STEEL, 0., 1
REBAR_BOT_LONG, 0.19635, 9.5, -2.59503, MAISI_4340_STEEL, 0., 1
REBAR_TOP_TRAN, 0.19635, 6.5, 2.3466, MAISI_4340_STEEL, 90., 1
REBAR_BOT_TRAN, 0.19635, 6.5, -2.8466, MAISI_4340_STEEL, 90., 1
```

Figure 3.13 Deck reinforcement was modeled using rebar layer command in Abaqus 11.3.

3.1.9 Modeling Composite Action

Composite action between the concrete deck and steel girders was modeled using tie constraint. The tie constraint is a built-in constraint function in Abaqus 11.3 that constrains translations and rotations of the surfaces that are connected by the ties. There are two types of surface configurations that are available in Abaqus, node based surfaces and element based surfaces. An element based surface refers to a set of elements that are located on the rigid body, while a node based surface refers to a set of nodes that are located on the rigid body. In order to tie two surfaces together one surface is designated to be the slave surface and the other to be the master surface. Abaqus 11.3 then forms constraints between the slave nodes on the slave surface and the master nodes on the master surface. The motions (translations and rotations) of the master surface nodes govern the motions of the slave surface nodes (Figure 3.15).

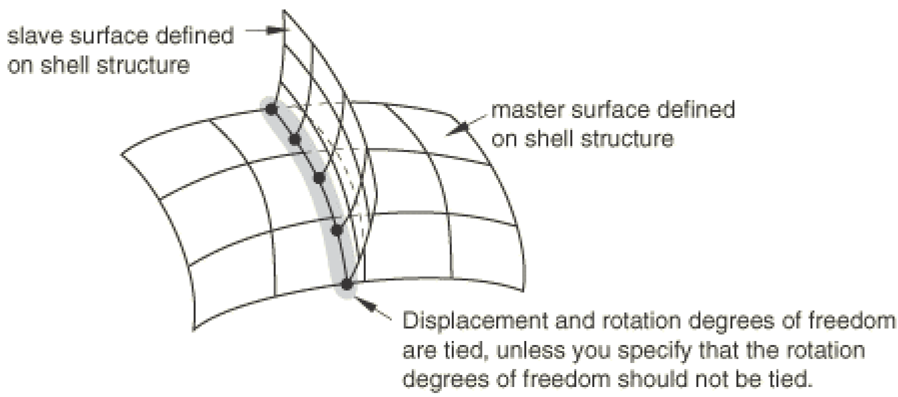

Figure 3.14 Tie constraint modeled between two shell surfaces (master and slave) in Abaqus 11.3 (Dessault Systems, 2014)

The constraint created for each slave node is determined by the tie coefficients. According to Abaqus (2014) “these coefficients are used to interpolate quantities from the master nodes to the tie point. Abaqus 11.3 can use one of two approaches to generate the coefficients: the “surface-to-surface” approach or the “node-to-surface” approach.” The “surface-to-surface “approach refers to a constraint configuration that involves only one slave node, making it inappropriate for the present application. In contrast, the “node-to-surface” approach sets “the coefficients equal to the interpolation functions at the point where the slave node projects onto the master surface” (Abaqus 11.3 Documentation, 2014). For example, nodes 202, 203, 302, and 303 are used to constrain node *a*; nodes 204 and 304 are used to constrain node *b*; and node 402 is used to constrain node *c* (Abaqus 11.3 Documentation, 2014).

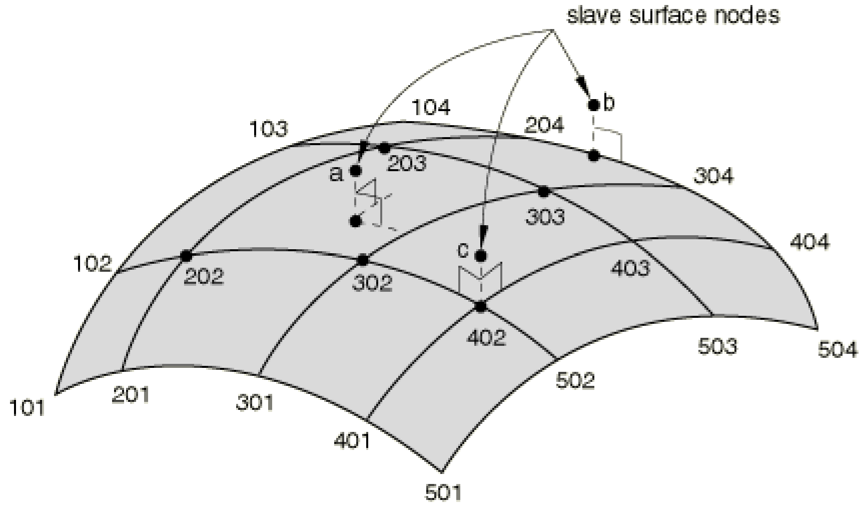

Figure 3.15 Schematic representation of how Abaqus determines which master nodes affect slave node motion (Dessault Systems, 2014)

There are multiple advantages of using tie constraint to model composite action. For example, previous studies (Ross 2007, Radovic & McConnell 2014, McConnell, at el. 2015) used rigid links to connect pairs of nodes on bridge components and to constrain nodes movement in all 6 degrees of freedom. These rigid links were used to connect the top flange elements nodes to the corresponding nodes of the haunch and deck elements. In order to mimic full composite action using this technique, top flange and haunch nodes as well as haunch nodes and deck nodes need to be in the same vertical plane, within small tolerances. While adjustments, namely creating an extremely dense mesh for the haunch, have been previously implemented to make this modeling possible, it proved to be very time inefficient and computationally expensive to implement this technique for the all models, especially in the parametric study.

By using tie constraint, there is no need for very dense element meshes, making modeling and computation very efficient. Furthermore, for calibration purposes, the level of composite action between the deck and girders can be controlled by relaxing or stiffening the tie connection by selecting how many nodes are used in the connection. For example, a stiffer connection requires more nodes to be paired between surfaces, while a more flexible connection requires fewer nodes to be paired.

3.1.10 Boundary Condition Modeling

Bridge 7R is simply supported bridge with supports placed 1ft from the end of the girders. Each girder's bottom flange cross-section has 10 elements and 11 nodes making a total of 88 boundary nodes among the 2 ends of each of the 4 girders. Constraints in the vertical direction at these boundary nodes will first be discussed. McConnell, et al. (2015) noted that due to the skew of the bridge alignment, the torsional loads within the bridge were significant enough to cause uplift at the acute corners of the bridge. Therefore, for this analysis the supports needed to be modeled in a way to allow uplift but restrain the nodes from moving downward. To solve this problem, a nonlinear spring with infinite compression stiffness and no tensile stiffness was used in the vertical direction at the location of the bearing. In Abaqus this type of spring action can be modeled with an element type called gap elements (Figure 3.16). Gap elements are generally used to model contact between two nodes when the contact direction is fixed in space. In the present models, 2in. long gap elements with initial separation distance $d=0$ connect each of the boundary nodes and a node placed 2in. below each boundary node that is constrained in the vertical direction (y-direction).

```
*GAP, ELSET=PGAP_ELEMENT
      0.
```

Figure 3.16 Abaqus gap command, with initial separation distance =0. The command also lists the element set ("ELSET") to which this function is applied.

In addition, in order to model the supports at one end of the bridge as pinned, the central node of the boundary nodes on each girder's bottom flange cross-section was constrained longitudinally (x-direction) and laterally (z-direction) (Figure 3.17). In order to model the supports at the opposite end of the bridge as a roller, the central node of the boundary nodes on each girder's bottom flange cross-section was constrained only laterally (z-direction). These central nodes are constrained in the lateral direction to avoid instability problems in the analysis and to more accurately simulate the physical boundary conditions. Only the central nodes, versus the entire bottom flange cross-section are constrained in the longitudinal and transverse directions in order to avoid the effect of constraining minor axis rotation if the entire line of nodes is constrained. Otherwise, unrealistically large lateral bending strains would occur at this location. Thus, in summary, this modeling approach yielded a total of 88 boundary nodes that were constrained from moving downward in the vertical (y) direction via gap elements, 8 of these boundary nodes were also constrained in the lateral direction (z) and 4 of these nodes were also constrained in longitudinal direction (x).

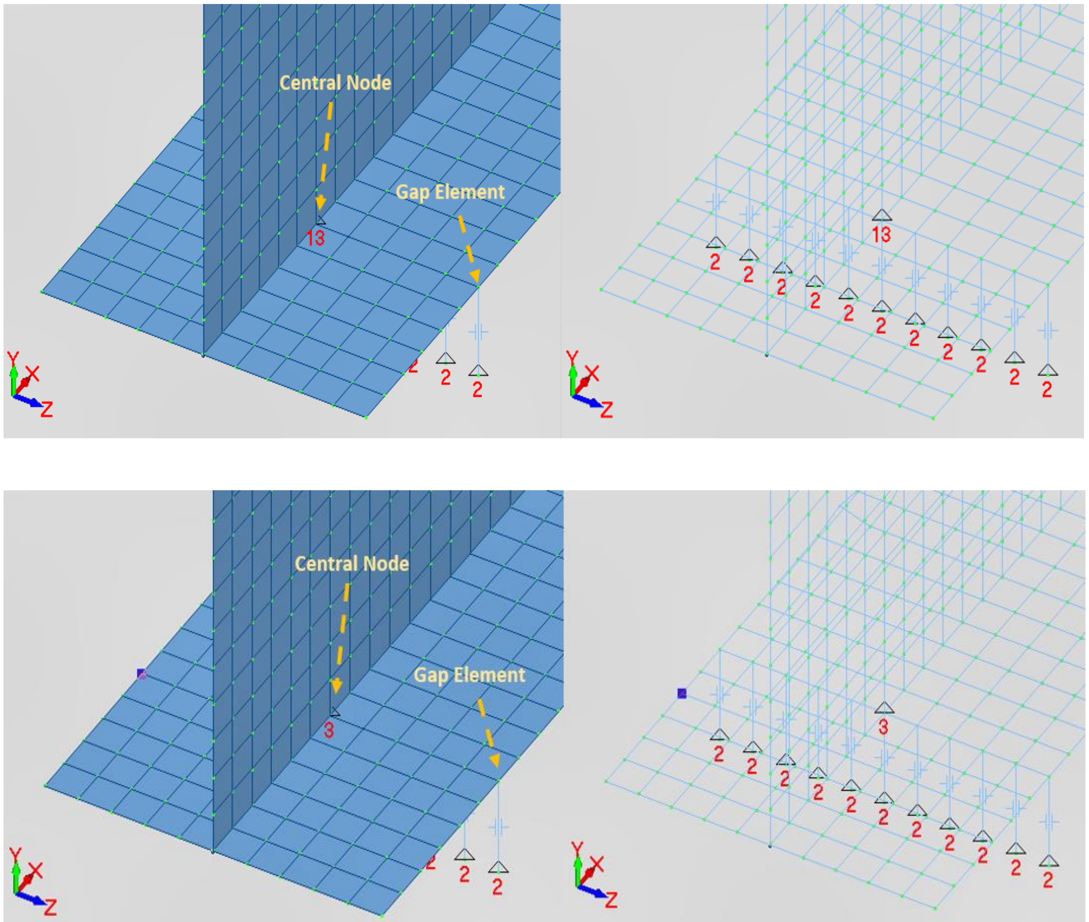

Figure 3.17 Modeling boundary conditions with gap elements. Figures on the top show a “pinned” support (full and wire frame view) and figures on the bottom show a “roller” supports (also full and wire frame view). The central node which determines the type of the support is located at the midpoint of the girder’s bottom flange width. The longitudinal direction was labeled as 1, vertical direction was labeled as 2 and lateral direction was labeled as 3.

3.1.11 Load Modeling

The location of the load in the FE model of Bridge 7R replicated the field study conducted by McConnell, et al. (2015) (Figure 3.18). This testing reproduced the equivalent of an AASHTO HS20 design truck, with back, middle and front axle loads of 32,000lb, 32,000lb and 8,000lb respectively, spaced at 14ft. During the field testing, to avoid puncture-type failure of the concrete deck, each pair of loads serving as the wheel loads for each of the three axles were positioned over a 8ft x 4ft steel plate.

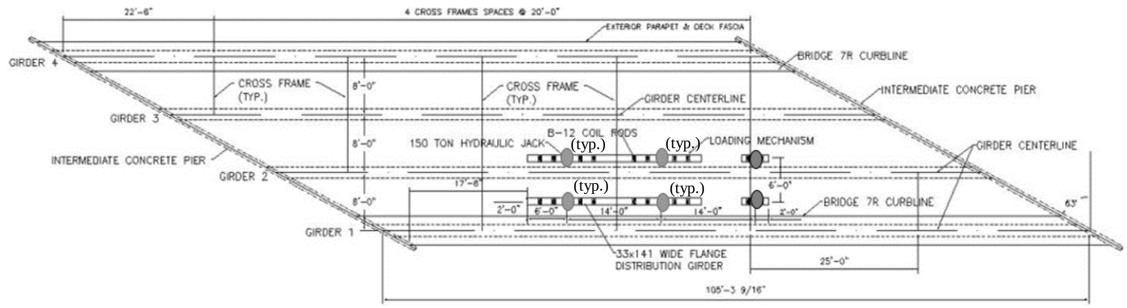

Figure 3.18 Loading used during destructive testing of the bridge 7R. Light ovals represent locations of the back and mid axle loading jacks, while dark ovals represent the location of the front axle loading jacks (adapted from Michaud (2011)).

To accurately model the experimental loading two load modeling approaches were considered (McConnell, at al. 2015). The first approach assumed that the loading jacks applied concentrated load relatively directly to the structure. Therefore, the load was modeled as six loads centered about the node closest to the center of the hydraulic jacks used during the field test. Each load consisted of dividing the concentrated load at that location over a 3-node by 3-node square.

As an opposite extreme, the second approach assumed that the loading jacks distributed load to the deck through the entirety of the steel plates. Therefore, the experimental load was modeled using a loading area equivalent to the full area of the 4ft by 8ft load plates located underneath the loading jacks (Figure 3.19).

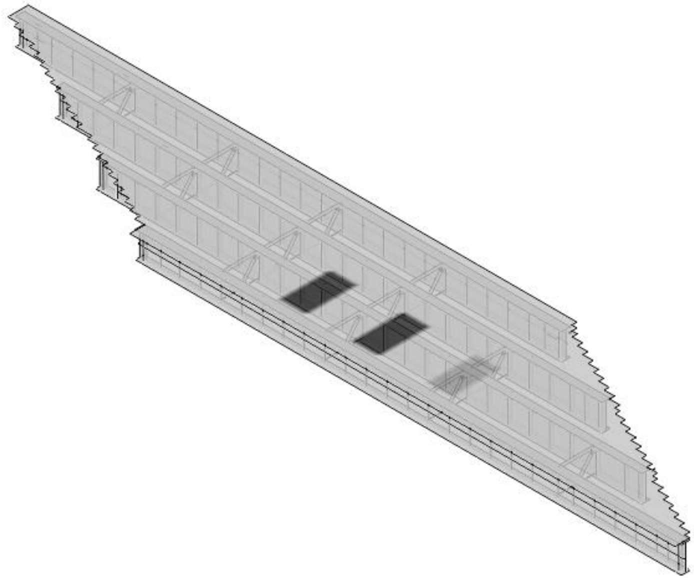

Figure 3.19 Experimental loading was simulated in FE models as distributed nodal load shown as dark (corresponding to back and mid axle) and light (corresponding to front axle) areas.

Each node that was located under back and mid axle steel plates (dark areas with light outline in Figure 3.19) were loaded with force of 640lb, resulting in each axle area having a total load of 32,000lb (each mesh had 50 nodes x 640lb per node = 32,000lb). The nodes located under the front axle (light area in Figure 3.19) were loaded with force of 160lb, resulting in total load of 8,000lb (50 nodes x 160lb = 8,000lb). Since negligible results were observed between these two modeling approaches (McConnell et al. 2015), the distributed load approach was used in further analysis, as this was considered the easier approach to implement in Abaqus 11.3.

3.1.12 Riks Analysis

For many applications in bridge engineering, a linear static analysis is a sufficient analysis. However, in cases where material nonlinearity and geometric nonlinearity might be a matter of concern (such as in cases of ultimate loadings), a non-linear analysis must be performed. The non-linear analysis method used in this work is the Modified Riks Method.

The Modified Riks Method (i.e., Riks method) is a built-in function in Abaqus 11.3 that can be used for load cases where the loading is proportional to a single scalar parameter. The basic function of this method is that it applies progressively larger magnitudes of load, while searching for a combination of forces and displacements (and thus other associated structural response metrics such as stress) that satisfy equilibrium at each magnitude of loading. Furthermore, the Riks method is ideally suited to analyzing the behavior after a peak loading has been reached. In this study, the scalar parameter is the HS-20 load. HS-20 specifies a specific weight and geometry of a truck used in bridge design (AASHTO, 2015). The load is expressed in terms of load-proportionality factors (a multiple of the input load),

$$P_{total} = P_0 + \lambda\left(P_{ref}\right) \tag{3.3}$$

where Po is dead load , λ is load proportionality factor (LPF) and P_{ref} is the reference load factor, which in this case is the magnitude of load equivalent to an HS-20 truck. Because each LPF is a multiple of the input load and the input load is a HS-20 vehicle, the results of the Riks method are expressed in terms of the number of these design vehicles. For example, if the Riks analysis shows that model reached fifteen LFPs that means that the load on the bridge model was equal to fifteen co-located HS-20 trucks at that loading increment.

The first step of the present analyses was to apply the dead load of the structure consisting of the self-weight of its members via density and gravitational constant inputs. The second step is to define parameters for the static Riks analysis, after which the Riks algorithm solves for load and displacement simultaneously. Since both loads and displacements are unknown another parameter needs to be introduced in the process in order to obtain the solution. That parameter is the arc length of the static equilibrium path in scaled load-displacement space.

Abaqus 11.3 uses eight inputs for the Riks function (Figure 3.20, Table 3.2). and an automatic time stepping procedure (increments of the arc) to try to find the solution. This means that the Abaqus will try to optimize the solution process by choosing the largest time increment (i.e., arc length) for which equilibrium can be achieved with minimum iterations. If a solution that satisfies equilibrium within acceptable tolerances with a reasonable number of iterations cannot be found, Abaqus will reduce the time step and again try to find the solution satisfying equilibrium. The procedure will be repeated until the time increment is reached for which solution can be found. The maximum arc length (also called time increment) allowed in the models analyzed in this work is 1.25. This is the value that is suggested by Abaqus Documentation Manual (Abaqus, 2014). A minimum arc length is also specified (in the example in Figure 3.21 this value is 10-6). If a satisfactory solution cannot be obtained at this time increment, the analysis will terminate. The model also accounts for geometric non-linearity, specified by activating the NLGEOM option ("NLGEOM=Yes").

Table 3.2 Riks method Abaqus 11.3 parameter inputs descriptions and values

Command Description	value
Initial time increment	0.005
Time period of the step	0
Minimum time increment allowed	0.0000001
Maximum time increment allowed	1.25
Maximum value of LPF	100
Node set label of the node where max deflection is evaluated	"riks"
Magnitude of the node's deflection	2
Direction of the node's deflection	-50

```
*STEP, INC=5000, NLGEOM=Yes
*STATIC, RIKS
0.005, 0, 0.00000001, 1.25, 100, riks, 2, -50
```

Figure 3.20 Riks command in Abaqus 11.3 requires 8 inputs

There are four parameters that have the purpose of governing the end of the analysis process: minimum time increment, maximum value of LPF, deflection of the target node, and maximum number of increments. If any of these parameters limits are reached, the analysis will be concluded.

3.1.13 Model Creation, Processing and Output

After the element mesh was built, element properties were assigned, and boundary conditions and loads were applied, the model was exported from the FEMAP program in the form of an Abaqus 11.3 input file (.inp). Then this file was imported into Abaqus 11.3 user interface CAE. The Abaqus 11.3 CAE platform was used to model composite action between the steel girders and concrete deck using tie constraint.

Because of the size of the model, the processing could not be efficiently executed on local computing machines. Therefore, the file was exported from Abaqus 11.3 and uploaded on the University of Delaware High Performance Computing Center's cluster (UD HPC). At this location, the processing took place. After the model processing was completed, the output database file (.odb) was downloaded from the cluster to the local computing machine where the data were extracted manually into spreadsheets for further analysis. The extraction procedure is outlined as follows:

1. Visual inspection of every model with Abaqus post-processing CAE platform was conducted to make sure that models' deflections and stresses were reasonable.
2. Elements that form bridge components of interest, such as girder or deck, are grouped together manually, using CAE display commands, into a new element set.
3. At desired load magnitude (selected using Step/Frame function) data were exported using visualization module queries, which is a specialized user interface function that allows probing values from element sets created in the prior step.
4. Once the element set of interest is selected using visualization module queries, stresses, strains or deflections of all elements in the group are exported into external application such as Excel spreadsheets for data analysis.

Further processing consists of finding peak values for each element set at each load level of interest, creating histograms of each set at each load level of interest, plotting stress curves etc. This procedure was repeated for every parametric model. The data were organized in spreadsheets with each column representing all element stresses extracted from one element set from one parametric model under one loading condition.

3.2 FE Model Validation

Validation is a procedure that establishes whether the results obtained from an experiment meet the requirements of the scientific research method or established theoretical expectations. In this case, validation consists of comparing theoretical values with results obtained from the FEA models. Two parameters were used to test the validity of the FEA models: a) neutral axis location and b) applied load needed to cause the full cross-sectional yielding of the bottom flange of the girder (APL).

3.2.1 Calculating Neutral Axis

The first metric used to validate the FE model is comparing the location of the neutral axis of the girder obtained from the FE model with the theoretical location of the neutral axis of the composite girder. To determine the location of the neutral axis for the FE models, the following procedure was used. Pairs of bottom flange strains at gauge locations G2-BF1-A and G2 BF2-A, web strains at gauge locations were G2-W1-A and G2-W2-A and top flange strains at gauge locations G2-TF1-A and G2-TF2-A were extracted from the FEA models and averaged. Since preliminary FEA and field data results showed that these data points are not collinear, therefore, the most accurate way to compute NA is to use linear least square method. The result of linear least square method is aa regression line that fits the best these three data points. The intercept of the regression lines is the location of NA.

The regression line equation is obtained by following procedure

$$Y = mX + b \tag{3.4}$$

where

$$m = \frac{N \cdot \sum xy - \sum x \cdot \sum y}{N \sum x^2 - (\sum x)^2} \quad \text{and } b = \frac{\sum y - m \sum x}{N} \tag{3.5}$$

and where x values correspond to the average strains measured at gauge locations, y values correspond to distances of the gauge locations measured from the bottom face of the bottom flange, and N corresponds to the number of points in the dataset.

For example, if

$$x_1 = 216.41, x_2 = 77.08, x_3 = -89.0;$$

$$y_1 = 2.5, \;\; y_2 = 27.5, \;\; y_3 = 62.5;$$

then:

$$\sum x = 216.41 + 77.08 + (-89) = 204.48$$

$$\sum y = 2.5 + 27.5 + 62.5 = 92.5$$

$$\sum xy = 216.41 \cdot 2.5 + 77.08 \cdot 27.5 + (-89 \cdot 62.5) = -2901.78$$

$$\sum x^2 = 216.41^2 + 77.08^2 + (-89)^2 = 60{,}695$$

$$m = \frac{3 \cdot (-2901.78) - 204.48 \cdot 92.5}{3 \cdot 60{,}695 - 204.48^2} = -0.1969$$

$$b = \frac{92.5 - (-0.1969) \cdot 204.48}{3} = 44.255$$

Therefore, the final form of the regression equation is Y= -0.1969X + 44.255 with correlation coefficient of R^2=0.99. Because the location of the neutral axis on the girder's cross-section is where the strain is zero (X=0), the intercept *b* gives the location of the neutral axis. This, the neutral axis is calculated to be at 44.255in from the bottom face of the bottom flange.

Once the neutral axis from the FE model (e.g., 44.255in) was computed using the procedure outlined above, it was compared with the neutral axis computed by the conventional theoretical calculations for composite girders. An example of this for the same conditions used in the example in the previous paragraph (an interior girder with concrete compressive strength of 4 psi) is shown in Table 3.3.

Table 3.3 Example of calculating the location of the neutral axis using parallel axis theorem for Girder 2

	height(in)	width (in)	$\mathbf{Y_I}$ (in)	**A** (in^2)
BF	2.5	20.00	1.3	50
Web	60	0.375	32.5	23
TF	0.875	18.00	62.9	16
Haunch	1.375	2.38*	64.1	3
Deck	8	12.69*	68.8	102
$\sum A_i$=	193.06	in²		193
NA=	46.49	in		

*concrete effective width based on f'c=4ksi

Finally, the percent error between the theoretical and FEA results was computed.

$$\%\ \text{error} = \left(1 - \frac{44.255}{46.49}\right) \cdot 100 = 4.8\%$$

3.2.2 Calculating Applied Load Needed to Cause the Full Cross-sectional Yielding of the Bottom Flange (APL)

Applied loads needed to cause full cross-sectional yielding of the bottom flange of one girder (APL) is the second parameter used to validate FE models. APL can be expressed in terms of bending moment (e.g., units of kip-ft). However, for the practical purposes in this dissertation, APL was expressed in terms of number of AASHTO HS-20 vehicles. This conversion allows direct comparison between the APL results obtained from the FE models in terms of LPFs and theoretically.

In the FE models, full cross-sectional yielding of the bottom flange of the girder refers to the case in which all shell elements constituting a girder's bottom flange cross-section equaled or exceeded the yield stress (36,045psi for these models).

To help detect bottom flange yielding, stress contours intervals ($[-\infty$ to 0], [0 to 36,045] and [36,045 to $+\infty]$) were set during visual post-processing. This resulted in clear visual distinction between yielded and un-yielded bottom flange elements (Figure 3.21), with elements equaling or exceeding yielding limit in tension being lightly colored, while the gray colored were elements in tension that did not exceed yielding limit. Since Bridge 7R is simply supported beam, it is expected that its bottom flange yield in tension. The dark colored elements were elements that were in compression. The example in Figure 3.21 shows full cross-section yielding of the bottom flange of Girder 3; in contrast, Girder 2 bottom flange shown here is not considered fully yielded because not all elements that constitute bottom flange cross-section are yielded. The visual inspection of all girders was conducted for each load increment. Once the full yielding of the bottom flange is observed, the location of the first yield and load increment at which yielding occurred were recorded.

This load increment (LPF) is then compared to the number of HS-20 trucks obtained by theoretical calculations. To theoretically obtain the number of HS-20 vehicles needed to fully yield cross section of the bottom flange, the following steps are followed. The theoretical location where bottom flange yielding should first occur is obtained from the beam bending equations (i.e., the location of the largest bending moment on the beam). Then, the maximum applied moment due to an HS-20 truck at this location was calculated. The location of the HS-20 truck on the girder of interest was based on the location of the load in the FE model then transversely shifting the load perpendicular to the girder of interest (Figure 3.21).

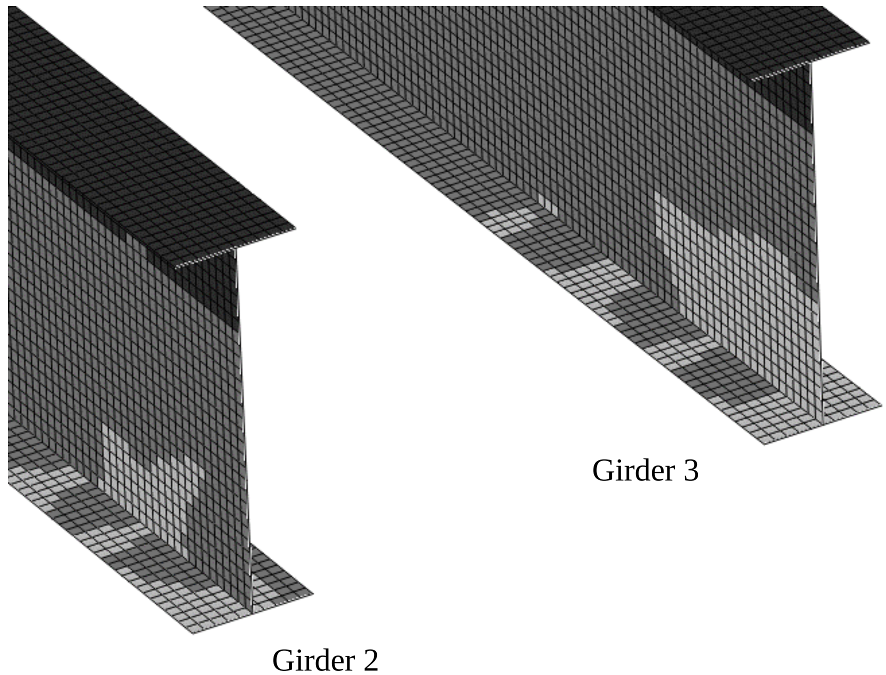

Figure 3.21 Visual representation of bottom flange yielding at FE models.

Figure 3.22 shows the location of the load in the FE model (dark and light rectangles). The centroid of the outmost dark rectangular area, corresponding to the back-axle load, is positioned over Girder 2 and it is located 44ft away from the closest end of the Girder 2. However, relative to the end of Girder 1, the transverse projection of this load (represented by black arrows in Figure 3.22) is only 28ft away from the edge of Girder 1. This load position is used for calculating the applied moment on Girder 1.

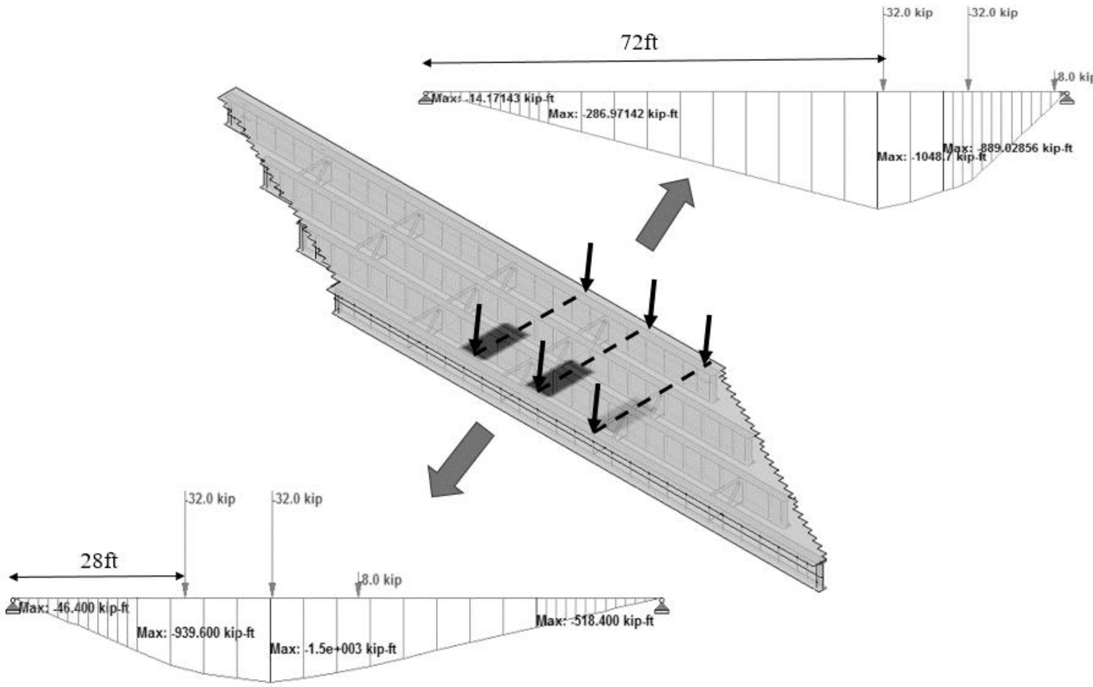

Figure 3.22 Location of the loads used to calculate theoretical APL. The dark and light rectangles on the bridge deck represent distributed loads applied in FE models. Moment diagrams on the right top and bottom left corners show the maximum moments at Girder 1 and Girder 4 due to transversely shifted point load equivalents of these distributed loads.

The exact location of first yield in each girder and corresponding moment can be calculated based on these load locations. Once the applied moment in each girder due to one HS-20 vehicle was determined in this way, calculation of APL (M_{AD}) was obtained by (3.8)

$$\boldsymbol{\sigma_y = \frac{M_{D1}}{S_{NC}} + \frac{M_{D2}}{S_{LT}} + \frac{M_{AD}}{S_{ST}}} \tag{3.6}$$

where, M_{D1} is dead load moment due to loads prior to curing of the concrete deck, M_{D2} is dead load moment due to components placed after curing of the concrete deck, σ_y is the yield strength of the steel and S_{NC}, $S_{ST,}$ and S_{LT} and are non-composite steel, short term composite, and long term composite section moduli respectively.

During the experimental testing, concrete parapets were removed from the bridge; therefore, M_{D2} is equal to zero, which makes S_{LT} irrelevant for the present calculations. $M_{D1,}$ S_{NC} and S_{ST} were calculated from bridge geometry and cross-sectional properties. M_{D1} was calculated based on the dead load of steel girder, deck, haunch and cross-frames. The dead load of the girder was equal to steel area ($67.5in^2/144in^2/ft^2=0.47ft^2$) multiplied by steel density ($500lb/ft^3$), which equals to girder dead load of 0.234k/ft. The dead load of the concrete deck was calculated by multiplying cross-sectional deck area ($18.6ft^2$) by concrete density ($150lb/ft^3$) which equals to 2.8k/ft. It is assumed that concrete deck load is equally shared by all four girders therefore, concrete deck load per girder equals to 0.7k/ft. The haunch dead load was calculated by multiplying cross-sectional area of the haunch ($0.313ft^2$) by concrete density ($150lb/ft^3$), which equals to 0.047k/ft. The weight of the cross-frames was assumed 0.11k/ft. The total dead load on the bridge per girder was calculated to be $w_d=0.234+0.7+0.047+0.11=1.09k/ft$.

Since the FE model showed that first full yield of the bottom flange occurred in the exterior girder, the AASHTO (2015) load distribution factor equations for exterior girders were used. Two equations are applicable to calculating load distribution factors for exterior girders with one lane loaded, i.e., the present scenario (the lever rule and a special case applicable to bridges with cross-frames and diaphragms (AASHTO Equation C4.6.2.2.2d-1). AASHTO also specifies that when two or more design lanes are loaded, a correction factor is applied to the interior DF in order to calculate the percent of wheel loads distributed to exterior girders. However, because the FEA models had only one lane loaded, this GDF calculation was not considered.

Since GDF obtained by the special case equation was larger than the GDF obtain by lever rule, the former results were used because AASHTO stipulates that “distribution of live load to the exterior girder is not to be less than that computed from the special analysis.”

$$R=\frac{N_L}{N_b}+\frac{X_{\text{ext}}\cdot\sum^{NL}\cdot e}{\sum^{Nb}\cdot X^2} \tag{3.7}$$

where, R is the number of lanes distributed to the girder of interest, NL is a number of loaded lanes under consideration, Nb is number of girders, Xext is horizontal distance from the center of gravity of the pattern of girders to the exterior girder (ft), e is eccentricity of a design truck or design lane load from the center of gravity of the pattern of girders (ft), and X is the horizontal distance from the center of gravity of the pattern of girders to the each girder (ft). The eccentricity of a design truck or design lane load from the center of gravity of the pattern of girders (ft) was calculated based on positioning one line of truck wheels 2ft from the curb per the field test, which was based on AASHTO specifications for truck placement. The curb is 2ft inside the centerline of the exterior girder (Figure 3.18). Thus, the first line of wheels is 4ft inside the exterior girder and the center of design truck is another 3ft from the first line of wheels. This means that the center of the truck axis was 7ft from the centerline of the exterior girder. The location of the center of gravity of the pattern girders was 12ft from the exterior girder. Subtracting these two quantities results in e= 12-7 = 5ft.

For Bridge 7R,

$N_L = 1$; $X_{ext} = 12$; $\sum^{NL} \cdot e = 5$

$\sum^{Nb} X^2 = 12^2 + 4^2 + (-12)^2 + (-4)^2 = 320$;

$N_b = 4$; and $R = \frac{1}{4} + \frac{12 \cdot 5}{320} = 0.44$.

Additionally, this theoretical load distribution factor (0.55) was reduced by the **skew correction factor** (SCF) given in the Table 4.6.2.2e-1 of the AASHTO Bridge Design Manual (2015).

$$SCF = 1 - c_1 (\tan \theta)^{1.5} \qquad 3.8a$$

$$c_1 = 0.25\left(\frac{K_g}{Lt_s^3}\right)^{0.25}\left(\frac{S}{L}\right)^{0.5} \qquad 3.8b$$

$$K_g = n(I + Ae_g^2) \qquad 3.8c$$

where, Kg is longitudinal stiffness parameter (1,466,300), n is modular ratio (7.56 for f'c=4,000psi), I is moment of inertia of non-composite girder (60,043in^4), A is area of steel girder (80in^2), e_g is distance between centers of gravity of steel girder and concrete deck (43.5in), S is girder spacing (8ft), L is length of the girder (105.3ft), t_s is slab thickness (8in), θ is skew angle (63º, but if bigger than 60°, input is 60°).

$$c1 = 0.25 \cdot \left(\frac{1{,}466{,}300}{12 \cdot 105.3 \cdot 8^3}\right)^{0.25} \cdot \left(\frac{8}{105.3}\right)^{0.5}$$

$$c1 = 0.0845$$

$$SCF = 1 - 0.0845 \cdot (\tan(60^\circ))^{1.5}$$

$$SCF = 0.767$$

$$GDF = SCF \cdot R = 0.767 \cdot 0.44 = 0.348$$

This procedure was repeated for four concrete strength values of 4ksi, 4.5ksi, 6ksi and 9ksi, yielding four GDFs respectively: 0.348, 0.343, 0.339 and 0.338.

In the final step, M_{AD} is divided by the maximum applied moment due to HS-20 truck (M_A) at the cross-section where first yield occurred and the load distribution factors for that cross-section (computed in the previous step). For example, in the "4ksi" FE model, first yield occurred at Girder 1 bottom flange, 19.2ft from the girder support, which occurs just prior to the cover-plated region of the beam beginning at 20.4ft from the girder support ((length of the bridge – length of the cover plate)/2=(105.3-2·32.25)/2=24.4ft). Theoretically, it is expected that first yield will occur in the section without the cover-plate because the girder section with the cover plate had higher yielding capacity. Maximum applied moment (M_A) and M_{D1} of this cross-section were used to compute theoretical M_{AD}. Maximum applied live load (M_A) moment due to HS-20 vehicle at bottom flange cross-section was 939.6kip-ft. The dead load moment at this cross-section was calculated to be M_{D1}= 943kip-ft. The section moduli of the cross section without cover plate was S_{NC} =1,674in^3 and S_{ST} =2,083in^3, assuming a modular ratio of 7.56, which corresponds to a concrete compressive strength of 4.0ksi.

$$M_{AD} = 2{,}083 \cdot \frac{\left(36 - \frac{943 \cdot 12}{1{,}674}\right)}{12} = 5{,}075\text{kips-ft}$$

To calculate the theoretical number of HS 20 trucks needed to cause bottom flange yielding M_{AD} was divided with applied maximum live load moment, M_A computed at the location of the bottom flange yielding and multiplied by distribution factor (DF).

$$\# \text{ HS-20} = \frac{M_{AD}}{M_A \cdot DF} = \frac{5{,}075}{939.6 \cdot 0.348} = 15.52$$

The resulting quantity is the number of HS-20 trucks theoretically needed to yield girder's bottom flange. This number is then compared to the value obtained from the FE models in terms of load proportionality factors (LPF).

$$\# \text{ HS-20} = \frac{M_{AD}}{M_A \cdot DF} = \frac{5{,}075}{939.6 \cdot 0.338} = 15.98$$

The resulting quantity is the number of HS-20 trucks theoretically needed to yield girder's bottom flange. This number is then compared to the value obtained from the FE models in terms of load proportionality factors (LPF).

3.2.3 FE Validation Results –Neutral Axis

Four FE models with varying values of concrete compressive strengths (4ksi, 4.5ksi, 6ksi and 9ksi) were built and locations of their neutral axes were computed at four load increments (4LPFs, 8LPFs, 12LPFs and 16LPFs). Once neutral axis locations for all four FE models at four load increments were computed they were compared to the theoretical neutral axis locations. The difference between the FE and theoretical values was assessed by calculating percent difference. Both individual and average percent differences at the four load increments were assessed (4LPF, 8LPF, 12LPF and 16LPF).

Evaluating data from the four load increments assessed whether the model behaved properly during low and high magnitudes of load. Theoretically, it is expected that the neutral axis location should stay the same between all four load increments, because the field test results showed that girder stresses were still in the elastic range. Evaluating four different concrete compressive strength values ensured that modeling (particularly composite action modeling) is not influenced by concrete compressive strength.

The results show that all models behave as theoretically predicted. The average percent error for all models at all load increments was 4.95%. Considering the complexity of the model (the number of components and component interactions, unconventional boundary conditions, material and geometrically non-linear Riks analysis) such a small percent error is considered acceptable. It is worth noting that acceptable levels of error in comparable FE models found in the available literature is around 10%. Therefore, these models fall well under this conventional limit, indicating good validity of the FE models for this metric. There was also good consistency between the results of the different models. The smallest average percent error (4.58%) was obtained for the model with concrete compressive strength of 4.5ksi, while the largest average percent error (5.20%) was obtained for the model with concrete compressive strength of 9ksi (Figure 3.23). The results also show low difference in percent error between load levels, as the largest average difference (1.26%) was found between "4ksi" models (5.29%) and "9ksi" models (4.03%). Such as small percent difference, indicate good and reliable model performance regardless of the load. Furthermore, Figure 3.23 indicates results obtained at load level of 16LPF consistently show the lowest percent error (4.1%) regardless of the concrete strength, compared to average percent errors computed at 4LPF, 8LPF and 12LPF (5.3%, 5.9% and 5.2%, respectively).

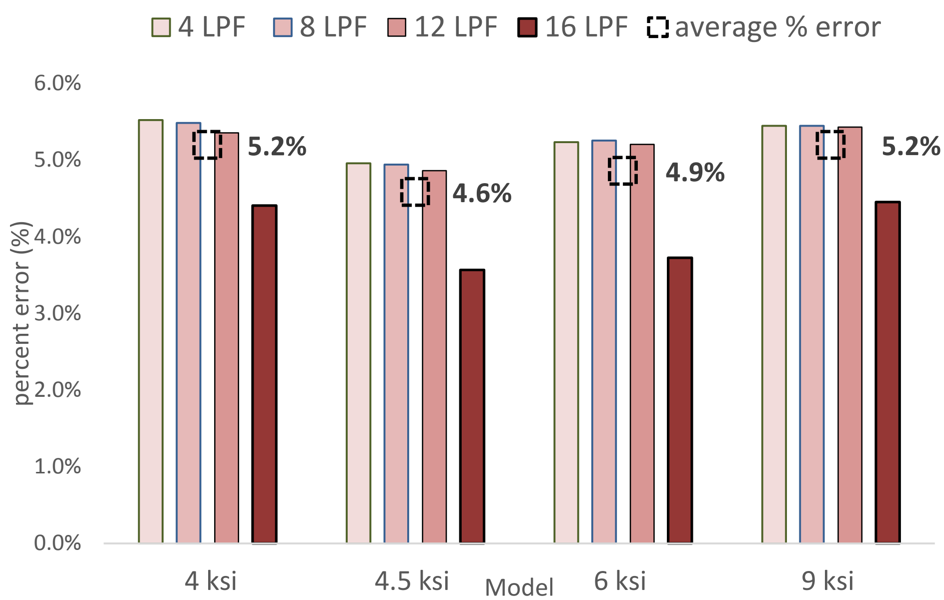

Figure 3.23Percent error and average percent error (dotted square) for FE models and theoretical neutral axis location

3.2.4 Validation Results – Applied Load Needed to Cause Full Cross-sectional Yielding of the Bottom Flange (APL)

APLs in terms of LPFs were extracted from four FEA models with different concrete compressive strengths and then compared with theoretically computed APLs. The results show that theoretical and FEA results are in reasonable agreement. The FEA APL results were 14.79LPFs, 14.81LPFs, 14.84LPFs and 14.89LPFs for the “4ksi”, “4.5ksi”, “6ksi” and “9ksi” FE models respectively, while theoretical APL results were calculated to be 15.52LPFs, 15.75LPFs, 15.93LPFs and 15.98LPFs for the “4ksi”, “4.5ksi”, “6ksi” and “9ksi” models respectively. The results (Figure 3.24) show that as the compressive strength of the concrete is increasing both theoretical APL and FEA APL are increasing. The reason theoretical values are increasing with increasing concrete strength is that GDF skew correction factor used in calculations of APL is inversely proportional to the increase in compressive strength of concrete, i.e.

higher concrete strength would yield lower GDFs. Considering that GDF is used as denominator to calculate theoretical APL, lower GDF would yield larger APL. It is interesting to note that smallest percent error (4.7%) was found at 4ksi model.

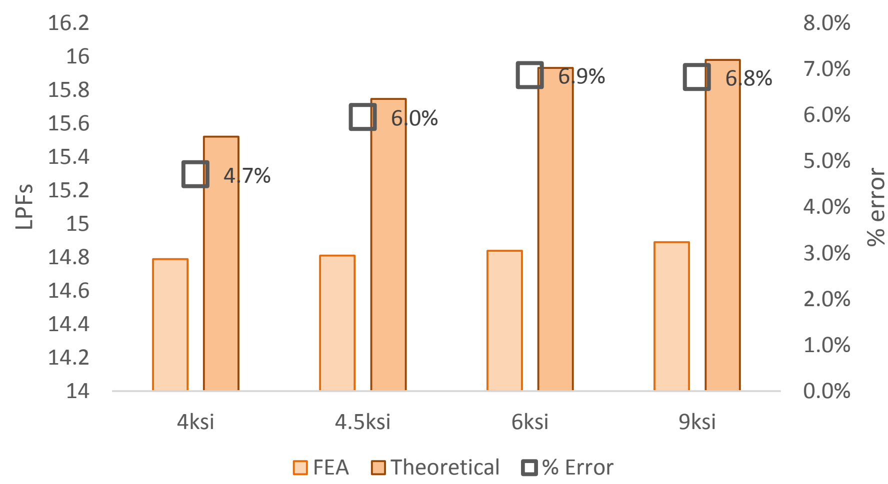

Figure 3.24 Comparison of APL from FE and theoretical calculations using FEA distribution factors. Columns refer to APL quantified by number of HS-20 trucks (LPF) while squares represent computed percent error between FEA and theoretical APLs.

Considering that load distribution could considerably affect the theoretical APL results was compared AASHTO GDFs with FEA GDFs. To compute FEA distribution factors (for live and dead load) following procedure was applied:

a. Find the girder section were first yield occurred.
b. Average strains of all elements composing maximally loaded bottom flange cross-section of each girder.
c. Divide average strain at maximum loaded section of each girder by the sum of the average strains in the maximum loaded sections of all girders, LDF

$= \frac{\varepsilon_{max}}{\sum^{N} \varepsilon_{max}}$, where N is number of girders and ε_{max} is the average strain in the maximum loaded section in the girder of interest.

The result showed (Table 3.4) that the average percent difference between AASHTO GDFs and FEA GDFs is 8.6%, and the “4.0ksi” model had lowest percent error (4.5%) while the “4.5ksi” model had the largest percent error (10.2%).

Table 3.4 FEA vs. theoretical comparison (APLs and GDFs)

	4 ksi	*4.5 ksi*	*6 ksi*	*9 ksi*
APL FEA (LPF)	14.79	14.81	14.84	14.89
APL Theoretical	15.52	15.75	15.93	15.98
Percent error (%)	4.7%	6.0%	6.9%	6.8%
GDF FEA	0.365	0.382	0.376	0.374
GDF AASHTO	0.348	0.343	0.339	0.338
Percent error (%)	4.7%	10.2%	9.8%	9.6%

Thus, the difference between the approximate AASHTO GDFs and the FEA GDFs were a clear source of error in the APL validation presented above. Therefore, it was decided to use FEA GDFs to calculate theoretical APLs. Replacing AASHTO GDFs with FEA GDFs gave significantly better results. For example, for “4ksi” model, percent error was calculated to be only 0.05%.

$$\# \text{HS-20} = \frac{M_{AD}}{M_A \cdot DF_{FEA}} = \frac{5{,}075}{939.6 \cdot 0.365} = 14.8$$

$$\%\ \text{error} = 1 - \frac{\text{APL FEA}}{\text{APL Modified Theoretical}} = 1 - \frac{14.79}{14.8} = 0.0005 \text{ or } 0.05\%$$

This procedure was repeated for all four models and results show (Figure 3.25) that average error between models was very small (2%). The modified theoretical APL results were calculated to be 14.8LPFs, 14.18 LPFs, 14.5 LPFs and 14.7 LPFs for the "4ksi", "4.5ksi", "6ksi" and "9ksi" models, respectively.

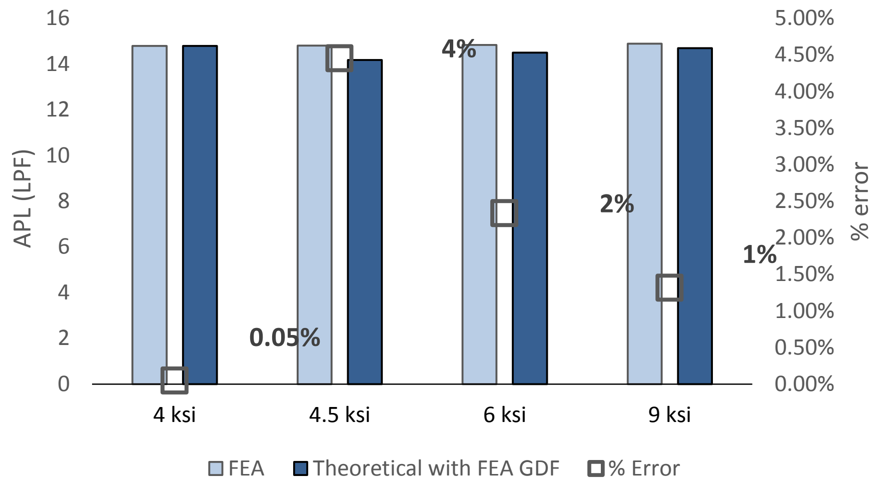

Figure 3.25 Comparison of APL from FE and theoretical calculations using FEA distribution factors. Columns refer to APL quantified by number of HS-20 trucks (LPF) while squares represent computed percent error between FEA and theoretical APLs.

The largest error (4%) was recorded for the "4.5ksi" model while the smallest error was recorded at "4ksi" model (0.05%). Both metrics (NA and APL) showed that our FEA models replicate well theoretical expectation. The average % error for NA metrics was 4.9%, while the average percent error for APL metrics (modified) was 2.0%. These results indicate that our FEA model is a valid mathematical representation of Bridge "7R" structure.

3.3 FE Model Calibration

Calibration refers to a process that scales the measurements from the instrument to a reference measurement in order to improve its accuracy. The FE model needs calibration due to the uncertainty of certain system parameters. For example, Bridge 7R had been in the service for more than 40 years before it was decommissioned and destructively tested. At the time of the testing, the compressive strength of the concrete deck was unknown. In order to ensure that the FE model accurately captured the behavior of the actual bridge, multiple values of concrete compressive strengths (f'_c) were varied in the FE models. It was hypothesized that compressive strength of the concrete was in the range between 4ksi and 9ksi. Therefore, four FE models with concrete compressive strengths of 4ksi, 4.5ksi, 6ksi and 9ksi were built for the calibration purposes.

Additionally, due to the age of the bridge, the condition of the composite interaction between bridge deck and girders was also unknown, and it was hypothesized that this parameter could also affect the accuracy of the FEA models. Therefore, it was decided that composite action between girders and bridge deck should be calibrated as well. Consequently, knowing that the degree of composite action between deck and girders can be simulated by varying the spacing of tie constraints connecting the deck and girders, this was a second parameter that was varied. This resulted in building FE models with four different spacings of tie constraints (2in, 4in, 8in and 16in tie spacing). All possible combinations of these two varied parameters (concrete compressive strength and tie spacings) were combined to produce a total of 16 FE models for model calibration.

3.3.1 FE Model Calibration Results-Concrete Compressive Strength

The experimental data obtained from the destructive testing of Bridge 7R was compared with the data obtained from the FE models with variable concrete stiffness (4ksi, 4.5ksi, 6ksi, and 9ksi) at four tie spacings (2in, 4in, 8in and 16in). More specifically, bottom flange strains measured during field testing at two bottom flange locations (G2-A and G3-A in Figure 3.4) were compared with bottom flange strains extracted from FE models at the same locations. Furthermore, cross-frame strains measured at the cross-frame connecting Girder 2 and Girder 3 (CF3 in Figure 3.4) were compared with cross-frame strains extracted from FE models at the same location.

The qualitative and quantitative comparison between FE models and field data were conducted. Qualitative comparison consisted of visual inspecting strain curves during 17 load increments, while quantitative comparison consisted of numerical evaluation of the slope of the strain curves.

3.3.1.1 Concrete Compressive Strength- Bottom Flange Results

The visual inspection (Figure 3.26) of the field data bottom flange strain curves shows a non-linear behavior between the 5th and 13th load increment. Considering that the girders and cross-frames were still in the elastic range, this was an unexpected result. One of the explanations for this behavior (McConnell, et al. 2015) was that there was a significant loss of composite action between the concrete deck and steel girders. This may have led to global and local losses of stiffness and decreased flexural capacity of the girder at the point of the load application. This partial loss of composite action could not be experimentally measured or accurately quantified. However, linear behavior in field strain measurements were observed during first four and last four increments. Therefore, the slopes of the of the strain curves for the first four load increments and last four increments were used for quantifying the difference between field data and FE data for the bottom flange data. Visual inspection of the bottom flange strain curves for all 17 load increments (Figure 3.26 a. and b.) showed that there is a marginal effect of the different concrete compressive strengths on bottom flange strains at both of gauge locations. The difference between models is visible only at high load levels (above 13 LPFs) and with only the 6ksi model differing significantly from the other three models. Bottom flange results (Table 3.5) show relatively good matching between FEA and experimental results. Average overall percent error for both gauges was only 8.36%. The largest average percent error (12.1%) was found at the "4ksi" model at gauge location G2-BF-A, while the smallest average percent error (4.6%) was found at the same gauge location at the "6ksi" model.

Table 3.5 Slopes of strain curves for bottom flange field data and FEA data for load increments 1-4 and 14-17. Average percent error is computed by averaging absolute values of percent errors computed for both load increment ranges.

Model	**Load Increment**	**G2 -BF-A**	**G3-BF-A**	**% error**		**average % error**	
Field	1-4	0.022	0.0353	**G2 -BF-A**	**G3-BF-A**	**G2 -BF-A**	**G3-BF-A**
	14-17	0.0211	0.0399				
"4ksi"	1-4	0.0201	0.0369	9.5%	4.3%	12.1%	8.8%
	14-17	0.0184	0.0352	14.7%	13.4%		
"4.5ksi"	1-4	0.0200	0.0374	10.0%	5.6%	11.1%	7.6%
	14-17	0.0188	0.0364	12.2%	9.6%		
"6ksi"	1-4	0.0208	0.0388	5.8%	9.0%	4.6%	5.8%
	14-17	0.0204	0.0389	3.4%	2.6%		
"9ksi"	1-4	0.0205	0.0376	7.3%	6.1%	8.9%	8.0%
	14-17	0.0191	0.0363	10.5%	9.9%		

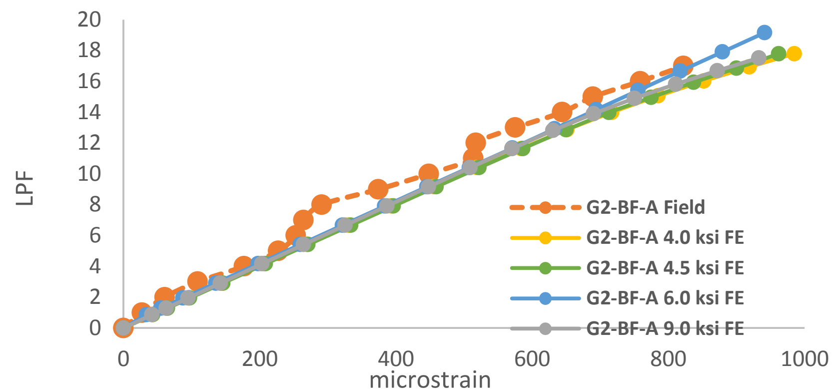

a)

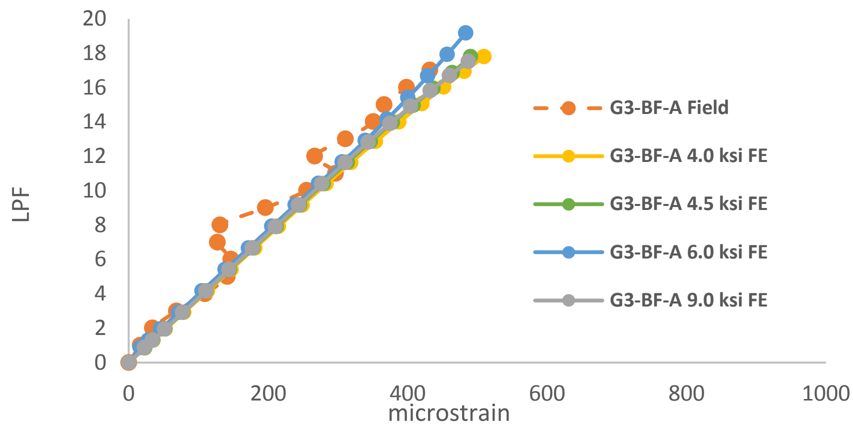

b)

Figure 3.26 Comparison between field data and FE models for bottom flange gauge location a) G2-BF-A; b) G3-BF-A.

3.3.1.2 Concrete Compressive Strength-Cross-frames Result

A visual inspection of the cross-frame field data (Figure 3.27) showed that linear strain behavior was only detected during the first four load increments. Therefore, for the cross-frame data, slopes of strain curves during first four load increments were used for the quantitative comparison. Visual inspection of the strain curves at gauge location CF3-BA2-A (Figure 3.27a) shows that post yielding behavior (strain values > 1243με) are better matched with FE models that have larger concrete compressive strengths (“9ksi” and “6ksi”) compared to models that have lower concrete compressive strength (“4ksi” and “4.5ksi”). Furthermore, it seems that all four models were able to replicate the significant softening action observed in the field data after 13h load increment. Results (Table 3.6) show that the FEA cross-frame data match very well with experimental data. The overall average percent error for all models at both gauges was 9.9%. The smallest percent error (1.06%) was found at gauge CF3-BA-2-A in the “6ksi” model, while the largest percent error (28.72%) was found at gauge CF3-TA1-A in the “4ksi” model. The percent errors are significantly less for the CF3-BA gauge location compared to the CF3-TA gauge location, across all models. For example, average percent error for CF3-BA gauge location is 3.5%, while the average percent error for CF3-TA is 25.3%.

Table 3.6 Slopes of strain curves for cross-frame field and FEA data for load increments 1-3.

Model	**CF3-BA2-A**	**CF3-TA1-A**	**CF3-BA2-A**	**CF3-TA1-A**
Field	0.0094	0.0954	**% error**	**% error**
“4ksi”	0.0087	0.0680	7.45%	28.72%
“4.5ksi”	0.0091	0.0698	3.19%	26.83%
“6ksi”	0.0095	0.0718	1.06%	24.74%
“9ksi”	0.0104	0.0755	10.64%	20.86%

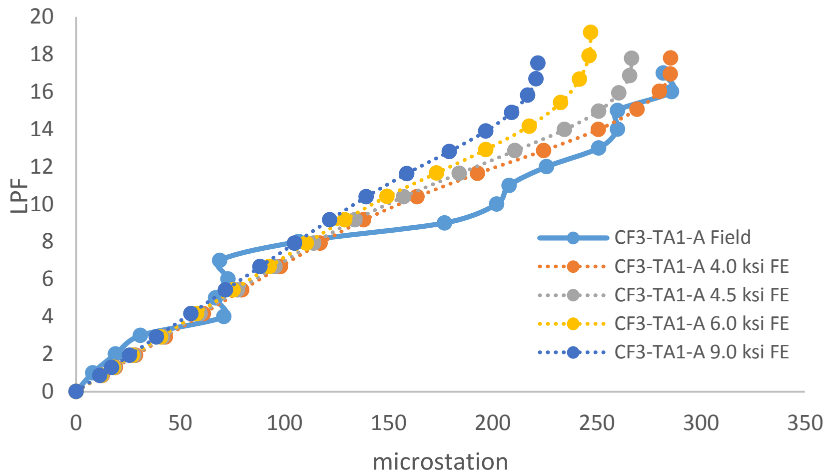

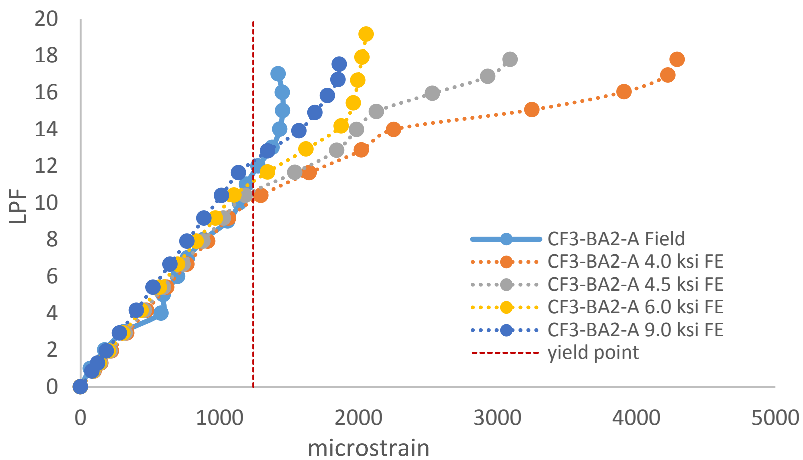

Figure 3.27 Comparison between field and FE data for cross-frame gauge location (a) CF3-BA2-A and (b) CF3-TA1-A. The dashed vertical line in (a) represents the theoretical yielding point for 36ksi steel (1243με).

3.3.2 FE model calibration Results –Tie Spacing Results

Beside concrete compressive strength, the other parameter calibrated is the composite action between the concrete deck and steel girders. The composite action between the deck and steel girders is achieved in the field by the shear studs. The composite action in FE models is achieved using tie constraint (see Section 3.1.9).

Therefore, by changing the number of tie constraints (i.e., spacing between tie constraints), relaxing or stiffening of the composite action could be achieved. For this purpose, four different tie spacings were considered. The location of the tie constraints is related to the location of the nodes on the top flange elements, therefore tie spacing was limited to increments of 2in because this is the element size of the top flange and haunch while deck element size is 12x12in.

Specifically, a model that had tie constraints placed every node was the “1-node” model; the model that had tie constraints placed every two nodes is labeled the “2-node” model; the model that had tie constraints placed every 4 nodes was labeled the “4-node” model; and finally, the model that had tie constraints placed every 8 nodes was labeled the “8-node” model. Considering that the width of the top flange elements was kept constant at 2in (meaning the nodes were located 2” apart), the “2-node” model had a tie constraint every 4in, the “4-node” model had a tie constraint every 8in, and the “8-node” model had a tie constraint every 16in. Additionally, each tie-spacing model (“1-node”, “2-node”, “4-node” and “8-node”) had four different concrete compressive strengths (4ksi, 4.5ksi, 6ksi, and 9ksi). This yielded a total of 16 FE models that were built and compared with the experimental data (Figures 3.28 to 3.31). The qualitative and quantitative comparison was conducted between FEA results and field data. Qualitative analysis consisted of visual inspecting strain curves during 17 load increments, while quantitative analysis consisted of numerical evaluation of the slope of the strain curves.

3.3.2.1 Tie Spacing -Bottom Flange Results

The visual inspection (Figure 3.28) of the bottom flange results showed good matching between FEA data and experimental results regardless of the tie spacing. However, it seems “4 ksi” models with “2-node” and “4-node” tie spacing replicate bottom flange field data especially well (blue dotted lines in Figure 3.28a and c).

Quantitative analysis of the bottom flange slope data (Table 3.7) showed that FEA data is matching very well with experimental data. The overall average percent error among all models is only 9%. The results show that the lowest absolute percent error was calculated for the “4.5ksi 2-node” model at the gauge location G3-BF-A for the slope during the first four load increments. The slope of this model during first four load increments was the same as the slope measured during field experiment (0.0353). For the contrast purpose, the largest absolute percent error (34%) was calculated for the “4 ksi 4-node” model at the same gauge location.

Furthermore, the results also show that the smallest average percent error (calculated by averaging errors obtained at two load increments, 1-4 and 14-17) was 4.4% at G3-BFA in the 4-node spacing model (“6ksi 4-node”) while, the largest percent error (19.9 %) at G3-BF-A was found at “4ksi 4-node””model.

3.3.2.2 Tie Spacing -Cross-frames Results

The visual inspection of the cross-frame data (Figure 3.29 and 3.30) shows that experimental data and FE strains match well up to the point when the cross-frame’s bottom chord reached its yielding point (1243με for 36ksi steel). This point is marked in Figures 3.30-3.31(a) and (b) with a dashed vertical line. After reaching the yielding point, the FE models’ response to the increasing load became highly non-linear and more influenced by tie spacing (Figure 3.30a and 3.30b; Figure 3.31a and 3.31b). Results show that less composite FE models (such as”8-node” models) show significantly larger bottom chord strains than more composite models (such as “1-node”, “2-node” and “4-node” spacing models). While all FE models show this same general pattern, this behavior is less prominent for the “9ksi” models as the response to the post- yielding behavior is less prominent. Furthermore, most FE models accurately captured the softening action of the cross-frame top chord that was present in the field data after 16th load increment (LPF=16).

The quantitative analysis of the cross-frame data (Table 3.8) showed good matching between FEA and experimental data in some cases. The average percent error for all models was 16.8%. The lowest percent error was calculated for the “4.5ksi 8-node” model at gauge location CF3-BA2-A. The slope calculated for this model was identical to the slope calculated for the field data (0.094). The largest percent error (51. 7%) was calculated for the “6ksi 4-node” model at gauge location CF3-TA1-A. The lowest average percent error 0.1%) was calculated for ““4.5ksi 8-node”” model (Table 3.9), while the ““6ksi 4-node”” model show the largest overall average percent error (33.1%). Average percent error for cross-frames was calculated by averaging percent errors at bottom chord and top chord gauges. Both qualitative and quantitative analysis showed that there is not one definite FE model that perfectly fits the experimental data. However, the calibration procedure proved that both compressive concrete strength and composite action can substantially affect the behavior of the bridge structure. The results also show that cross-frames strains are more sensitive to change in parameters than bottom flange strains.

3.4 FE Model Parameter Selection

The validation results indicate that the FEA model developed is an accurate mathematical representation of Bridge 7R. Both metrics used to validate the model (NA and APL) were matched well with the theoretical data (4.1% and 2.0 % error respectively). The calibration results showed that there is not a single model that consistently had lowest errors at bottom flange and cross-frame locations. Therefore, it was decided to average computed errors for all bottom flange and cross-frame gauges and all models at four concrete strengths. For example, Table 3.9 shows three columns labeled “girder average”, “cross-frame average” and “concrete strength average”. The first two columns contain average values of all girder and cross-frame errors per model, respectively. The last column (“concrete strength average”) contains average values of all errors per respective concrete strength. The results show that the lowest concrete strength average error was for 4.5ksi models (11.8%), while the highest was at 4ksi models (15.4%). Thus, it was decided to use 4.5ksi as concrete compressive strength parameter in further studies. This value is representative of values used in current bridge designs and seems reasonable approximation of real concrete strength of Bridge 7R.

To determine what spacing should be used for modeling composite action, beside the accuracy of the model, modeling effort was also taken into consideration. It is worth noting that “1-node” models were significantly less time consuming to build than any other models. To determine the best performing model, total percent errors (girders and cross-frames) where averaged based on node spacing. For example, all “1-node spacing“ percent errors (regardless of the concrete strength) were averaged together. The results show (Figure 3.39) that “8-node” spacing has the lowest overall percent error (6.8%), while “4-node” spacing has the highest overall percent error (18.1%). However, while the results indicate that 8-node spacing models would give the best overall result compared to Bridge 7R field data, it is questionable if 8-node spacing would accurately model full composite action between girder and deck. A preliminary study that modeled one girder with 8-node (16in) tie spacing between the girders and deck showed significant deviation from theoretical mid-span deflections. This result indicated that fully composite behavior was not able to be modeled with 8-node tie spacing. Furthermore, substantially more effort is needed to 8-node spacing models, vs. 1-node spacing models. This is especially true knowing that the total percent error difference between 1-node spacing models (14.1%) and (6.8%) is only 7.3%. For this reason, it was decided to use “1-node”spacing for modeling composite action between concrete deck and steel girders in the parametric study.

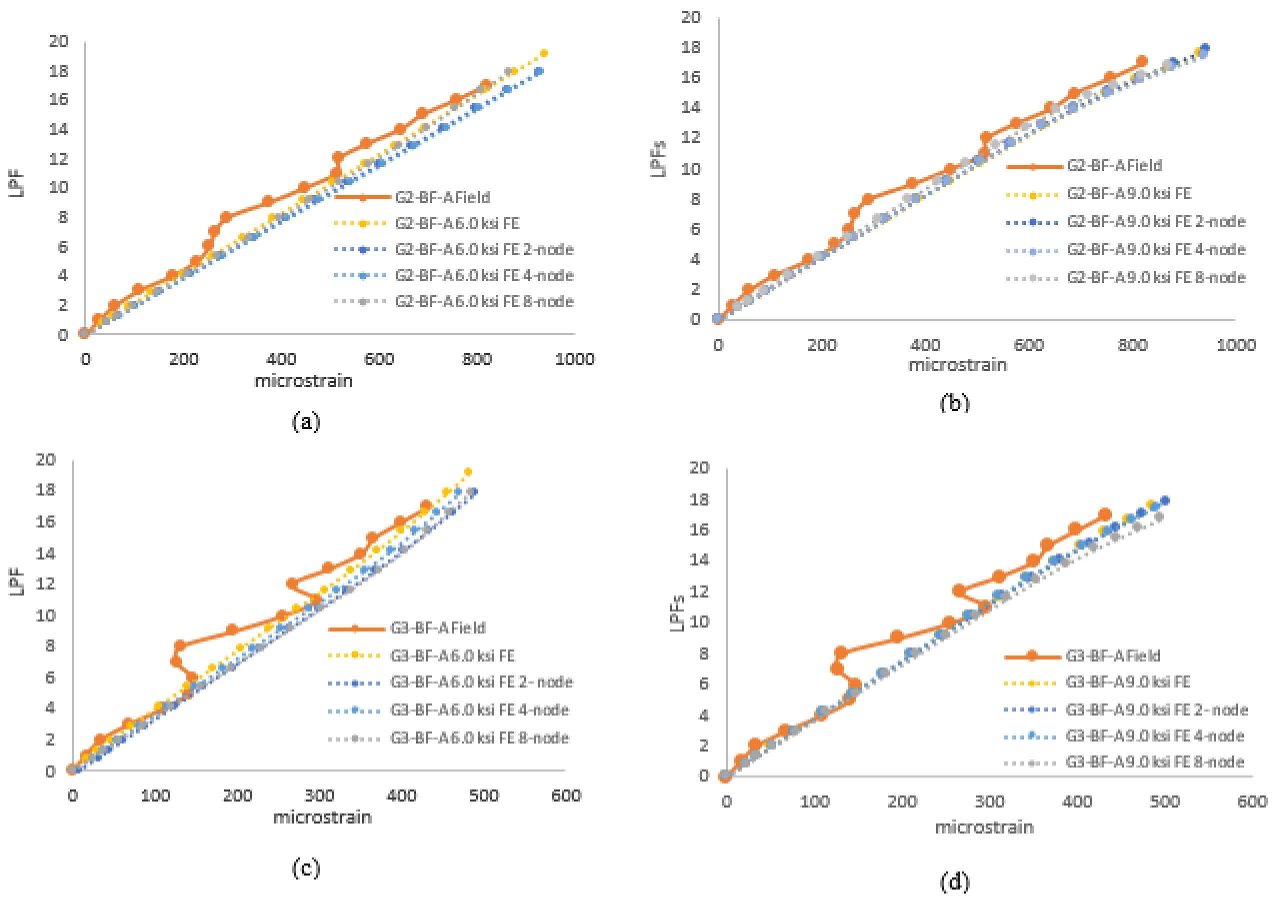

Figure 3.28 Comparison of bottom flange strains between field and FE data with different tie element spacings: (a) gauge location G2-BF-A “4.0 ksi” models, (b) gauge location G2- BF-A “4.5 ksi” models, (c) gauge location G3- BF-A “4.0 ksi” models and (d) gauge location G3-BF-A “4.5ksi” models.

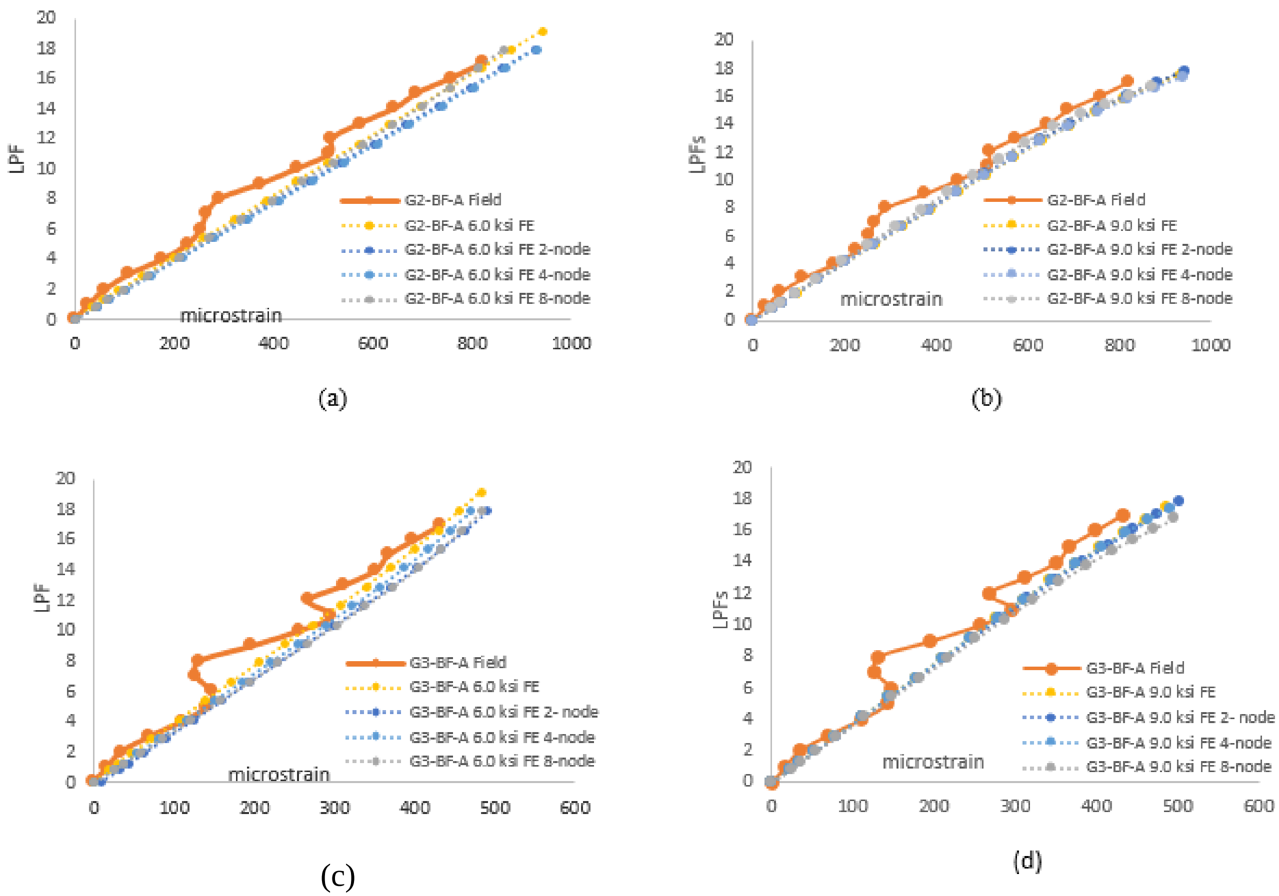

Figure 3.29 Comparison of bottom flange strains between field and FE data with different tie element spacings: (a) gauge location G2-BF-A “6.0 ksi” models, (b) gauge location G2- BF-A “9.0 ksi” models, (c) gauge location G3- BF-A “6.0 ksi” models and (d) gauge location G3-BF-A “9.0 ksi” models.

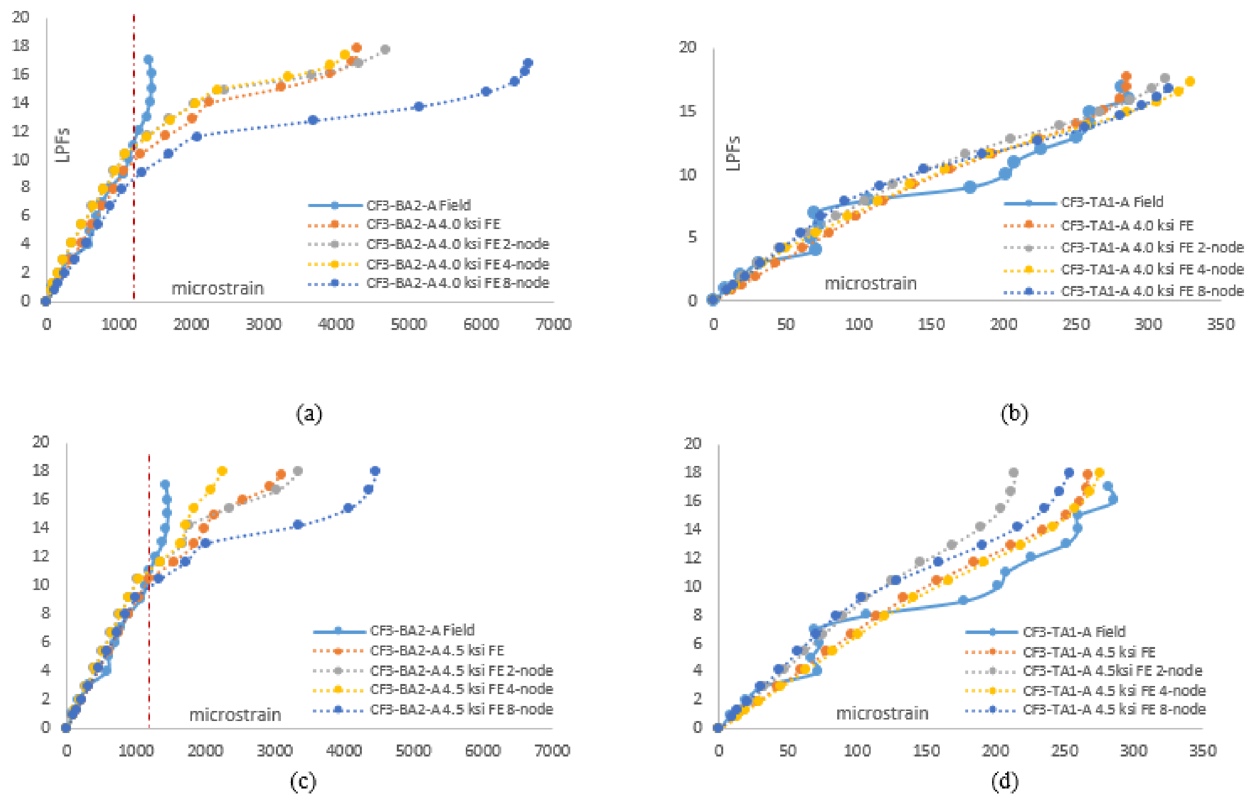

Figure 3.30 Comparison of cross-frame strain between field and FE data with different tie element spacings: (a) gauge location CF3-BF2-A “4.0 ksi” models, (b) gauge location CF3-BF2-A “4.5 ksi “models, (c) gauge location CF3- TA1-A “4.0 ksi” models and (d) gauge location CF3-TA1-A “4.5 ksi” models. The red dashed line represents the location of the yield strain (1243με)

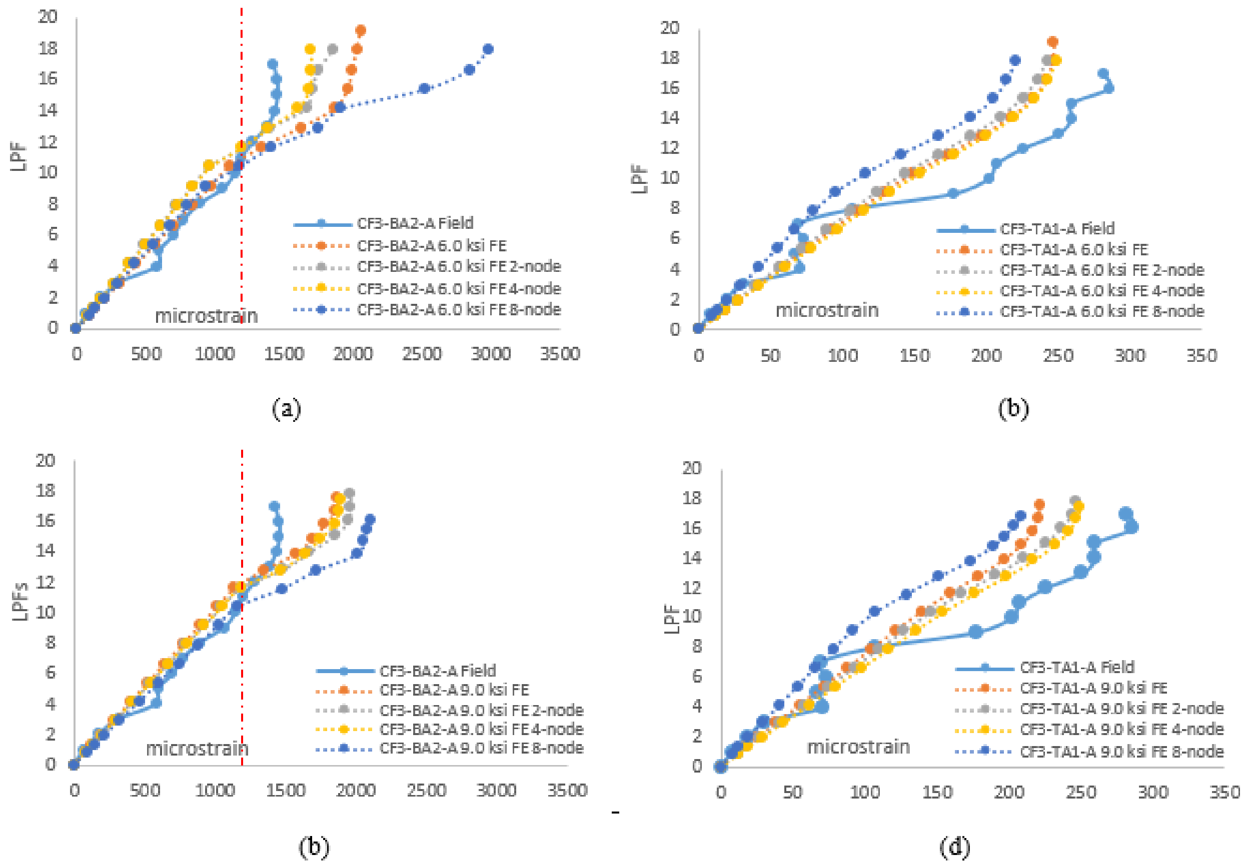

Figure 3.27 Comparison of cross-frame strain between field and FE data with different tie element spacings: (a) gauge location CF3-BF2-A "6.0 ksi" models, (b) gauge location CF3-BF2-A "9.0 ksi "models, (c) gauge location CF3- TA1-A "6.0 ksi" models and (d) gauge location CF3-TA1-A "9.0 ksi" models. The vertical dashed line in a) and b) represents the location of the yield strain (1243με)

Table 3.7 Slope comparison between FE and field testing data measured at bottom flange gauges

Model	Load Increment	G2 -BF-A	G3-BF-A	% error		average % error	
Field	1-4	0.022	0.0353	G2 -BF-A	G3-BF-A	G2 -BF-A	G3-BF-A
	14-17	0.0211	0.0399				
"4ksi 1-node"	1-4	0.0201	0.0369	9.5%	4.3%	12.1%	8.8%
	14-17	0.0184	0.0352	14.7%	13.4%		
"4ksi 2-node"	1-4	0.0289	0.053	23.9%	33.4%	15.2%	19.8%
	14-17	0.0198	0.0376	6.6%	6.1%		
"4ksi 4-node"	1-4	0.0288	0.0537	23.6%	34.3%	15.9%	19.9%
	14-17	0.0195	0.0378	8.2%	5.6%		
"4ksi 8-node"	1-4	0.0209	0.0359	5.3%	1.7%	6.7%	8.5%
	14-17	0.0195	0.0346	8.2%	15.3%		
"4.5ksi 1-node"	1-4	0.02	0.0374	10.0%	5.6%	11.1%	7.6%
	14-17	0.0188	0.0364	12.2%	9.6%		
"4.5ksi 2-node"	1-4	0.0185	0.0353	18.9%	0.0%	17.1%	5.3%
	14-17	0.0183	0.0361	15.3%	10.5%		
"4.5ksi 4-node"	1-4	0.019	0.0361	15.8%	2.2%	13.7%	4.5%
	14-17	0.0189	0.0374	11.6%	6.7%		
"4.5ksi 8-node"	1-4	0.0198	0.0343	11.1%	2.9%	7.5%	6.9%
	14-17	0.0203	0.036	3.9%	10.8%		
"6ksi 1-node"	1-4	0.0208	0.0388	5.8%	9.0%	4.6%	5.8%
	14-17	0.0204	0.0389	3.4%	2.6%		
"6ksi 2-node"	1-4	0.0194	0.0358	13.4%	1.4%	11.4%	5.1%
	14-17	0.0193	0.0367	9.3%	8.7%		
"6ksi 4-node"	1-4	0.0192	0.0362	14.6%	2.5%	12.2%	4.3%
	14-17	0.0192	0.0376	9.9%	6.1%		
"6ksi 8-node"	1-4	0.02	0.0362	10.0%	2.5%	6.2%	6.2%
	14-17	0.0206	0.0363	2.4%	9.9%		
"9ksi 1-node"	1-4	0.0205	0.0376	7.3%	6.1%	8.9%	8.0%
	14-17	0.0191	0.0363	10.5%	9.9%		
"9ksi 2-node"	1-4	0.0207	0.037	6.3%	4.6%	7.8%	8.0%
	14-17	0.0193	0.0358	9.3%	11.5%		
"9ksi 4-node"	1-4	0.0206	0.0375	6.8%	5.9%	9.2%	8.5%
	14-17	0.0189	0.0359	11.6%	11.1%		
"9ksi 8-node"	1-4	0.0215	0.0363	2.3%	2.8%	4.7%	9.5%
	14-17	0.0197	0.0343	7.1%	16.3%		

Table 3.8 Slope comparison between FE and field testing data measured at cross-frame gauges

Model	**CF3-BA2-A**	**CF3-TA1-A**	**% error**	**% error**
Field	0.0094	0.0954	**CF3-BA2-A**	**CF3-TA1-A**
“4ksi 1-node”	0.0087	0.0680	8.05%	40.29%
“4ksi 2-node”	0.0128	0.0964	26.56%	1.04%
“4ksi 4- node”	0.0127	0.0878	25.98%	8.66%
“4ksi 8-node”	0.0076	0.09	23.68%	6.00%
“4.5ksi 1-node”	0.0091	0.0698	3.30%	36.68%
“4.5ksi 2-node”	0.0107	0.0882	12.15%	8.16%
“4.5ksi 4- node”	0.0104	0.0659	9.62%	44.76%
“4.5ksi 8-node”	0.0094	0.0953	0.00%	0.10%
“6ksi 1-node”	0.0095	0.0718	1.05%	32.87%
“6ksi 2-node”	0.0111	0.0747	15.32%	27.71%
“6ksi 4- node”	0.011	0.0629	14.55%	51.67%
“6ksi 8-node”	0.0099	0.099	5.05%	3.64%
“9ksi 1-node”	0.0104	0.0755	9.62%	26.36%
“9ksi 2-node”	0.01	0.0722	6.00%	32.13%
“9ksi 4- node”	0.01	0.0678	6.00%	40.71%
“9ksi 8-node”	0.009	0.1014	4.44%	5.92%

Table 3.9 Average error for girders and cross-frames.

Model	Girder Average	Cross-frame Average	Concrete Strength Average	Model	Girder Average	Cross-frame Average	Concrete Strength Average
"4ksi 1-node"	10.5%	24.2%	15.4%	"6ksi 1-node"	5.2%	17.0%	13.0%
"4ksi 2-node"	17.5%	13.8%		"6ksi 2-node"	8.3%	21.5%	
"4ksi 4-node"	17.9%	17.3%		"6ksi 4-node"	8.3%	33.1%	
"4ksi 8-node"	7.6%	14.8%		"6ksi 8-node"	6.2%	4.3%	
"4.5ksi 1-node"	9.4%	20.0%	11.8%	"9ksi 1-node"	8.5%	18.0%	12.2%
"4.5ksi 2-node"	11.2%	10.2%		"9ksi 2-node"	7.9%	19.1%	
"4.5ksi 4-node"	9.1%	27.2%		"9ksi 4-node"	8.9%	23.4%	
"4.5ksi 8-node"	7.2%	0.1%		"9ksi 8-node"	7.1%	5.2%	

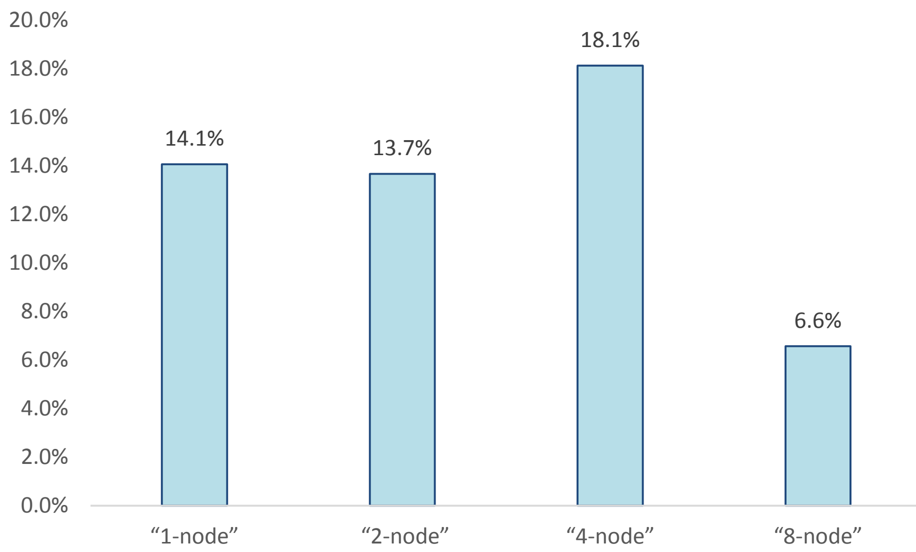

Figure 3.33 Node spacing overall percent error.

REFERENCES

Abaqus 6.11 Analysis User's Manual. (2011). Online Documentation Help. Dassault Systèmes.

American Association of State Highway and Transportation Officials –AASHTO. (2015). “LRFD Bridge Design Specifications”. *6th Edition*. AASHTO, Washington, DC.

Bathe, K.J. (1982). “Finite element procedures in engineering analysis”. Englewood Cliffs, N.J: Prentice-Hall.

Femap 11.1 Documentation (2012). Siemens.

McConnell, J., Chajes, M., Michaud, K. (2015). "Field Testing of a Decommissioned Skewed Steel I–Girder bridge: Analysis of System Effects". *Journal of Structural Engineering*, 141.1 D4014010.

Michaud, K. (2011). “Evaluating reserve bridge capacity through destructive testing of a decommissioned bridge”. *Master Thesis.* University of Delaware.

Radovic, M., McConnell, J (2014). “Evaluation of Cross-frame Designs for Highly Skewed Steel I-Girder Bridges”. *Proceedings of 48th International Bridge Conference*, Pittsburg, IBC-14-47.

Riks, E. (1979). "An incremental approach to the solution of snapping and buckling problems". *International Journal of Solids and Structures*, 15.7, 529-551.

Ross, J. H. (2007). “Evaluating Ultimate Bridge Capacity Through Destructive Testing of Decommissioned Bridges”. *Master Thesis*. University of Delaware.

Chapter 4

EVALUATION OF FEA PARAMETRIC STUDY DATA USING "DISCRETE" AND "HOLISTIC" METRICS

This chapter investigates the influence of cross-frames on the stress distributions in steel I-girder bridges through a parametric study. Additionally, this chapter introduces new methods that can be used to evaluate finite element analysis data. Furthermore, it investigates disadvantages and deficiencies in currently employed evaluation methods of FEA, especially when evaluating data obtained under post-elastic loads. The chapter ends by summarizing the main finding and makes recommendations for future research.

4.1 Parametric Study Design

4.1.1 Overview

From the literature review, it is implied that bridge skew, cross-frame design, and cross-frame layout affect load distribution in the bridge. To quantify these affects, a parametric study was designed for this purpose. Therefore, bridge skews, cross-frame design, and cross-frame layout are parameters that were varied in order to investigate stress distributions. Five bridge *skews* (0°, 25°, 46°, 55° and 63°), two cross-fame *designs* (K-frame vs. X-frame configurations) and two cross-frame *layouts* (inline vs. staggered) were modeled and analyzed for this parametric study. Additionally, FE models without cross-frames (no-frame models) were added at each bridge skew, for a total of 25 models (Table 4.1). Data were analyzed under three load levels: design load, yield of one girder, and system yield load.

Table 4.1 Conceptual summary of FE parametric models.

SKEW	**K-FRAME INLINE**	**K-FRAME STAG**	**X-FRAME INLINE**	**X-FRAME STAG**	**NO FRAME**
0°	x	x	x	x	x
25°	x	x	x	x	x
46°	x	x	x	x	x
55°	x	x	x	x	x
63°	x	x	x	x	x

4.1.2 Load Levels

All data were extracted under three loading levels:

a) design load,

b) first yield load, and

c) system yield load.

Design load refers to a load equivalent of the one HS-20 truck on the bridge. This load level was selected as a reference load because many bridge practitioners are familiar with this load level and because this is the load level on which most existing assumptions about bridge behavior are predicated. First yield load refers to a magnitude of load that causes the entire cross-section of bottom flange of one girder to yield. This load level represents an onset of post elastic behavior of the bridge. System yield refers to a magnitude of load that causes entire cross-sections of bottom flanges of all girders to yield. This load level was selected as a measure of system capacity of the bridge. The girders have compact cross-sections and theoretically they should be able to develop full plastic stress distribution. However, preliminary results for the skewed bridges showed that full plasticity of all girders could not be achieved even if the Riks analysis deflection limit was set to be unrealistically high mgnitude (200in). It is worth noting that some highway agencies (such as the California Transportation Agency, CalTrans) stipulate that for a section to be classified as compact it must also be tangent (0° skew) (Caltrans, 2014, Section 6.4.2.1). Conservatism in this stipulation is founded in the uncertainty of the behavior of skewed bridges. Therefore, it was decided to use yielding moment as measure of the girders theoretical capacity instead of plastic moment.

4.1.3 FEA Modeling

The FE models employed element types and sizes, material properties, boundary conditions, and simulation of composite action identical to the modeling described in detail in Chapter 3. However, a change was made to location of the applied load and magnitude of nodal loads. For the all parametric models, load was modeled as HS-20 truck load via nodal loads applied to deck element nodes. A total of 6 nodal loads were created with 2 nodal loads having the magnitude of 4,000lb and 4 nodal loads having the magnitude of 16,000lb (Figure 4.1). The longitudinal distance between nodal loads is 14ft, while the transverse distance between nodal loads is 6ft. To make the location of the nodal load uniform across the all parametric model, it was decided to place geometric center of the HS20 truck at the geometric center of the bridge. Once the geometric centers were aligned, the locations of the wheel loads and corresponding nodal loads were determined. The load magnitude and load parameters were then entered in Abaqus' Riks analysis function.

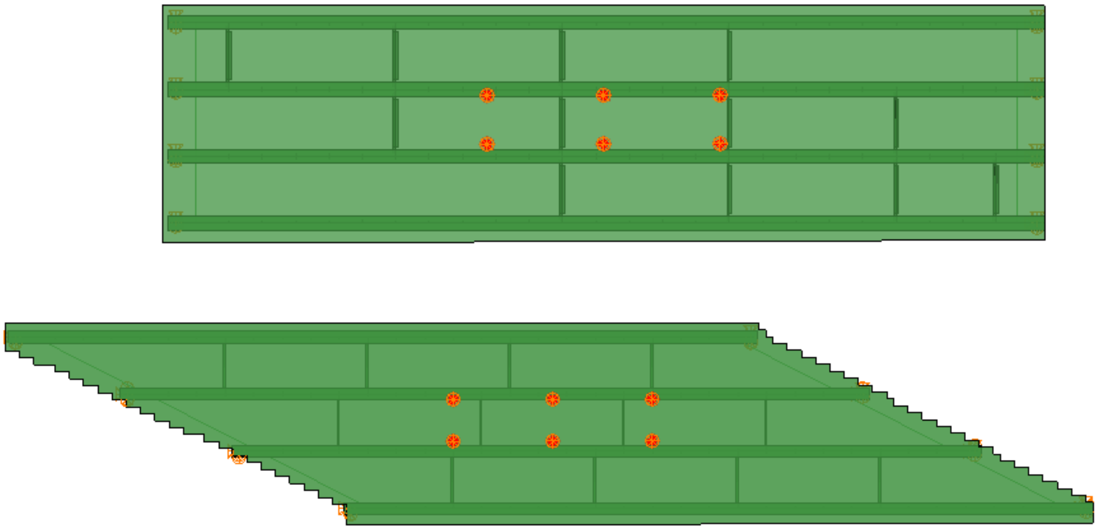

Figure 4.1 Nodal loads representing HS20 truck wheels were centered over geometric center of the bridge shown at different bridge skews (63°and 0°).

4.1.4 Data Organization

The main idea behind the parametric study was to investigate influence of cross-frame design and layout on stress distributions in the bridge's main structural components of the girders and deck. Therefore, two element groups (girders and deck) are created in each FE model. Stress data were then organized in such a way that the girder group contained girder elements stresses from *all girders*, while deck element group contains stresses from all elements in the deck. The size of the data set being analyzed consisted of 1372,264 elements x 3 loading conditions, which totals to 411,792 data points per model.

4.1.5 Data Output Types

The data output refers to different types of data extracted and computed from the FEA. At each of the three load conditions following data types were obtained either directly from the model results (items a-c in the list below) or from synthesis of the stress results (items d and e in the list below):

a) The locations of the first yield and system yield along the girders' longitudinal length.

b) The number of HS-20 trucks needed to cause first yield and system yield; this represents first yield and system yield capacities of the bridge.

c) Longitudinal (s11) stresses at design, first yield, and system yield load levels.

d) Bottom flange major axis and lateral bending stresses at design, first yield and system yield load levels (for detail procedure how these stresses are computed see Sections 4.3.1.1 and 4.3.1.2).

e) Stress histograms of each element group at design, first yield, and system yield load levels.

4.1.6 Parametric Models

4.1.6.1 Girder and Deck Characteristics

Each FE model used in parametric studies has following geometric specifications (Figure 4.2):

a. four steel plate I-girders spaced 8ft on center,

b. girder length of 105.3ft,

c. bottom flange dimensions of 20in x 1.25in,

d. top flange dimension of 20in x 1in,

e. web dimensions of 60in x 0.5in,

f. haunch thickness of 2in,

g. deck thickness 8in.

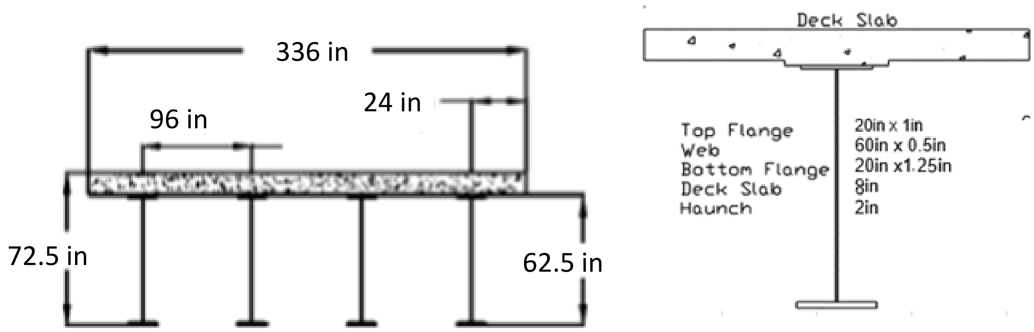

Figure 4.2 Geometry and cross-sectional properties of parametric models

Girder lengths, depths, spacings and deck thickness were the same as Bridge 7R. However, small adjustments were made to make the models more realistic relative to current design practices and to make them easier to build in FEA software. For example, web thickness was increased from 0.375in to 0.5in. The 0.5in thickness was chosen based on a recommendation listed in AASHTO /NSBA guidelines (2012) that 0.5in minimum web thickness is preferred even if smaller thickness would satisfy the strength and slenderness. The thicker web made longitudinal stiffeners unnecessary and they were thus excluded from the parametric models. Furthermore, to simplify modeling procedures, all girders' bottom flanges were modeled to have same width and thickness (20in x 1.25in) and all girders' top flanges were modeled to have same width and thickness (20in x 1in). These are dimensions of exterior girders' top and bottom flanges of Bridge 7R (without coverplates).

All FE models have concrete compressive strength f'c=4,500psi and steel strength of 36,000ksi. Interior girders have (5in x 0.5in) double-sided transverse stiffeners spaced every 4ft (same as Bridge 7R), while exterior girders have transverse stiffeners spaced 4ft only on the interior side of the web. Transverse stiffeners are connected to the top and bottom flanges and along the full web depth. Over the supports, each girder is stiffened with full depth bearing stiffeners (5in x 1.5in) connected to top and bottom flange. End diaphragms are modeled with beam elements as described in Section 3.1.7. A preliminary study was conducted to evaluate the effect of end diaphragm stiffness on bridge first yield and system capacities. The end diaphragm axial, bending and torsional stiffness were reduced to match the axial, bending and torsional stiffness of intermediate diaphragms. The results showed that this stiffness reduction of the end diaphragms did not change the first yield or system yield capacity of the bridge.

4.1.6.2 Bridge Skews

For the purpose of this study, five different bridge skews were analyzed (0°, 25°, 46°, 55° and 63°). To create parametric models with different skew, Bridge "7R" (63° skew) was used as a base model for all other designs (Figure 4.3e).

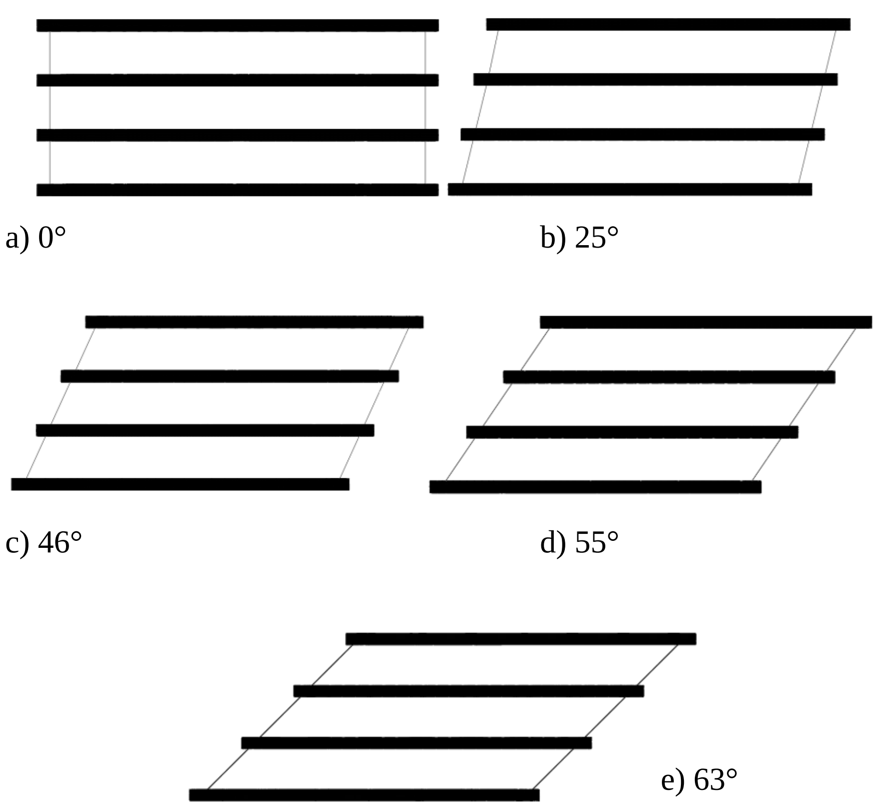

Figure 4.3 Girder layouts for different bridge skews in FE models. Cross-frames are not shown in the figures.

The most efficient and practical way to create multiple bridge skews based of Bridge "7R" was to use existing transverse stiffeners as connection plates for cross-frames. The transverse stiffeners in Bridge “7R” were spaced every 4ft, and moving girders 4ft longitudinally with respect to their initial position, would yield a bridge skew of 55° (Figure 4.3d). Accordingly, moving girders 8ft longitudinally with respect to their initial position, would yield a bridge skew of 46° (Figure 4.3c) and so on. Building FE models using this approach allowed identical cross-frame spacing to be used in all FE models, and reduce extra variability between parametric models (Figure 4.3).

4.1.6.3 Cross-frame Designs

Two cross-frame designs were considered for this study: K-frame and X frame. K-frame configurations (Figure 4.4) consist of a bottom chord, two diagonals, and a top chord. The bottom chord consisted of two discrete steel angle members (L4x4x0.5) with an unbraced length of 32in. These bottom chord steel angles are connected to one another and the diagonals by a 36x24x0.5in steel gusset plate. The diagonals are made of L4x3.5x0.5steel angles with an unbraced length of 43in. The top chord consists of L4x4x0.5 steel angle with an unbraced length of 65in. The top chord and each diagonal are connected to each other and the girder with 20x12x0.5in steel gusset plates.

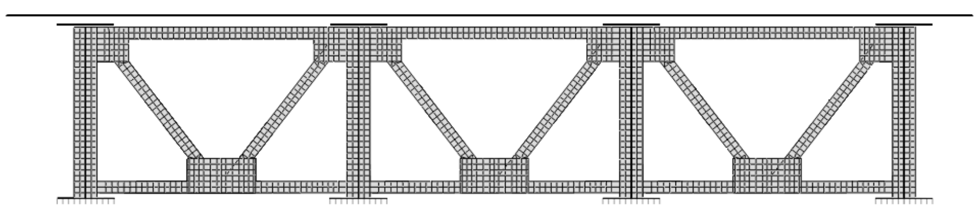

Figure 4.4 Schematic view of K-frame element mesh in parametric models

The total steel volume of steel in the K-frame configuration is 1212in^3. The equivalent axial stiffness of the K-frame configuration is 4,300,518 kip-in/rad. The equivalent axial stiffness was computed using equations proposed by Helwig & Yura (2012), which for K-frames is:

$$\beta_b = \frac{2ES^2{h_b}^2}{\frac{8{L_c}^3}{A_c} + \frac{S^3}{A_h}} \tag{4.1}$$

where, S is cross-frame width (88in), h_b is cross-frame depth (58in), L_c is length of the diagonal members (43in), E is Young's modulus (29,000,000psi), A_c is cross-sectional area of a diagonal member (3.75in²) and A_h is a cross-sectional area of horizontal member (3.75in²).

X-frame configurations (Figure 4.5) also consist of a bottom chord, a top chord and two diagonals of the same cross-section dimensions as the K-frame configurations. Specifically, the bottom chord consists of L4x4x0.5 steel angle with an unbraced length of 68in. The top chord consists of L4x4x0.5 with unbraced length of 68in. The diagonals are L4x3.5x0.5 steel angles with unbraced lengths of 80in. In the middle, where diagonal lines intersect each other, the element meshes of the concentric legs of the diagonals were connected using multi point constraint (MPC) elements. This constraint replicates the connection through a small gusset plate that is commonly found at this location in X-frame designs, which provides lateral support to out-of-plane bending. The bottom chord, top chord and diagonals are connected to transverse stiffeners with 20x12x0.5in gusset plates.

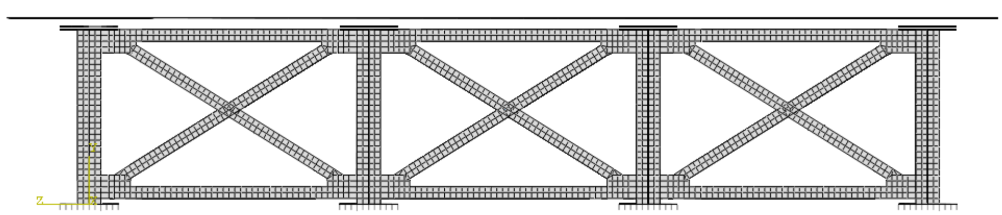

Figure 4.5 Schematic view of X-frame element mesh in parametric models

The total steel volume of the X-frame configuration is 1169 in^3. The equivalent axial stiffness of the X-frame configuration was also calculated using Helwig & Yura (2012) equations to be 5,533,254 k-in/rad.

$$\beta_b = \frac{A_c E S^2 {h_b}^2}{{L_c}^3} \tag{4.2}$$

In the equation (4.2), S is cross-frame width (88in), h_b is cross-frame depth (58in), L_c is length of the diagonal members (80in), E is Young's modulus (29,000,000psi) and A_c is cross-sectional area of diagonal member (3.75in²).

4.1.6.4 Cross-frame Layouts

Two cross-frame layouts were considered for this study: inline and staggered. The inline cross-fame layout consisted of cross-frames in the same transverse line (Figure 4.6). The staggered cross-frame layout is created by offsetting the cross-frames 4ft from each other, where transverse stiffeners are located on the girder (Figure 4.6). Bridge 7R had a total of 12 individual cross-frames spaced 20ft apart. Because the aim of this study is to investigate response of the cross-frames as a system, it was necessary to keep the number of cross-frames and their spacing as similar as possible.

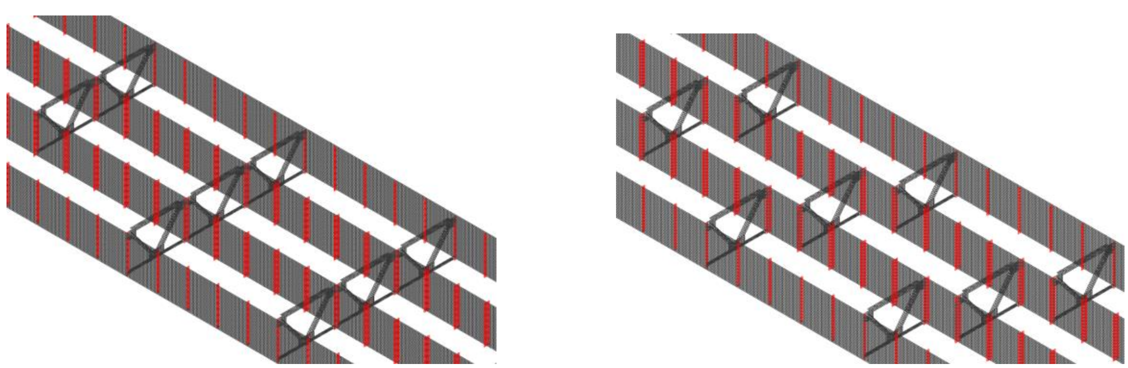

Figure 4.6 Cross-frame layout modeling. On the left is inline layout, on the right is staggered layout. To model staggered layout cross-fames were moved one vertical stiffener (red color) away from the nearest cross-frame.

Furthermore, because the cross-frames were considered to be a system whose influence on stress distribution was to be compared from model to model, it was prioritized to keep the cross-frame relative positions as identical as possible across skews. For example, when 55° skew models were created from 63° skew models the all distances between cross-frames and cross-frame locations in respect to 63° skew models, were kept the same while girders 1, 2, and 3 were moved 4 feet longitudinally. Accordingly, 45° skew models were created based on 55°, by keeping the same cross-frame distances and locations, but moving girders 1,2, and 3, four more feet in longitudinal direction. This procedure was repeated for 25° and 0° skews. This procedure required small adjustments to be made for the 0° and 25° models in the spacings of the cross-frames closest to the supports, where cross-frame demands should be minimal and thus the influence of variations here would be minimized. In the following subsections, the cross-frame layout of each model is described in detail.

4.1.6.4.1 0° Models

In practice, staggered cross-frame placements are not used for straight (0° skew) bridges. However, for the comparison purposes these models were built (as shown in Figure 4.7) and analyzed. This resulted in exceptionally large unbraced lengths between girder 1 and 2 on the left end (50ft) and girder 3 and 4 on the right end of the models (30ft) given the intent to keep the cross-frame spacing and relative positions as similar as possible across the models. In practice, at least 2 extra cross-frames (seen as dashed lines in Figure 4.7) would be expected for uniformity. Furthermore, the spacing between cross-frames X3 and X4 is 12ft instead of the 20ft spacing that is used at all other cross-frame in the 0° skew models.

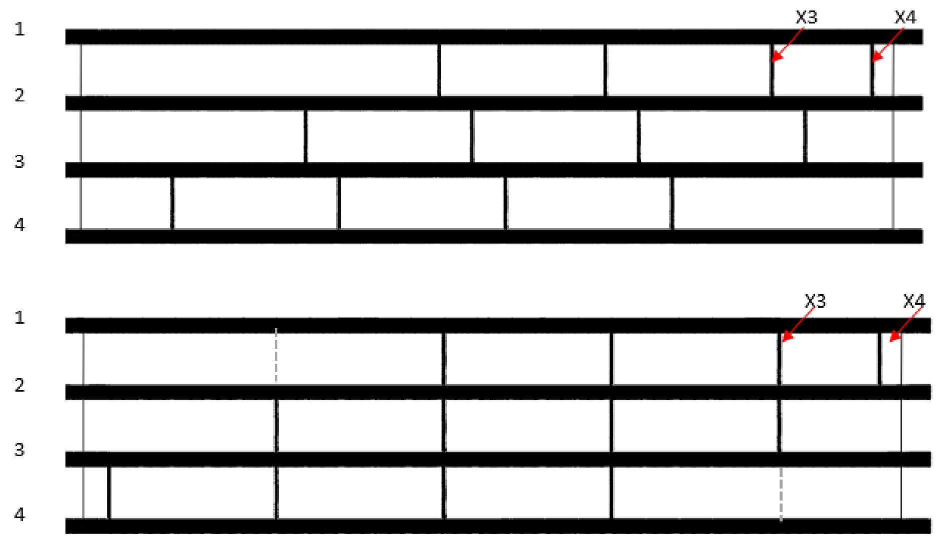

Figure 4.7 Cross-frame layout for 0° bridges. Gray dashed lines in bottom figure are showing the locations of cross-frames that would be expected in practice.

4.1.6.4.2 25° Models

The cross-frame layouts for the 25° models is shown in Figure 4.8. In practice, it would be expected that the 25° inline layout would have at least two extra cross-frames, while the staggered layout would have had one extra cross-frame (shown as dashed lines in Figure 4.8). In order to maintain the same total number and spacings at mid-span in all models, there are large unbraced lengths between girder 1 and girder 2 at the top left corner (38ft) and between girder 3 and 4 at the bottom right corner (36ft) that would also not likely be seen in practice. An additional difference between the 25° models and base model (63°) was in the spacing between cross-frames X3 and X4 (16ft instead of 20ft).

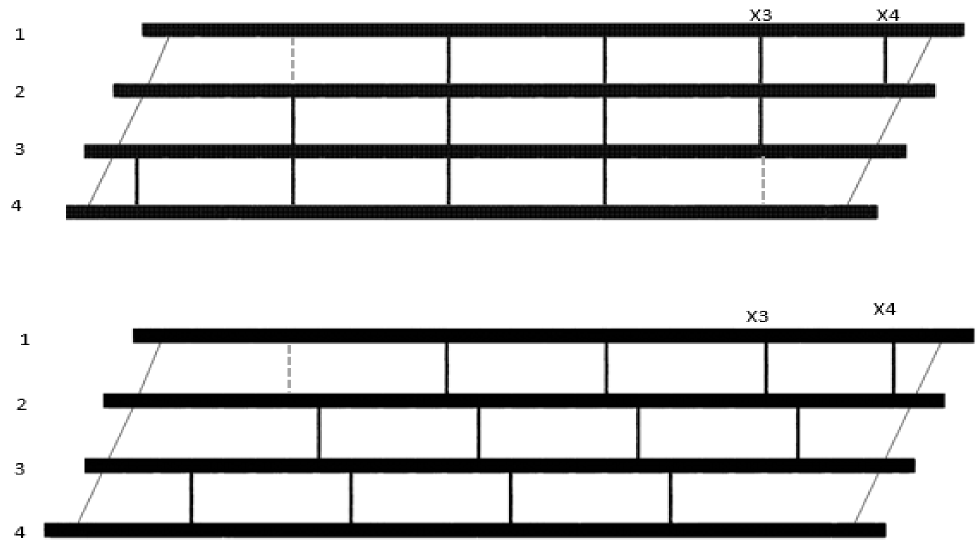

Figure 4.8 Cross-frame layout at 25° bridges. Gray dashed lines in both figures are showing the locations of cross-frames that would be expected in practice.

4.1.6.4.3 46° Models

The cross-frame layouts for the 46° models is shown in Figure 4.9. In practice, it would be expected that both the inline and staggered cross-frame layouts would have had at least one extra cross-frame (shown as dashed lines in Figure 4.9). There are also long unbraced lengths between girders 1 and 2 at the top left corner (28ft) and between girders 3 and 4 at the bottom right corner (28ft). There is no difference between the 46° models and base models (63°) in terms of spacing between cross-frames (cross-frame spacing is 20ft).

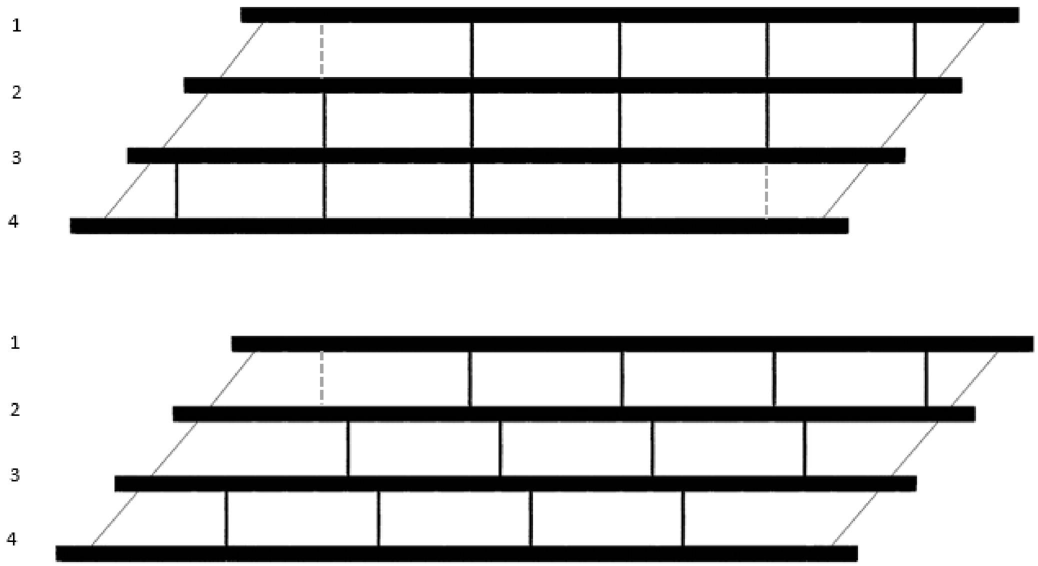

Figure 4.9 Cross-frame layout at 46° bridges. Gray dashed lines in both figures are showing the locations of cross-frames that would be expected in practice.

4.1.6.4.4 55° Models

The cross-frame layouts for the 55° models is shown in Figure 4.10. In practice, one extra cross-frame would be expected in the inline layout (location of the expected cross-frame is shown as dashed line in Figure 4.10). There is also a longer unbraced length between girders 3 and 4 at the bottom right corners for the inline models (26ft). There is no difference between the 55° models and base models (63°) in terms of spacing between cross-frames (all cross-frame spacings are 20ft).

Figure 4.10 Cross-frame layout at 55° bridges. Gray dashed line in the top figure shows the location of cross-frame that would be expected in practice.

4.1.6.4.5 63° Models

The 63° models did not have any deviation from the cross-frame layouts typically found in practice (Figure 4.11). The spacing between each cross-frame is 20ft. The maximum unbrace girder length at this skew was under recommended maximum spacing of 25ft.

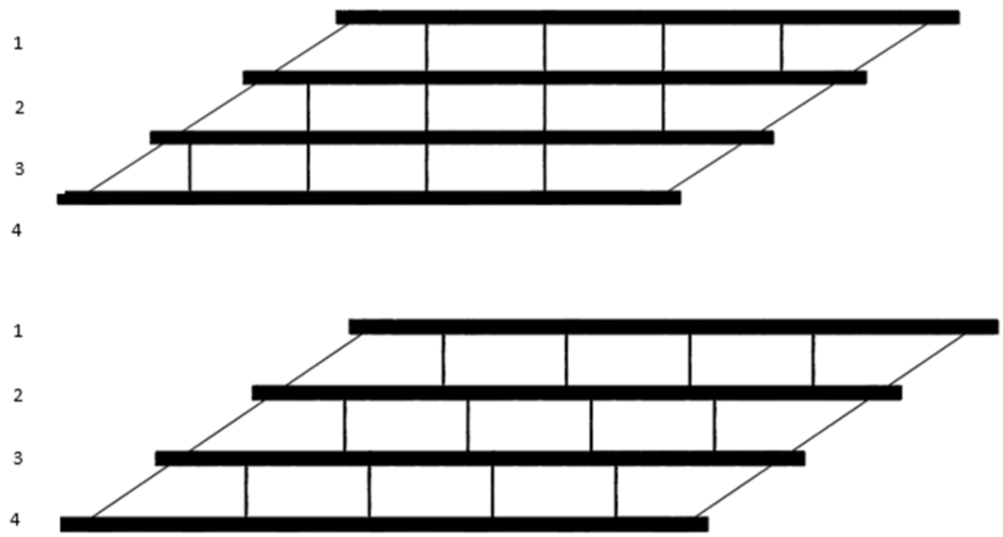

Figure 4.11 Cross-frame layout at 63° bridges.

4.2 AASTHO LRDF (2015) Strength

AASTHO LRDF Bridge Design Specifications (2015) were used to determine the theoretically expected flexural resistance of all models. To determine nominal flexural resistance, the first step is to determine if the section is compact or non-compact. If section is compact, it is expected to develop its full plastic moment capacity; if the section is non-compact it can't develop full plastic moment capacity. According to Article 6.10.6.2.2 (AASHTO, 2015), for a section to be considered compact it must satisfy three requirements:

a) minimum yield strength (F_y) of the flanges has to be <70ksi

b) $D/t_w \leq 150$

(4.3)

c) $\frac{2D_{cp}}{t_w} \leq 3.76\sqrt{\frac{E}{F_{yc}}}$

(4.4)

where D is the depth of web, t_w is thickness of the web, D_{cp} is the depth of the web in compression at the plastic moment, and F_y is the steel yield strength, with F_{yc} specifically referring to the yield strength of compression flange.

When parametric model girder's cross-section was tested, it was found out that,

a) 36ksi<70ksi. OK.

b) 60/0.5=120 < 150. OK.

c) $\frac{2 \cdot 0}{0.5} \leq 3.76\sqrt{\frac{29000}{36}} \rightarrow 0 < 107.$ OK (the location of PNA was calculated to be in the deck, therefore D_{cp}=0).

The results showed that the section does satisfy all slenderness requirements in addition to ductility requirement Dp<0.42Dt (where Dp is distance from the top of the concrete deck to the neutral axis of the composite section at the plastic moment, and Dt is total depth of composite section) Dp=9.06in, while Dt=71.25in; 0.42 · 71.5=30.03>>9.06). Therefore, theoretically this section could be classified as compact section. However, as mentioned in section 4.1.2, preliminary FEA results for the skewed bridges showed that full cross-sectional plasticity could not be reached and that some other metrics should be used to assess models system capacity. Therefore, it was decided to use yield moment as a reliable discrete metric for comparing theoretical vs. FEA models results.

Yielding moment capacity (My) was calculated first by solving for M_{AD}using AASHTO (2015) Equation D6.2.2-1 (4.5) and then calculating My using equation D6.2.2-2 (4.6)

$$\mathrm{Fy} = \frac{M_{D1}}{S_{NC}} + \frac{M_{D2}}{S_{LT}} + \frac{M_{AD}}{S_{ST}} \tag{4.5}$$

$$M_y = M_{D1} + M_{D2} + M_{AD} \tag{4.6}$$

where M_{D1} is moment due to factored (1.25) permanent loads applied to the non-composite section (1.25·1,340=1,675k·ft). M_{D2} is moment due to factored (1.25 for barrier and parapet and 1.5 for wearing surface) permanent loads applied to the composite section. M_{D2} =0 k·ft, because there were no barrier or walkways in the models and there was also no wearing surface in the models. M_{AD} is additional non-factored live load moment necessary to cause yielding in either steel flange, F_y is the yield strength of the steel (36ksi) and S_{NC} (1,739in^3), S_{ST} (2,222in^3) and S_{LT} (2,058in^3) are steel section, short term and long term and moduli respectively.

$M_{AD} = (Fy - M_{D1}/S_{NC})\cdot S_{ST} = (36 - (1{,}675\cdot 12)/(1{,}739))\cdot 2{,}222 = 54{,}309/12 = 4{,}525$ k·ft

My=1,675k·ft +0+4,525 k·ft = 6,200 k·ft.

For perspective on how the design capacity compared to the anticipated loading for these structures, the expected ultimate moment applied to the structure was also calculated. One step of this process is to calculate girder distribution factors (GDF) using AASHTO LRDF equations from Table 4.6.2.2.2b-1 and Table 4.6.2.2e-1.

$$\mathrm{GDF} = \left(0.06 + \left(\frac{S}{14}\right)^{0.4}\left(\frac{S}{L}\right)^{0.3}\left(\frac{K_g}{12Lt_s^3}\right)^{0.1}\right)\left(1 - c_1(\tan\theta)^{1.5}\right) \tag{4.7}$$

where S is girder spacing, L is length of the girder, K_g is a longitudinal stiffness parameter, θ is skew angle and c_1 is a skew correction factor. Once we calculated GDFs, we computed in-service ultimate moment demand (Mu) based on the governing AASHTO limit state in the absence of wind (Strength I)

$$M_u = 1.25\, M_{D1} + 1.5\, M_{D2} + 1.75\,(M_{LL}\cdot \mathrm{GDF}) \tag{4.8}$$

where M_{LL} is live load moment (1603 k·ft) and the other terms are as previously defined. Impact factor was not used in this calculation because the load on the FEA models was static. Ultimate moment capacity for 0° was calculated to be

$$M_u=(1.25 \cdot 1{,}340) +(1.5 \cdot 0) + 1.75\,(1{,}603 \cdot 0.47) \quad = \quad \underline{2{,}995 \text{ k·ft}}$$

The procedure is repeated for every skew models and results are presented in Table 4.2. The results show that all models are designed to satisfy Strength I requirements.

Table 4.2 AASHTO LRDF nominal moment capacity and ultimate moment demand of parametric models

	0°	25°	46°	55°	63°
Capacity: Yield moment (M_y) (k-ft)	6,750	6,750	6,750	6,750	6,750
Demand: Ultimate moment (M_u) (k-ft)	2,955	2,977	2,864	2,685	2,525
Capacity/Demand	2.10	2.08	2.16	2.31	2.46
Distribution factor*	0.47	0.46	0.42	0.36	0.30

*values for one loaded lane given the assumed loading of the parametric models and a clear width of the bridge of 24ft

4.3 Evaluation Methods

Two FEA data evaluation procedures were compared in this dissertation, “discrete” and “holistic”. “Discrete” evaluation method is the method that is currently being implemented in analysis of FEA data. “Holistic” evaluation method is the method that has been proposed in this dissertation. Following subsections describe in detail both methods.

4.3.1 Discrete Evaluation Method

“Discrete” evaluation of FEA data refers to identifying and extracting discrete values of interest in the dataset. These values could be maximum or minimum stresses, deflections, or temperature in the entire model or a specific location, natural frequencies, etc.

Three discrete metrics were used in this dissertation:

a) Peak stresses at three load levels (design, first yield and system yield).

b) The number of HS-20 trucks needed to cause yielding of the cross-section of the bottom flange of one girder in the bridge (i.e., at the first yield load level).

c) The number of HS-20 trucks needed to cause yielding of the cross-section of the

bottom flanges of all girders in the bridge (i.e., at the system yield load level).

4.3.1.1 Discrete Metric 1- Peak Stresses

Every steel I-girder bridge has two major load resisting components, deck and girders. Considering that simply supported bridges are analyzed in this study, it is expected that maximum longitudinal stresses in girders are going to be tensile stresses at the bottom flange, and that maximum longitudinal stresses at the deck are going to be compressive stresses. Therefore, maximum tensile stresses were extracted from models bottom flange elements and maximum compressive stresses are extracted from the deck elements at three load levels (design, first yield and system yield) at each model.

4.3.1.2 Discrete Metric 2- The number of HS-20 trucks needed to cause yielding of the cross-section of the bottom flange of one girder in the bridge

In the FE models, full cross-sectional yielding of the bottom flange of the girder refers to the case in which all shell elements constituting a girder's bottom flange cross-section equaled or exceeded the yield stress (36,045psi for these models). To help detect bottom flange yielding, stress contours intervals ([$-\infty$ to 0], [0 to 36,045] and [36,045 to $+\infty$]) were set during visual post-processing. This results in clear visual distinction between yielded and un-yielded bottom flange elements. Then the model's bottom flange was visually inspected at each load increments for full cross-sectional yielding. Once the bottom flange full cross-sectional yielding of one girder occurred, the load increment (LPF) was recorded. This number represents the number of HS-20 trucks needed to cause yielding of the cross-section of the bottom flange of one girder in the bridge.

4.3.1.3 Discrete Metric 3 - The number of HS-20 trucks needed to cause yielding of the cross-section of the bottom flanges of all girders in the bridge (i.e., at the system yield load level).

The model's bottom flange was visually inspected at each load increments for full cross-sectional yielding of each girder. Once the bottom flange full cross-sectional yielding of each girder occurred, the load increment (LPF) was recorded. This number represents the number of HS-20 trucks needed to cause yielding of the cross-section of the bottom flange of all girders in the bridge (system yield level).

4.3.2 Holistic Evaluation Method

The "holistic" evaluation of FEA consists of comprehensive assessment of all data in the dataset. The data can be expressed in terms of stresses, deflections, temperature, etc. In this work, stress data was evaluated using "holistic" methods. Specifically, holistic metrics used in this dissertation are:

1. Percent of bridge component that yielded
2. Total lateral bending energy (TLBE)
3. Performance Index (PI)
4. Chi-square distance (CsD) between stress histograms of FE models at same skew

All three metrics were computed for all FE models at three load levels (design, first yield and system yield). The following sub-sections explain in detail these metrics.

4.3.2.1 Holistic Metric 1 - Percent of Girder That Yielded

This "holistic" metric evaluated girders at first yield and system yield load levels. No deck elements yielded in tension or compression, therefore this metrics was not computed for the deck. To compute this metrics, total number of girder elements that were yielded, i.e, have stresses larger or equal to 36,045 were counted and then divided by total number of girder elements. Since all girder elements are of the same size, this metrics also can be used to assess total percent area of steel girders that yielded. Intuitively we would expect the girders yielding start at the mid-span of the most heavily loaded girder, which is followed by spread of plasticity towards the supports, transversely, and through the web. However, the relative spread of plasticity in the longitudinal, transverse, and vertical directions is unknown, as well as how bridge skew or cross-frame designs could affect the magnitude and direction of the spread of plasticity. Although there is no theoretically explicit way to compute or anticipate the percent of girder yielding at post-elastic load levels, this metric allows the difference in yielding behavior among different cross-frame configurations and at different skews to be quantified and contrasted.

4.3.2.2 Holistic Metric 2 - Total Lateral Bending Energy (TLBE)

It is known that skewed bridges' response to the applied load is more complex that the tangent bridges' response. For example, skewed bridges are exposed to greater amounts of lateral bending and torsion in addition to vertical bending. From the discussion above, it is also known that skewed bridges have larger system yield capacity than tangent bridges. It is hypothesized that part of the reason why skewed bridges have larger system yield capacity than tangent bridges might be related to differences in the relative magnitudes of vertical bending, lateral bending, and torsion. These resulting differences in strain energy may cause lower longitudinal strains in some bottom flange fibers of skewed bridges, indirectly increasing their system yield capacity. If this hypothesis is correct, the tangent bridges should have lower lateral bending strain energy than skewed bridges.

Quantifying lateral bending strain energy starts with computing lateral bending stresses along the length of the girder. Computing lateral bending stresses along the length of the girder's bottom flange effectively creates lateral bending stress curve for that girder (Figure 4.12). If the area under the lateral bending stress curve is integrated, the resulting quantity is lateral bending strain energy. To compute bottom flange lateral bending stresses, longitudinal stresses along opposing edges of each girder (f_{t1} and f_{t2}) were extracted at each element. Taking the average of longitudinal stresses along opposing edges of each girder, vertical bending stress (f_b) was obtained.

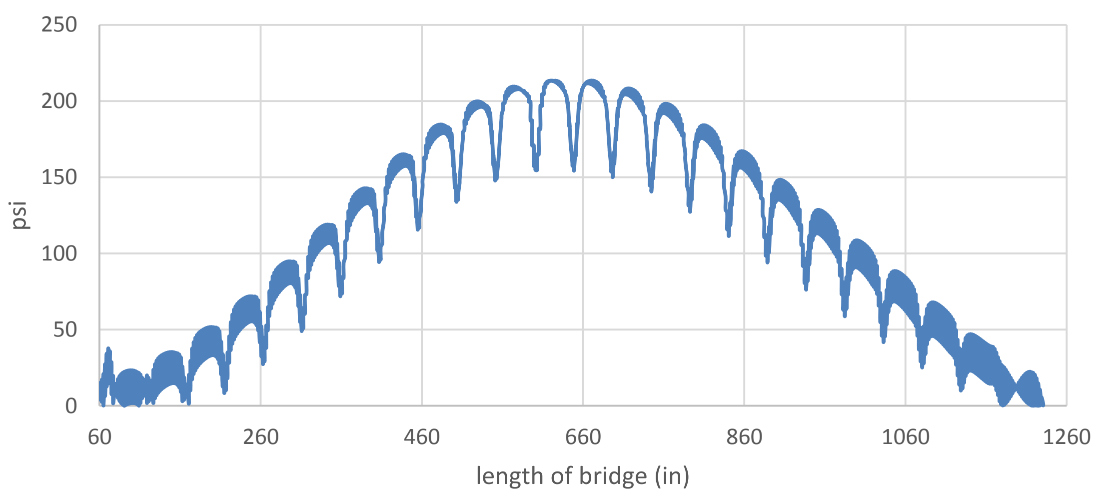

Figure 4.12 Lateral bending curves for No-frame models at design load level at 0°. The reoccurring intervals (small waves spaced every 48in) seen at 0° skew model correspond to the location of transverse stiffeners.

Subtracting vertical bending stress (f_b) from the larger value of longitudinal bending stresses, the lateral bending stress (f_l) was obtained. This procedure was repeated along the length of each girder at every element, and results were plotted to obtain lateral bending stress curve. Once the lateral bending curve ($g(f_l)$) is obtained, the area under the stress curve is integrated to get energy used for lateral bending of the bottom flange. Finally, lateral bending energy expenditure (LBE) that were obtained per each girder were summed to get the total lateral bending energy expenditure (TLBE) per bridge. This procedure is summarized in equations 4.10 -4.12.

$$f_b + f_l = f_{t1} \tag{4.10}$$

$$f_b - f_l = f_{t2} \tag{4.11}$$

$$TLBE = \sum^{n} \int_{0}^{l} g(f_l)dl \tag{4.12}$$

where f_{t1} and f_{t2} are longitudinal stresses at the opposing edges of the girder, f_b vertical bending stress, f_l is lateral bending stress, $g(f_l)$ is lateral bending stress curve, l is length of the girder and n is number of girders in the bridge. TLBE is computed for each model at all three load levels.

4.3.2.3 Holistic Metric 3 - Performance Index (PI)

The Performance Index (PI) is a third “holistic” metric designed for post-elastic FEA data evaluation. PI is the ratio of the applied load and the percent of girders yielding at that load. For example, if load causing system yield at 0° for K-Inline model was 14.9 HS-20 trucks, and at this load level model had 8.5% of bottom flange yielded, then

$$PI = \frac{\text{\# HS-20 trucks}}{\text{\% of bottom flange yielded}} = \frac{14.9}{0.085} = 175.2 \approx 175.$$

This metric is intended to evaluate bridge models in terms of effectiveness of cross-frame designs in resisting post elastic loads (first yield and system yield load levels). The rationale of this metric is that more efficient cross-frame designs are more efficient in transferring live load, leading to the bridge being able to resist more load with comparatively less girder yielding. Additionally, this metrics could be used to compare the influence of skew and conveniently take into account different load magnitude at first yield and system yield load levels among models. This metric is intuitive and easy to interpret; the model with the largest PI value is the best performing model according to this metric.

Furthermore, to get a clearer perspective of the relationship between models, the PI of all models were "normalized" (divided) by the largest PI value among all models and multiplied by 100. For example, at system yield load level, K –Inline model at 63° skew has PI of 306, this value is divided by the largest PI of all models (922 for the K-frame Staggered model at 0° skew) and multiplied by 100 ($\frac{306}{922} \cdot 100 = 33$). This means the K-frame Inline model at 63° performs 100/33 = 3 times worse than K-frame Staggered model at 0° according to this metric. PI was computed for all bridges at first yield and system yield load level.

4.3.2.4 Holistic Metric 4 - Chi-square Distance (CsD)

Stress histograms are graphical representations of the frequency of different stress magnitudes organized in pre-defined stress ranges (Figure 4.13). Stress histograms are used for the visual evaluation of stress distributions. However, they can be also used to numerically quantify the difference between two distributions if the bin ranges are kept constant. One of the mathematical tools used to compare the difference between histograms is called Chi-square Distance.

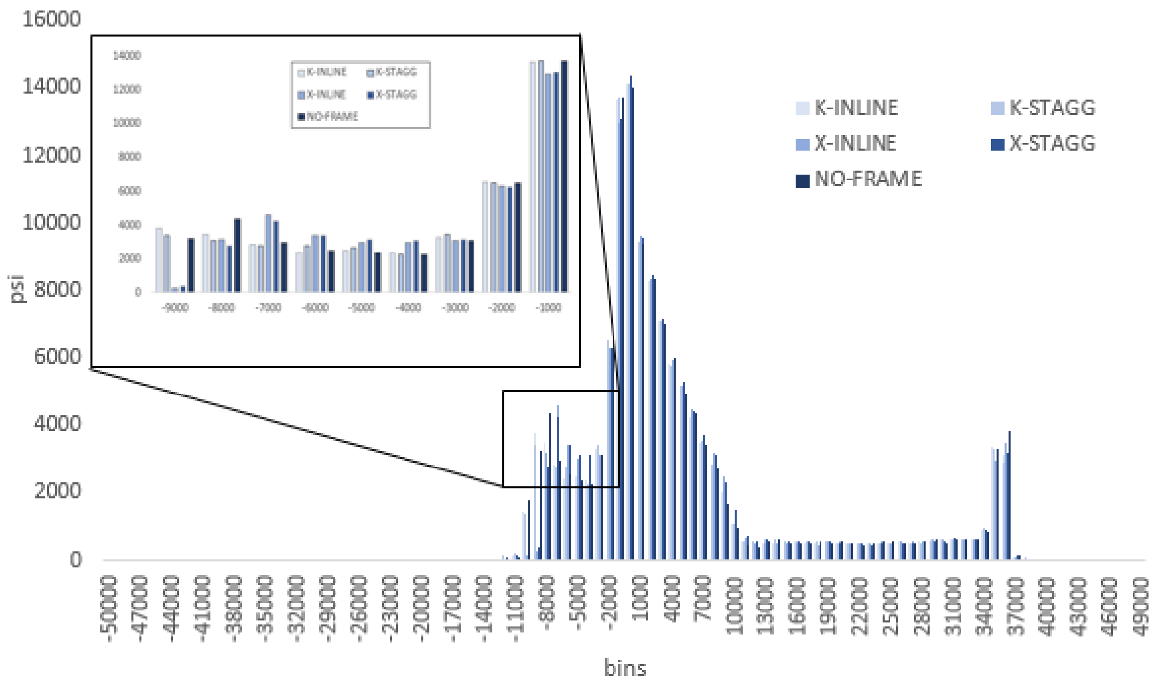

Figure 4.13 Bottom flange stress histograms of FE models at system yield load level.

The Chi-square Distance is a commonly used metric to compare similarities between two or more histograms in the image-processing field (Ahonen et al., 2006, Belongie et al., 2002). This measure is a robust tool and it is not overly sensitive to the presence of the outliers in the data. The name of the this method is derived from Pearson's Chi-squared test statistic

$X^2(x,y) = \Sigma$ ((xi-yi)2 / xi) for comparing discrete probability distributions (i.e, histograms). The distance d, which quantifies the difference between the models, is obtained by

$$d = \frac{1}{2}\sum_{i=1}^{n} \frac{(x_i - y_i)^2}{(x_i + y_i)} \tag{4.13}$$

where n is number of bins in the histogram, xi is the number of elements in i bin of first histogram and yi is the number of elements in i bin in second histogram. For example, let's say that the bottom flange of a K-frame model at 45 ° skew and first yield load level has 720 elements that are in the range of 1000 to 2000 psi (i=53; bin size in this work is fixed at 1000 psi). Alternatively, the bottom flange of No-frame model at 45 ° skew and first yield load level has 825 elements that are in the range of 1000 to 2000 psi (i=53). Then x53 =720, y53 =825 and d53 = $\frac{(720-825)^2}{(720+825)} = 7.13$. This procedure is repeated for all bins, and then individual distances are summed and divided by 2.

One of advantages of Chi-square Distance measure lays in the fact that is intuitive and easy to interpret. For example, a large Chi-square Distance between the models corresponds to stress distributions that differ significantly, and conversely, a smaller Chi-square Distance between the models corresponds to stress distributions that are more alike. This metric was used to compare the deck and girder stresses in all models.

4.4 Results of Evaluation of Stress Distribution Data

This section presents the results of the discrete and holistic evaluation of FEA data. The results are discussed with a primary focus on understanding differences (or similarities) between:

a) Skewed and tangent (0° skew) bridges;

b) Inline and staggered cross-frame layouts; and

c) No-frame models and cross-frame models; and

4.4.1 Discrete Evaluation Results

4.4.1.1 Discrete Metric 1- Peak Stresses

4.4.1.1.1 Discrete Metric 1 – Peak Stresses in Girders

Maximum tensile stresses in girders were recorded at the bottom flange. Therefore, maximum bottom flange tensile stresses at girders are extracted from all FEA models at three load levels: design, first yield, and system yield load. The results are presented in Tables 4.4 through 4.6 and Figures 4.14 through 4.16, for the design, first yield, and system yield load levels, respectively.

Design Load Level

- **Results**

The results show (Table 4.3 and Figure 4.14) that at design load level, skewed bridges generally have higher peak bottom flange stresses than tangent bridges. The only exceptions to this are at 63º skew. On average, skewed bridges have 5.7% higher peak bottom flange stresses ($\frac{13,114+13,025+12,748+12,293}{4}$ = 12,795psi) than bridges with 0º skew (12,064psi). Additionally, in all cases the models with staggered cross-frame layouts have higher peak stresses than their counterparts with inline cross-frame layouts. On average, bridges with staggered cross-fame layouts have 13.3% higher peak bottom flange stresses ($\frac{13,303+14,141}{2}$ =13,722psi), than bridges with inline cross-fame layouts ($\frac{11,639+12,156}{2} =$ 11,897psi), with K-frame Inline models have the lowest stresses of all cross-frame designs at 0 to 46° skew. However, on average, the results show that cross-frame models have higher peak bottom flange stresses than No-frame models (12,810psi vs. 12,006psi respectively) for skewed bridges and the No-frame model has higher peak bottom flange stress than most of the peak bottom flange stress of cross-frame models (the X-frame Staggered model being the exception).

- **Discussion**

This study found that maximum bottom flange stresses at skewed bridges are higher than maximum bottom flange stresses at straight bridges. This result is somewhat surprising, because Marx et al. (1995) reported that skewed bridges have smaller peak moments when compared to non-skewed bridges, and consequently should have smaller peak bottom flange stresses. The possible reason why there is a difference between the results of Marx's (1995) study and this study might be because the bridge models in these studies have different load locations, different width to length ratios, deck to girder stiffness ratios and different cross-frame stiffness. One must have these variables in mind when comparing results from this study to the results found in published literature. For example, the centroid of the load in the current study is located at the centroid of the bridge while the load location in Marx's study was governed by the maximum moment that could be produced at each skew.

Furthermore, this study found that staggered cross-frame layouts yield higher bottom flange stresses than inline cross-frame layouts. This result agrees with the trend Radovic & McConnell (2014) reported, that on average bridges with staggered cross-frame layouts have 2.8% larger peak bottom flange stresses than bridges with inline cross-frame layouts.

Table 4.3 Maximum bottom flange stresses at design load level (psi)

SKEW	K-FRAME INLINE	K-FRAME STAG	X-FRAME INLINE	X-FRAME STAG	NO FRAME	Average
0°	11,270	12,134	11,643	12,643	12,632	12,064
25°	12,006	14,128	12,619	14,607	12,212	13,114
46°	11,669	13,875	12,336	14,449	12,794	13,025
55°	11,668	13,766	12,188	14,583	11,537	12,748
63°	11,582	12,614	11,992	14,425	10,853	12,293
Average	11,639	13,303	12,156	14,141	12,006	

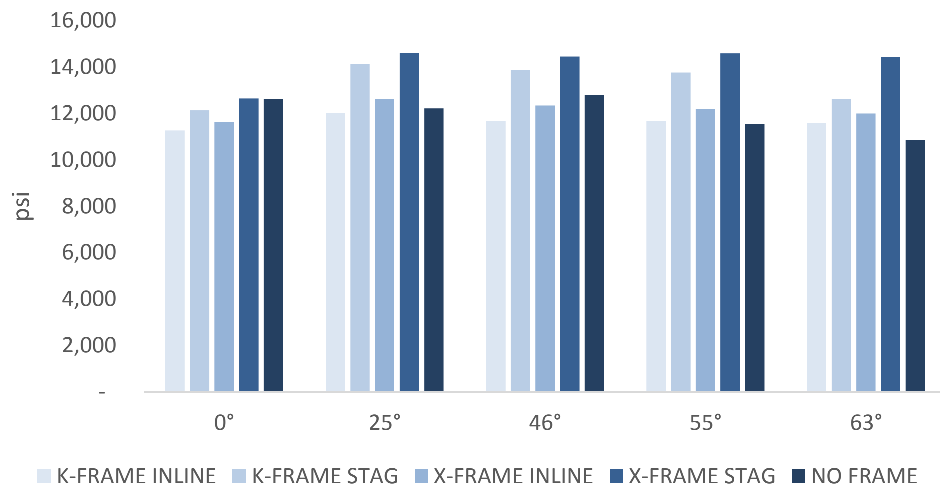

Figure 4.14 Maximum bottom flange tensile stresses at design load level

Finally, this study found that removing cross-frames from the bridge would increase peak bottom flange stresses at straight bridges. This result aligns with line Tadesco’s, et al. (1995) study that found that removing cross-frames from the tangent (0 º skew) bridge would increase bottom flange stresses by 8%. Although, a more detailed look at the data shows that in skewed bridges cross-frame designs result in an average of 9.1% larger peak bottom flange stresses than No-frame bridges (13,032psi vs. 11,849psi respectively), reversing the trend found for tangent bridges.

First Yield Load Level

- **Results**

The results show (Table 4.4 and Figure 4.15) that at first yield load level, skewed bridges consistently have (5.2% higher on average) higher peak bottom flange stresses (38,223psi) than tangent (0º skew) bridges (36,231psi). Additionally, bridges with staggered cross-fame layouts on average have 2.8% higher peak bottom flange stresses (38,480psi) than bridges with their counterparts with inline cross-frame layouts (37,430psi). Furthermore, the results show that No-frame models generally have lower (1.5% on average) peak bottom flange stresses than cross-frame models (37,357psi vs.

37,942psi respectively). The exception of this rule was found at X-frame Inline models, where peak bottom flange stresses at 0°, 55° and 63° skew, were smaller than corresponding peak bottom flange stresses at No-frame models (as well as all other models). However, the average difference in peak stresses between these models was only 0.3% (37,068psi vs. 37,173psi respectively).

Table 4.4 Maximum bottom flange stresses at first yield load level (psi)

SKEW	K-FRAME INLINE	K-FRAME STAG	X-FRAME INLINE	X-FRAME STAG	NO FRAME	Average
0°	36,156	36,350	36,083	36,442	36,123	36,231
25°	37,732	38,825	37,790	38,008	37,703	38,012
46°	37,620	38,935	37,737	39,228	37,564	38,217
55°	37,769	39,275	37,591	39,005	37,665	38,261
63°	38,022	38,932	37,531	39,803	37,731	38,404
Average	37,460	38,463	37,346	38,497	37,357	

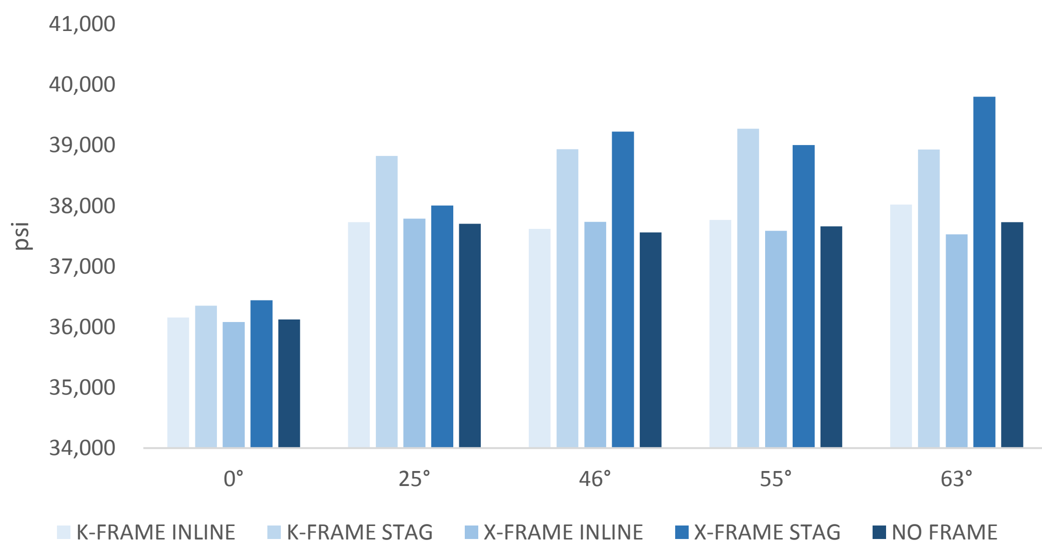

Figure 4.15 Maximum bottom flange tensile stresses at first yield load level

System Yield Load Level

- **Results**

The results show (Table 4.5 and Figure 4.16) that skewed bridge have 6.6% higher peak stresses than tangent (0° skew) bridges (36,580psi vs 39,178psi, respectively). Furthermore, staggered cross-frame layouts consistently have higher peak stresses than inline cross-frame layouts (1.6% higher on average, or 38,972psi vs. 38,366psi), while cross-frame models have on average 0.1% higher peak stresses than No-frame models (38,669psi vs 38,617psi). Although, inline cross-frame layouts on average have 0.7% lower peak bottom flange stresses (39,366psi) when compared to No-frame models (38,617psi), while staggered cross-frames on average have 0.9 higher peak bottom flange stresses (38,972psi) than No-frame models.

- **Discussion**

Steel in the FEA models was modeled with elasto-plastic properties, with true yielding strength of 36,045psi and strain hardening between true stresses of 36,611psi and 85,463psi. The results show that majority of peak bottom flange stresses are in the strain hardening region. Only two models (K-frame Inline and X-frame Inline at 0° skew) have peak stresses that are on the yielding plateau (36,511psi and 36,251psi, respectively). Furthermore, the results also show that peak stresses between first yield and system yield load levels have similar magnitudes, even if the load magnitudes were significantly higher at system yield than the load magnitudes at first yield load level. The average overall peak bottom flange stresses of all models at system yield was 38,658psi while the average overall peak bottom flange stress at first yield was 37,825psi. The average overall load at first yield load level and system yield load level was 13.3 HS-20 and 16.1 HS-20 trucks, respectively. This means while, on average, the load on the bridge was increased 17.5%, peak girder stress, on average, was increased by only 2.2%. On more particular level, the largest percent difference in load magnitudes between first yield and system yield was recorded at No-frame 63º skew model, where the load at system yield was 29% larger than load at first yield load level, while the peak girder stress was only 4% larger. These results indicate that using maximum tensile stress, as a metric to compare bridge designs in the post-elastic range is not adequate, because the differentiation between the models becomes trivial or non-existent. These results also show that there is a need for better measuring tool of bridge performance at post-elastic load levels.

Table 4.5 Maximum bottom flange stresses at system yield load level (psi).

SKEW	K-FRAME INLINE	K-FRAME STAG	X-FRAME INLINE	X-FRAME STAG	NO FRAME	Average
0°	36,511	36,673	36,251	36,684	36,780	36,580
25°	38,618	39,442	38,268	39,671	38,982	38,996
46°	38,770	39,405	38,773	39,228	38,806	38,996
55°	39,092	39,680	39,125	39,528	39,196	39,324
63°	39,251	39,622	38,996	39,784	39,322	39,395
Average	38,448	38,964	38,283	38,979	38,617	

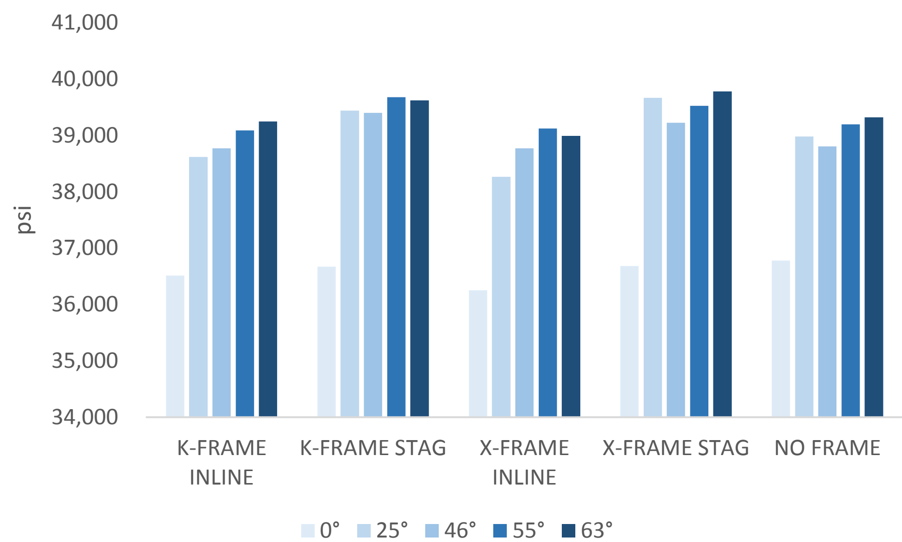

Figure 4.16 Maximum bottom flange tensile stresses at system yield load level

4.4.1.1.2 Discrete Metric 1 – Peak Stresses in Deck

The maximum deck compressive stresses are extracted from all FEA models at three load levels: design, first yield, and system yield load (Tables 4.4 through 4.6 and

Figures 4.14 through 4.16, for the design, first yield, and system yield load levels, respectively). Furthermore, trends in relative magnitudes between different groups of models for peak deck stress results were contrasted to corresponding trends in peak girder stresses results in order to detect similarities or differences in behavior between these two bridge components.

Design Load Level

- **Results**

The results show that the in at design load level, deck longitudinal (s11) stresses are very low. The average peak stress across all models was only 331psi with a standard deviation of 31psi in the peak stress values. Considering that the model was based on an assumed concrete compressive strength of 4,500psi, average stress demand was only 7% of the theoretical deck capacity. Furthermore, results show that peak average stress for inline models (333psi) is 1.7% higher than peak average stress for staggered models (327psi). This result is also contrary to girder results where staggered cross-frame layouts have larger peak average stresses than inline cross-frame layouts, although the percent difference is much less for deck stresses than girder stresses.

The results also show that the No-frame models on average have 2.2% higher peak stresses than cross-frame models (337psi vs. 330psi respectively). However, X-frame models and No-frame models have approximately the same stresses at 46° skew while K-frame models and No-frame models have approximately the same stresses as one another at all other skew levels.

This result is contrary to girder results, where both cross-frame designs on average have larger peak stresses than No-frame models. Furthermore, the largest overall peak stress was recorded at X-frame Inline 63° skew model (384psi). It is interesting to note that in general K-frame models have larger peak stresses than X-frame models at every skew except 63°.

- **Discussion**

On average, skewed bridges have higher deck compressive stresses (332psi) than straight (0º skew) bridges (328psi), but the difference is very low (1%). This result occurs because the minimum deck stresses occur in the 46º models, with increasing deck stress as the skew deviates from 46º. The question is what is so specific about 46º skew? The explanation to this phenomenon might be related to Kar, et al. (2012) findings, who investigated the effects of bridge skews on deck transverse moments. The study found that transverse moments increased as skew increased to 30°, remained the same when further increased to 45° and then decreased when further increased to 60°. A similar pattern was detected for torsional moment, where there is negligible torsional moment for skews up to 30°, then an abrupt increase at 45°, and then a decrease to 20% of the moment at 45° when the skew is increased to 60°. This finding would indicate that bridge deck, rather than cross-frames may play significant roles in stress distribution.

A related study has shown (Fu & Wang, 2014) that bridge decks in straight bridges mostly bend along their longitudinal axis with negligible bending along transverse axis and small twisting moment due to biaxial curvature. The load from the deck is transferred to the supports directly by longitudinal bending action. However, very different behavior is detected in decks of skewed bridges. Load transfer from a deck of a skewed bridge becomes more complicated because there is uncertainty in which direction and by what action (uniaxial or biaxial bending) load will be transferred to the supports. With increase in skew angle, the stresses in the bridge deck and reactions at the supports could vary significantly from straight deck.

Furthermore, at skewed bridges the load is distributed between supports through a strip of area connecting obtuse corners of the bridge (Kar, et al. 2012). According to this hypothesis, the bending occurs mainly along the line connecting obtuse corners, and load is distributed to supports “in proportion to the rigidity of the various possible paths.” (Kar, et al. (2012)). Also, the greater the skew is, the narrower the load transfer strip is

(Rajagopalan, 2006). Rajagopalan (2006) states that "the width of this primarily bending strip is a function of the skew angle and the ratio between the skew span and the width of the deck (aspect ratio). The areas on either side of the strip do not transfer the load to the supports directly but transfer the load only to the strip as cantilever. Hence the skew slab is subject to twisting moments and this twisting moment is not small and hence cannot be neglected."

Table 4.6 Maximum deck longitudinal compressive stresses at design load level (psi)

SKEW	K-FRAME INLINE	K-FRAME STAG	X-FRAME INLINE	X-FRAME STAG	NO FRAME	Average
0°	349	349	297	299	344	328
25°	350	350	293	292	346	326
46°	349	348	292	289	289	313
55°	357	349	295	289	350	328
63°	363	359	384	347	357	362
Average	353	351	312	303	337	

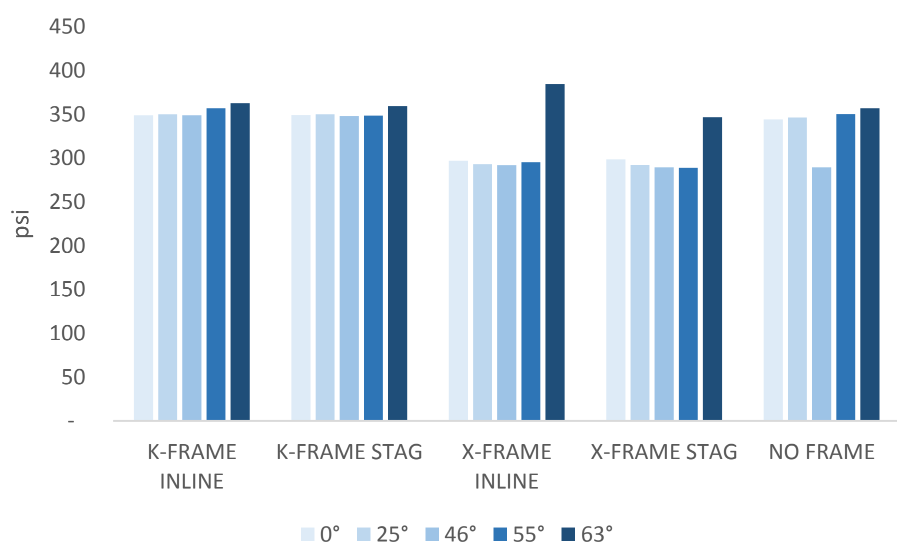

Figure 4.17 Maximum deck longitudinal compressive stresses at design load level

First Yield Load Level

- **Results**

The results show (Table 4.7 and Figure 4.18) that at first yield load, the average of peak compressive deck stresses (1,111psi) is 3.3 times higher than at design load level (331psi), but still significantly lower than concrete's compressive strength of 4,500psi. Comparing the results at different skews shows that minimum deck stress occurs at 46° skew, as was the case at the design load level and consequently tangent (0° skew) bridges have on average 2.6% higher peak compressive stresses than skewed bridges (1,135psi vs. 1,105psi respectively). Finally, the results show that on average staggered cross-frame layouts have 7.7% higher stresses than inline cross-frame layouts (1,162psi vs. 1,079psi, respectively). The results also show that on average cross-frame models have 4.3% higher peak stresses than No-frame models (1,121psi vs. 1,073psi respectively), but more specifically K-frame models have greater stresses than No-frame models while K-frame models have lower stresses than No-frame models.

- **Discussion**

While average results show that cross-frame models have higher peak stresses that No-frame models, more detailed analysis shows, that X-frame models in general have lower peak stresses than No-frame models, while K-frame models have higher peak stresses than No-frame models regardless of the skew. Exception to this rule was found at 46° skew where both X-frame layouts (staggered and inline) had higher peak stresses than No-frame model. This trend of different relative magnitudes between X-frame, K-frame, and No-frame models at 46° skews compared to other skews is consistent to the anomaly in these trends that were observed at 46° skew for the design load level results. However, K-frame and No-frame models generally had more similar magnitudes of stress as one another at the design load level, while K-frame models generally have greater stress than No-frame models at the first yield load level.

Table 4.7 Maximum deck longitudinal compressive stresses at first yield load level (psi)

SKEW	K-FRAME INLINE	K-FRAME STAG	X-FRAME INLINE	X-FRAME STAG	NO FRAME	Average
0°	1,193	1,318	987	1,073	1,104	1,135
25°	1,175	1,241	965	891	1,115	1,077
46°	1,151	1,284	930	1,070	860	1,059
55°	1,180	1,310	898	1,025	1,128	1,108
63°	1,229	1,293	1,081	1,118	1,156	1,175
Average	1,185	1,289	972	1,035	1,073	

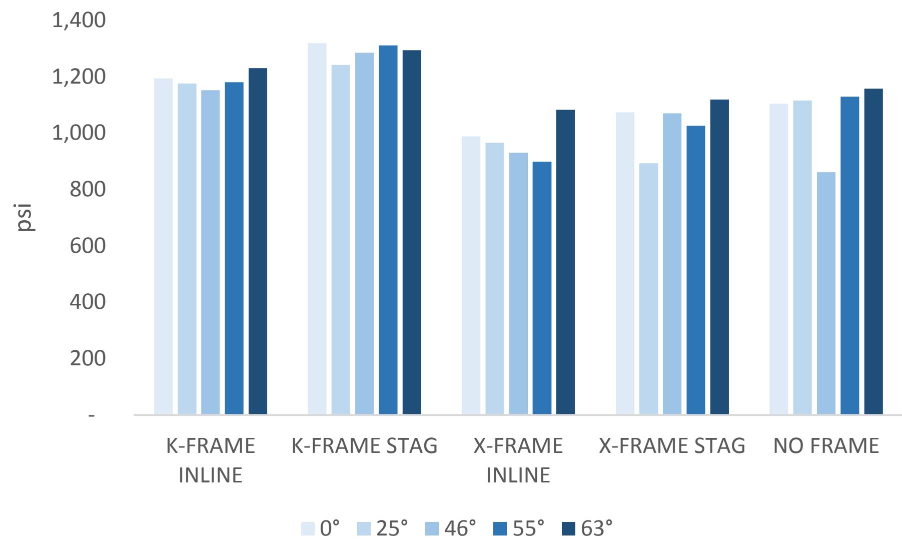

Figure 4.18 Maximum deck longitudinal compressive stresses at first yield load level

System Yield Load Level

- **Results**

The results show (Table 4.8 and Figure 4.19) that at system yield load level, the average of peak compressive deck stresses (1,322psi) is 16.0% higher than at first yield load level (1,111psi). Considering that the average load at system yield load level is 17.5% higher than the average load at first yield load level, it seems that deck peak stresses aligned well with the loading conditions. Furthermore, the results show that the minimum deck stresses again occurred at 46° skew. On average, skewed bridges have

4.2% larger stresses than tangent (0° skew) bridges (1,333psi vs. 1,277psi, respectively), which is contrary to first yield load deck stress results but aligned with design load deck stress results. The results also show that on average inline cross-frame layouts have 5.6% larger stresses than staggered cross-frame layouts (1,339psi vs. 1,264psi, respectively), but staggered layouts result in greater stresses than inline layouts for 0 and 25° skew. Furthermore, No-frame models on average have 7.3% larger stresses than cross-frame models (1,404psi vs. 1,301psi, respectively), with K-frame models generally having higher stresses than X-frame models (the exception being at 63° skew).

- **Discussion**

The system yield load level results agree with the results at other load levels with respect to the influence of skew on peak longitudinal deck stresses and with K-frame models generally resulting in higher stresses than X-frame models. K-frame or No-frame models generally result in the highest deck stresses, with the specific configuration that produces the maximum varying based on load level (K-frame and No-frame generally the same at design load, K-frame being maximum at first yield load, and No-frame being maximum at system yield load) and with exceptions occurring at 46° skew. There was no consistent trend between load levels with respect to the influence of staggered versus inline cross-frames.

Table 4.8 Maximum deck longitudinal compressive stresses at system yield load level (psi)

SKEW	K-FRAME INLINE	K-FRAME STAG	X-FRAME INLINE	X-FRAME STAG	NO FRAME	Average
0°	1,372	1,382	1,103	1,110	1,420	1,277
25°	1,354	1,381	1,075	1,110	1,461	1,276
46°	1,385	1,383	1,099	1,070	1,108	1,209
55°	1,465	1,407	1,131	1,104	1,478	1,317
63°	1,520	1,472	1,882	1,221	1,554	1,530
Average	1,419	1,405	1,258	1,123	1,404	

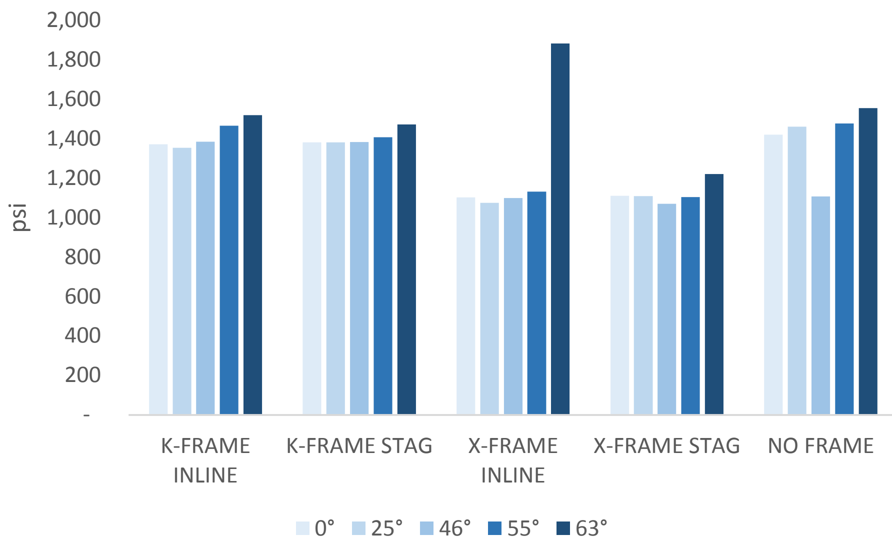

Figure 4.19 Maximum deck longitudinal compressive stresses at system yield load level

4.4.1.2 Discrete Metric 2 - First Yield Capacity

- **Results**

The second metric used for "discrete" assessment of FEA data is the number of HS-20 trucks needed to cause cross-sectional yielding of the bottom flange of one girder in the bridge. This metric is designed to measure the load corresponding to the onset of post-elastic behavior of the bridge. The "first yield" capacity could be seen as transitional point between elastic and post elastic range, therefore it is important to observe the bridge behavior at this stage. The results show (Table 4.9 and Figure 4.20) that there is significant first yield capacity in steel I-girder bridges, as the average overall load that will cause cross-sectional yielding of the bottom flange of one girder in the bridge was calculated to be equivalent to 13.3 HS-20 trucks.

On average, skewed bridges have 5.7% larger capacity than tangent (0º skew) bridges (13.4 HS-20 trucks vs. 12.7 HS-20 trucks, respectively), and in general, as the bridge skew increases the first yield capacity of the bridge increases as well. However, an exception of this rule was found at 25º skew staggered models having the minimum capacities for these cross-frame configurations and the first yield capacity for inline model was not increased between 0° and 25° skew. These results indicate that the correlation between bridge skew and bridge capacity is non-linear. The best-fit line was obtained by polynomial regression equation in form of

$$y = 0.0016x^2 - 0.0655x + 12.689 \tag{4.14}$$

where, y represents bridge first yield capacity and x represents bridge skew. The correlation coefficient was very high (R^2=0.98 or 98%) indicating strong, but non-linear association between bridge skew and bridge first yield capacity.

Furthermore, the cross-frame models consistently had higher first yield capacity than No-frame models (on average, 11% higher, or 13.5 HS-20 trucks versus 12.1 HS-20 trucks, respectively). Additionally, the results also show that staggered models generally have higher first yield capacity than inline models (on average, 8% higher, or 13.0 HS-20 trucks vs. 14.1 HS-20 trucks respectively). There was no consistent relationship regarding whether K=frames or X-frames resulted in higher first yield capacity.

Table 4.9 Number of HS-20 trucks needed to cause cross-sectional yielding of the bottom flange at one girder (First yield)

SKEW	K-FRAME INLINE	K-FRAME STAG	X-FRAME INLINE	X-FRAME STAG	NO FRAME	Average
0°	12.3	13.7	12.5	13.5	11.3	12.7
25°	12.5	13.0	12.5	11.2	11.4	12.1
46°	12.5	13.9	12.6	14.8	11.4	13.0
55°	13.1	15	12.7	14.6	12.6	13.6
63°	14.7	15.5	14.8	16.1	13.7	15.0
Average	13.0	14.2	13.0	14.0	12.1	

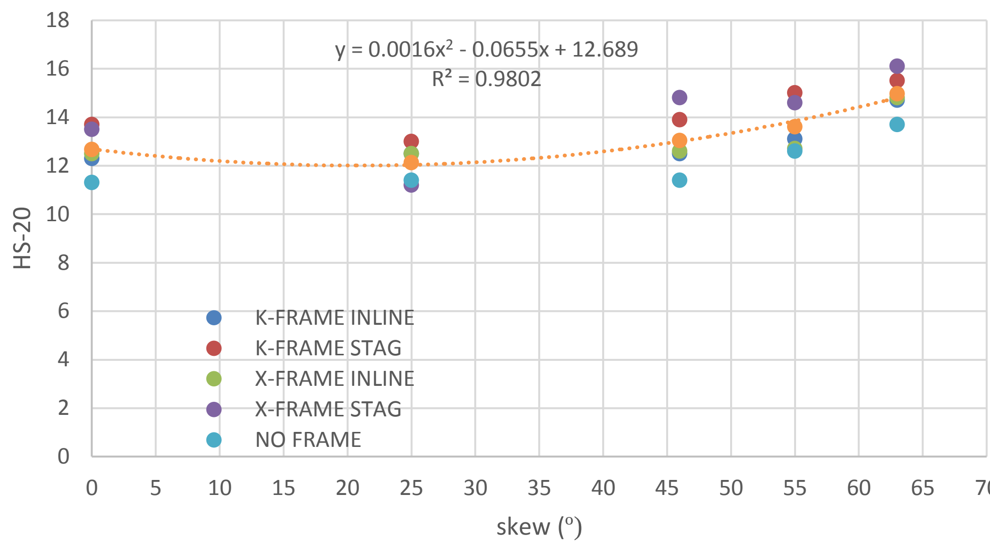

Figure 4.20 Bridge capacity in terms of number of trucks needed to cause complete cross-sectional yielding of bottom flange of one girder. The dotted line represents the line of best fit.

- **Discussion**

Theoretical first yield capacities were calculated for all skews and compared to average first yield capacities obtained from FEA models at each skew (Table 4.10). For example, to calculate the theoretical number of HS-20 trucks needed to cause bottom flange yielding of one girder (M_{AD}) was divided by the product of the applied maximum live load moment due to one HS-20 vehicle (M_A) and the AASHTO distribution factor (GDF). For example, theoretical first yield capacity for 0º skew models was calculated to be

$$\# \text{ HS-20} = M_{AD} / (M_A \cdot DF) = \frac{4{,}525}{1604 \cdot 0.47} = 6.0.$$

The results show that theoretically calculated first yield capacities are significantly lower than the FEA computed first yield capacities at each skew. The largest percent difference (53%) was found at 0° skew, while the smallest percent difference (37%) was found at 63° skew.

Table 4.10 Comparison between theoretical and FEA first yield capacities at each skew

Skew	Theoretical # HS-20 trucks	FEA# HS-20 trucks	% difference between theoretical and FEA
0°	6.0	12.7	53%
25°	6.1	12.1	49%
46°	6.7	13.0	48%
55°	7.8	13.6	42%
63°	9.4	15.0	37%

4.4.1.3 Discrete Metric 3 -System Yield Capacity

The third metric used for "discrete" assessment of FEA data is the number of HS-20 trucks needed to cause the cross-sectional yielding of the bottom flange of all girders in the bridge. This metrics is designed to measure system capacity of the bridge.

- **Results**

The results (Figure 4.16 and Table 4.11) show significant system yield capacity of steel I-girder bridges. The overall average load that will cause cross-sectional yielding of the bottom flange of all girders in the bridge was calculated to be equivalent to 16.1 HS-20 trucks. The general trend, similar to first yield results for the staggered models, is that the minimum capacity occurs at 25º skew. On average, skewed bridges have 8.5% larger capacity than tangent (0º skew) bridges (15.0 HS-20 trucks vs. 16.4 HS-20 trucks, respectively). Similarly, to first yield results, the correlation between bridge skew and bridge capacity is also non-linear. The best fit was obtained by polynomial regression equation in form of

$$y = 0.0022x^2 - 0.0858x + 15.104 \tag{4.15}$$

where, y represents bridge system yield capacity and x represents bridge skew. The correlation coefficient was very high (R^2=95%) indicating strong, but also non-linear, association between bridge skew and bridge system yield capacity.

The No-frame models generally have higher system yield capacity than cross-frame models (3.6% higher on average, or 16.6 HS-20 trucks vs. 16.0 HS-20 trucks, respectively). Additionally, the results also show inline models generally have higher system yield capacity than staggered models for skews of 46° and above, resulting in the inline models having 4% greater capacity on average (16.3 HS-20 trucks vs. 15.7 HS-20 trucks, respectively). Furthermore, the K-frame models have more system capacity than X-frame models in the skewed and tangent inline models.

Table 4.11 Number of HS-20 trucks needed to cause cross-sectional yielding of the bottom flange at all bridge girders (system yield)

SKEW	K-FRAME INLINE	K-FRAME STAG	X-FRAME INLINE	X-FRAME STAG	NO FRAME	Average
0°	14.9	14.8	14.8	14.9	15.5	15.0
25°	14.7	14.8	14.2	14.6	15.4	14.7
46°	15.9	15.2	15.7	14.8	15.5	15.4
55°	17.1	16.2	17.1	15.9	17.0	16.7
63°	19.3	18.0	19.1	17.6	19.4	18.7
Average	16.38	15.8	16.18	15.56	16.56	

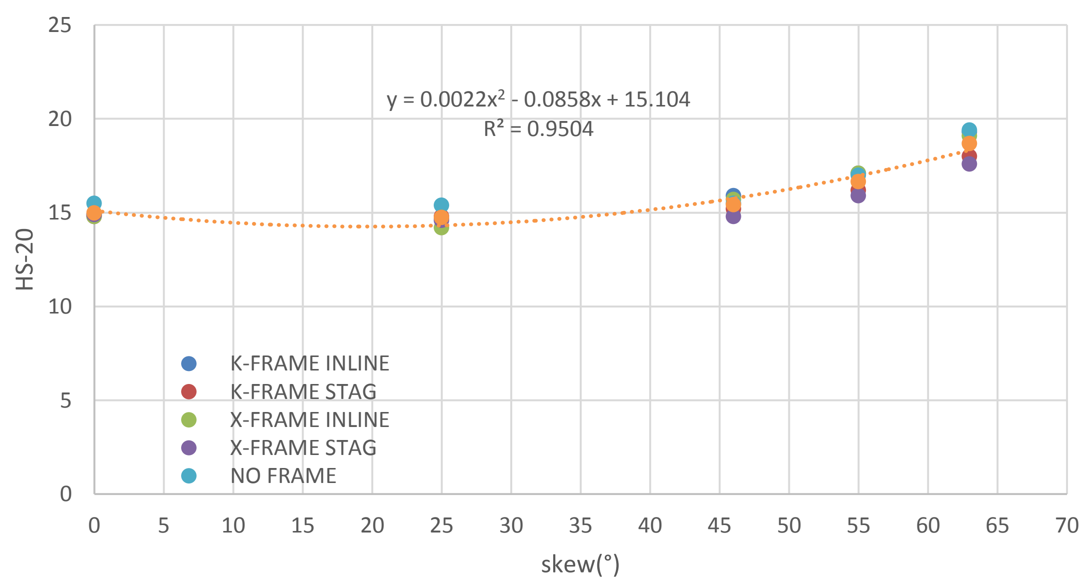

Figure 4.21 Bridge capacity in terms of number of trucks needed to cause complete cross-sectional yielding of bottom flanges of all girders in the bridge.

The results shown are in general very surprising especially considering that, intuitively, it would not be expected that No-frame models should have larger system capacities than cross-frame models. For example, when system capacities between No-frame model and cross-frame models where compared at each skew it was found that only four (K-frame and X-frame Inline models at 46º and 55° skew) out of 20 cross-frame models have larger capacities than the No-frame models. That means that in 80% of the cases No-frame models have larger system capacities than cross-frame models.

This was a surprising result because traditional line of thinking is that, in bridges with high skews, cross-frames tend to act not just as load transferring members, but also as primary load carrying members assisting girders and deck. This assumption would imply that No-frame models would have substantially smaller overall system capacity when compared to cross-frame models, which is not the case according to results presented.

In an effort to better understand this behavior, the stress distribution and deflection patterns between No-frame and K-frame Inline models at 0º skew where compared (Figure 4.22). Figure 4.22 shows that stress and deflection profiles for these two models look very similar to each other. The graphics on the left show models' deflection patterns, while the graphics on the right show typical stress distribution pattern of the bottom flanges. It seems that presence or absence of the cross-fame did not significantly affect the visual yielding pattern of the girders bottom flanges.

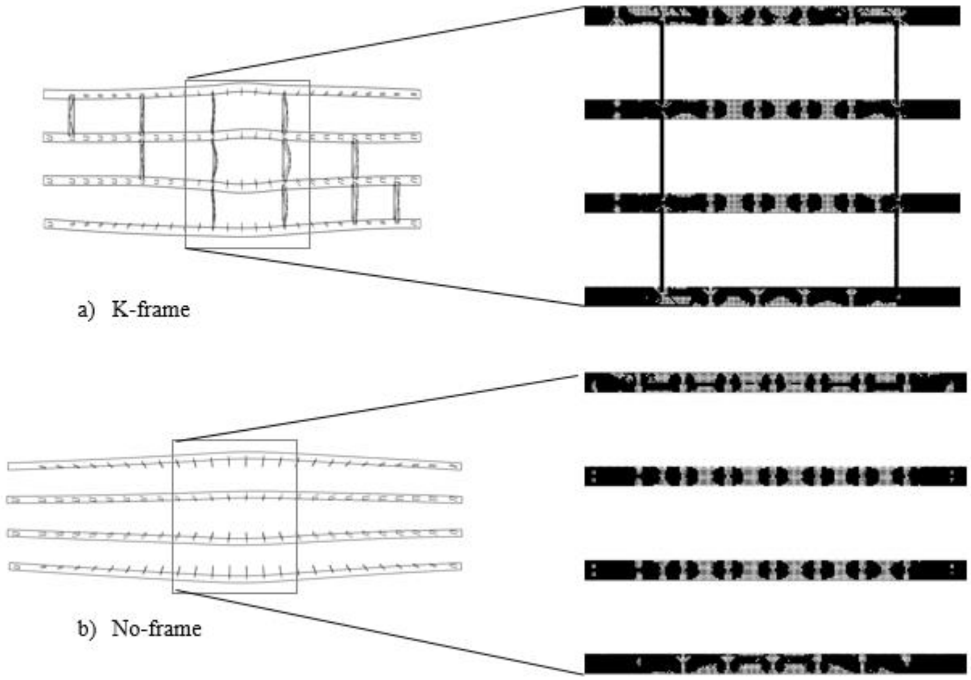

Figure 4.22 Bottom flange lateral deflection (left) and stress distribution (right) of K-frame (top) and No-frame (bottom) models for 0° skew at system load level. White areas are elements that are yielded in tension (true stress>36045psi), while black areas represent stresses that are not yielded yet.

Furthermore, 46° skew X-frame Staggered model showed the same first yield and system yield capacity. This was very unusual finding because theoretically it would be expected that it would need additional load on the bridge to cause other girders to yield after yielding of the first girder took place. However, it seems that system yield at this bridge model experienced abrupt instantaneous yielding of all four girders at the same load step. The left of Figure 4.233a shows the state of bottom flange yielding of bridge X-frame Staggered at 46° skew at load of 13.8 HS-20 trucks. While there is significant amount of yielding in 3 out of 4 girders, the yielding of the whole bottom flange cross-section did not occur at single girder at this load level. However, at the next load increment (load equivalent of 14.8 HS-20 trucks shown in Figure 4.23b), bottom flange cross-sections of all four girders were completely yielded.

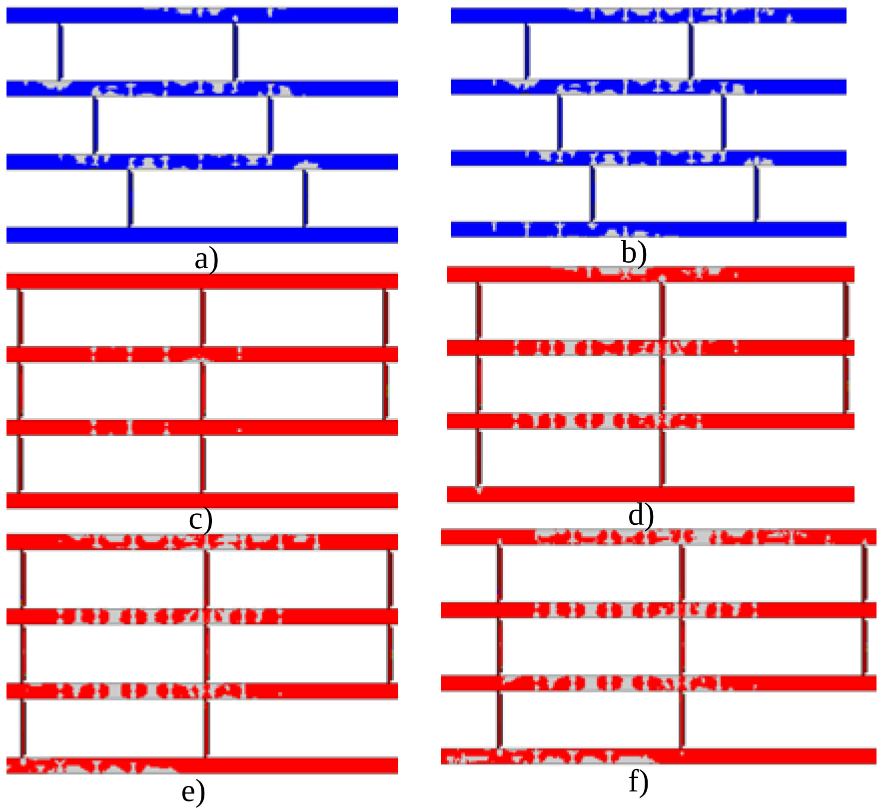

Figure 4.23 The spread of bottom flange yielding at a) X-frame Staggered at 46° skew under 13.8 HS-20 trucks; b) X-frame Staggered at 46° skew under 14.8 HS-20 trucks (first yield and system yield simultaneously); c) X-frame Inline at 46° skew under 11.6 HS-20 trucks; d) X-frame Inline at 46° skew under 12.6 HS-20 trucks (first yield) and f) X-frame Inline at 46° skew under 15.7 HS-20 trucks (system yield).

To contrast this, Figures 4.23c through f show the gradual spread of bottom flange yielding that occurred in the 46° skew X-frame Inline model. Figure 4.23c shows the yielding one load increment before first yield, while Figure 4.23d shows the spread of bottom flange yielding at first yield load level (12.7 HS-20 trucks). Figure 4.23e shows the spread of bottom flange yielding one load increment before system yield, while Figure 4.23f shows the spread of bottom flange yielding at system yield load level (15.7 HS-20 trucks). This result graphically shows how the different cross-frame’s layout can affect the spread of bottom flange yielding.

- **Discussion**

The theoretical values for system yield capacities in terms of HS-20 trucks were computed and compared to FEA results. To calculate the theoretical system yield capacity of the bridge the first yield capacities of all girders in the bridge were summed,

$$\text{System capacity} = \sum_{1}^{k} My_i \qquad (4.15)$$

Where i is an integer from 1 to k, k is number of girders in the bridge and My_i is first yield capacity of each girder. Considering that each girder had the same cross-section amd material properties and thus each girder would have same first yield capacity, which means that system capacity in terms of number of HS-20 vehicles is calculated as

$$\text{\# HS-20} = 4 \cdot M_{AD} / M_A = \frac{4 \cdot 4{,}525}{1604} = 11.3$$

where M_{AD} is the moment that cause bottom flange yielding and M_A maximum applied moment on the bridge. As an approximate way to consider the skew effect, maximum applied load was multiplied by skew correction factor SCF = 1- $c_1 (\tan \theta)^{1.5}$ (AASHTO LRDF equations from Table 4.6.2.2e-1), where c1 is bridge stiffness parameter (0.08985) and θ is bridge skew. (Another way of considering this effect, that was not explored, includes revising M_A for each girder based on the longitudinal position of the truck relative to each girder.) The results show that the largest percent error (25%) was calculated at 0° skew, while the lowest percent error (19%) was calculated at 46° skew.

Table 4.12 Comparison between theoretical and FEA system yield capacities at each skew

Skew	Theoretical # HS-20 trucks	FEA# HS-20 trucks	% difference between theoretical and FEA
0°	11.3	15.0	25%
25°	11.6	14.7	21%
46°	12.5	15.4	19%
55°	13.3	16.7	20%
63°	15.0	18.7	20%

4.4.2 Holistic Evaluation Results

4.4.2.1 Holistic Metric 1 - Percent of Girders That Yielded

The percent of bridge component that yielded is the first metric used for "holistic" evaluation of FEA data. This metric was only computed for first yield and system yield load levels, because during design load level no element reached or exceeded the true yielding stress of 36,045 psi.

First Yield Load Level

- **Results**

The results show (Table 4.14 and Figure 4.22) that on average there is no difference in percent yielding between tangent bridges (0° skew) and skewed bridges (1.1% and 1.1%, respectively). Bridges with staggered cross-frame layouts generally have higher percent girder yielded than bridges with inline cross-frame layouts (58.1% higher on average, 1.7% vs. 0.7%, respectively). There was no consistent relationship between whether the K-frame or X-frame models produced the highest percentage of girder yielding. The results also show that on average cross-frame models have 41.3% higher percent girder yielded than No-frame models (1.2% vs. 0.7%, respectively), with only the X-Frame Inline models giving lower percentages of girder yielding in some cases.

- **Discussion**

The results show that there was no difference in percent yielding between tangent bridges and skewed bridges. This was somewhat unexpected result because the average first yield load for straight bridges (0° skew) was 12.7 HS-20 trucks, while the average load for skewed bridges was 13.4 HS-20 trucks. This means that while the average load between two bridge skews increased 5.7%, the average percent of yielded girder was not increased at all. What is more interesting is the average percent of girder yielding actually slightly decreased from 0° skew bridges (1.1%) to 25° skew bridges (1.0%), which matches with discrete metrics where 25° skew bridges had the lowest average first yield capacity and lowest system yield capacities. Closer examination of the results shows that the main culprit for the drop in percent yielding at 25° skew was the bridges with X-frame Staggered cross-frame design. The results show that at X-fame Staggered 0° skew bridge percent of girder yielding is 1.6%, while at 25° skew the percent of girder yielding is dropped to 0.7%. There is also the large drop in first yield capacity for this model between 0° and 25° skew (13.5 vs 11.2 HS-20 trucks respectively).

Table 4.12 Percent of girder yielded at first yield load level

Skew	K-Frame Inline	K-Frame Stagg	X-Frame Inline	X-Frame Stagg	No-frame	Average
0°	0.9%	1.4%	0.8%	1.6%	0.9%	1.1%
25°	0.9%	1.4%	1.0%	0.7%	0.8%	1.0%
46°	0.5%	1.7%	0.6%	3.3%	0.5%	1.3%
55°	0.7%	1.8%	0.2%	1.9%	0.7%	1.1%
63°	0.9%	1.5%	0.6%	1.9%	0.7%	1.1%
Average	0.8%	1.6%	0.7%	1.9%	0.7%	

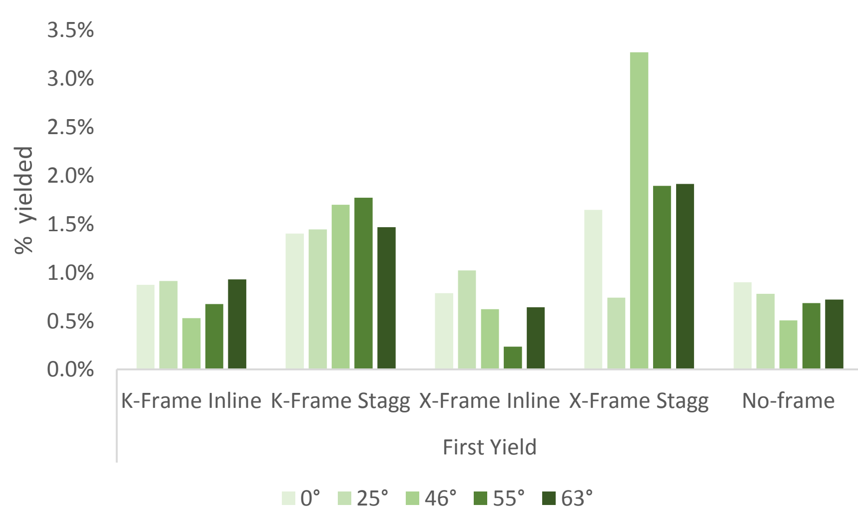

Figure 4.24 Percent of girder yielded at first yield load level

To further investigate this phenomenon, stress contours of X-frame Staggered models at four skews were plotted (Figure 4.25a to 4.25d) and analyzed. The results show that three out of four girders at bridges with 0°, 46° and 55° skew have some of the bottom flange yielding before reaching first yield capacity threshold (Figure 4.25a, c and d). However, at 25° bridge, only two girders showed some bottom flange yielding before first yield capacity threshold is reached (Figure 4.25b).

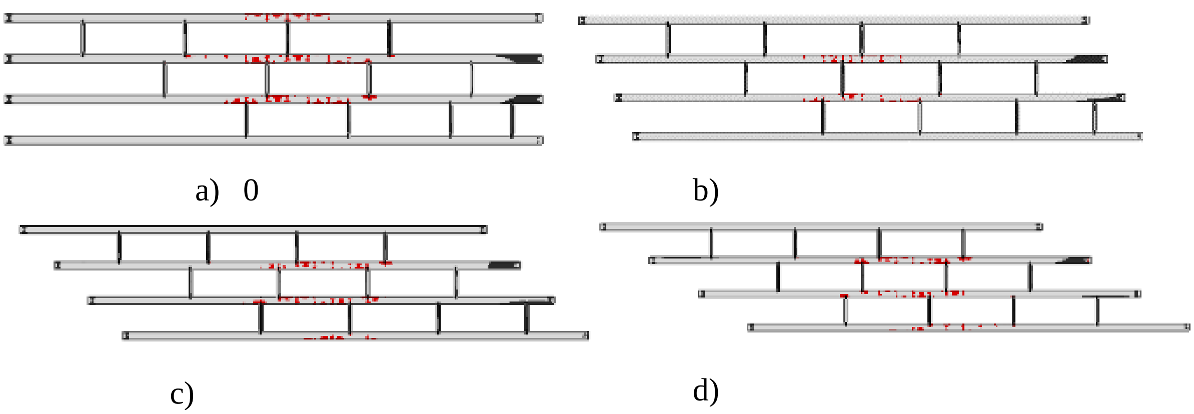

Figure 4.25 Bottom flange stress contours at first yield load level of X-frame staggered models at four different bridge skews (0°, 25°, 46° and 55°). Red are yielded elements, gray are elements in tension and black are elements in compression.

System Yield Load Level

- **Results**

The results show (Table 4.15 and Figure 4.24) that skewed bridges have higher percent girder yielding that tangent (0° skewed) bridges (on average 58.1% higher, or 4.5% and 1.9%, respectively). Furthermore, bridges with inline cross-frame layouts generally have higher percent of girder yielding than bridges with staggered cross-frame layouts, with the exception at 25° skew bridges. This contributes to inline cross-frame layouts having 23.0% higher percent of girder yielding than bridges with staggered cross-frame layouts on average (4.1% vs. 3.3%, respectively). X-frame models generally have larger percent girder yielding than K-frame models (on average 5.2% higher, 3.9% vs.

3.7%, respectively), the exception being the 63° staggered models. The results also show that No-frame models on average have 23.9% higher percent yielding than cross-frame models (4.7% vs. 3.8%, respectively), but there is not consistent trend contributing to this result.

Table 4.13 Percent of girder yielded at system yield load level

Skew	K-Frame Inline	K-Frame Stagg	X-Frame Inline	X-Frame Stagg	No-frame	Average
0°	1.7%	1.6%	2.0%	1.8%	2.2%	1.9%
25°	2.9%	3.4%	3.0%	3.9%	5.2%	3.7%
46°	4.4%	3.2%	4.8%	3.3%	4.4%	4.0%
55°	5.4%	3.4%	5.5%	3.9%	5.0%	4.7%
63°	6.3%	4.2%	6.3%	4.0%	6.6%	5.5%
Average	4.1%	3.2%	4.3%	3.4%	4.7%	

Discussion

Results also show (Figure 4.25) that percent of girder yielding and system yield capacity are moderately correlated (R^2 =0.62), meaning that as the load on the bridge is increased the percent of girder yielding is increased as well. However, this moderate correlation also indicate that some other factors also contribute to percent of girder yielding.

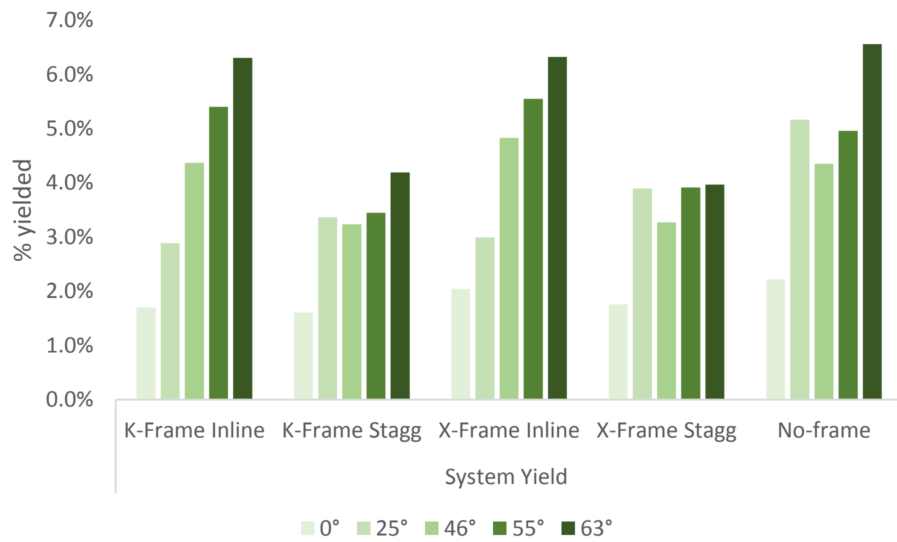

Figure 4.26 Percent of girder yielded at system yield load level

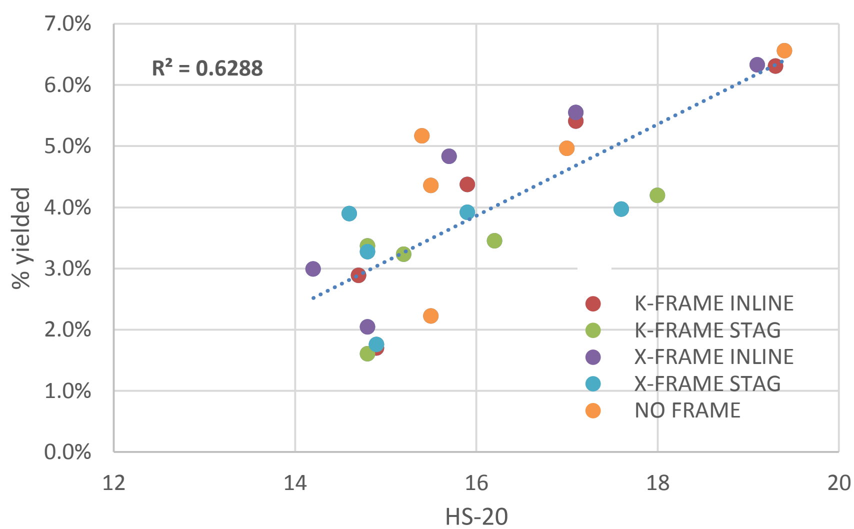

Figure 4.27 Scatter plot between percent yielding and system capacity of the bridge

4.4.2.2 Holistic Metric 2 - Total Lateral Bending Energy (TLBE)

The TLBE results for the three load levels are detailed below. Common trends at all three load levels are that the TLBE increases with increasing skew and that in general no-frame models have the lowest TLBE, followed by inline models, then staggered models.

Design Load Level

- **Results**

The results show (Table 4.14 and Figure 4.28) that on average skewed bridges have 80% larger TLBE than tangent bridges (8.13·105in·lb vs. 4.17·106in·lb, respectively). Furthermore, bridges with staggered cross-frame layouts have on average 27% larger TLBE than bridges with inline cross-frame layouts (3.91·106in·lb vs. 2.84·106in·lb, respectively). Results also show that bridges with cross-frames have on average 29% larger TLBE than bridges without cross-frames (3.71·106in·lb vs. 2.65·106in·lb, respectively).

- **Discussion**

The results indicate that the hypothesis that skewed bridges have larger TLBE than tangent bridges is correct. What is more interesting is that bridges without cross-frames in general have lower TLBE than bridges with cross-frames, with the exception found at tangent inline bridges. It seems that presence of both bridge skew and cross-frames increase TLBE in the bridges. On a more particular level, X-frame Staggered bridge at 63° skew is the model with the largest TLBE (7.82·106in·lb). This is not an unexpected result, considering that it is known from the literature that staggered cross-frames tend to increase lateral bending stresses. Furthermore, the reason why on average X-frame Staggered models have 5% larger TLBE than K-frame Staggered models might lay in the fact that X-frame models have 30% higher axial stiffness than K-frame models.

Table 4.14 Total lateral bending energy expenditure (in·lb) at design load level

Design	0°	25°	46°	55°	63°	Average
K-Frame Inline	3.08E+05	1.58E+06	3.20E+06	4.44E+06	5.79E+06	3.07E+06
K-Frame Stagg	1.47E+06	2.53E+06	4.18E+06	5.94E+06	6.84E+06	4.19E+06
X-Frame Inline	2.78E+05	1.66E+06	3.25E+06	4.75E+06	5.92E+06	3.17E+06
X-Frame Stagg	1.61E+06	2.19E+06	4.30E+06	6.12E+06	7.82E+06	4.41E+06
No-frame	3.96E+05	1.39E+06	2.73E+06	3.89E+06	4.83E+06	2.65E+06
Average	8.13E+05	1.87E+06	3.53E+06	5.03E+06	6.24E+06	

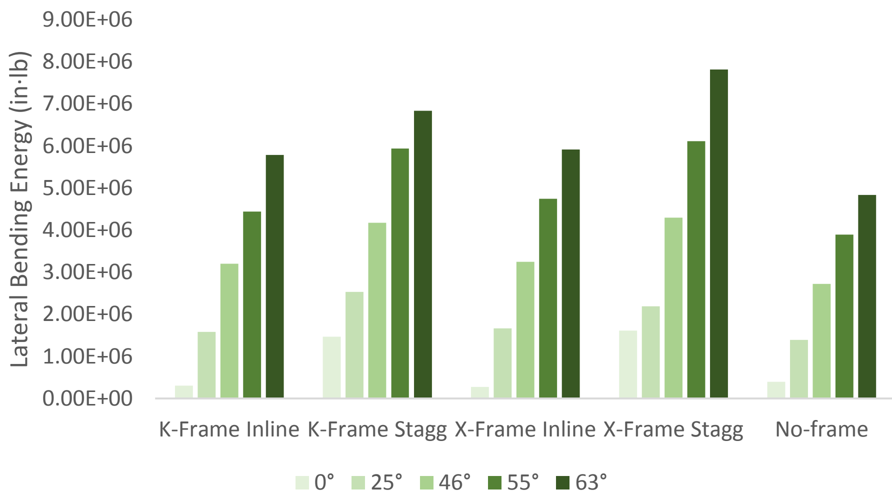

Figure 4.28 Total lateral bending energy expenditure (in·lb) at design load level

First Yield Load Level

- **Results**

The results show (Table 4.15 and Figure 4.29) that on average skewed bridges have 59% larger total lateral energy expenditure than tangent bridges TLBE (6.24·106in·lb vs. 1.51·106in·lb, respectively). Furthermore, bridges with staggered cross-frame layouts have on average 45% larger TLBE than bridges with inline cross-frame layouts (1.07·106in·lb vs. 9.37·106in·lb, respectively). Results also show that bridges with cross-frames have on average 40% larger TLBE than bridges without cross-frames (1.45·107in·lb vs. 8.65·106in·lb, respectively).

- **Discussion**

The results indicate that bridge behavior in terms of TLBE is generally the same at design and at first yield load level. Skewed bridges have larger TLBE than tangent bridges, staggered layouts have larger TLBE than inline layouts. Furthermore, bridges without cross-frames have consistently the lowest TLBE regardless of the skew. Even tangent bridges with inline cross-frame layouts bridges higher TLBE than No-frame bridges. On a more particular level, X-frame Staggered model at 63° skew is still model with the largest TLBE (3.20·107in·lb) among all other models.

Table 4.15 Total lateral bending energy expenditure (in·lb) at first yield load leve

Design	0°	25°	46°	55°	63°	Average
K-Frame Inline	2.56E+06	5.70E+06	1.00E+07	1.39E+07	1.98E+07	1.04E+07
K-Frame Stagg	1.18E+07	1.41E+07	1.90E+07	2.47E+07	2.59E+07	1.91E+07
X-Frame Inline	2.02E+06	5.87E+06	9.96E+06	1.45E+07	1.88E+07	1.02E+07
X-Frame Stagg	1.30E+07	9.40E+06	1.23E+07	2.53E+07	3.20E+07	1.84E+07
No-frame	1.89E+06	4.69E+06	8.16E+06	1.24E+07	1.61E+07	8.65E+06
Average	6.24E+06	7.95E+06	1.19E+07	1.81E+07	2.25E+07	

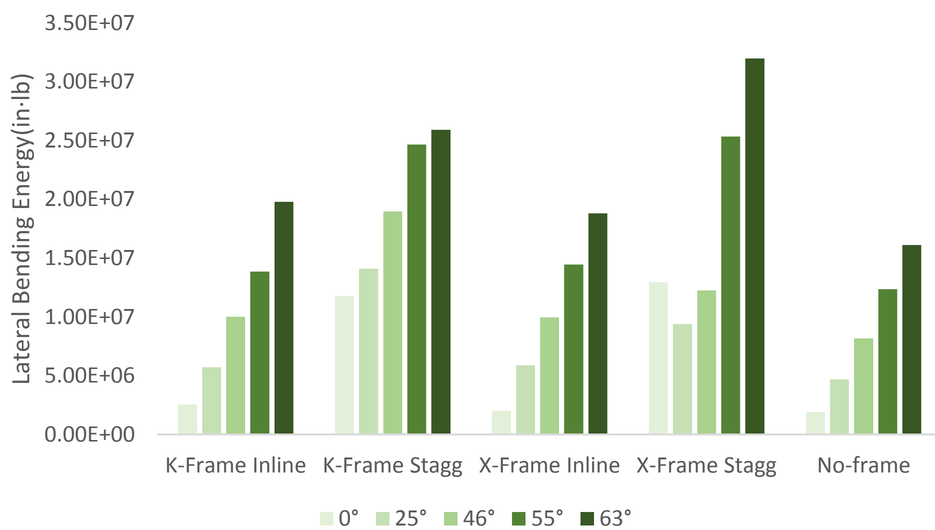

Figure 4.29 Total lateral bending energy expenditure (in·lb) at first yield load level

System Yield Load Level

- **Results**

The results show (Table 4.16 and Figure 4.30) that on average skewed bridges have 61% larger total lateral energy expenditure than tangent bridges TLBE ($1.65 \cdot 10^7$in·lb vs. $6.40 \cdot 10^6$in·lb, respectively). Furthermore, bridges with staggered cross-frame layouts have on average 40% larger TLBE than bridges with inline cross-frame layouts ($1.74\cdot10^{6}$in·lb vs. $1.04\cdot10^{6}$in·lb, respectively). Results also show that bridges with cross-frames have on average 27% larger TLBE than bridges without cross-frames ($1.53\cdot10^{7}$in·lb vs. $1.11\cdot10^{7}$in·lb, respectively).

- **Discussion**

The results indicate that models at system yield load level exhibit the same global behavior as they did at first yield load level (with respect to qualitative comparisons of skew vs. tangent, inline vs. staggered, and cross-frame vs. No-frame TLBE). X-frame Staggered model at 63° skew still had the largest TLBE (3.33·107in·lb) among all models.

Table 4.16 Total lateral bending energy expenditure (in·lb) at system yield load level

Design	0°	25°	46°	55°	63°	Average
K-Frame Inline	3.15E+06	6.25E+06	1.08E+07	1.59E+07	2.16E+07	1.15E+07
K-Frame Stagg	1.19E+07	1.47E+07	1.94E+07	2.54E+07	2.73E+07	1.97E+07
X-Frame Inline	2.54E+06	6.31E+06	1.05E+07	1.61E+07	2.15E+07	1.14E+07
X-Frame Stagg	1.32E+07	9.84E+06	1.22E+07	2.64E+07	3.33E+07	1.85E+07
No-frame	1.14E+06	1.23E+07	9.43E+06	1.42E+07	1.84E+07	1.11E+07
Average	6.40E+06	9.88E+06	1.20E+07	1.96E+07	2.44E+07	

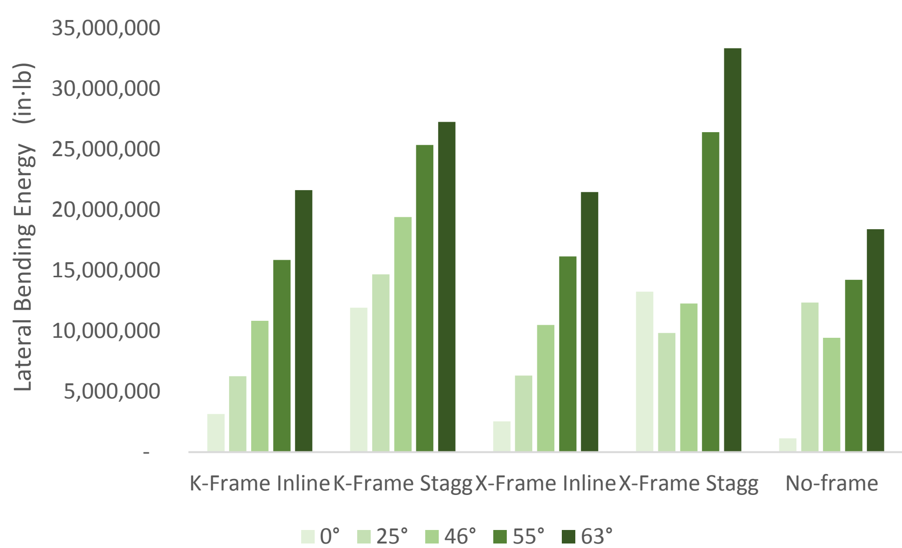

Figure 4.30 Total lateral bending energy expenditure (in·lb) at system yield load level

4.4.2.3 Holistic Metric 3 - Performance Index

The Performance Index (PI) is the third "holistic" metric designed for FEA data evaluation. PI is defined as the ratio of the bridge capacity expressed in terms of number of HS-20 trucks (at different load levels) to the percent of girder yielding at that load level. This metric is intended to evaluate bridge models in terms of effectiveness in distributing stresses at post-elastic load levels. As described in Section 4.3.2.2, the bridge with the best performance has a score of 100%. The rest of the bridges are ranked as a percentage of the best performing bridge. It is important to note that, according to this metrics larger the PI indicates that more effective the bridge is in distributing stresses without causing first or system yield.

First Yield Results

- **Results**

The results show (Table 4.17 and Figure 4.31) that on average skewed bridges perform 28% better than tangent bridges (PI=30 vs. PI= 22, respectively). Models with inline cross-frame layouts generally perform better than bridges with staggered cross-frame layouts (on average 57.7% better, or PI=39 vs. PI=17, respectively), the exception being 25° staggered models. The results also show that on average, No-frame bridges perform 13.3% better than cross-frame bridges (PI=32 vs. PI=28, respectively), although there is no consistent trend contributing to these results.

- **Discussion**

On more particular level, the results show that X-frame Inline bridge at 55° skew is by far the best performing bridge (PI=100), while X-frame Staggered bridge at 46°skew is the worst performing bridge (PI=8). The reason why X-frame Staggered at 46°skew is the worst performing bridge at first yield load level, lay in the fact that this bridge reached first yield and system yield capacity simultaneously (under the same load of 14.8 HS-20 trucks).

Table 4.17 Performance Index for first yield load condition

Skew	K-FRAME INLINE	K-FRAME STAG	X-FRAME INLINE	X-FRAME STAG	NO FRAME	Average
0°	26	18	29	15	23	22
25°	25	17	23	28	27	24
46°	44	15	38	8	42	29
55°	36	16	100	14	34	40
63°	29	20	43	16	35	29
Average	32	17	47	16	32	

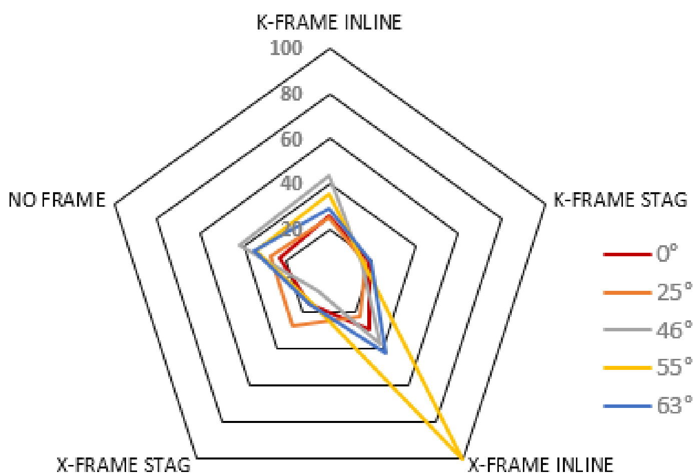

Figure 4.31 Performance Index for first yield load level

System Yield Results

- **Results**

The results show (Table 4.18 and Figure 4.32) that tangent bridges consistently perform better than straight bridges (111.7% better on average, or PI=83 vs. PI= 42, respectively). Bridges with staggered cross-frame layouts generally perform better than bridges with inline cross-frame layouts (on average, 16.6% better, or PI=57vs. PI=49, respectively). It was also found that K-frame models generally perform better than X-frame models, with the exception being the 63° staggered models. More specifically, K-frame Staggered bridge at 0° skew is the best performing bridge, while No-frame bridges at 25° and 63°skew are the worst performing bridges (PI=32). The results also show that on average, bridges with cross-frames have 22% larger PIs than No-frame bridges (PI=53 vs. PI=43, respectively). However, No-frame bridges have PIs that are comparable to the Inline models at the 46°, 55° and 63°skews. The average PI for No frame models at 46°, 55° and 63°skews is PI=36, while the average PI for inline cross-frame models at 46°, 55° and 63°skews is PI=35.

- **Discussion**

PI results show that there is a significant difference in bridge behavior between first yield and system yield load levels. Comparisons between skewed and tangent bridges; inline and staggered; and bridges with and without cross-frames show opposite trends at first yield vs. system yield load levels. For example, first yield results show that skewed bridges perform better than tangent bridges, while at system yield tangent bridges perform better than skewed bridges. At first yield bridges with inline cross-frame layouts perform better than bridges with staggered cross-frame layout, while at system yield load level, staggered cross-frames perform better than inline. At first yield load level, bridges without cross-frame perform better than bridges with cross-frame, while at system yield load level opposite is true.

The limitation of PI metric may lie in the fact that even small load increments, at post-elastic load levels, could lead to large girder yielding (as seen in Figure 4.23). This is one of the reasons a new, more robust holistic evaluation method, such as Chi-square Distances is needed, as will be discussed in the next section.

Table 4.18 Performance Index for system yield load

Skew	K-FRAME INLINE	K-FRAME STAG	X-FRAME INLINE	X-FRAME STAG	NO FRAME	Average
0°	95	100	79	92	76	88
25°	55	48	51	41	32	45
46°	39	51	35	49	39	43
55°	34	51	33	44	37	40
63°	33	47	33	48	32	39
Average	51	59	46	55	43	

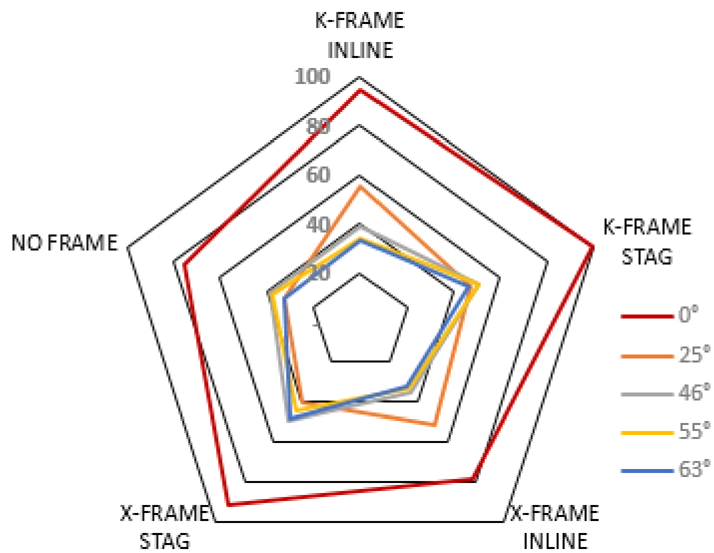

Figure 4.32 Performance Index for system yield load level

4.4.2.4 Holistic Metric 4 - Chi-square Distances (CsD)

Chi-square Distances (CsD) is the third "holistic" evaluation metric that was used for assessment of FEA data. First step in data assessment using this instrument was to visually inspect the stress histograms of each model. Therefore, all models were plotted, visually inspected and compared to each other in order to detect if any anomaly existed that could negatively affect the computations (for example presence of extreme number of outliers). Additionally, by plotting histograms the information about the models in terms of the direction of the response (tension vs. compression) and in terms of magnitude of stresses could be obtained. For easier visual comparison between the models, their stress distributions are plotted as three-dimensional histogram (Figure

4.33). These three-dimensional plots are organized in the following manner, on x axis are plotted stress bins (width of the bin =1000psi); on y axis are plotted frequencies; and on z axis are plotted models of different cross-frame configurations at different skews. Each 3D plot has a total of 25 stress distributions.

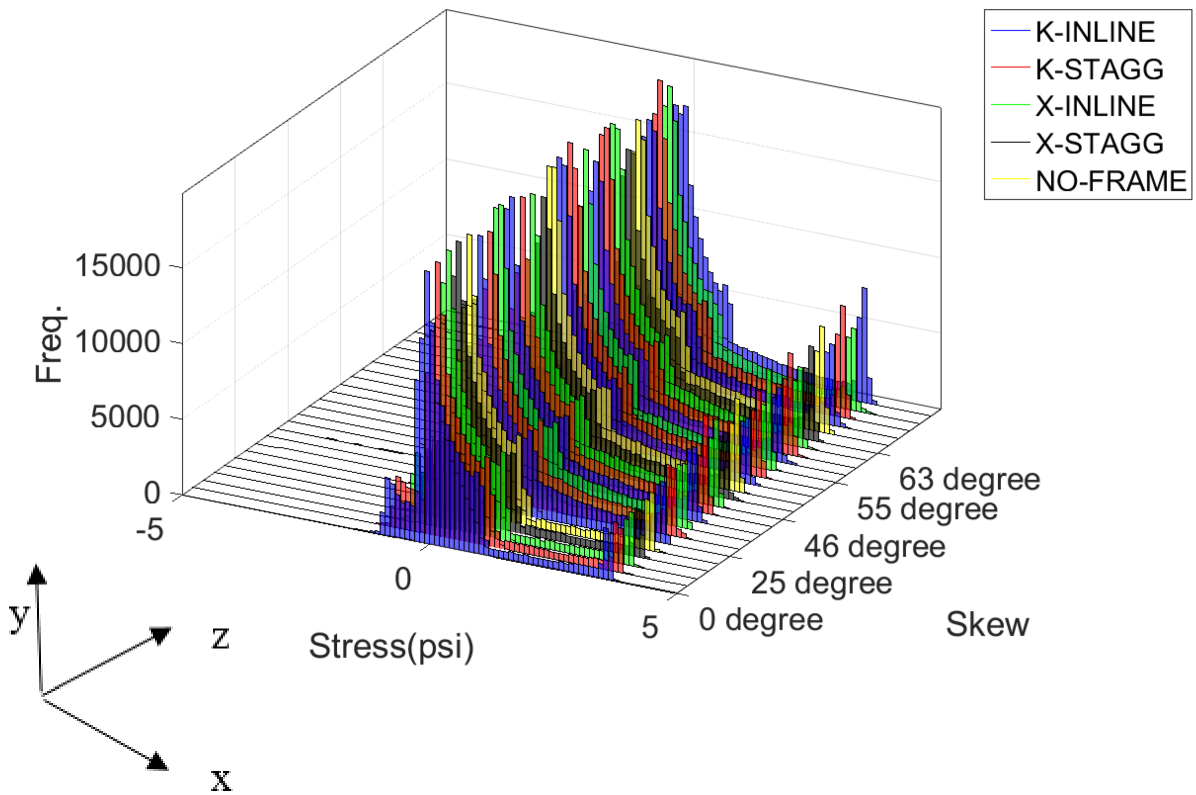

Figure 4.33 Example of 3D stress histograms for girders, at system yield load level.

Once visual inspections were conducted and models were validated, CsD were computed for stress histograms among the models at design, first yield and system yield load level. To interpret CsD data, two important concepts needed to be considered. First concept relates to comparison between models based on bridge skew. Note that CsD between models at different skews can't be compared at first yield and system yield load level because the applied load level was not the same. Intuitively, if the applied loads are not the same, stress distributions will not be the same, therefore, CsD comparison would be inexact.

The second concept is related to the magnitude of CsD. It is important to note that the larger the CsD between two models is, the larger the difference in stress distribution is. For example, if it is assumed that all cross-frame configurations transfer the load equally efficiently, that would mean that the difference in stress distribution between the models should be small and therefore CsD between models should be also small. Conversely, if the CsD between two models is very large that indicates that these two models have substantially different stress distributions.

A special look should be given to the relative difference between the cross-frame models and No-frame models. If it is assumed that cross-frames play significant role in stress redistribution in bridges, then the difference between stress histograms of No-frame models and cross-frame models should be substantial. In other words, it would be expected to see that at every load level and at every skew, the CsD between cross-frames and No-frame models should be larger than the distances between cross-frame models.

However, preliminary observations showed that the difference between No-frame models and cross-frame models is sometimes smaller than the difference between cross-frame models. For example, Table 4.24 shows the outcome of CsD analysis computed for girders at 0º skew at design load level. In the second row (labeled K-Stagg) there were three CsD entries that compare bridges with K-Staggered cross-frame layout with bridges with other cross-frame layouts. It can be seen see that the difference between X-Inline model and K-Staggered model is 1577, the difference between K-Staggered and X-Staggered is 1363, and the difference between K-Staggered model and No-frame model is 330 (the first row of the table also shows that the CsD between K-Staggered and K-Inline is 255).

Table 4.24 Chi-square Distance between models at 0º skew at design load level

Design	K-INLINE	K-STAGG	X-INLINE	X-STAGG	NO-FRAME
K-INLINE	0	225	1317	1439	555
K-STAGG		0	1577	1363	330
X-INLINE			0	236	1768
X-STAGG				0	1800
NO-FRAME					0

Thus, it can be seen for example that there is a larger difference in stress distribution between K-Staggered and X-Inline models than between K-Staggered and No-frame models. Since this occurrence is not intuitively anticipated and represents significant deviation of expected results, it is relevant to count the rate at which this occurrence happens at each skew and load level. Therefore, in order to count this rate of occurrence (RO) and evaluate it at girder's component level, following method is proposed:

a) Count instances in which No-frame to cross-frame model pairs have smaller CsDs than cross-frame to cross-frame model pairs at the same skew/load level, then;

b) Divide the number of counted instances with the total number of possible pairs to obtain Rate of Occurrence (RO).

Considering that there are six cross-frame pairs CsDs and four No-frame to cross-frame pairs, there are (6 x 4=) 24 pair comparisons per skew. If occurrence (RO) algorithm is applied on data from Table 4.24, it can be seen that there are total of 8 occurrences where cross-frame CsD pair is larger than cross-frame to No-frame CsD pair. For example, K-Stagg/X-Inline CsD =1577 is larger than No-frame/K-Stagg CsD=330, and, K-Inline/X-Inline CsD =1317 is larger than No-frame/K-Inline CsD=55, and so on.

Since, there are total of 24 cross-frame pairs comparisons per skew, the rate of occurrence (RO) is

$$RO = \frac{\text{total \# pairs-\# of deviations}}{\text{total \# of pairs}} = (24-8)/24 = 0.67 \text{ or } 67\%.$$

That means that in only 67% of cases cross-frame models would have stress distributions that are more similar among themselves than the stress distribution of No-frame models. A RO measure is easy to interpret and very intuitive. For example, larger RO means that bridges with cross-frames behave as theoretically expected in terms of distributing stresses, while smaller RO means that bridges with cross-frames are not acting as theoretically expected in terms of distributing stresses. Furthermore, RO allows to compare results across the skews and load levels addressing the limitations of CsD algorithm. Chi-Square Distances were computed for girders and decks at three load levels: design, first yield and system yield. The corresponding data at each load level can be found in Appendices A through C, respectively.

4.4.2.4.1 Chi-square Distances - Girder Results

The girder results show (Table 4.19) that overall average RO is 58%. This is means that on average, in 42% of the cases, cross-frames did not significantly contribute to the girder stress distribution. The results also show that the comparison of skewed versus tangent bridges is affected by the load level, with RO being higher for tangent bridges compared to skewed bridges at the design load level and the opposite trend occurring at higher load levels. On average, skewed bridges have 4.2% larger RO than tangent bridges (58% vs. 56%). In other words, in both skewed and tangent bridges, in more than 40% of the cases, cross-frames did not contribute to the girder stress distribution. Furthermore, the results also show that the lowest average RO was detected at design load level (49%), while the largest average RO was detected at system yield load level (73%). Thus, as the load was increasing, the cross-frames are generally getting more involved in stress distribution, but this is not a consistent trend.

Table 4.19 Rate of occurrence (RO) for girders at design, first yield and system yield load level.

	0°	25°	46°	55°	63°	Average
Design	67%	50%	38%	42%	50%	49%
First Yield	38%	50%	75%	42%	50%	51%
System Yield	63%	79%	67%	79%	75%	73%
Average	56%	60%	60%	54%	58%	

4.4.2.4.2 Chi-square Distances - Deck Results

The deck results show (Table 4.20) that overall average RO is 40.0%. This means that on average, in 60% of the cases, cross-frames did not affect stress distribution in decks. The results also show that skewed bridges on average have 23.3% larger RO than tangent bridges (42% vs. 32%, respectively), but this result is largely influenced by relatively high RO values at 46° skew and the tangent and skew results are often similar to one another. Furthermore, the results also show that the lowest average RO was generally detected at first yield load level (34% on average, with only the 46° skew model deviating from this trend), while the largest average RO was detected at system yield load level (45% on average, again only the 46° skew model deviating from this trend). It is interesting to note that consistently the largest RO was found at bridges at 46° skew regardless of the load level. These results clearly indicate that cross-frames have very limited effect on longitudinal stress distribution in bridge decks.

Table 4.20 Rate of occurrence (RO) for deck at design, first yield and system yield load level.

	0°	25°	46°	55°	63°	Average
Design	33%	33%	67%	33%	33%	40%
First Yield	25%	25%	67%	29%	25%	34%
System Yield	38%	29%	63%	38%	58%	45%
Average	32%	29%	65%	33%	39%	

4.5 Conclusion

Bridge stress distributions at design, first yield, and system yield load were evaluated using "discrete" and "holistic" metrics. Both metrics gave insights in the bridge behavior in elastic and post elastic load ranges. While the "discrete" metrics give "snapshots" of behavior of one section of bridge, "holistic" metrics give more comprehensive evaluation of all bridge sections.

4.5.1 Discrete Metrics Summary

The results show that in general skewed bridges have higher average peak girder stresses than tangent bridges regardless of the load level. In contrast, deck results show that at design load level, skewed bridges have higher average peak longitudinal stresses than tangent bridges, but at first yield and system yield load level, tangent bridges have larger peak stresses than skewed bridges.

The results also show that bridges with inline cross-frame layout have lower peak girder stresses than bridges with staggered cross-frame layouts, regardless of the load level. When contrasted with deck stresses, results show that bridges with staggered cross-frame layouts have higher peak than bridges inline cross-frame layouts with at first yield load level.

Results also show that in general, the bridges with inline cross-frame layouts have lower peak bottom flange stresses than bridges without cross-frames (No-frame models), while bridges with staggered cross-frame layouts in general have higher peak <u>bottom flange</u> stresses than bridges without cross-frames. Similarly, X-frame models in general have lower peak <u>deck</u> stresses than No-frame models, while K-frame models have higher peak <u>deck</u> stresses than No-frame models regardless of the skew.

The results show that steel I-girder bridges have significant first yield and system yield capacities. Furthermore, the results show that in general skewed bridges have larger load capacities when compared to tangent bridges, except at 25° skew. The results (Table 4.10) also show that No-frame models on average have larger system yield capacities than cross-frame models. This was an unexpected result, as intuitively, it would be expected that cross-frame presence would allow more efficient load transfer throughout the bridge. Consequently, this efficient load transfer could allow more uniform spread of bottom flange yielding, allowing bridges to resist more load before reaching its yielding capacity.

Nevertheless, "discrete" data evaluation confirmed that steel I-girder highway bridges have very high system capacity, and that bridge's capacity to carry load is severely underestimated by current design practices. For example, average system capacity for all models across all skews and all cross-frame designs is 16.1 HS-20, which is more than 16 times the magnitude of current bridge design truck load; it should also be noted that bridge live load includes lane load that has not been factored into this comparison. Interestingly, results showed that No-frame modes (models with cross-frame removed) had larger system level capacity than other cross-frame models at 0°, 25°, and 63° skews.

4.5.2 "Holistic" Metrics Summary

The percent of bridge component that yielded is the first metric used for "holistic" evaluation of FEA data. This metric was only computed for the girders under first yield and system yield load levels. The results showed that at the first yield load level there was no difference between tangent and skewed bridges in terms of percent of girder that yielded. Although, at the system yield load level, skewed bridges had higher percent of girders yielded than tangent bridges. This was somewhat expected, because the results also showed moderate correlation (R^2=0.62) between percent of girder yielded and applied load. Interestingly, the results also show that bridges with staggered cross-frame placement had higher percent of girder yielded under first yield load level, but lower under system yield load level. Similarly, bridges without cross-frames on average had lower percent of girder yielding at first yield than bridges with cross-frames, while at system yield opposite was true. No-frame models have higher percent of girder yielded than cross-frame model.

The Total Lateral Bending Energy Expenditure (TLBE) was a second "holistic" metric used for evaluation of finite element analysis data. The results showed that skewed bridges have significantly larger TLBE than tangent bridges regardless of the load levels. Furthermore, the results showed that bridges with staggered cross-frame layouts have also significantly larger TLBE than bridges with inline cross-frame layouts regardless of the load level. And finally results showed that in general bridges without cross-frames have smaller TLBE than bridges with cross-frames at all three load levels.

The Performance Index (PI) was a third "holistic" metric used for evaluation of finite element analysis data. This metric is specifically designed for post-elastic FEA data evaluation, and it is calculated as a ratio of the applied load to the percent of girders yielding at that load. The idea behind designing this metric was that the bridge with the most efficient load transferring mechanism would be able to resist the highest load with the least percent of girder yielding. In other words, yielding would not be able to concentrate at one location at the bridge, but stress would be distributed before causing element yielding. The PI helps quantify bridge behavior in relative terms such as ratios between girder yielding and system capacity, not just in absolute terms.

The results showed that first yield load level, skewed bridges on average had larger PI than tangent bridges, while at system yield load level, opposite trend was detected. Average PI for tangent bridges was higher than average PI for skewed bridges. Furthermore, bridges with inline cross-frame layout had higher PI at first yield load level, but lower PI at system yield load level when compared to bridges with staggered cross-frame layout. On more particular level, X-frame Inline bridge at 55° skew and K-frame Staggered at 0° skew were the best performing models at first yield load leva and system yield load level respectively.

Although, PI proved to be affected by existence of non-linear relationship between the applied load and girder yielding, where even small load increments could lead to significant amount of girder yielding. This would also cause tangent bridges, while having lower system capacity than skewed bridges, to have higher PI than skewed bridges at system yield load level However, it seems that PI could be a good tool to evaluate or rank different types of cross-frame designs based on their effectiveness in helping distribute stresses.

Furthermore, results showed that in general, on average bridges without cross-frames had higher PI at first yield load level, but lower PI at system yield load level when compare to bridges with cross-frames. This was one of the most surprising results of this dissertation as the initial motivation for this work was to evaluate the best performing cross-frame configuration per given skew. Furthermore, even at system yield load level in 14/20 or in 70% of the cases, No-frame models outperformed or performed equal to cross-frames models when it comes to efficacy in distributing stresses in girders.

The fourth "holistic" metric, Chi-square Distance, showed that the difference in stress distributions between models with and without cross-frames is sometimes is so small, and that it is more likely than not, that bridges will have similar stress distributions regardless of the presence or absence of the cross-frames. For example, at design load level, in both skewed and tangent bridges, in more than 40% of the cases, cross-frames presence did affect girder stress distribution. Furthermore, deck results show that overall average RO is 40.0%. This means that on average, in 60% of the cases, presence of cross-frames did not affect stress distribution in decks. Remember that low RO generally indicates small contribution of cross-frames in stress distribution level and vice versa.

One of the main premises underlying this dissertation, states that a role of cross-frames is to help distribute the live load. The majority of findings in this chapter indicate that this premise should be reconsidered. While there are some results (such as shown with PI metric) that show that cross-frames do have a role in stress distribution, CsD results indicate that role is inconsequential and probably not worth the cost associated with cross-frames installation and maintenance. While the role of cross-frames during bridge construction phase is invaluable, their usefulness for in-service bridges is debatable. The question rises, how beneficial are cross-frames in in-service bridges if their role in stress distribution is not as assumed by current bridge design codes? From the literature review, it can be seen that cross-frames contribute to distortion induced fatigue cracks. From the contractor perspective, it is known that cross-frames are very expensive to fabricate and install and from the designer perspective, it is known that they are very hard to properly size because their role in the bridge is not concisely defined. While “holistic” approach for evaluating stress distribution data revealed many important trends that could not be otherwise detected by using “discrete” approach, it seems that further inspection of stress distribution could further benefit researchers interested in identifying latent trends in complex dataset. This topic will be the focus of Chapter 5.

REFERENCES

Ahonen, T., Hadid, A., Pietikainen. M. (2006). "Face description with local binary patterns: Application to face recognition". *IEEE transactions on pattern analysis and machine intelligence*, 28. 2037-2041.

Belongie, S., Jitendra, M., Puzicha., P. (2002). "Shape matching and object recognition using shape contexts". *IEEE transactions on pattern analysis and machine intelligence,* 24.4, 09-522.

Caltrans, (2014). “California Amendment to AASHTO LRFD Bridge Design Specifications”. *6th Edition,* California Department of Transportation, Sacramento, CA.

Helwig, T., and Yura, J. (2012). “Steel bridge design handbook: Bracing system design.” *Federal Highway Administration Report No. FHWA1F-12-052*, Vol. 13, hhttp://www.fhwa.dot.gov/bridge/steel/pubs/if12052 /volume13.pdfi(May31,2015).

Kar, Ansuman, et al. (2012). "Study on Effect of Skew Angle in Skew Bridges". *International Research Journal of Engineering and Technology, (*02):12, 13-18.

Fu, C. C., & Wang, S. (2014). Computational Analysis and Design of Bridge Structures. CRC Press/Spon Press.

McConnell, J., Chajes, M., Michaud, K. (2015). "Field Testing of a Decommissioned Skewed Steel I–Girder bridge: Analysis of System Effects". *Journal of Structural Engineering*, 141.1 D4014010.

McConnell, J., Radovic, M., Ambrose, K. (2014) “Cross-Frame Forces in Skewed Steel I-Girder Bridges: Field Measurements and Finite Element Analysis”. *Final Report to Delaware Department of Transportation,* University of Delaware Center for Bridge Engineering.

Ross, J. H. (2007). “Evaluating Ultimate Bridge Capacity Through Destructive Testing of Decommissioned Bridges”. *Master Thesis,* University of Delaware.

Radovic, M., McConnell, J. (2014). “Evaluation of Cross-frame Designs for Highly Skewed Steel I-Girder Bridges”. *Proceedings of 48th International Bridge Conference,* Pittsburg. IBC-14-47.

Rajagopalan, N. (2006). “Bridge Superstructure”. Alpha International, Oxford.

Skillicorn, D. (2007). “Understanding Complex Datasets: Data Mining with Matrix Decompositions”. *CRC Data Mining and Knowledge Discovery Series*, Chapman & Hall/ ISBN 978-1-58488-832-1.

Quinn, P. (2005). “Understanding Steel Bridge Behavior through Destructive Testing”. *Master’s Thesis*, University of Delaware, Newark, DE.

Van, V. L. H. (1970). “Materials science for engineers”. Reading, Mass: Addison-Wesley Pub. Co.

Chapter 5

MULTIWAY ANALYSIS

In order to investigate the effect of removing cross-frames on the stress distribution of steel I-girder bridges, investigative tools allowing deeper insight into bridge system behavior can be used, as such behavior cannot be fully understood using traditionally employed data analysis, as presented in Chapter 4 results. The results presented in Chapter 4 also showed that analyzing complex data can be very challenging if discrete level of analysis is used, especially if discovering the trends across data is the one of the goals of the analysis.

Therefore, the aim of this chapter is to use multiway analysis tools to investigate the difference in stress distributions between No-frame models and cross-frame models at five bridge skews (0°, 25°, 46°, 55°, and 63°) and under three load levels (design, first yield, and system yield). Multiway analysis is a mathematical exploratory tool for obtaining information about complex systems. Multiway data analysis describes a special set of mathematical methods used to interpret highly inter-correlated, multidimensional, and complex data sets. The special case of multiway analysis called tensor decomposition was used to analyze the dataset in question.

The following is the organization of the Chapter 5. The chapter starts with identifying the problem statement in Section 5.1. This is followed by a discussion of tensor decomposition methods in Section 5.2, beginning with an introduction to basic tensor operations in Section 5.2.1. The mathematical basis for tensor decomposition is explained by introducing singular value decomposition (SVD) method and principal component analysis (PCA) in Section 5.2.2. This is followed by detailed explanation of

Tucker decomposition method used in this work in Section 5.2.3. Tensor decomposition applications and corresponding literature review is covered in Section 5.3, while tensor decomposition of finite element analysis data is covered in Section 5.4. Finally, Section 5.5 offers concluding comments on this work.

5.1 Problem Statement

The goal of this work is to explore the effect that cross-frame removal in steel I-girder highway bridges has on stress distributions at different load levels due to different cross-frame designs and bridge skews using Tucker tensor decomposition.

5.2 Tensor Decomposition Methods

The purpose of this section is to introduce readers to tensor notation, the basic structure of tensor operations, and tensor results interpretation. Furthermore, this section also covers in detail procedures behind the matrix decomposition methods of singular value decomposition (SVD) and principal component analysis (PCA). Mathematically speaking, tensor decompositions such as Tucker tensor decomposition can be seen as the extension of matrix decompositions on higher dimensional data sets. Therefore, the reader should be familiar with SVD and PCA algorithms. Additionally, since SVD and PCA algorithms work on two dimensional datasets, they are intuitively easier to comprehend when compared to higher dimensional datasets.

5.2.1 Basic Tensor Operations

This sub-section introduces the reader to tensor notation, tensor data structure and basic tensor operations. In most of the cases, tensor operations are extension of matrix algebra on three or more dimensional datasets. Therefore, the reader should be familiar with matrix algebra operations such as matrix multiplication methods, finding determinants and ranks of matrices, and calculating eigenvalues and eigenvectors.

Detailed explanation and worked out examples of these operations are covered by Gentle (1997).

5.2.1.1 Notations and Organization

All data can be mathematically presented as set of scalars, vectors, and matrices. A scalar is represented as data point, and this data configuration is known as a zero-order tensor, tensor being the generic term for a data array. If data are arranged in one-directional vector form (such as a one-dimensional time series) they are referred to as a 1st-order tensor; if presented in matrix form having data along two directions (rows and columns), then this configuration is called 2nd-order tensor. Data sets having dimensions greater than two (Table 5.1) are referred to as higher-order tensors, or n-dimensional tensors (N-way arrays). Table 5.1 conveys the scalar, vector, matrix, and tensor hierarchy and associated notation while Table 5.2 defines notations commonly used throughout this chapter.

Table 5.1 Tensor notations

Number of ways	Name	Notation
Zero	Scalar	x
One	Vector	$\boldsymbol{x} \in \mathbb{R}^{\boldsymbol{I}}$
Two	Matrix	$\boldsymbol{X} \in \mathbb{R}^{\boldsymbol{I \times J}}$
Three	3-way tensor	$\boldsymbol{\mathcal{X}} \in \mathbb{R}^{\boldsymbol{I \times J \times K}}$
N-way	N-way tensor	$\boldsymbol{\mathcal{X}} \in \mathbb{R}^{\boldsymbol{I \times K \times \ldots \times N}}$

Table 5.2 Alternative tensor notations and operations

N-way tensor alternative notation	$\boldsymbol{\mathcal{X}} \in \mathbb{R}^{\boldsymbol{I_1 \times I_2 \times \ldots \times I_n}}$
Tensor represented as a sum of element products	$[X]_{i \times j \times k} = \sum_{p=1}^{P} \sum_{q=1}^{Q} \sum_{r=1}^{R} g_{pqr} a_p \circ b_q \circ c_r + e_{ijk}$

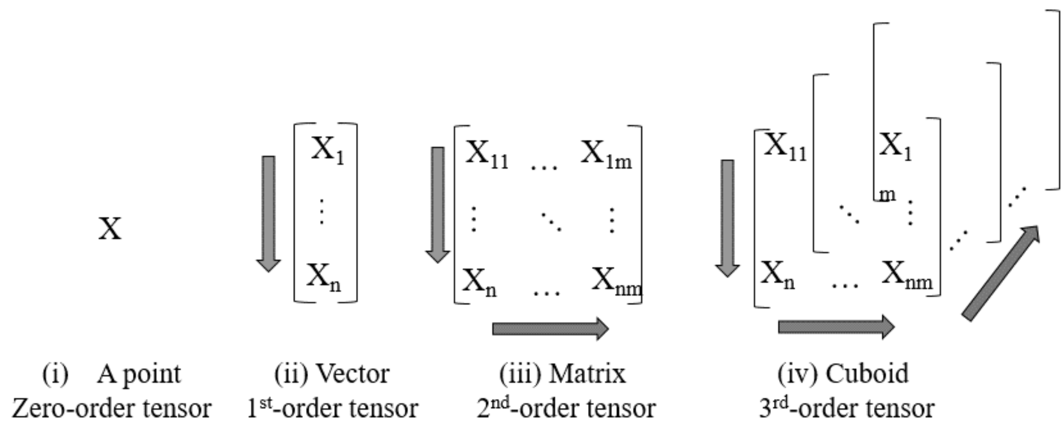

Figure 5.1 Representation of data using tensors. While graphical representation of the datasets using tensors can be visualized in three dimensions, mathematically speaking there can be unlimited numbers of tensor dimensions.

Conventional data analysis such as analysis of variance (ANOVA), multiple regression analysis, or multiple analysis of covariance (MANCOVA) deals with analyzing data in the two-way form, which is the form of two dimensional matrixes. However, the addition of a third mode will result in the data being in the form of a data cuboid, which is a typical example of a higher-order data set. For example, consider a higher order data set that consists of stress values along the length of a structural system such as bridge. If we assume that the bridge consists of five girders, we could organize the data in such a way that Mode 1 in the data matrix will be represented by five girders and Mode 2 will be represented by the distances along the length of the girder. Typically, Mode 1 data is organized as the row variable and Mode 2 data is organized as the column variable. The data inside the matrix would consist of stresses in each girder at each distance along the length of the girder. If behavior under increasing magnitudes of load is of interest, then a third mode could consist of load magnitudes (usually the third mode is called a "tube" in 3-D array).

In models with increasing complexity, additional modes can be added. For example, the influence of temperature fluctuations on the bridge member's stresses, during incremental loading, could serve as a 4th mode in the present example. Depending of the complexity of the problem, as many modes as needed can be added.

One of the multiway analysis tools used to investigate multi-dimensional datasets is tensor decomposition. Tensor decomposition, a data analysis method, was used in discovering latent structures in higher-order data sets (Comon, et al. 2008; Acar, et al. 2008). Higher-order data sets are data sets with more than two dimensions.

5.2.1.2 Tensor Subarrays

This subsection describes the basic tensor structure and nomenclature. Any tensor can be divided into subsets called subarrays which are subsets of rows and/or columns. As matrix operations are conducted using rows and columns, consequently tensor operations are conducted using subarrays. To explain how tensor subarrays are formed, the example of a three-way tensor is considered. In a three-way tensor, if one index is kept fixed, it forms subarrays called slices (Figure 5.2); while if two tensor indices are kept fixed, then subarrays called fibers are formed (Figure 5.3).

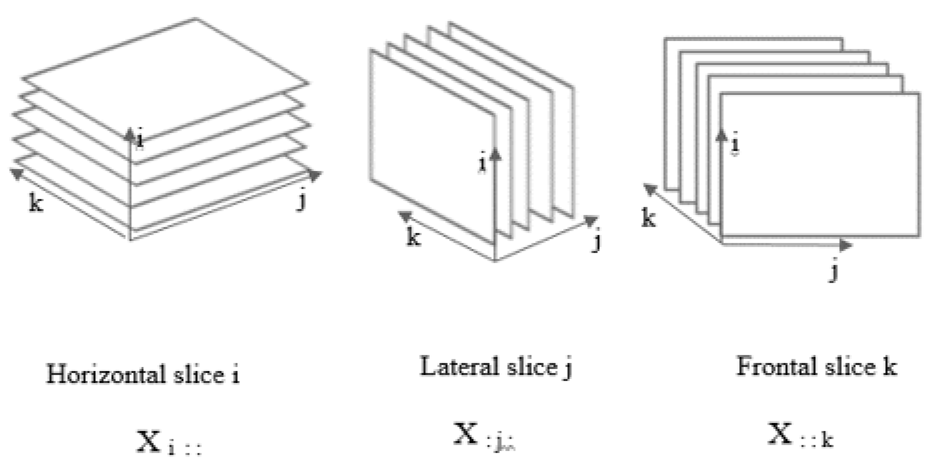

Figure 5.2 Slices of three-way tensor show how data from the three-dimensional dataset can be partitioned to form two dimensional matrices.

There are three slices in three-way tensor, horizontal, frontal and lateral (Figure 5.2). For a three-way tensor of dimensions $I \times J \times K$, horizontal, frontal and lateral slices are denoted by $\boldsymbol{X}_{i::}$, $\boldsymbol{X}_{:j:}$ and $\boldsymbol{X}_{::k}$ respectively. Horizontal slice is formed when tensor index $\boldsymbol{i}$ is kept fixed, then data are organized in two-dimensional subarray (matrix) with the size of the array being [k, j]. A frontal slice is formed when tensor index $\boldsymbol{k}$ is kept fixed, then data are organized in a matrix form with [i, j] dimensions. A lateral slice is formed when tensor index $\boldsymbol{j}$ kept fixed, then data are organized in matrix form [i, k]. In three-way tensors, fibers are created when two of the tensor indices are fixed, while the remaining index is not (Figure 5.3).

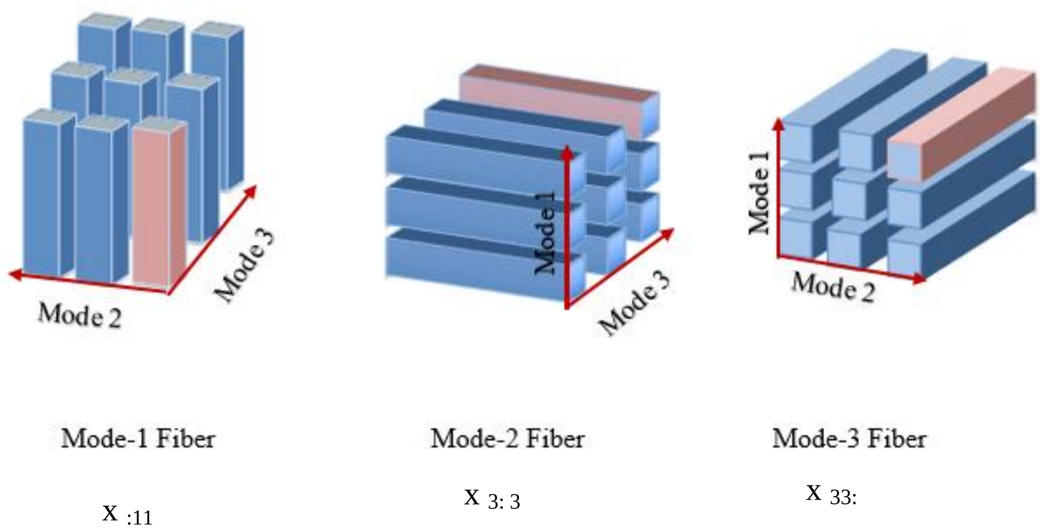

Figure 5.3 Graphical representation of fibers in three-way tensor. The highlighted (lighter colored) tubes are selected fibers. Each fiber has a subscripts reference that describes where the fiber is in the tensor. Origin of the matrix is at the location where arrows intersect.

For a three-way tensor, fibers are analogous to vectors in a matrix. Mode 1, 2, and 3 fibers are labeled as $\boldsymbol{x}_{:jk}, \boldsymbol{x}_{i:k}$ and $\boldsymbol{x}_{ij:}$, respectively, with the variable index representing the mode. For example, assume that we have 3 bridges (labeled B1, B2 and

B3 organized in Mode 1), and that maximum thermal stress is measured at 3 locations (labeled L1, L2 and L3 organized in Mode 2), during 5-year period (labeled Y1-Y5 organized in Mode 3). Then Mode 3 $\mathcal{X}_{13:}$ fiber consist of thermal stress data from the bridge B1 at location L3 during five years period (the fiber data presented in vector form is [B1 L3 Y1, B1 L3 Y2, B1 L3 Y3, B1 L3 Y4 and B1 L3 Y5]).

5.2.1.3 Tensor Unfolding – Matricization

Tensor unfolding is a procedure in which tensors are presented in matrix form. This is a fairly simple procedure which involves organizing tensor's modes as rows and columns. Figure 5.4 shows a tensor $\boldsymbol{\mathcal{X}} \in \mathbb{R}^{\mathbf{2\times2\times2}}$ with matricizations along the k mode. The resulting matrix $\boldsymbol{X}_{(i)}$, is shown in Equation 5.1.

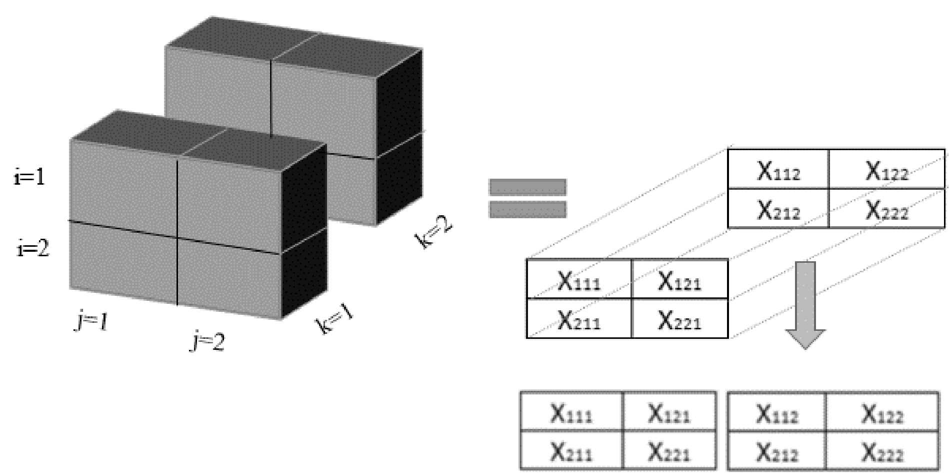

Figure 5.4 Figure on the right represents a 2x2x2 three-way tensor. Figure on the left shows unfolding the tensor along k mode, and becoming 2x4 matrix, shown in Equation 5.1

$$\boldsymbol{X}_{(i)} = \begin{bmatrix} x_{111} & x_{121} & x_{112} & x_{122} \\ x_{211} & x_{221} & x_{212} & x_{222} \end{bmatrix} \tag{5.1}$$

5.2.1.4 Tensor Inner Product

The tensor inner product (Equation 5.2) corresponds to a dot product in vector space. If two tensors have equal dimensions (number of modes) and size (number of entries per mode), then the tensor inner product is the sum of the products of corresponding modes. The inner product of two tensors $\boldsymbol{\mathcal{X}} \in \mathbb{R}^{\boldsymbol{I_1} \times \boldsymbol{I_2} \times \ldots \times \boldsymbol{I_n}}$ and $\boldsymbol{\mathcal{Y}} \in \mathbb{R}^{\boldsymbol{I_1} \times \boldsymbol{I_2} \times \ldots \times \boldsymbol{I_n}}$ is defined as

$$\langle \mathcal{X}, \mathcal{Y} \rangle = \sqrt{\sum_{i_1=1}^{I_1} \ldots \sum_{i_n=1}^{I_n} x_{I_1 \ldots \ldots I_n} y_{I_1 \ldots I_n}} \tag{5.2}$$

More details on tensor inner products can be found at Kroonenberg (2008).

5.2.1.5 Scalar Multiplication

For a tensor $\boldsymbol{\mathcal{X}} \in \mathbb{R}^{I \times J \times K}$ and a scalar ρ, scalar multiplication (Equation 5.3) of the tensor is simply defined as

$$\rho \boldsymbol{\mathcal{X}} = \boldsymbol{\mathcal{Y}} \tag{5.3}$$

where $y_{ijk} = \rho x_{ijk}$.

5.2.1.6 Kronecker Product

The Kronecker product (Equation 5.4) is another type of matrix product that can be used to decompose tensors in matrix form. The Kronecker product of two tensors $\boldsymbol{X} \in \mathbb{R}^{I \times J}$ and $\boldsymbol{Y} \in \mathbb{R}^{K \times L}$ is defined as:

$$\boldsymbol{X} \otimes \boldsymbol{Y} = \boldsymbol{Z} \tag{5.4}$$

where $\boldsymbol{Z} \in \mathbb{R}^{IK \times JL}$

$$\boldsymbol{X} \otimes \boldsymbol{Y} = \begin{bmatrix} x_{11}Y & \cdot & \cdot & x_{1j}Y \\ \cdot & & & \cdot \\ \cdot & & & \cdot \\ x_{i1}Y & \cdot & \cdot & x_{ij}Y \end{bmatrix} \tag{5.5}$$

For example, let $\boldsymbol{X} = \begin{bmatrix} 1 & 2 \\ 3 & 4 \end{bmatrix}$ and $\boldsymbol{Y} = \begin{bmatrix} 5 & 6 \\ 7 & 8 \end{bmatrix}$ then

$$\boldsymbol{Z} = \boldsymbol{X} \otimes \boldsymbol{Y} == \begin{bmatrix} 1 \cdot 5 & 1 \cdot 6 & 2 \cdot 5 & 2 \cdot 6 \\ 1 \cdot 7 & 1 \cdot 8 & 2 \cdot 7 & 2 \cdot 8 \\ 3 \cdot 5 & 3 \cdot 6 & 4 \cdot 5 & 4 \cdot 6 \\ 3 \cdot 7 & 3 \cdot 8 & 4 \cdot 7 & 4 \cdot 8 \end{bmatrix} = \begin{bmatrix} 5 & 6 & 10 & 12 \\ 7 & 8 & 14 & 16 \\ 15 & 18 & 20 & 24 \\ 21 & 24 & 28 & 32 \end{bmatrix}$$

5.2.1.7 Khatri-Rao Product

The Khatri-Rao product (Equation 5.6) is another matrix product frequently used to decompose tensors in matrix form. The Khatri-Rao product between two tensors $\boldsymbol{X} \in \mathbb{R}^{I \times J}$ and $\boldsymbol{Y} \in \mathbb{R}^{K \times J}$ is defined as:

$$\boldsymbol{X} \odot \boldsymbol{Y} = \boldsymbol{Z} \tag{5.6}$$

where $\boldsymbol{Z} \in \mathbb{R}^{IK \times J}$

For example, let $\boldsymbol{X} = \begin{bmatrix} 1 & 2 \\ 3 & 4 \end{bmatrix}$ and $\boldsymbol{Y} = \begin{bmatrix} 5 & 6 \\ 7 & 8 \end{bmatrix}$ then

$$\boldsymbol{Z} = \boldsymbol{X} \odot \boldsymbol{Y} = \begin{bmatrix} 1 \cdot 5 & 2 \cdot 6 \\ 1 \cdot 7 & 2 \cdot 8 \\ 3 \cdot 5 & 4 \cdot 6 \\ 3 \cdot 7 & 4 \cdot 8 \end{bmatrix} = \begin{bmatrix} 5 & 12 \\ 7 & 16 \\ 15 & 24 \\ 21 & 32 \end{bmatrix}$$

5.2.1.8 Matrix rank and Tensor rank

Matrix rank refers to the maximum number of linearly independent vectors (rows) in a matrix. Tensor rank is defined as sum of “rank-1 tensors”. A rank-1 tensor is a tensor for which the elements can be defined as

$$x_{ijkl}=a_i\, b_j\, c_k\, d_l \tag{5.7}$$

The rank of the tensor is the smallest number of rank-1 tensors "sufficient to fully decompose the tensor additively" (Kiers, 2000).

5.2.2 Matrix Decompositions

Mathematically speaking a tensor decomposition is simply expressing a higher dimensional data structure as a product of a new set of matrices, also known as factor matrices. The motivation for this is to present a higher order data set into visually simplistic matrix form, revealing valuable information hidden or obscured by the complexity of the original dataset. There are many ways to factor, or decompose, the tensor by using different tensor operations. All these methods use different matrix products that are equivalent to each other (Bader and el. 2008). Furthermore, many concepts and methods used in the matrix decomposition algorithms are used in higher order tensor decomposition algorithms too. Therefore, it is beneficial to briefly familiarize the reader with matrix decomposition methods before moving to more complex tensor decomposition methods.

There are two main matrix decomposition methods that are going to be reviewed in this section.

a) Singular Value Decomposition (SVD)

b) Principal Component Analysis (PCA)

5.2.2.1 Singular Value Decomposition (SVD)

Singular value decomposition (SVD) is one of the most used matrix decomposition methods and can be introduced as a mathematical foundation for all tensor decomposition algorithms. The main advantage of SVD is that it is a powerful dimension reduction tool. Using SVD, a matrix of any size can be reduced to a desired number of dimensions. The resulting new matrix is an approximation of the original matrix, but it still carries a significant amount of the information contained in the original matrix. There is a reciprocal trade-off in terms of accuracy and dimension reduction. If the new matrix is desired to be a very close approximation of the original matrix, the dimension reduction will be very small. Conversely, reducing too many dimensions will render a very low level of approximation. The best approach is to have a new data set that will produce a fairly accurate approximation of the original data set while keeping a relatively small number of dimensions from the original dataset.

For example, let's say there are n=100 bridges in a certain region that need to be analyzed. And let's say that condition of R=20 structurally essential components that describe each bridge, such as web, bottom flange, and parapet were rated. In this case, R represents a unique vector of bridge components. So, data vector space is the matrix of the size n x R (or, 100x20). It is more likely that some bridge components contribute more to overall condition of the bridge than others. Therefore, we should try to find 5 or 6 bridge structural components that best describe overall condition of all 100 bridges, rather than dealing with all 20 components.

SVD is illustrated via numerical example (Table 5.3). Let say that there are 7 bridges with 5 components that describe the condition of the bridges such as: deck rating, super-structure rating, sub-structure rating, averaged daily truck (ADT), and average daily truck traffic (ADTT). The goal is to determine if the number of components describing the bridge condition can be reduced by reducing the dimension of the matrix while still maintaining a high level of accuracy in describing the bridge.

Table 5.3 SDV Numerical Example- Bridge Matrix A

	Deck Rating	Super-structure Rating	Sub-structure Rating	ADT (1000s)	ADTT (1000s)
Bridge 1	6	6	6	5.2	0.33
Bridge 2	8	8	8	5.7	0.37
Bridge 3	9	9	9	5.1	0.31
Bridge 4	8	9	8	5	0.3
Bridge 5	5	7	5	9.37	0.81
Bridge 6	5	5	5	9.01	0.88
Bridge 7	5	6	5	7.3	0.6

To accomplish this goal, the data from the Table 5.1 is written in the form of matrix $\boldsymbol{A}$, which can be decomposed into P, Δ snd Q matrices using singular value decomposition via the following steps **(**Green, 2014).

1. From the matrix $\boldsymbol{A}$, such that $\boldsymbol{A} \in \mathbb{R}^{7\times5}$, compute matrix product of matrix $\boldsymbol{A}$ and $\boldsymbol{A}^T$, i.e., $\boldsymbol{AA}^T$and $\boldsymbol{A}^T\boldsymbol{A}$.

2. Find eigenvalues by solving vector equation, in form of matrix product A and A^T. $\boldsymbol{AA}^T$x =λx. Find the solution for x and λ using characteristic equation$|\lambda I - \boldsymbol{AA}^T| = 0$, where I is identity matrix and solution λ are eigenvalues.

3. Calculate the square root of the eigenvalues calculated in previous step. The larger an eigenvalue is, the larger the contribution is of that component to the variation in the dataset. In other words, if this component is removed from the dataset, a large amount of information will be lost. Conversely, the smaller an eigenvalue is, the smaller the contribution to the dataset; thus, if this component is removed from the data set, a small amount of information is lost. The square root of the eigenvalues of the matrix $\boldsymbol{AA}^T$are the singular values (nonzero diagonal entries) in the matrix $\boldsymbol{\Delta}$, which are placed in descending order along the diagonal of $\boldsymbol{\Delta}$.

4. Calculate the orthonormal set of eigenvectors for $\boldsymbol{A}^T\boldsymbol{A}$. The eigenvectors are the directions along which a linear transformation occurs. The resultant eigenvectors are the columns of the right singular matrix $\boldsymbol{Q}$. Transpose $\boldsymbol{Q}^{\boldsymbol{T}}$.
5. Calculate the left singular matrix $\boldsymbol{P}$, from $\boldsymbol{A}$, $\boldsymbol{\Delta}$ and $\boldsymbol{Q}$, such that $\boldsymbol{P}= \boldsymbol{A}$ $\boldsymbol{Q}\,\boldsymbol{\Delta}^{-\mathbf{1}}$.
6. Check the results by multiplying $\boldsymbol{A} = \boldsymbol{P\Delta Q}^T$

Applying SVD algorithm on matrix $\boldsymbol{A} \in \mathbb{R}^{I\times J}$, we factorized matrix A into a set of matrices P, $\boldsymbol{\Delta}$, and $\boldsymbol{Q}$ such that

$$\boldsymbol{A} = \boldsymbol{P\Delta Q}^T \tag{5.8}$$

where,

$\boldsymbol{A} \in \mathbb{R}^{I\times J}$ is original data matrix with dimensions $I \times J$;

$\boldsymbol{P} \in \mathbb{R}^{I\times I}$ is a matrix of eigenvectors of symmetric $\mathbf{AA^T}$ of order $I \times I$;

$\boldsymbol{Q}^T \in \mathbb{R}^{J\times J}$ is a matrix of eigenvectors of symmetric $\mathbf{A^T A}$ of order $J \times J$;

The columns of $\boldsymbol{P}$ and $\boldsymbol{Q}$ are called the left and right singular vectors of $\boldsymbol{A}$;

$\boldsymbol{\Delta} \in \mathbb{R}^{I\times J}$ is a diagonal matrix of nonzero diagonal entries;

The number of nonzero diagonal entries (also called singular values) in $\boldsymbol{\Delta}$ represents the rank (r) of the matrix $\boldsymbol{A}$. The rank of the matrix $\boldsymbol{A}$ is also the largest number of rows or columns that are linearly independent (r($\mathbf{A}$) ≤ min (I, J)). There are two important features of the SVD; the first is that the columns of $\boldsymbol{P}$ and $\boldsymbol{Q}$ are orthonormal eigenvectors derived from the matrix **A** and the second is that the values in the diagonal matrix $\boldsymbol{\Delta}$ are square roots of eigenvalues of the matrix $\mathbf{AA^T}$. $\boldsymbol{\Delta}$ matrix represents the amount of variance retained by the columns in P matrix.

Continuing with the previous example, by executing SVD algorithm on the dataset A (Table 5.1), dataset A is represented by seven bridges (rows), with each bridge having 3 condition ratings (columns 1-3) and 2 traffic counts (columns 4-5).

$$\boldsymbol{A} = \begin{bmatrix} 6 & 6 & 6 & 5.20 & 0.33 \\ 8 & 8 & 8 & 5.70 & 0.37 \\ 9 & 9 & 9 & 5.10 & 0.31 \\ 8 & 9 & 8 & 5.00 & 0.30 \\ 5 & 7 & 5 & 9.37 & 0.81 \\ 5 & 5 & 5 & 9.01 & 0.88 \\ 5 & 6 & 5 & 7.30 & 0.60 \end{bmatrix} \tag{5.9}$$

Transform matrix A into $\boldsymbol{A^T}$, matrix products $\boldsymbol{AA^T}$ and $\boldsymbol{A^TA}$.

$$\boldsymbol{A^T} = \begin{bmatrix} 6 & 8 & 9 & 8 & 5 & 5 & 5 \\ 6 & 8 & 9 & 9 & 7 & 5 & 6 \\ 6 & 9 & 9 & 8 & 5 & 5 & 5 \\ 5.2 & 5.7 & 5.1 & 5 & 9.37 & 9.01 & 7.3 \\ 0.33 & 0.37 & 0.31 & 0.3 & 0.81 & 0.88 & 0.60 \end{bmatrix} \tag{5.10}$$

Then multiply A and $\boldsymbol{A^T}$ to get $\boldsymbol{AA^T}$.

$$\begin{bmatrix} 6 & 6 & 6 & 5.20 & 0.33 \\ 8 & 8 & 8 & 5.70 & 0.37 \\ 9 & 9 & 9 & 5.10 & 0.31 \\ 8 & 9 & 8 & 5.00 & 0.30 \\ 5 & 7 & 5 & 9.37 & 0.81 \\ 5 & 5 & 5 & 9.01 & 0.88 \\ 5 & 6 & 5 & 7.30 & 0.60 \end{bmatrix} x \begin{bmatrix} 6 & 8 & 9 & 8 & 5 & 5 & 5 \\ 6 & 8 & 9 & 9 & 7 & 5 & 6 \\ 6 & 9 & 9 & 8 & 5 & 5 & 5 \\ 5.2 & 5.7 & 5.1 & 5 & 9.37 & 9.01 & 7.3 \\ 0.33 & 0.37 & 0.31 & 0.3 & 0.81 & 0.88 & 0.60 \end{bmatrix} = \begin{bmatrix} 135.1 & 173.8 & 188.6 & 176.1 & 151.0 & 137.7 & 134.2 \\ 173.8 & 224.6 & 245.2 & 228.6 & 189.7 & 171.7 & 169.8 \\ 188.6 & 245.2 & 269.1 & 250.6 & 201.0 & 181.2 & 181.4 \\ 176.1 & 228.6 & 250.6 & 234.1 & 191.1 & 170.3 & 170.7 \\ 151.0 & 189.7 & 201.0 & 190.1 & 187.5 & 170.1 & 160.9 \\ 137.1 & 171.7 & 181.2 & 170.3 & 170.1 & 157.0 & 146.3 \\ 134.2 & 169.8 & 181.4 & 170.7 & 160.9 & 146.3 & 139.7 \end{bmatrix} \tag{5.11}$$

Multiply $\boldsymbol{A^T}$ and A to get $\boldsymbol{A^TA}$.

$$\begin{bmatrix} 6 & 8 & 9 & 8 & 5 & 5 & 5 \\ 6 & 8 & 9 & 9 & 7 & 5 & 6 \\ 6 & 9 & 9 & 8 & 5 & 5 & 5 \\ 5.2 & 5.7 & 5.1 & 5 & 9.37 & 9.01 & 7.3 \\ 0.33 & 0.37 & 0.31 & 0.3 & 0.81 & 0.88 & 0.60 \end{bmatrix} x \begin{bmatrix} 6 & 6 & 6 & 5.20 & 0.33 \\ 8 & 8 & 8 & 5.70 & 0.37 \\ 9 & 9 & 9 & 5.10 & 0.31 \\ 8 & 9 & 8 & 5.00 & 0.30 \\ 5 & 7 & 5 & 9.37 & 0.81 \\ 5 & 5 & 5 & 9.01 & 0.88 \\ 5 & 6 & 5 & 7.30 & 0.60 \end{bmatrix} = \begin{bmatrix} 320 & 343 & 320 & 291.1 & 21.6 \\ 343 & 372 & 343 & 322.1 & 24.1 \\ 320 & 343 & 320 & 291.1 & 21.6 \\ 291.1 & 322.1 & 291.1 & 332.8 & 26.8 \\ 21.58 & 24.1 & 21.6 & 26.8 & 2.22 \end{bmatrix} \tag{5.12}$$

In this step calculate eigenvalues of $\boldsymbol{AA^T}$.

$$eigen\left[\begin{bmatrix} 135.1 & 173.8 & 188.6 & 176.1 & 151.0 & 137.7 & 134.2 \\ 173.8 & 224.6 & 245.2 & 228.6 & 189.7 & 171.7 & 169.8 \\ 188.6 & 245.2 & 269.1 & 250.6 & 201.0 & 181.2 & 181.4 \\ 176.1 & 228.6 & 250.6 & 234.1 & 191.1 & 170.3 & 170.7 \\ 151.0 & 189.7 & 201.0 & 190.1 & 187.5 & 170.1 & 160.9 \\ 137.1 & 171.7 & 181.2 & 170.3 & 170.1 & 157.0 & 146.3 \\ 134.2 & 169.8 & 181.4 & 170.7 & 160.9 & 146.3 & 139.7 \end{bmatrix}\right] = \begin{bmatrix} 1295.3 & & & \\ & 49.76 & & \\ & & 1.94 & \\ & & & 0.068 \end{bmatrix} \tag{5.13}$$

Take a square root of eigenvalues $\boldsymbol{AA^T} = \boldsymbol{\Delta}$.

$$\begin{bmatrix} \sqrt{1295.3} & & & \\ & \sqrt{49.76} & & \\ & & \sqrt{1.94} & \\ & & & \sqrt{0.068} \end{bmatrix} = \begin{bmatrix} 35.99 & & & \\ & 7.05 & & \\ & & 1.39 & \\ & & & 0.08 \end{bmatrix} \tag{5.13}$$

Calculate orthonormal set of eigenvectors for $\boldsymbol{A^T A} =\mathbf{Q}$.

$$\text{Q= eigenvector}\left[\begin{bmatrix} 320 & 343 & 320 & 291.1 & 21.6 \\ 343 & 372 & 343 & 322.1 & 24.1 \\ 320 & 343 & 320 & 291.1 & 21.6 \\ 291.1 & 322.1 & 291.1 & 332.8 & 26.8 \\ 21.58 & 24.1 & 21.6 & 26.8 & 2.22 \end{bmatrix}\right] = \begin{bmatrix} 0.49 & 0.32 & -0.39 & 0.00 & 0.71 \\ 0.53 & 0.18 & 0.82 & -0.03 & 0.00 \\ 0.49 & 0.32 & -0.39 & 0.00 & -0.71 \\ 0.48 & -0.86 & -0.11 & 0.11 & 0.00 \\ 0.04 & -0.10 & -0.04 & -0.99 & 0.00 \end{bmatrix} \tag{5.14}$$

Transpose Q to get $\mathbf{Q^T}$.

$$\begin{bmatrix} 0.49 & 0.32 & -0.39 & 0.00 & 0.71 \\ 0.53 & 0.18 & 0.82 & -0.03 & 0.00 \\ 0.49 & 0.32 & -0.39 & 0.00 & -0.71 \\ 0.48 & -0.86 & -0.11 & 0.11 & 0.00 \\ 0.04 & -0.10 & -0.04 & -0.99 & 0.00 \end{bmatrix}^T = \begin{bmatrix} 0.49 & 0.53 & 0.49 & 0.48 & 0.04 \\ 0.32 & 0.18 & 0.32 & -0.86 & -0.1 \\ -0.39 & 0.82 & -0.39 & -0.11 & -0.04 \\ 0 & -0.03 & 0 & 0.11 & -0.99 \\ 0.71 & 0 & -0.71 & 0 & 0 \end{bmatrix} \tag{5.15}$$

Inverse $\boldsymbol{\Delta}$ to get $\boldsymbol{\Delta^{-1}}$.

$$\begin{bmatrix} 35.99 & & & \\ & 7.05 & & \\ & & 1.39 & \\ & & & 0.08 \end{bmatrix}^{-1} = \begin{bmatrix} 0.027 & & & \\ & 0.141 & & \\ & & 0.719 & \\ & & & 12.5 \end{bmatrix} \tag{5.16}$$

In final step compute P, $\boldsymbol{A\ Q\ \Delta^{-1}} = \boldsymbol{P}$

$\boldsymbol{A}$ $\quad$ $\boldsymbol{Q}$ $\quad$ $\boldsymbol{\Delta^{-1}}$ $\quad$ $\boldsymbol{P}$

$$\begin{bmatrix} 6 & 6 & 6 & 5.20 & 0.33 \\ 8 & 8 & 8 & 5.70 & 0.37 \\ 9 & 9 & 9 & 5.10 & 0.31 \\ 8 & 9 & 8 & 5.00 & 0.30 \\ 5 & 7 & 5 & 9.37 & 0.81 \\ 5 & 5 & 5 & 9.01 & 0.88 \\ 5 & 6 & 5 & 7.30 & 0.60 \end{bmatrix} \begin{bmatrix} 0.49 & 0.32 & -0.39 & 0.00 & 0.71 \\ 0.53 & 0.18 & 0.82 & -0.03 & 0.00 \\ 0.49 & 0.32 & -0.39 & 0.00 & -0.71 \\ 0.48 & -0.86 & -0.11 & 0.11 & 0.00 \\ 0.04 & -0.10 & -0.04 & -0.99 & 0.00 \end{bmatrix} \begin{bmatrix} 0.027 & & & & \\ & 0.141 & & & \\ & & 0.719 & & \\ & & & 12.5 & \\ & & & & 0 \end{bmatrix} = \begin{bmatrix} -0.32 & -0.64 & 0.24 & 0.75 \\ -0.41 & -0.23 & 0.22 & 0.18 \\ -0.44 & -0.43 & 0.14 & -0.27 \\ -0.44 & -0.35 & -0.42 & -0.33 \\ -0.36 & 0.51 & -0.56 & 0.04 \\ -0.33 & 0.52 & 0.59 & -0.45 \\ -0.32 & 0.28 & -0.14 & 0.24 \end{bmatrix}$$

$$(5.17)$$

Multiply matrix P with $\boldsymbol{\Delta}$ and $\mathbf{Q^T}$ matrices to get matrix that should have the same entries as matrix A. This operation is conducted to make sure that no errors were made during decompositions.

$$\underset{\boldsymbol{A}}{\begin{bmatrix} 6 & 6 & 6 & 5.20 & 0.33 \\ 8 & 8 & 8 & 5.70 & 0.37 \\ 9 & 9 & 9 & 5.10 & 0.31 \\ 8 & 9 & 8 & 5.00 & 0.30 \\ 5 & 7 & 5 & 9.37 & 0.81 \\ 5 & 5 & 5 & 9.01 & 0.88 \\ 5 & 6 & 5 & 7.30 & 0.60 \end{bmatrix}} = \underset{\boldsymbol{P}}{\begin{bmatrix} -0.32 & -0.64 & 0.24 & 0.75 \\ -0.41 & -0.23 & 0.22 & 0.18 \\ -0.44 & -0.43 & 0.14 & -0.27 \\ -0.44 & -0.35 & -0.42 & -0.33 \\ -0.36 & 0.51 & -0.56 & 0.04 \\ -0.33 & 0.52 & 0.59 & -0.45 \\ -0.32 & 0.28 & -0.14 & 0.24 \end{bmatrix}} \underset{\boldsymbol{\Delta}}{\begin{bmatrix} 35.99 & & & \\ & 7.05 & & \\ & & 1.39 & \\ & & & 0.08 \\ & & & \end{bmatrix}} \underset{\mathbf{Q^T}}{\begin{bmatrix} 0.49 & 0.53 & 0.49 & 0.48 & 0.40 \\ 0.32 & 0.18 & 0.32 & -0.86 & -0.1 \\ -0.39 & 0.82 & -0.39 & -0.11 & -0.04 \\ 0 & -0.03 & 0 & 0.11 & -0.99 \\ 0.71 & 0 & -0.71 & 0 & 0 \end{bmatrix}} \tag{5.18}$$

Furthermore, to numerically evaluate how much importance each column (component) we square each singular value from the diagonal matrix Δ and divide it with the sum of the squares of the entries in the diagonal matrix Δ. This number is the measure of how much information is contained in the dataset if one or more dimensions (columns and rows in P and Q matrices) were removed. For example, summation of all squared singular values 35.992+7.052 +1.392+0.082=1346. It is easy to notice that the first and second entry have significantly more importance than any other entry and account for the 99.8% of the variance in the dataset. ($\frac{35.99^2+7.05^2}{1346} = 0.998$). This means that two columns and rows could be removed from the diagonal matrix without compromising the original dataset, because the new data set is 99.8% similar to the original dataset, but could be represented with two less dimensions (components). In this way the data space can be effectively reduced from four dimensions to only two. Furthermore, keeping only one entry from the diagonal matrix, 96% of the variance contained in original dataset is retained ($\frac{35.99^2}{1346} = 0.96$).

To reduced number of dimensions to two (n=2) delete two last columns form the matrix P, two lowest entries from the matrix **Δ** and delete two last rows and two last columns from the matrix $\mathbf{Q^T}$.

$$\begin{array}{ccc} \boldsymbol{P} & \boldsymbol{\Delta} & \mathbf{Q^T} \\ \begin{bmatrix} -0.32 & -0.64 & 0.24 & 0.75 \\ -0.41 & -0.23 & 0.22 & 0.18 \\ -0.44 & -0.43 & 0.14 & -0.27 \\ -0.44 & -0.35 & -0.42 & -0.33 \\ -0.36 & 0.51 & -0.56 & 0.04 \\ -0.33 & 0.52 & 0.59 & -0.45 \\ -0.32 & 0.28 & -0.14 & 0.24 \end{bmatrix} & \begin{bmatrix} 35.99 & & & \\ & 7.05 & & \\ & & 1.39 & \\ & & & 0.08 \end{bmatrix} & \begin{bmatrix} 0.49 & 0.53 & 0.49 & 0.48 & 0.40 \\ 0.32 & 0.18 & 0.32 & -0.86 & -0.1 \\ -0.39 & 0.82 & -0.39 & -0.11 & -0.04 \\ 0 & -0.03 & 0 & 0.11 & -0.99 \\ 0.71 & 0 & -0.71 & 0 & 0 \end{bmatrix} \end{array} \tag{5.19}$$

and then multiply newly created matrices $\boldsymbol{P^*}$, $\boldsymbol{\Delta^*}$, $\mathbf{Q^{T*}}$ to get new matrix $\boldsymbol{A}^*$.

$$\begin{array}{ccccc} \boldsymbol{P^*} & \boldsymbol{\Delta^*} & \mathbf{Q^{T*}} & = & \boldsymbol{A}^* \\ \begin{bmatrix} -0.32 & -0.64 \\ -0.41 & -0.23 \\ -0.44 & -0.43 \\ -0.44 & -0.35 \\ -0.36 & 0.51 \\ -0.33 & 0.52 \\ -0.32 & 0.28 \end{bmatrix} & \begin{bmatrix} 35.99 & \\ & 7.05 \end{bmatrix} & \begin{bmatrix} 0.49 & 0.53 & 0.49 & 0.48 & 0.04 \\ 0.32 & 0.18 & 0.32 & -0.86 & -0.1 \end{bmatrix} & = & \begin{bmatrix} 5.81 & 6.22 & 5.81 & 5.13 & 0.37 \\ 7.81 & 8.18 & 7.81 & 5.58 & 0.36 \\ 8.96 & 9.20 & 8.96 & 5.11 & 0.28 \\ 8.25 & 8.52 & 8.25 & 5.08 & 0.30 \\ 5.37 & 6.43 & 5.37 & 9.53 & 0.85 \\ 4.64 & 5.64 & 4.64 & 8.90 & 0.80 \\ 5.01 & 5.76 & 5.01 & 7.26 & 0.62 \end{bmatrix} \end{array} \tag{5.20}$$

Newly create matrix $\boldsymbol{A}^*$ retained 99.8% of information of the original matrix A**.**

Similarly if further reduction is needed (n=1), then delete three last columns form the matrix P, three lowest entries from the matrix **Δ** and delete there last rows and three last columns from the matrix $\mathbf{Q^T}$ to get $\boldsymbol{A}^{**}$. Newly created matrix A ** retained is 96% similar to the original matrix A.

$$\underset{\boldsymbol{P}^{**}}{\begin{bmatrix}-0.32\\-0.41\\-0.44\\-0.44\\-0.36\\-0.33\\-0.32\end{bmatrix}} \quad \underset{\boldsymbol{\Delta}^{**}}{[35.99]} \quad \underset{\mathbf{Q}^{\mathbf{T}**}}{[0.49 \quad 0.53 \quad 0.49 \quad 0.48 \quad 0.04]} \overset{=}{=} \underset{\boldsymbol{A}^{**}}{\begin{bmatrix}5.72 & 6.19 & 5.72 & 5.54 & 0.42\\7.33 & 7.94 & 7.33 & 7.11 & 0.54\\7.94 & 8.60 & 7.94 & 7.70 & 0.58\\7.43 & 8.05 & 7.43 & 7.20 & 0.54\\6.48 & 7.02 & 6.48 & 6.29 & 0.47\\5.87 & 6.36 & 5.87 & 5.69 & 0.43\\5.73 & 6.21 & 5.73 & 5.56 & 0.42\end{bmatrix}} \quad (5.21)$$

5.2.2.2 Principal Component Analysis (PCA)

Principal component analysis (PCA) is mathematical tool used to reduce complex data sets to lower dimensions in order to uncover a simplified structure underneath. In many experimental settings, one or more outcomes are measured in an effort to understand some phenomena. However, if the data is inter-correlated, redundant, or deceptive, it becomes very hard to observe patterns in the phenomenon. To solve this problem, a tool able to "untangle" complex data is needed so it is clearer to understand which components in the data set are independent and which are dependent.

PCA uses matrix decomposition method by transforming a correlated multivariate data set into a set of uncorrelated components that are linear combinations of the original variables in the data (Fernandez, 2014). It is important to note that SVD can be used to compute PCA. For example, PCA can be computed by using a SVD algorithm if columns in the matrix are divided by the Z-score (a measure of standard deviation in the data set, described below). However, PCA is usually computed by algorithm that uses eigen-decomposition of the covariance matrix, where covariance matrix is a matrix that measures variability and spread of the components in the dataset. Eigen-decomposition is a mathematical method used to calculate eigen values and eigen vectors.

The PCA algorithm (adapted from Andersson, 2000) starts with defining a data set $\boldsymbol{A} \in \boldsymbol{R}^{I \times J}$. This data set can be decomposed using eigenvalues into a score matrix (S), loading matrix (L) and residuals (E)

$$\boldsymbol{A} = \boldsymbol{S}\boldsymbol{L}^T + \boldsymbol{E} \tag{5.22}$$

where $\boldsymbol{A} \in R^{I \times J}$ is the data set

$\boldsymbol{S} \in R^{I \times N}$ is the score matrix;

$\boldsymbol{L} \in R^{J \times N}$ is the loading matrix;

$\boldsymbol{E} \in R^{I \times J}$ represents the residuals, or error matrix;

$\boldsymbol{L}^T$ is a transpose of the loading matrix $\boldsymbol{L}$, and;

N represents the number of components that contribute to the observed variation in the data.

The PCA algorithm has five steps.

1. Compute mean and standard deviation of matrix A and then "standardize" matrix A using z-score standardization (which is labeled matrix B in Equations 5.26 and 5.27). Mean and standard deviation of matrix A refers of computing means and standard deviation of the matrix columns. "Z-score standardization" means subtracting the sample mean from each observation, then dividing by the sample standard deviation. This centers and scales the data about zero.
2. Compute the covariance matrix, **C**, of standardized matrix **A**.
3. Calculate eigenvectors and eigenvalues of the covariance matrix. The eigenvector matrix is the loading matrix, **L**, and contains coefficients of principal components.
4. Calculate score matrix **S**. Matrix S is a simple matrix product of standardized matrix **A** and loading matrix **L.**

The data in Table 5.1 is used to provide an example illustrating PCA algorithm.

A is the dataset in question.

$$A = \begin{bmatrix} 6 & 6 & 6 & 5.20 & 0.33 \\ 8 & 8 & 8 & 5.70 & 0.37 \\ 9 & 9 & 9 & 5.10 & 0.31 \\ 8 & 9 & 8 & 5.00 & 0.30 \\ 5 & 7 & 5 & 9.37 & 0.81 \\ 5 & 5 & 5 & 9.01 & 0.88 \\ 5 & 6 & 5 & 7.30 & 0.60 \end{bmatrix} \tag{5.23}$$

Find the average and standard deviations of columns in dataset A.

$$\text{average (A)= [6.57 7.14 6.57 6.66 0.51]} \tag{5.24}$$

$$\text{stdev(A)= [1.718 1.573 1.718 1.893 0.248]} \tag{5.25}$$

Standardize entries in dataset A by subtracting column means and dividing it with column standard deviation.

$$\text{B=z-score(A)} = \begin{bmatrix} -0.33 & -0.72 & -0.33 & -0.77 & -0.74 \\ 0.81 & 0.54 & 0.83 & -0.51 & -0.58 \\ 1.41 & 1.18 & 1.41 & -0.82 & -0.82 \\ 0.83 & 1.18 & 0.83 & -0.88 & -0.86 \\ -0.91 & -0.09 & -0.91 & 1.42 & 1.18 \\ 0.91 & -1.36 & -0.91 & 1.23 & 1.47 \\ 0.91 & -0.72 & -0.91 & 0.33 & 0.34 \end{bmatrix} \tag{5.26}$$

Find covariance matrix C of standardized scores from the dataset.

$$\text{C=cov(B)=} \begin{bmatrix} 1.0 & 0.88 & 1.0 & -0.80 & -0.81 \\ & 1.0 & 0.88 & -0.63 & -0.68 \\ & & 1.0 & -0.80 & -0.81 \\ & & & 1.0 & 99 \\ & & & & 1.0 \end{bmatrix} \tag{5.27}$$

Find eigenvectors of covariance matrix C.

$$\mathbf{L}\text{=eigenvectors (C)=} \begin{bmatrix} 0.71 & -0.07 & 0.46 & 0.25 & -0.46 \\ 0.0 & 0.17 & -0.69 & 0.55 & -0.42 \\ -0.70 & -0.07 & 0.46 & 0.25 & -0.46 \\ -0.00 & -0.70 & 0.01 & 0.56 & 0.43 \\ 0.0 & 0.68 & 0.29 & 0.49 & 0.44 \end{bmatrix} \tag{5.28}$$

Find eigenvalues of covariance matrix C.

$$\text{eignevalues (C)=} \begin{bmatrix} 4.33 & & & & \\ & 0.543 & & & \\ & & 0.12 & & \\ & & & 0.0039 & \\ & & & & 0 \end{bmatrix} \tag{5.29}$$

Multiply standardized scores matrix with eigenvector matrix to calculate score matrix S.

$$\mathbf{S= B}\cdot \boldsymbol{L}\text{=} \begin{bmatrix} -0.33 & -0.72 & -0.33 & -0.77 & -0.74 \\ 0.81 & 0.54 & 0.83 & -0.51 & -0.58 \\ 1.41 & 1.18 & 1.41 & -0.82 & -0.82 \\ 0.83 & 1.18 & 0.83 & -0.88 & -0.86 \\ -0.91 & -0.09 & -0.91 & 1.42 & 1.18 \\ 0.91 & -1.36 & -0.91 & 1.23 & 1.47 \\ 0.91 & -0.72 & -0.91 & 0.33 & 0.34 \end{bmatrix} \begin{bmatrix} 0.71 & -0.07 & 0.46 & 0.25 & -0.46 \\ 0.0 & 0.17 & -0.69 & 0.55 & -0.42 \\ -0.70 & -0.07 & 0.46 & 0.25 & -0.46 \\ -0.00 & -0.70 & 0.01 & 0.56 & 0.43 \\ 0.0 & 0.68 & 0.29 & 0.49 & 0.44 \end{bmatrix} = \begin{bmatrix} -0.0 & -0.035 & -0.028 & -1.37 & -0.05 \\ -0.0 & -0.78 & 0.21 & 0.14 & -1.48 \\ 0.0 & -0.005 & 0.23 & 0.48 & -2.54 \\ 0.0 & 0.096 & -0.31 & 0.14 & -2.04 \\ -0.0 & -0.05 & -0.41 & 0.88 & 2.04 \\ 0.0 & 0.054 & 0.55 & 0.22 & 2.61 \\ 0.0 & 0.023 & -0.23 & -0.50 & 1.45 \end{bmatrix} \tag{5.30}$$

Once the principal components are computed they are geometrically orthogonal to each other, and statistically speaking uncorrelated. This is a very important outcome of the PCA, as the scoring matrix allows researchers to reduce the number of variables needed to explain the variance in the data, while data orthogonality makes data patterns more detectable. The PCA algorithm linearly transforms the original data set into a new coordinate system, where the principal component with the highest eigenvalue (highest score in the scoring matrix) is the one that has the largest variance and by extension the largest influence in the original data set. Therefore, PCA is a good method to highlight similarities and difference between the variables in the data set.

It is important to note that the reduction in dimensionality comes from the user not the method itself. The user is one who ultimately chooses how many principal components to keep. There are three generally adopted criteria to select the appropriate number of principal components.

a) Ignore all principal components after point where new principal components do not considerably increase the total variance explained. The total variance is a sum of squared eigenvalues from the matrix C. Total variance explained is just a percentage of a total variance.

b) Only use the principal components up to the pre-determined percentage of total variance explained.

c) Ignore all PCs with a variance explained less than one (Holland, 2008). That means all eigenvalues less than one should not be disregarded.

Sometimes an issue with PCA might be interpretability of the selected principal components. The issue rises from the fact that the principal components can be complex linear combinations of the real variables from the original data set. To solve this problem not only does the score matrix (eigenvalues of the principal components) need to be evaluated but the loading matrix does as well. Loadings are the projections of the principal components onto the variables from the original data set. A particularly high (positive) or low (negative) loadings for a specific variable indicates strong relationship between that principal component and the variable in question. Therefore, it is essential to look at both the eigenvalue of the principal component and at the variable that contributes the most to the principal components in terms of the absolute value of their loadings. The next section will discuss the Tucker tensor decomposition method, in which a similar approach is used.

5.2.3 Tucker Decompositions Method (Higher Order Decomposition Method)

While PCA is great tool for investigating hidden patterns in the dataset, this method shows some deficiencies when analyzing complex multidimensional datasets. For example, Singh (2006) showed that using PCA on multiway data set does not allow "describing or inferring similarity or general behavior patterns for the sampling sites despite information that is present in original data set". In other words, because the data of interest had a three-dimensional structure, analyzing it with two-way methods was unable to uncover the trends or extract information otherwise present in the data. Furthermore, SVD is shown to be great dimension reduction tool, but has limited strength in discovering trends in complex and multidimensional dataset.

One of the methods available for the analysis of higher order dimensional data sets is the Tucker decomposition method (Kolda, 2009). This method was proposed by L.R. Tucker in the early sixties, and was recently brought to the scientific prominence by work of Bro and el. (1998, 2003a, 2003b). Additionally, tensor decomposition methods have been used in pattern recognition, dimension reduction, and data mining. The main difference between tensor and matrix decompositions is that tensor decomposition methods work on higher order data sets, while matrix decomposition methods work on 2D data sets. In general, the Tucker decomposition method works on any multidimensional data set, and due to its applicability and interpretability, Tucker3 decomposition is the most widely used of these methods. Tucker3 decomposition is as special case of Tucker decomposition, used for analyzing three-dimensional data formats. Additionally, Tucker3 decomposition is easier to conceptualize than higher order decompositions. Therefore, it is used to explain the mathematical foundations behind this method. The name Tucker3 stems from the fact that the three-dimensional tensor is decomposed into three loading matrices and a core tensor, as explained below (Adarkawa, 2015).Tucker3 tensor decomposition, mathematically, can be expressed in element form as:

$$[X]_{i\times j\times k} = \sum_{p=1}^{P} \sum_{q=1}^{Q} \sum_{r=1}^{R} g_{pqr} a_p \circ b_q \circ c_r + e_{ijk} \tag{5.31}$$

where, g is the core tensor array entry; a, b, and c are the loading matrix element entries; e is an entry from the error array; and P, Q, and R are the numbers of components in the loading matrices A, B, and C, respectively.

As seen from the equation 5.13) this is a trilinear decomposition method, which decomposes the three-dimensional array into sets of scores (or loadings) that potentially describe the data in a more condensed form than the original data array. Figure 5.5 graphically shows decomposition of three-way array.

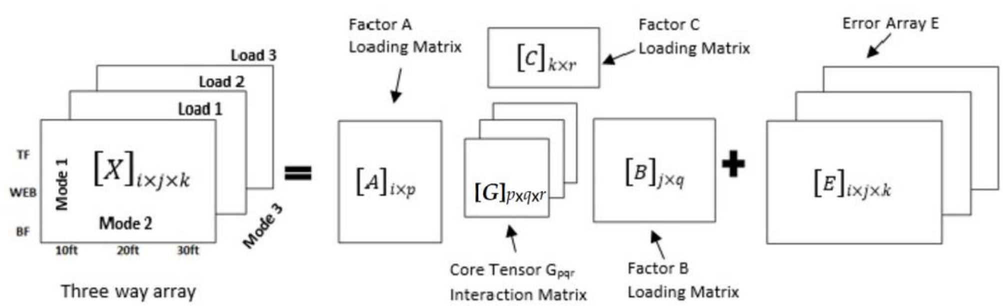

Figure 5.5 Tucker decomposition model of tensor $\boldsymbol{\mathcal{X}}$ shows three-way data set {X} graphically being decomposed in {G} the core tensor array; [A], [B], and [C] loading matrixes and {E} an error array.

The core tensor contains the elements that show the level of association between loading matrices A, B, and C (Kroonenberg, 2008). The larger the value of the core tensor element, the stronger is the association between the vectors from the loading matrices. Strong association means that this component strongly contributes to the variation in the dataset. Conversely, the lower the value of the core tensor element, the weaker the strength of the association between loading matrices. For example, if the core element $q_{1,2,1} \approx 0$, this implies that interaction between vectors $A_{i,1}$, $B_{j,2}$ and $C_{k,1}$ is very weak and that this model will lack component uniqueness. The model structure uniqueness is a very important concept in the tensor decomposition algorithms. If the model structure is not unique, there is a number of solutions that give exact fit of the data. Interpreting the model becomes almost impossible. To obtain unique solution for the decomposition, model sometimes needs to be constrained.

Model constraints are used to obtain parameters that do not contradict prior knowledge, obtain a unique solution to the model, avoid degeneracy and numerical problems, and speed up the algorithms (Bro, 1998). Model degeneracy refers to the inability to find a model with a good fit to the data. There are multiple ways to constrain the model. For example, the model can be constrained so it produces a diagonal core tensor. A diagonal core tensor is a special type of tensor where only the diagonal entries in the tensors are non-zero values, which generally results in faster computations. Another way to constrain a model is to have a model with orthonormal projection matrices (orthogonality constraint), which allow a unique solution to be obtained. Typically, Tucker3 models have orthonormal projection matrices (orthogonality constraint). We can also constrain the model by imposing non-negativity on the regression vector.

For example, the following simple numerical example shows how non-negativity constraint is imposed on the model (adapted from Bro, 1998). Let say we have an arbitrary matrix **Z** of independent variables and matrix **Y** of dependent variables.

$$\mathbf{Z}=\begin{bmatrix} 73 & 71 & 52 \\ 87 & 74 & 46 \\ 72 & 2 & 7 \\ 80 & 89 & 71 \end{bmatrix}, \qquad \mathbf{Y}=\begin{bmatrix} 49 \\ 67 \\ 68 \\ 20 \end{bmatrix} \tag{5.32}$$

The regression vector **a** of the least square equation

$$\min_a \|y - Za\|_F^2 \tag{5.33}$$

can be found as $a = (Z^T Z)^{-1} Z^T y$, which yields $a=[1.123\ 0.917, -2.0685]^T$. Imposing the non-negativity constraint on the regression vector **a** essentially means setting all negative elements from that vector equal to zero. Thus, after applying non-negativity constraint on the regression vector **a**, it results in following change

$$a=[1.123\ 0.917, 0]^T.$$

All constrains are imposed on the model in order to reduced computing effort and to produce good and reliable fitting model. Tucker models with orthonormal projection matrices are known as higher-order singular value decomposition models (Barnathan, 2010). These models can be estimated using algorithm adopted from Kolda and Bader (2009). This algorithm served as foundation for MatLab N-way toolbox that was used for tensor decompositions in this dissertation.

5.2.4 Applications of Tensor Decompositions

Tensor-decomposition methods have been extensively used in psychometrics and chemometrics analysis for many years (Carol et al., (1989), Harshman, et al. (1970), Gealdi, (1970), Bro, et al. 2003). Singh, et al. (2006) has shown that tensor-decomposition methods better predict cause-effect relationships between soil pollution concentration, site location, and depth of pollutant penetration than other statistical methods. Kotura, et al. (2012) used tensor decomposition to track anomalies in the internet network traffic, in order to recognize spam and detect fraud. Tensor decompositions are also used for data filtering (Ricci et al., 2012), and social media platform algorithms (Zheng, et al. (2010)) and in facial recognition programs (Vasilescu and Terzopoulos, 2002). Recently, Adarkwa (2015) used tensor decomposition analysis to investigate bridge structural deficiency and functional obsolescence on bridge designs in the USA. He found that girder & floor-beam bridge designs showed the most variation with respect to structural deficiency across all states.

5.2.5 Using Tensor Decompositions to Differentiate Stress Distributions among Bridge Components

Only the author's preliminary work has used tensor decomposition to analyze stress data in bridge structures. Specifically, Radovic and McConnell (2014) investigated ultimate capacity of a steel I-girder highway bridge by building the FE model of the structure. The data extracted from the FEA was then organized into element groups representing different structural members of the bridge in different locations in the bridge structure under increasing loads. For example, cross-frame elements belonging to one group were labeled XG1; cross-frame elements belonging to a second group were labeled XG2 and so on. Similarly, Girder 1 bottom flange elements are labeled G1BF, Girder 2 bottom flange elements are labeled G2BF, and so on. The stress data extracted from element groups was expressed in terms of stress histograms (Figure 5.6), where the x – axis is stress bins, the z-axis is different load levels as quantified by load proportionality factors (LPFs), and the vertical (y-) axis represents the percent of the total area of the given bridge component with stresses in each of the stress bins at each load level. Considering that the number of elements in each girder was the same, by counting the number of elements in each stress bin and dividing it with total number of girder elements gives the percent of girder area that is in that stress bin, hence the x-axis label name "% area".

The percent area from the each bin was then structured into a three-dimensional tensor such that first (i) mode of the tensor consists of bridge components (bottom flange of girders G1 to G4 and cross-frames groups XG1 to XG3) organized in rows, the second mode (j) consists of stress ranges (stress histogram bins) organized in columns, and the third mode (k) consists of the loading increments, expressed as LPF organized in tubes. Tensor decomposition of the resulting three-way array, mathematically expressed as $\boldsymbol{\mathcal{X}} \in \mathbb{R}^{\boldsymbol{I \times J \times K}}$ was performed using the N-way Toolbox in Matlab R2014 (Mathworks, 2014). The results showed that tensor decomposition was able to quantify difference in stress distribution among the bridge components at different load levels.

For example, in Figure 5.6, seven stress profiles of bridge structural components are presented. Looking at these seven stress profiles, it is very hard to numerically asses which stress profiles are alike and which ones are different. Furthermore, by looking at the stress profiles it is very hard to detect at what load level the behavior of these structural components start to diverge from one another, such as due to the development of plastic behavior. Using Tucker Decomposition, researchers were able to visually and numerically differentiate the behavior of bridge structural components and to determine at what load levels bridge behavior starts changing. This study proved that multiway analysis could be used by researchers when assessing different design options.

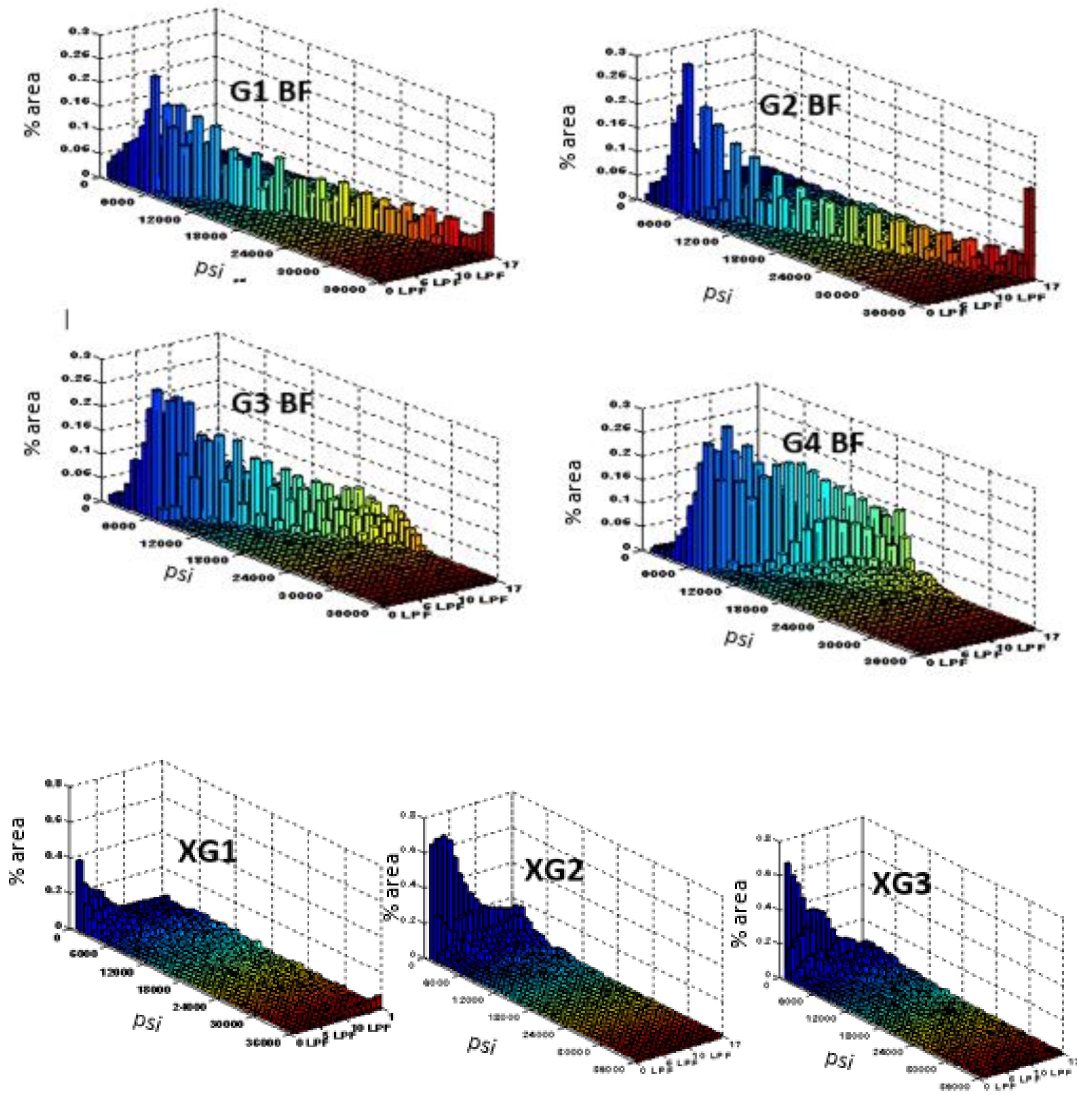

Figure 5.6 Preliminary results of stress profiles of seven element groups. Longitudinal axes consist of 51 stress bins, transverse axes consists of 17 loading increments (LPFs) and vertical axis represents frequency of occurrence expressed as a percent of the total number of elements in the corresponding element group.

5.3 Tensor Decomposition of Finite Element Analysis Data

In current civil engineering practice, finite element analysis (FEA) is used to assess and predict the behavior of various structures in general and steel girder bridges in particular. The physical shape of these structures is numerically expressed in terms of geometric shapes (elements) bounded by vertices (nodes). Usually, an external load is placed somewhere in the model and the response is calculated via a system of partial differential equations. The resulting outcome is typically expressed in terms of quantities such as nodal deflections and element stresses. The number of elements in a typical bridge model could vary anywhere from hundreds to millions, resulting in extremely large dataset. In current practice, only a small fraction of this available data is quantitatively analyzed. For example, it is often the case that only the peak (discrete) values in the data set, such as maximum deflection, maximum tensile stress in the bottom flange or maximum stress in cross-frames are evaluated.

While this "discrete level approach" to data analysis has been used for years for the design and analysis of steel girder highway bridges, supplemental, more "holistic" evaluation of the data may provide additional understanding of the behavior of bridges. "Holistic" approach to FE data analysis refers to a more comprehensive evaluation of bridge response variables (such as deflections or stresses) by analyzing their distributions not just peak values. As shown in Chapter 4, a "holistic" approach to FE data analysis was used to assess the effect of removing cross-frames from the bridge on the overall stress distribution of the bridge. The Chapter 4 results showed that removing cross-frames from the bridge had a minimal effect on stress distribution throughout the bridge as well as no effect on the overall load resisting capacity of the bridge. Furthermore, the Chapter 4 results indicate that in order to fully comprehend the latent behavior of the bridge, and to understand why this occurrence happened, a more rigorous mathematical analysis is needed. Datasets such as these that are large in volume and complexity, inter-correlated, and multi-dimensional are most comprehensively evaluated and quantified by using tensor decomposition analysis in general and Tucker decompositions in particular.

Therefore, the objective of this section is to investigate the effects of cross-frame removal on stress distribution throughout the bridge by implementing tensor decomposition method. This section begins with a methodology sub-section that reviews the FE modeling and how stress distribution data are analyzed using “holistic” approach. Then the results sub-section discusses evaluating and interpreting tensor decomposition outcomes.

5.3.1 “Holistic” FFA Evaluation Methodology

This sub-section summarizes the methodology used for assessment of stress distributions in steel I-girder highway bridges. Finite element analysis (FEA) models of bridges with different skews and cross-frame configurations were built for this purpose. Stress distributions among bridge models were evaluated using Chi-square Distances, a novel, “holistic” type metric for evaluating FEA data. These distances are organized in tensor form for further analysis.

5.3.1.1 FEA Models

A total of 25 bridge FE models were built for this study. Two cross-frame designs (K-frame vs. X-frame configurations) and two cross-frame layouts (inline vs. staggered) at five skews (0°, 25°, 46°, 55° and 63°) were modeled and analyzed. To investigate the effect that removing cross-frame from the bridge has on bridge stress distribution, additional FE models without cross-frames (No-frame) were added at each bridge skew. All parametric models were based on a 63° skewed simply supported steel I-girder bridge labeled “7R”, as previously described in Chapter 3. Stress data of all girder, cross-frame, and deck elements are extracted from the models and evaluated using Chi-square Distance metrics (see Section 4.3.2.3).

5.3.1.2 Organizing FEA Data for “Holistic” Evaluation

The main idea of the parametric analysis was to investigate the response of the bridge as a system by analyzing stress distribution in the two main structural components: the girders and deck. Therefore, two element groups are created in each FE model and longitudinal stresses were computed and extracted for each element. Stress data were then organized in such a way that girder group contained elements stresses from all girders in the bridge, while deck (D) group contained all deck element stresses.

Furthermore, stress data were extracted under three loading conditions as described in detail in Chapter 4:

a) Design load (HS-20 truck),

b) First yield load, and

c) System yield load.

The design load refers to a load equivalent of the one HS-20 truck on the bridge. First yield load refers to a load that causes the full cross-section of the bottom flange of one girder to yield, while system yield load refers to a load that causes the entire cross-sections of the bottom flanges of all girders to yield. Full cross-sectional yield of the bottom flange of the girder in the FE model refers to the case in which all shell elements constituting a girder's bottom flange cross-section exceed the yield stress. At each of the three load conditions, stress histograms of each element group at design, first yield, and system yield load levels were constructed and analyzed (Figure 5.7). Histogram bins for girders are organized in increments of 1000psi, while histogram bins for deck are organized in increments of 100psi due to the smaller magnitude of these stresses.

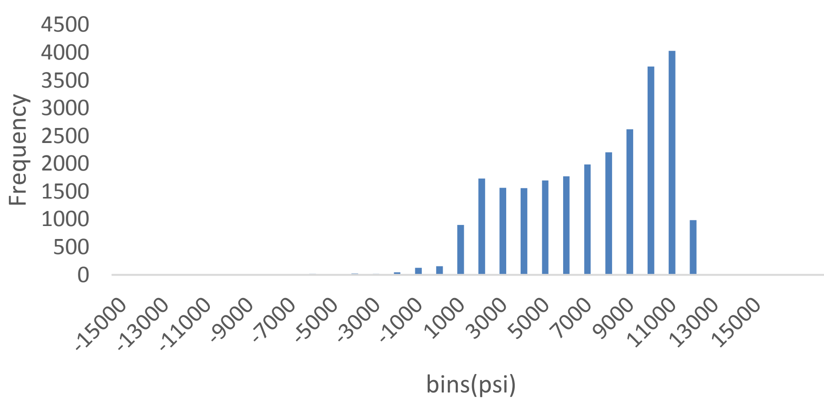

a)

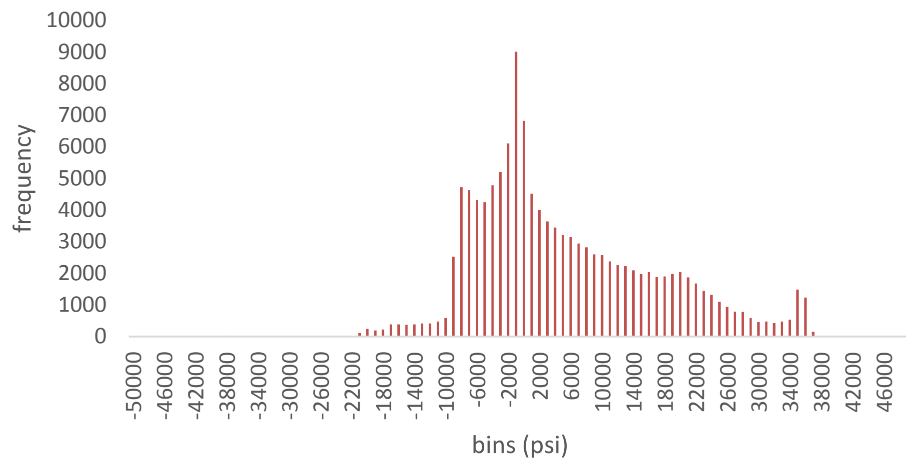

b)

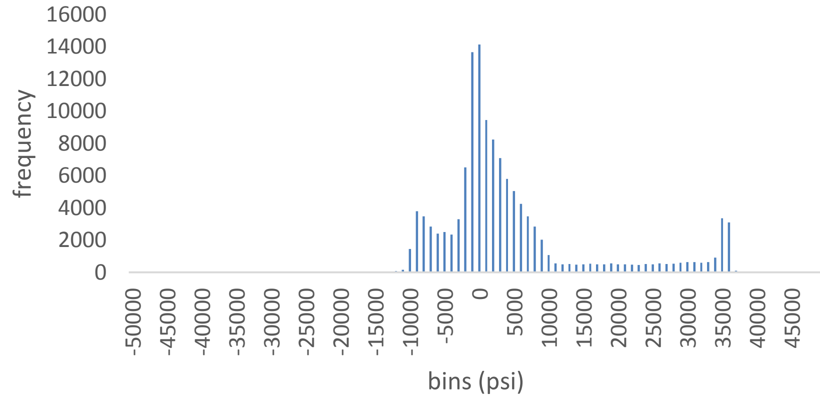

c)

Figure 5.7 Stress histograms of the girder stresses at a) design load, b) first yield load, c) system yield load

5.3.1.3 Data Processing using Chi-Square Distances

To numerically assess the difference between stresses histograms of two different bridge models at the same skew and load level, the measure known as Chi-square Distance was used (this topic is covered in detail in Section 4.3.2.3). It is worth remembering that a large distance between the models corresponds to stress distributions that differ significantly, and conversely, a smaller distance between the models corresponds to stress distributions that are more alike. It is hypothesized that if the cross-frame design does not play a role in bridge system response, then the stress distribution among the models at the same load level and the same skew should be similar and Chi-square Distances between the models should be small.

To evaluate the effect that cross-frames removal has on stress distribution, Chi-square Distances between No-frame models and corresponding cross-frame models were computed and used as data entries to construct a 4D dimensional tensor as explained in the following section. To illustrate this point, Table 5.2 shows a typical outcome of Chi-square distances between girder stress distributions, among the models at design load level at 25° skew. Four data points from this analysis (442, 209, 4876 and 4202), from the comparisons between each cross-frame design and the no-frame model were used as data entries to construct the 4D tensor. The entire dataset used for this analysis can be found in Appendix D.

Table 5.4 Typical outcome of the Chi-square Distance comparison. Note that results are symmetric and for the clarity purposes identical data entries (located to the left of the diagonal) were replaced with star (*) symbols

Design	K-INLINE	K-STAGG	X-INLINE	X-STAGG	NO-FRAME
K-INLINE	0	282	4874	4064	442
K-STAGG	*	0	4537	3598	209
X-INLINE	*	*	0	411	4876
X-STAGG	*	*	*	0	4202
NO-FRAME	*	*	*	*	0

5.3.1.4 Tensor Data Structure

The data structure of the (5 x 4 x 3 x 2) 4D tensor analyzed in this work consists of the following: the first dimension consists of five skews (0°, 25°, 46°, 55°, and 63°), the second dimension consists of four cross-frame designs (K-Inline, K-Stagg, X-Inline and X-Stagg), the third dimension consists of three load conditions (design, first yield and system yield), and the fourth dimension consist of two bridge structural components (girders (G) and deck (D)).Each value in the tensor represents the Chi-square distance between the no-frame model and corresponding cross-frame model under the given conditions. This tensor configuration yields a total of 240 data points. To visualize the data, the 4D tensor is displayed in 3D space by combining structural components and skews on one axis and design configurations and load levels dimensions together in Figure 5.8. Once the data were organized in the tensor structure, it is ready to be processed using Tucker tensor decomposition method.

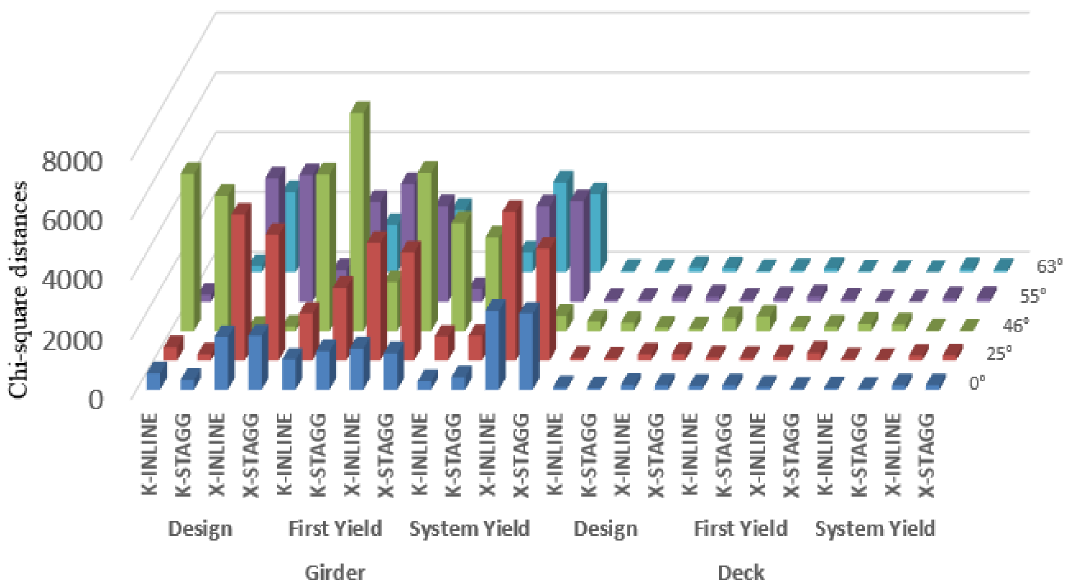

Figure 5.8 Graphical representation of the data structure of 4D tensor. X-axis represents skew, y-axis is Chi square distance, and z-axis is element groups, load level and cross-frame configuration.

5.3.1.5 Tucker Tensor Decomposition Methodology

5.3.1.5.1 Overview

The biggest advantage of using Tucker tensor decomposition method is its ability to compress variation, extract features, explore data, and generate parsimonious models (which are able to capture or explain the most variation in the data set with the least number of variables possible), especially from highly correlated data sets (Bro, 1998). The biggest disadvantage of using Tucker tensor decomposition method is that it sometimes requires complex data interpretation, and somewhat arbitrary (subjective) judgement before optimal model parameters are chosen. Thus, expertise in the subject matter is required to make Tucker tensor decomposition analysis valuable.

Parameters that need to be determined by the analyst are the size of the core tensor G (p x q x r x s); core tensor and loading matrix constraints, such as orthogonality or non-negativity; and the selection of an optimization algorithm based on the data structure and /or software used. Due to these restrictions, the user must be familiar with the practical significance of the data set of interest in order to interpret and conduct the analysis in meaningful and accurate manner.

There are two ways to constrain the Tucker decomposition models. First way is to constrain the model so it produces diagonal core tensor. Diagonal core tensor is a special type of tensor where only diagonal entries in the tensors are non-zero values. And the second way to constrain a model is to have a model with orthonormal projection matrices (orthogonality constrains). Tucker models with orthonormal projection matrices are known as higher-order singular value decomposition models (Barnathan, 2010) and these models can be estimated using algorithm adopted from Kolda & Bader (2009). Model fit is determined by the loss function and the fitting iterations stop once the difference between the original data set and the model is in the range of the loss function. This function is defined as:

$$\min_{\mathcal{G},A^{(1)},A^{(2)},\dots,A^{(N)}} \left\| \mathcal{X} - [\mathcal{G};\ A^{(1)}, \dots,\ A^{(N)}] \right\| \qquad (5.17)$$

Model constraints and data centering will be discussed in the following two sections. Although many data sets require data to be scaled because the data is in different quantities, that is not the case with the data presented in this work. Thus, data scaling was not conducted in this work.

5.3.1.5.2 Data centering (normalization)

Before conducting tensor decomposition, the tensor data needs to be preprocessed. The first step in preprocessing is called data normalization (also known as zero centering). This step includes moving the centroid of the data towards the origin. This is very important step, because if zero centering is not conducted, the model might fail to capture all the factors that contribute to variation in the data set. Bro (1998) suggests that if the data is not on a ratio scale, centering must be done. Furthermore, according to Bro and Smilde (2003), there are a few more advantages to using data centering, such as, removing offsets and constant terms, increasing fit of model to the original dataset, and reducing rank representation of the data.

The procedure for zero centering is fairly straight forward. All the mean values are calculated for each column of data and then all entries from that column are subtracted from the mean. This procedure yields zero mean for the data set and it is described by

$$x_{ij}^{c} = x_{ij} - \frac{\sum_i x_{ij}}{I} \tag{5.18}$$

where x_{ij}^{c}= zero centered data entry for object *i* and attribute *j*; x_{ij}= data entry for attribute *j* of object *i*; and I= dimension of mode *i*. The data in this study was normalized by default using the Tucker3 function in N-way toolbox (Matlab, 2014). Before inputting data into the N-way toolbox, the data needs to be organized as a tensor (as described in Section 5.3.1.4).

5.3.1.5.3 Model Constraints

As discussed above, constraints were applied to speed up algorithms and improve the results of these algorithms. In the Matlab's N-way Toolbox there is a built-in function that was used to impose orthogonality constraint on to the data and non-negativity constraint onto the core tensor, G.

5.3.2 Tensor Decomposition Analysis Results

5.3.2.1 Model Fitting

Using the Tucker decomposition method, the 4D tensor was decomposed into four loading matrices (A, B, C, D) and a core array (G). Loading matrix A represents bridge skews, loading matrix B represents cross-frame designs, loading matrix C represents level of applied load, and loading matrix D represents bridge components. Orthogonality constraints were imposed on the loading matrices. The non-negativity constraint was imposed on the core array, while the dimensions of the core array were selected based on two criteria: percentage variance explained and optimal model complexity. Percentage variance explained shows how well the decomposed model fits the original data, where models with higher percentages of variance explained indicate more accurate models.

The optimal model complexity is the one that requires the smallest number of components but still captures a high percent of the variance in the model (Singh 2006). Models with large variance explained, but with larger core array size, will be ultimately excluded because they are less interpretable. For example, Figure 5.9 shows that models with core arrays size of $p \times q \times r \times w > 18$ have high values of explained variances, but these models also have larger number of components that needs to be interpreted. It is also noted that higher variance captured can be the result of the overfitting (making the model unreasonably complex, such as having too many components relative to the number of observations) and not necessarily an ideal model for a given data set. Once the proper model was selected, the loading scores from different factors (skew, cross-frame design, level of loading, bridge component) were computed and analyzed.

The total variance explained versus model complexity was plotted and the model with the highest variance explained relative to the minimal complexity was selected as the best fitting model. With a total of 54 models tested, the results showed that model

[2x2x2x2] was a primary candidate for a best fitting model. This model had high percent of variance explained (94.2 %) and relatively low levels of complexity 16.

The next step is to cross-validate these potential models by split-half analysis. Split-half analysis is measure of model reliability. The model is divided in half across one of the modes (skew angle in this case). The remaining half of the data set is then tried to be fitted with the same decomposition model. If the model retains a similar percent of the variance explained that means that model indeed captures latent structure of the dataset. When the model was cross-validated by split-half analysis, it was able to maintain a similar percent of variance explained (93.7%) compared to the original data (94.2%). Therefore, this model was selected for further processing.

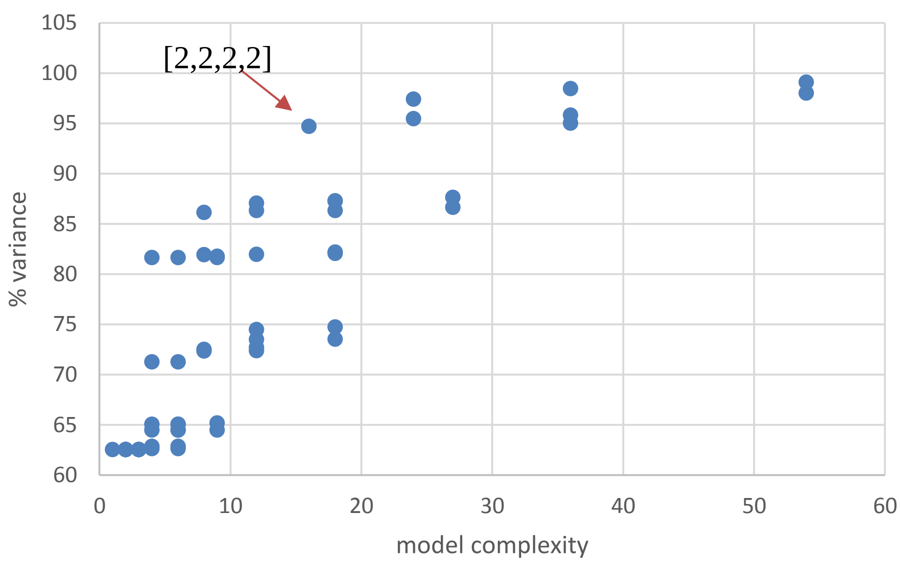

Figure 5.9 Percent of variance explained vs level of complexity for 54 Tucker models.

5.3.2.2 Interpretation of Data

Before interpreting the decomposed data, it is important to understand what the data is supposed to represent. Note that one purpose of doing the tensor analysis is to find similarities and differences in the responses of bridges with and without cross-frames. It is important to remember that all tensor decomposition results (individual and global) describe how stress distributions in models with and without cross frames differ. For example, low Chi-square distances indicate that cross-frames might not be contributing to lateral load distribution as intended by the design or that lateral load distribution is equivalently achieved in the absence of cross-frames.

The tensor results were plotted in bi-plots. Bi-plots of loading scores show both, how variables are correlated inside its loading matrix, and how they are correlated with variables from other loading matrixes. Every bi-plot has two axes, called components (Component 1 and Component 2). The value of each component is called loading score. Therefore, every variable included in a bi-plot (such as X-frame Inline design or 25° skew) will have two loading scores per bi-plot. The higher the loading scores are, the higher the contribution to variance of the dataset. Conversely, the lower the loading score is, the lower the contribution to the variance in the dataset is.

To better understand this concept, let assume that there was a difference in stress distribution between No-frame models and cross-frame models at different skews and different load level. If the resulting bi-plots show variables being clustered near the origin of the plot (low absolute values of loadings scores in both components), that would indicate that the variables do not contribute to the variance in the dataset. Now let's assume that all models show high variation in stress distributions, but only at system yield load level. In this case, the clustering of other variables in all bi-plots would still be near the origin of the plot, while system yield variable in a bi-plot related to load condition on the bridge would have high score in one or both bi-plots components, indicating that load level rather than skew or cross-frame design contributes to the variations in the data set. However, when more than one variable has high component scores in multiple bi-plots, more complex interpretation of data is required.

5.3.2.3 Results

The goal of the tensor decomposition analysis is to find latent trends in the data and/or to find the most influential factor contributing to the trends. It is suggested that analyzing the dominant core tensor loadings [G] could help in interpreting complex behavior the system is manifesting (Adarkwa, 2015). Additionally, evaluating core tensor loading scores together with the analysis of bi-plots could help better understand trends in the dataset. If variables have similar scores in both loadings they will form clusters in bi-plots, revealing the underlying structure of the dataset. Furthermore, the sign convention (positive or negative) of the score in core tensor [G] is a product of loading component scores. For example, if one loading component score is positive, and another is negative, core tensor score will be negative. Conversely, if both component scores are positive or negative, core tensor score will be positive.

The core tensor results are presented in the Table 5.5. The results show that [1,1,2,2] core tensor value had by far the largest score (7065). That means that variables with high scores at Component 1 at loading matrix A, Component 1 at loading matrix B, Component 2 at loading matrix C and Component 2 at loading matrix D correspond with the highest score. If the core tensor results are compared with bi-plots from the Figure 5.10 it can be seen that Figure 5.10a shows loading matrix A (cross-frame configuration) in which both X-frame (X-Stagg and X-Inline) models have large negative Component 1 loadings. Also, from Figure 5.10b (loading matrix B), it can be seen that 25° (and 55° to a lesser extent) models have the largest Component 1 scores and these are positive. The largest Component 2 scores at loading matrix C (Figure 5.10c) occur for the design load level with negative scores and the first yield load level for positive scores. Finally, Figure 5.10d shows that deck elements have the largest Component 2 loading score at loading matrix D and these are positive. Thus, because the bi-plot data from loading matrices A, B, and D, clearly shows that the signs contributing to the largest (positive) core tensor values are negative, positive, and positive, respectively, the negative value from loading matrix C (corresponding to design load) indicates the design load contributes to the largest core tensor value. Thus, from Table 5.5 together with the bi-plots it is concluded that the largest core tensor value is associated with deck elements of the X-frame configuration at the 25° skew model at the design load level. This core tensor value explains 62% of the variance in the dataset, which is calculated by summing the squares of the highest core tensor score and then dividing it by the sum of squares of all core tensor scores.

The second largest [G] score (-2855) belongs to the [2,2,2,2] core tensor value. Comparing to the bi-plots in the same manner as described in the previous paragraph reveals that the loadings from this core tensor value corresponds to deck elements (high positive Component 2 score) of both K-frame models (high positive Component 2 score) under design load levels (high negative Component 2 score) at 46° skew (high positive Component 2 score). The third largest [G] score (-2597) belongs to the [1,2,2,1] core tensor value. The loadings from this core tensor value belong to girder elements (high positive Component 1 score) of X-frame configuration models (high negative Component 1 score) under first yield and system yield loads (high positive Component 2 score) at 46° skew (high positive Component 2 score). These three core tensor values explain 80.0% of the variance in the dataset.

Table 5.5 Core tensor G scores for the model Tucker [2,2,2,2] in unfolded form

	D1 C1 B1	**D1 C1 B2**	**D1 C2 B1**	**D1 C2 B2**	**D2 C1 B1**	**D2 C1 B2**	**D2 C2 B1**	**D2 C2 B2**
A1	-1902	-20	-1035	-2597	-41	1123	7065	-522
A2	18	1062	2208	-1850	-690	-24	228	-2855

The two highest core tensor scores were both associated with deck elements at the design load. That means that there is a large portion of the variance in the data set can be attributed to behavior of the deck at 25°, 46º and 55º skews under design load levels. Finding that one of the most important factors that affects the difference in stress distribution among the models was related to these intermediate skews was somewhat unexpected. Theoretically, the dataset could be divided into two main categories tangent (0º skew) and skewed bridges. Therefore, it would have been expected that 0° skew models would have a high loading in one or both components indicating that bridge skew is a defining factor that affects stress distribution between bridges with and without cross-frames. Furthermore, intuitively it would have been expected that tangent models (0° skew) and models with low bridge skew (25°) have more similar distribution to each other, while bridges with high skew (46°, 55° and 63°) should have stress distribution similar to each other. However, the results show (Figure 5. 11a) that 46° skew models have high positive Component 2 loadings, while 55° and 25° skew models have high positive Component 1 loadings. Furthermore, 0° skew and 63° skew models have low loadings in both components. These results indicate that bridge skew does not influence difference in stress distributions between models with or without cross-frames. In other words, some other factors such as bridge geometry, girder to deck stiffness and etc. might be more influential in terms of stress distribution.

Note that Chapter 4 results showed that there is a significant difference in deck stresses and stress distributions between 46 ° skew models and other models and possible theoretical explanations for this were discussed in Section 4.4.1.1.2. The same finding is replicated by tensor analysis as can be clearly seen from the dendogram plot in Figure 5.11 (the reader is referred to Everitt et al. (2011) for an explanation of this plot if necessary). The dendogram also clarifies that as the skew increases or decreases compared to 46°, the relative magnitude of the change in skew is more important than the direction of the change, as indicated by 25° and 55° models being grouped together in the dendogram and 0° and 63° models also being grouped together.

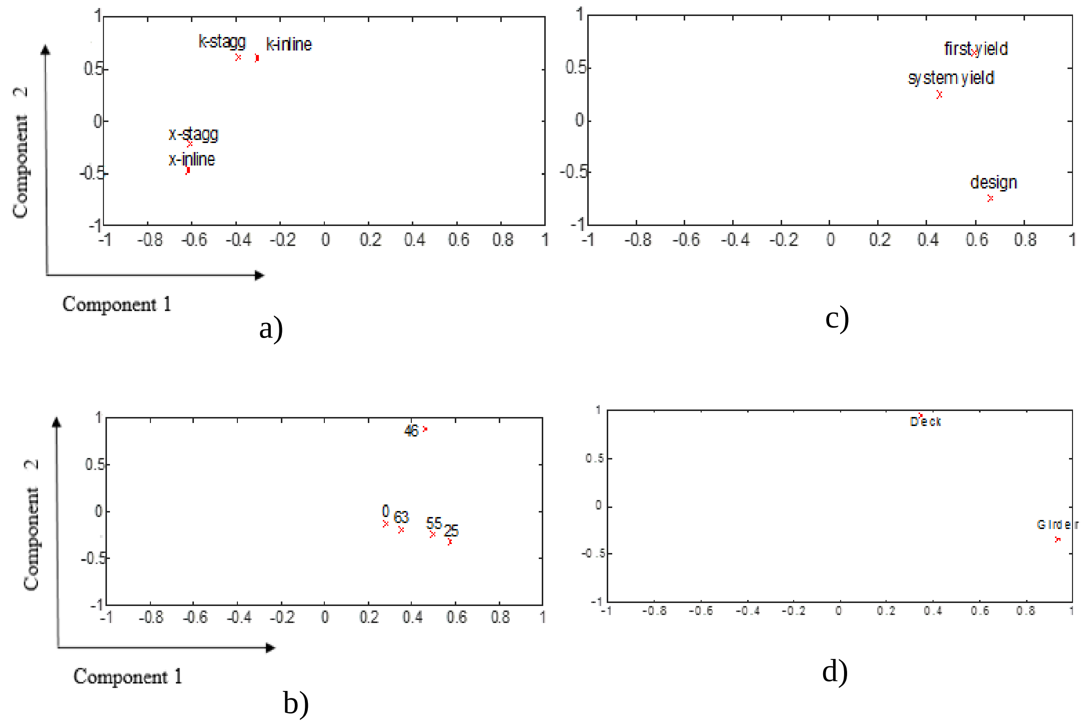

Figure 5.10 Bi-plots of Tucker3 (2x2x2x2) model

The results also show that in loading matrix A (cross-frame designs) X-frame models have high negative loadings in Component 1, while and K-frame models have high positive loadings in Component 1 (Figure 5.10a). Results also show that the K-frame Inline models loadings are grouped with K-frame Stagg models' loadings and X-frame Inline models loadings are grouped with X-frame Stagg models loadings. These two groups formed two distinguished clusters (K-frame and X-frame clusters). These results suggest that cross-frame design (K- versus X-frames) rather than cross-frame layout (staggered versus inline) contributes more to difference in stress distribution among the bridge components for the specific cross-frame configurations considered in this work. While this might be counterintuitive, bear in mind that X-frames and K-frames have different axial stiffness in this work, which might be one of the reasons for this result.

The result also show (Figure 5.10c) that first yield and system yield load levels have both high positive loadings in Component 2, while design load level has negative loading in Component 2. The results indicate that there is significant difference in stress distribution between No-frame and cross-frame models between design and yield load levels which are theoretically expected. This significant difference is visually replicated in the dendogram presented in the Figure 5.12.

The results also show that girder group has high positive Component 1 loadings, while deck has high positive Component 2 loadings (Figure 5.10d). This result indicates that stress distributions at deck and girders is independent of each other regardless of the cross-frame design, skew or load level. In other words, large difference in stress distributions detected at girder models is not translated in similar differences in stress distributions at deck models. This finding is counter-intuitive, as theoretically (and for design purposes) it would be expected that the longitudinal bending stress in the deck is proportional to the longitudinal bending stress in the girders. However, the results indicate that this is not the case and that more complex behavior is taking place (such as lateral bending of the bottom flange).

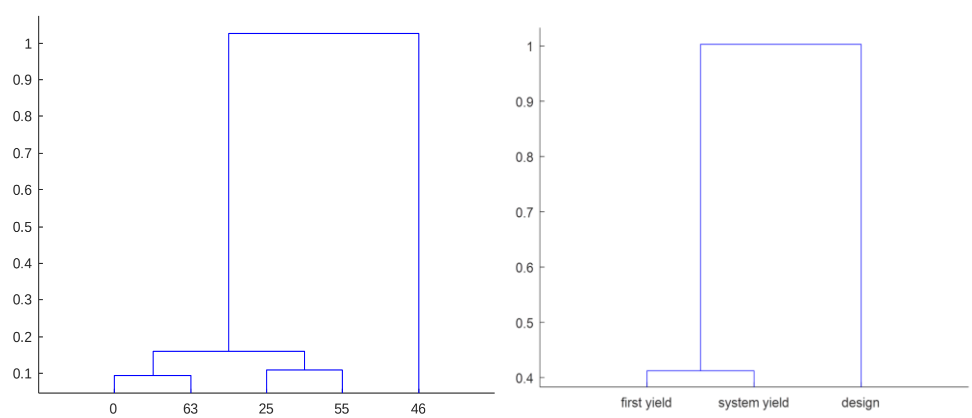

Figure 5.11 Dendogram plot of loading matrix A (on the left) and loading matrix C (on the right) of Tuker3 (2x2x2x2) decomposition.

5.4 Conclusions

This chapter investigated the influence of removing cross-frames on the global behavior of the bridge as quantified by stress distributions. The comparison was made at five different bridge skews (0°, 25°, 46°, 55° and 63); at three different loading levels (design, first yield and system yield); and for four different cross-frame configurations (X-frame Inline, X-frame Staggered, K-frame Inline, and K-frame Staggered). Chi-square Distances between stress histograms of No-frame models and corresponding cross-frame models was used as a measure to differentiate the stress distributions among models. The data were analyzed using a specific type of multiway analysis called Tucker tensor decomposition method.

It was shown that the tensor decomposition method is able to quantify trends in the data detected by some of the discrete and holistic analysis methods presented in Chapter 4. The following conclusions were drawn from this study:

1) A correlation between the Chapter 4 findings and tensor decomposition findings was found regarding skew. For example, RO at girders at 46° skew is significantly lower than RO at other skews at the design load level and significantly higher than RO at other skews at first yield load level. Consequently loading matrices B and C (Figure 5.10) show that 46° skew variable and design and first yield load variables have high Component 2 scores. Furthermore, discrete metrics that measured peak stress in the deck also found deviations at 46 ° skew models. Subsequently, loading matrix D shows that the deck variable has high positive Component 2 scores.
2) Cross-frame design (K-frame vs X-frame) contributes more to the difference in stress distribution between no-frame models and cross-frame

models than cross-frame layout (staggered vs. inline). This finding is based on bi-plot data shown in Figure 5.10a showing K-frame Inline and K-frame Staggered have high positive loadings in Component 2 while X-frame Inline and X-frame Staggered have high negative loadings in Component 1.

3) The difference in stress distributions at deck are not associated with the difference in stress distribution in girders as indicated by the highest loadings for these member types being associated with different components (i.e., Component 1 for girders and Component 2 for decks). This indicate that different stress distribution mechanisms govern at these two load carrying systems.

REFERENCES

Abaqus 6.11 Analysis User's Manual. (2011). *Online Documentation Help*. Dassault Systèmes.

Acar, E., Aykut-Bingol, C., Bingol, H., Bro, R., Yener, B. (2007). “Multiway analysis of epilepsy tensors”. *Vol. 23,* ISMB/ECCB 2007*,* i10-i18.

Adarkwa, O. (2015). “Tensor factorization in civil infrastructure systems”. *Doctoral Dissertation*, University of Delaware.

Andersson, C.A. (2000). “Exploratory Multivariate Data Analysis with Applications in Food Technology”. *Doctoral Dissertation,* Royal Veterinary and Agricultural University, Department of Dairy and Food Science, Chemometrics Group, Food Technology.

Bader, B.W., Berry, M.W., Browne, M. (2008). “Discussion Tracking in Enron Email Using PARAFAC”. *Survey of Text Mining II*. Print ISBN 978-1-84800-045-2,147-163.

Barnathan, M., Megalooikonomou, V., Faloutsos, C., Faro, S., & Mohamed, F. B. (2011). “TWave: High-order analysis of functional MR”I. *Neuroimage*, 58(2), 537-548.

Bathe, K.-J. (1982). “Finite element procedures in engineering analysis”. Englewood Cliffs, N.J: Prentice-Hall.

Bowman, D. (2012). “Fatigue evaluation of steel bridges”. *Vol. 721*. Transportation Research Board.

Bro, R. (1998). “Multi-way analysis in the food industry: models, algorithms, and applications”. *Doctoral Dissertation*. Amsterdam: Universiteit van Amsterdam.

Bro, R., Smilde, A.K. (2003). “Centering and scaling in component analysis”. *J. Chemometrics*, 17-1, 16-33.

Bro, R., Kiers, H.A.L. (2003). “A new efficient method for determining the number of components in PARAFAC models”. *Journal of Chemometrics*, (17)-5, 274-286.

Carroll J.D., J. Chang, “Analysis of individual differences in multidimensional scaling via an N-way generalization of "Eckart-Young" decomposition”. *Psychometrika,* (35)-3, 283-319.

Cichocki, A., Zdunek, R., Phan, A.H., Amari, S., (2009). “Nonnegative Matrix and Tensor Factorizations- Applications to Exploratory Multi-way Data Analysis and Blind Source Separation”. Wiley, ISBN: 978-0-470-74666-0.

Comon, P., Golub, G., Lim, L. H., & Mourrain, B. (2008). “Symmetric tensors and symmetric tensor rank”. S*IAM Journal on Matrix Analysis and Applications*, 30(3), 1254-1279..

Geladi P., (1989). “Analysis of multi-way (multi-mode) data”. *Chemom. Intell. Lab. Syst*., 7.1-2 11-30.

Fernandez, G. (1970). “Principal Component Analysis”. *ERS701D*. http://www.cabnr.unr.edu/saito/classes/ers701/pca2.pdf, Accessed: 3/3/2016.
Harshman, R. (1970). “Foundations of the PARAFAC procedure: Model and conditions for an 'explanatory' multi-mode factor analysis.” *UCLA Working Papers in phonetics*, 1-84.

Holland, S.M. (2008). “Principal Components Analysis (PCA)”. Department of Geology, University of Georgia, Athens, GA. http://strata.uga.edu/software/pdf/pcaTutorial.pdf Accessed: 3/8/2016.

Kar, Ansuman, et al. (2012). "Study on Effect of Skew Angle in Skew Bridges." *International Research Journal of Engineering and Technology, (*02):12, 13-18.

Kiers, Henk AL. (2000). "Towards a standardized notation and terminology in multiway analysis". Journal of chemometrics, 14.3 105-122.

Kolda, T.G., Bader, B.W. (2007). “Tensor Decompositions and Applications”. *SAND2007-6702,* Sandia National Laboratories, 26-27.

Kolda, T., Bader, B. (2009). "Tensor decompositions and applications". *SIAM Review* 51.3, 455-500.

Kroonenberg, P.M. (2008). “Applied Multiway Data Analysis”. Wiley Series in Probability and Statistics. ISBN 978-0-470-16497-6, 7-6.

MATLAB and Statistics Toolbox Release 2014b, The MathWorks, Inc., Natick, Massachusetts, United States.

Radovic, M., McConnell, J. (2014). “Evaluation of Cross-frame Designs for Highly Skewed Steel I-Girder Bridges”. *Proceedings of 48th International Bridge Conference,* Pittsburg. IBC-14-47.

Ricci, G., de Gemmis,M., Semeraro, G. (2012)."Matrix and Tensor Factorization Techniques applied to Recommender Systems: Survey". *Matrix 1.01*.

Vasilescu, M., Terzopoulos, D. (2002). "Multilinear analysis of image ensembles: Tensorfaces". *Computer Vision—ECCV 2002*. Springer Berlin Heidelberg, 447-460.

Shimazaki, H., & Shinomoto, S. (2007). “A method for selecting the bin size of a time histogram”. *Neural Computation*, 19(6), 1503-1527.

Singh, K. P., Malik, A., Singh, V. K., & Sinha, S. (2006). “Multi-way data analysis of soils irrigated with wastewater–A case study”. *Chemometrics and Intelligent Laboratory Systems*, 83(1), 1-12.

Zheng, N., Li, Q., Liao, S., Zhang, L. (2010). "Flickr Group Recommendation based on Tensor Decomposition". *SIGR '10.* ACM 978-1-60558-896-4/10/07.

Chapter 6

CONCLUSIONS & RECOMMENDATIONS

6.1 Overview

Cross-frames are bridge structural members that are intended to provide lateral-load resistance and stability during construction, reduce the buckling length of the compression flanges of steel girders, and facilitate distribution of traffic loads among girders. The main goal of the study was to quantify how much cross-frame contribute to stress distributions in steel I-girder bridges in general and in skewed I-girder bridges in particular. For that purpose, a total of 25 finite element models of bridges were built and analyzed. Stress distribution data from these models were evaluated using both “discrete” and “holistic” methods. The discrete approach to data analysis refers to limited evaluation of peak stresses in the dataset, while the holistic approach refers to comprehensive evaluation of the complete stress distribution data, not only peak stress values. This study suggested that to better understand the stress distribution at steel I-girder bridges, and role cross-frames play in it, a holistic approach is needed to analyze the stress data. Furthermore, this study found that removing cross-frame from the bridge did not substantially affect stress distributions throughout the bridge at both elastic and post-elastic load levels. The following sections review main findings from the dissertation’s three main chapters: a) finite element modeling, validation, and calibration; b) evaluation of FEA parametric study data using “discrete” and “holistic” metrics; and c) multiway analysis.

.

6.1.1 Finite Element Modeling, Validation, and Calibration

A finite element model of a steel I-girder bridge labeled “7R” was built and evaluated. This bridge had been previously destructively tested, and the data obtained from that experiment was used for the finite element model (FEM) validation and calibration. The validation results showed that the FE modeling techniques used were accurate, with the average FE results being very close to expected theoretical values for two metrics that were evaluated (4.1% and 2.0% errors respectively). Furthermore, three main advances were made with respect to currently employed FEA modeling techniques:

a) implementation of uniform and conforming finite element mesh across bridge components to enable holistic” evaluation of FEA data and robust computational performance even in the presence of material and geometric non-linearity;

b) using shell elements without offset to model cross-frames;

c) using tie constraints to control composite action between the concrete deck and steel girders.

6.1.2 Data Evaluation of FEA Parametric Study Data Using “Discrete” and “Holistic” Metrics

A total of 25 FEA models were built and analyzed for the purpose of evaluating the role of cross-frames in stress distribution at steel I-girder bridges. Two cross-frame designs (K-frame vs. X-frame) and two cross-frame layouts (inline vs. staggered) at five skews (0°, 25°, 46°, 55° and 63°) were parameters that were varied in the parametric study. Additional FE models without cross-frames (No-frame) were added at each bridge skew. Discrete and holistic evaluation of FEA data were conducted.

Discrete evaluation of FEA data showed that steel I-girder bridges have significant system capacity not accounted for by current bridge designs. Average system capacity for the steel I-girder bridges analyzed in this work is 16.0 HS-20 trucks. That means that current bridge live load capacity is underestimated by factor of 16 for the subject bridges, ignoring lane load effects. Interestingly, results showed that No-frame modes (models with cross-frame removed) had larger system level capacity than other cross-frame models at 0°, 25° and 63° skews. Furthermore, “discrete” evaluation metrics showed that bridge models without cross-frames have the largest average system capacity (16.6 HS-20 trucks) of all FEA models. In particular, the “No-frame“ model at 63° skew had the largest overall capacity (19.4 HS-20 trucks).

Four “holistic” metrics (percent of component yielded, Total Lateral Bending Energy Expenditure (TLBE), Performance Index (PI) and Chi-squared Distance (CsD)) were introduced for FEA data evaluation in order to comprehensively assess stress distributions throughout the bridge. TLBE showed that skewed bridges are exposed to significantly larger lateral bending actions than tangent (0° skew) bridges regardless of the load level. The results also showed that bridges with staggered cross-frame layouts have significantly larger TLBE than bridges with inline layouts regardless of the load level. And bridges with cross-frames in general have higher TLBE than bridges without cross-frames.

Performance of cross-frame designs was measured by PI (a scaled ratio of the applied load to the percent of girder yielding), and the results showed that on average bridges without cross-frames had higher PI at first yield load level, but lower PI at system yield load level when compared to bridges with cross-frames. However, even at system yield load level, in 70% of the cases, No-frame models outperformed or performed equal to cross-frames models as quantified by PI.

Additionally, another holistic metric (Chi-square Distance) showed examples where the difference in stress distribution between models with cross-frames and models without cross-frames at all bridge skews and all load levels is negligible. For example, the Chi-squared Distances showed that differences in stress distributions between models with the same cross-frame designs but different layouts can be larger than the difference in stress distributions between models with cross-frames and models without cross-frames. In other words, CsD showed that the difference in stress distributions between K-frame and X-frame designs at some skews is larger than the difference in stress distributions between K-frame and No-frame models or X-frame and No-frame models. Furthermore, at design load level for both skewed and tangent bridges, in only 49% of the cases on average, cross-frames presence did affect girder stress distribution. Furthermore, deck results show that overall average RO is 40% at the design load. Remember that low RO indicates small contribution of cross-frames in stress distribution and vice versa. This means that on average, in 60% of the cases, the presence of cross-frames did not affect stress distribution in decks. This finding cast doubts on prevailing assumptions in current bridge design codes, which state that cross-frames play an important role in stress distribution of traffic loads for in-service bridges.

6.1.3 Multiway Analysis of FEA Data

Analyzing complex data can be very challenging, especially if one of the goals of the analysis is discovering the trends in a multidimensional dataset. One of the methods available for achieving this goal is a Tucker decomposition method. The goal of using this method was to explore the effect that cross-frame removal in steel I-girder highway bridges has on stress distributions at different load levels due to different cross-frame designs and bridge skews. Four main findings resulted from this analysis. The first one was that tensor decomposition could be a useful data exploration tool in bridge engineering. It was also found that intermediate values of bridge skew behave differently from tangent or highly skewed bridges, which are more similar to one another, in terms of differences in stress distribution with and without cross-frames. The third finding was that cross-frame design (K-frame vs X-frame) contributes more to the difference in stress distribution between no-frame models and cross-frame models than cross-frame layout (staggered vs. inline), although K-frame and X-frame configurations did not have the same axial or bending stiffness in this work, which may be a reason for this result. And the fourth finding was that difference in stress distributions in deck are not associated with the difference in stress distribution in girders. This indicates that different stress distribution mechanisms are associated with these two load carrying systems.

6.2 Conclusion

Although discrete analysis is deemed sufficient when analyzing certain bridge behaviors, it was shown that this data approach is not sufficient to quantify the role that cross-frames play in stress distribution in steel I-girder bridges, especially at post-elastic load levels. The results also showed that using holistic evaluations, such as Total Lateral Bending Energy Expenditure, Performance Index and Chi-squared Distance, the author was able to effectively quantify how the presence of absence of cross-frames affect stress distributions throughout the bridge. The results indicate that removing cross-frames from bridges did not substantially affect stress distributions throughout the bridge. This finding is an important contradiction to current bridge engineering practice which assumes cross-frames play a significant role in stress distribution in steel I-girders in general and at skewed I-girders in particular. Furthermore, using a new multiway data analysis method, the author was able to extract information form the data that was not intuitive or clearly visible if traditional data analysis tools were used. For example, the results obtained by Tucker Decomposition indicate that intermediate values of bridge skew behave differently from tangent or highly skewed bridges, which are more similar to one another, and that cross-frame design (K-frame vs X-frame) rather than cross-frame layout (staggered vs. inline) contributes to the difference in stress distribution between bridges with cross-frames and bridges without cross-frames.

6.3 Recommendations

There are over 80,000 simply supported steel I-girder bridges in the USA and 21% of these bridges are skewed (NBI, 2015). Typical configurations of these bridges have cross-frames or diaphragms as lateral bracing members. Although one of the intended roles of cross-frames is to facilitate distribution of traffic loads among girders, many undesirable results are also associated with cross-frames. For example, fatigue cracks due to out-of-plane stresses (see Section 2.4.3), fit-up erection stresses (see Section 2.4.4), unwanted load paths and "nuisance" stresses (see Section 2.4.2), as well as the increased labor and material costs associated with the installation of cross-frames. Sometimes these problems are amplified by the presence of the skew. It is obviously desirable to prevent these undesirable consequences. On the other hand, the results from this study indicate that cross-frames play a very limited role in stress distribution in steel I-girder bridges and no role in bridge system capacity. While cross-frames intended role during bridge construction is invaluable, their role during service was insignificant for the simple span bridges evaluated in this work.

The question resulting from these observations is: if cross-frames do not perform the role for which they have been designed in service, should current implementation of cross-frames be continued? Furthermore, the finding of this study questions the currently implemented design practice of placing cross-frames in staggered layouts in skewed bridges. The origin of staggered layouts is based on the notion that the cross-frames closest to the supports of highly skewed bridges could induce large lateral bending stresses in the girders that they brace. Therefore, design recommendations were implemented in order to move these cross-frames farther from the end of the girder, towards mid-span. To conform to this recommendation and at the same time keep cross-frame spacing uniform, bridge designers were forced to stagger the cross-frames, significantly complicating bridge erection procedures. However, the results from this study showed that having large unbraced girder lengths (as long as sufficient bracing to prevent buckling of the compression flange is provided, e.g., via a composite concrete deck) will not affect overall performance of the bridge in terms of stress distribution or system capacity, and therefore there is no need to for complex staggered layouts.

Furthermore, current AASHTO (2015) and many Departments of Transportations specifications do not allow installing parallel to the skew cross-frames for skews larger than 20°. The main reason why AASHTO (2015) does not allow parallel to the skew placement is because of "concerns about increased cross-frame flexibility and reduced effectiveness in distributing live loads" (Hassel, et al. 2013). Considering that average cross-frame stiffness is order of magnitudes larger that required for the lateral bracing purposes (Mertz, 2001), that means that only reduced effectiveness in distributing live loads should be a concern for parallel to the skew placement. Since the results from this study indicate that cross-frames play very limited role in stress distribution (especially at highly skewed bridges), the need for these limitations when designing skewed bridges is rightly questioned.

Finally, this study suggests implementing a "3R" approach in the design of cross-frames for simply supported steel I-girder bridges:

1) Remove intermediate cross-frames in the bridge structures where lateral-torsional buckling limits allow such action.

2) Resize all cross-frames so they only satisfy minimum slenderness requirements for bracing members.

3) Relax all remaining connections between intermediate cross-frames and girders.

Implementing these steps could lead to:

a) minimization of potential fatigue problems caused by out-of-plane distortion of the girders through reducing the number and stiffness of cross-frames;

b) reduction of construction costs in terms of eliminating labor intensive installation of cross-frames and their connections; and

c) avoidance of fit up stresses during erection, for which the structure may not be adequately designed.

6.4 Future Research

Future research should instigate and investigate changes in how cross frames are analyzed, designed and, most importantly, deployed, especially for skewed bridges. The proposed overall goal of such research is to determine if the current practices regarding analysis and proportioning of cross-frames in steel I-girder bridge systems can be revised so that the quantity of cross-frames is (a) reduced or (b) eliminated entirely for certain bridge configurations. This requires analyzing the short term and long term effects of relaxing cross-frame requirements on overall behavior of the bridge. This could be accompanied by cost-benefit analyses of short term and long term effects of removing, reducing, and/or relaxing the cross-frames in bridges. Expanding the scope of the research from simply supported to continuously supported bridges should also be one of the objectives of future studies.

Future research could also explore further advancement of the holistic assessment of stress distribution data piloted in this work. This could involve improving the current or designing new numerical instruments for assessment of stress distribution data.

REFERENCES

American Association of State Highway and Transportation Officials –AASHTO. (2015). “LRFD Bridge Design Specifications”. *6th Edition.* AASHTO, Washington, DC.

Federal Highway Administration. (2015). National Bridge Inventory (NBI) Dataset. http://www.fhwa.dot.gov/bridge/nbi/ascii.cfm. Accessed 02/01/2017

Hassel, H. L., Bennett, C. R., Matamoros, A. B., Rolfe, S. T. (2013). “Parametric analysis of cross-frame layout on distortion-induced fatigue in skewed steel bridges”. *J Bridge Eng.*,10.1061/(ASCE)BE.1943-5592 .0000388,601–611.

Mertz, D. R. (2001). Designer's Guide to Cross-frame Diaphragms. American Iron and Steel Institute.

APPENDIX

APPENDIX A

Table A.1. Girder Chi-square Distances at design load level

	Design	K-INLINE	K-STAGG	X-INLINE	X-STAGG	NO-FRAME
0°	K-INLINE	0	122	2570	2366	286
	K-STAGG		0	2403	2055	425
	X-INLINE			0	142	2640
	X-STAGG				0	2547
	NO-FRAME					0
25°	K-INLINE	0	390	3499	2837	797
	K-STAGG		0	3516	2556	825
	X-INLINE			0	553	4968
	X-STAGG				0	3734
	NO-FRAME					0
46°	K-INLINE	0	543	3402	3752	3610
	K-STAGG		0	3008	2666	3129
	X-INLINE			0	474	177
	X-STAGG				0	508
	NO-FRAME					0
55°	K-INLINE	0	877	3679	3832	420
	K-STAGG		0	3082	2463	632
	X-INLINE			0	544	3191
	X-STAGG				0	3363
	NO-FRAME					0
63°	K-INLINE	0	445	2385	2140	287
	K-STAGG		0	2590	1530	662
	X-INLINE			0	948	3004
	X-STAGG				0	2616
	NO-FRAME					0

Table A.2 Deck Chi-square Distances at design load level

	Design	K-INLINE	K-STAGG	X-INLINE	X-STAGG	NO-FRAME
0°	K-INLINE	0	3	326	325	59
	K-STAGG		0	284	284	37
	X-INLINE			0	1	153
	X-STAGG				0	153
	NO-FRAME					0
25°	K-INLINE	0	4	293	302	42
	K-STAGG		0	246	257	21
	X-INLINE			0	4	158
	X-STAGG				0	168
	NO-FRAME					0
46°	K-INLINE	0	1	190	196	242
	K-STAGG		0	170	176	222
	X-INLINE			0	1	20
	X-STAGG				0	14
	NO-FRAME					0
55°	K-INLINE	0	1	145	154	6
	K-STAGG		0	140	152	7
	X-INLINE			0	2	115
	X-STAGG				0	119
	NO-FRAME					0
63°	K-INLINE	0	0.1	140	90	8
	K-STAGG		0	144	94	7
	X-INLINE			0	18	112
	X-STAGG				0	71
	NO-FRAME					0

APPENDIX B

Table B.1 Girder Chi-square Distances at first yield load level

	Design	K-INLINE	K-STAGG	X-INLINE	X-STAGG	NO-FRAME
0°	K-INLINE	0	321	1950	1532	1012
	K-STAGG		0	2195	1217	1289
	X-INLINE			0	1239	1383
	X-STAGG				0	1222
	NO-FRAME					0
25°	K-INLINE	0	668	3448	4221	1568
	K-STAGG		0	3605	4953	2428
	X-INLINE			0	1491	3930
	X-STAGG				0	3614
	NO-FRAME					0
46°	K-INLINE	0	2015	3006	3949	5235
	K-STAGG		0	4572	2694	7285
	X-INLINE			0	3082	1633
	X-STAGG				0	5293
	NO-FRAME					0
55°	K-INLINE	0	1869	4193	3680	1059
	K-STAGG		0	6685	2788	3332
	X-INLINE			0	3030	3936
	X-STAGG				0	3195
	NO-FRAME					0
	K-INLINE	0	504	2536	1679	756
	K-STAGG		0	3408	1510	1576
	X-INLINE			0	2055	3069
	X-STAGG				0	2077
	NO-FRAME					0

Table B.2 Deck Chi-square Distances at first yield load level

	Design	K-INLINE	K-STAGG	X-INLINE	X-STAGG	NO-FRAME
0°	K-INLINE	0	51	255	175	128
	K-STAGG		0	254	195	151
	X-INLINE			0	54	89
	X-STAGG				0	42
	NO-FRAME					0
25°	K-INLINE	0	39	312	457	102
	K-STAGG		0	287	451	86
	X-INLINE			0	105	133
	X-STAGG				0	258
	NO-FRAME					0
46°	K-INLINE	0	57	320	161	434
	K-STAGG		0	347	198	480
	X-INLINE			0	104	123
	X-STAGG				0	150
	NO-FRAME					0
55°	K-INLINE	0	53	309	185	67
	K-STAGG		0	349	238	115
	X-INLINE			0	76	172
	X-STAGG				0	77
	NO-FRAME					0
63°	K-INLINE	0	47.7	183	70	36
	K-STAGG		0	198	101	73
	X-INLINE			0	101	121
	X-STAGG				0	27
	NO-FRAME					0

APPENDIX C

Table C.1 Girder Chi-square Distances at system yield load level

	Design	K-INLINE	K-STAGG	X-INLINE	X-STAGG	NO-FRAME
0°	K-INLINE	0	225	1317	1439	555
	K-STAGG		0	1577	1363	330
	X-INLINE			0	236	1768
	X-STAGG				0	1800
	NO-FRAME					0
25°	K-INLINE	0	282	4874	4064	442
	K-STAGG		0	4537	3598	209
	X-INLINE			0	411	4876
	X-STAGG				0	4202
	NO-FRAME					0
46°	K-INLINE	0	335	5076	4919	5251
	K-STAGG		0	4538	4172	4526
	X-INLINE			0	230	99
	X-STAGG				0	151
	NO-FRAME					0
55°	K-INLINE	0	291	4423	4538	226
	K-STAGG		0	3583	3533	156
	X-INLINE			0	155	4128
	X-STAGG				0	4229
	NO-FRAME					0
63°	K-INLINE	0	66	2418	1417	191
	K-STAGG		0	2332	1245	203
	X-INLINE			0	435	2673
	X-STAGG				0	1605
	NO-FRAME					0

Table C.2 Deck Chi-square Distances at system yield load level

		K-INLINE	K-STAGG	X-INLINE	X-STAGG	NO-FRAME
0°	K-INLINE	0	18	200	244	87
	K-STAGG		0	155	190	57
	X-INLINE			0	40	164
	X-STAGG				0	153
	NO-FRAME					0
25°	K-INLINE	0	21	287	329	86
	K-STAGG		0	222	283	64
	X-INLINE			0	83	205
	X-STAGG				0	218
	NO-FRAME					0
46°	K-INLINE	0	22	251	298	321
	K-STAGG		0	195	247	278
	X-INLINE			0	39	115
	X-STAGG				0	84
	NO-FRAME					0
55°	K-INLINE	0	55	217	253	59
	K-STAGG		0	165	212	70
	X-INLINE			0	43	162
	X-STAGG				0	167
	NO-FRAME					0
63°	K-INLINE	0	31.9	157	138	48
	K-STAGG		0	131	115	51
	X-INLINE			0	31	156
	X-STAGG				0	139
	NO-FRAME					0

APPENDIX D

Table D.1. Data structure of 4D tensor (5x4x3x4)

		Design				First Yield				System Yield			
	Skew	**K-INLINE**	**K-STAGG**	**X-INLINE**	**X-STAGG**	**K-INLINE**	**K-STAGG**	**X-INLINE**	**X-STAGG**	**K-INLINE**	**K-STAGG**	**X-INLINE**	**X-STAGG**
BF	**0°**	743	411	1083	1026	1369	1608	1688	1803	270	238	300	268
	25°	370	378	343	718	766	1736	1386	1243	88	116	104	106
	46°	516	241	484	226	2122	1963	1426	2583	32	61	54	99
	55°	256	372	201	583	980	2067	1460	2570	64	87	111	132
	63°	112	143	260	534	531	768	1643	2347	73	323	84	146
WEB	**0°**	81	55	374	359	299	698	607	1383	246	563	668	881
	25°	68	36	408	385	190	1906	1599	771	304	622	1167	1358
	46°	504	460	90	47	3108	2711	423	2468	596	837	146	405
	55°	111	58	465	392	202	1587	676	2101	122	319	1089	1205
	63°	19	20	531	257	201	237	695	1777	236	736	862	990
TF	**0°**	11	21	1134	1158	1051	1377	958	635	157	297	2553	2504
	25°	66	83	1929	1961	179	1936	3169	2602	372	514	4775	3926
	46°	2054	1935	0.2	9	6342	6087	947	3096	3921	3628	275	491
	55°	12	18	2184	2002	317	2857	2912	501	110	388	3533	3350
	63°	103	87	1942	1278	964	942	2263	908	333	545	2813	2175
D	**0°**	59	37	153	153	128	151	88	37	87	57	163	152
	25°	31	20	279	280	64	156	149	149	66	65	200	214
	46°	400	357	15	9	556	535	151	240	323	309	104	100
	55°	25	12	155	154	76	181	157	50	66	66	196	203
	63°	4	3	94	41	116	27	200	53	382	357	364	366